Kinetic ballooning mode studies and the treatment of electromagnetic microinstabilities and turbulence in complex geometry

Robert Davies

DOCTOR OF PHILOSOPHY

UNIVERSITY OF YORK

PHYSICS

October 2022

Abstract

Magnetically confined thermonuclear fusion is promising as a future power source. However, the viability of fusion power plants is strongly influenced by how well the thermal energy can be confined in the plasma fuel. Often, the dominant process governing confinement is microinstability-driven plasma turbulence. This thesis studies microinstabilities and turbulence using gyrokinetic simulations, which may ultimately inform fusion reactor design and operation.

The effect of plasma triangularity on stability in spherical tokamaks (STs) is examined using linear simulations of hypothetical ST equilibria. It is found that the kinetic ballooning mode (KBM), an electromagnetic pressure-driven microinstability, likely prohibits negative triangularity in ST power plants, since negative triangularity closes the “second stability window” for $n = \infty$ ideal magnetohydrodynamic (MHD) ballooning modes. ST equilibria with positive triangularity can access the second stability window, although remain weakly unstable to KBMs.

Secondly, microinstabilities are studied for the optimised stellarator Wendelstein 7-X (W7-X). Electrostatic “stability valley” results are reproduced using `stella`: a gyrokinetic code which offers flexibility in time-marching schemes by using operator splitting. `stella` is extended to include $A_{||}$ and $B_{||}$ fluctuations linearly using both implicit and explicit schemes. Benchmarking against the code `GS2` shows good agreement for electromagnetic tokamak simulations. Using this implementation, the W7-X stability valley at finite β (=plasma pressure/magnetic pressure) is preliminarily explored. The electromagnetic instabilities observed may be relevant to future W7-X experiments.

Finally, a non-interpolating semi-Lagrangian scheme, aiming to efficiently simulate electromagnetic turbulence by eliminating the Courant-Freidrichs-Lewy timestep constraint in nonlinear gyrokinetics, is implemented in `stella`. A new operator splitting scheme is developed and used to mix single and multi-step numerical methods. Unfortunately, nonlinear tests show low accuracy and currently unexplained numerical instability. Elucidating the reasons for this would be an interesting area of future research.

Contents

List of Tables

List of Figures

Author's declaration

I declare that this thesis is a presentation of original work and I am the sole author. This work has not previously been presented for an award at this, or any other, University. All sources are acknowledged as References.

The present work led to the publication of the following article: R. Davies, D. Dickinson and H. Wilson *Kinetic ballooning modes as a constraint on plasma triangularity in commercial spherical tokamaks*, Plasma Phys. Control. Fusion **64** 105001. DOI:`https://doi.org/10.1088/1361-6587/ac8615` . The material presented in chapter 5 is heavily based on this publication.

Acknowledgements

The author would like to acknowledge the following people, without whom this thesis would not have been written:

Firstly, I would like to thank my supervisor, Dr David Dickinson, to whom I owe an enormous debt of gratitude. Over the course of my PhD he has provided support, physics insight, encouragement, inspiration and debugging in vast quantities. He is not only an excellent scientist but an excellent supervisor.

I would also like to thank my close collaborators, Professor Michael Barnes and Dr Jason Parisi. They are brilliant scientists and collaborators, and have provided many hours of physics discussion and assistance. Professor Michael Barnes' supervision for the `stella` code development has been invaluable and I am extremely grateful to him.

I would also like to thank Professor Howard Wilson, a collaborator and co-author, who has seemingly limitless knowledge of tokamaks and their instabilities. Many thanks also to Dr José-Manuel García-Regaña, a collaborator based at CIEMAT, Madrid, as well as Hanne Thienpondt and Antonio González-Jerez. I would like to thank my other research collaborators, Dr Stephen Biggs-Fox and Dr Michail Anastopoulos-Tzanis, and thesis advisory panel member Professor Ben Dudson. There are many other scientists I have learnt from and exchanged ideas with in person, by email, video call and conference throughout my PhD, but these are too numerous to name.

Apart from my collaborators, but just as important, this thesis would also not have happened without the large number of people who have supported me in one way or another. I would like to thank my family for their love and care and, in the case of my mother, their diligent proofreading. I would like to thank my Centre for Doctoral Training (CDT) cohort and the community of staff and students at the York Plasma Institute, who have shown great friendship, academic & non-academic support and cheerful bonhomie. I would like to thank Dr Koki Imada for his wild outdoor schemes and diligent proofreading. I would like to thank my regular climbing, pub-going and dancing friends who have been a source of fun and comradeship. I would like to thank Thomas Wright for his eternal friendship and diligent proofreading. I would like to thank my wonderful housemates for bringing me happiness on a daily basis. Finally, I would like to thank the North British Sword dancers, Black Swan rapper the Sallyport Sword dancers and bringing me their own distinctive brands of fun, usually unexpectedly and in short bursts.

Chapter 1

Introduction and Background

1.1 Controlled thermonuclear fusion

It has long been known (see e.g. [1, 2]) that the fusing of light atomic nuclei releases energy, owing to differences in the average binding energy per nucleon of the reactants and products. This has motivated efforts to use controlled nuclear fusion as a power source (for a brief history and current status, see [3] and [4]). Fusion now forms part of the energy policy of several nations (see e.g. [5, 6]). Benefits of fusion energy include reliability and security of energy supply, high energy-density of reactants and relatively benign waste products. However, there are serious challenges which must be overcome in order to realise economical fusion power plants. As of today, there are no fusion devices which provide a net surplus of electricity (or indeed a net surplus of energy in a useful way.)

Fusion requires the reactant nuclei to overcome their electrostatic repulsion (the "Coulomb barrier") and this behooves a thermonuclear approach, whereby the fuel is confined and heated to sufficiently high density and temperature. Each reactant nucleus undergoes (on average) many collisions, and a small fraction of these are sufficiently energetic for fusion to occur. Confinement of fuel at high temperature is challenging, and thus virtually all fusion efforts focus on the DT reaction:

$$^2_1\mathrm{D} +^3_1 \mathrm{T} \rightarrow^4_2 \mathrm{He} +^1_0 \mathrm{n} \tag{1.1.1}$$

(where $^2_1\mathrm{D},^3_1\mathrm{T},^4_2\mathrm{He},^1_0\mathrm{n}$ respectively denote deuterium, tritium, helium-4 ()and a neutron), which has a high reactivity at relatively low temperatures ($\sim 10 - 100$keV) [7] (hydrogenic reactants, in general, have higher reactivities at lower temperatures as their low charge minimises the Coulomb barrier). The DT reaction also has a high energy yield (17.6MeV; $E_n = 14.1$MeV in the neutron and $E_\alpha =$

3.5MeV in the α (i.e. the helium-4) particle). Deuterium is naturally abundant and although tritium is not, it can be synthesised by bombarding lithium with energetic neutrons. Since 14.1MeV neutrons are a DT product, it is thought that DT reactors can be self-sustaining by breeding their own supply of tritium [4].

The problem remains to confine the mixture of DT fuel at sufficiently high temperature and density for fusion to occur. A popular metric parametrising this is the fusion triple product, $nT\tau_E$ [8]. By considering the balance of heating power (externally injected heating P_H plus fusion α heating P_α) with the power lost from the fuel (characterised by the *energy confinement time* τ_E, $\frac{\mathrm{d}W}{\mathrm{d}t} = -P_l \simeq -W/\tau_E$ where W is the stored thermal energy of the fuel and P_l the power loss rate), it can be shown that the externally provided heating power must satisfy

$$P_H = P_l - P_\alpha \simeq \left(\frac{3nT}{\tau_E} - \frac{n^2}{4} \langle \sigma v \rangle E_\alpha \right) V, \tag{1.1.2}$$

where n is the DT fuel number density, T the temperature, $\langle \sigma v \rangle$ the reactivity of reaction (1.1.1) and V the fuel volume. If one further applies the fit $\langle \sigma v \rangle \simeq 1.1 \times 10^{-24} T^2 \mathrm{m}^3 \mathrm{s}^{-1}$ (an approximation which is reasonable for $10\text{keV} < T < 20\text{keV}$) and sets $P_H = 0$ one finds:

$$nT\tau_E = 3 \times 10^{21} \mathrm{m}^{-3} \mathrm{keV} \cdot \mathrm{s}, \tag{1.1.3}$$

which is a requirement for a self-heated (or “ignited”) fuel, and provides a ballpark estimate for reactor viability.

To date, the most promising scheme to overcome the challenge of confinement (i.e. to satisfy (1.1.3)) is magnetic confinement fusion (MCF), which utilises strong magnetic fields. Since the heated fuel is a plasma (a highly ionised gas), the constituent particles experience a Lorentz force **F**:

$$\mathbf{F} = q(\mathbf{E} + \mathbf{v} \times \mathbf{B}), \tag{1.1.4}$$

where q is the particle charge, **v** is the velocity and **E** and **B** are the electric and magnetic fields respectively. **F** constrains particle motion perpendicular to **B** (to leading order) to the particle “Larmor orbit” (see section 1.2.2), thus confining heat and particles.

However, the apparent simplicity of the MCF concept belies the enormous complexity of designing and building a working machine. A principle (and unavoidable) difficulty is the plasma itself, which is extremely difficult to model accurately. Although the dynamics of each charged particle may be almost completely described by the Lorentz force (1.1.4) and Maxwell's equations:

$$\nabla \cdot \mathbf{E} = \frac{\rho}{\epsilon_0} \tag{1.1.5}$$

$$\nabla \times \mathbf{E} = -\frac{\partial \mathbf{B}}{\partial t} \tag{1.1.6}$$

$$\nabla \cdot \mathbf{B} = 0 \tag{1.1.7}$$

$$\nabla \times \mathbf{B} = \mu_0 \mathbf{j} + \mu_0 \epsilon_0 \frac{\partial \mathbf{E}}{\partial t} \tag{1.1.8}$$

(where ρ is the charge density, ϵ_0 the permittivity of free space, t is time, μ_0 the permeability of free space and **j** the charge density), particle interactions are long-range and thus each particle simultaneously interacts with many others. This gives rise to complex, collective and multiscale phenomena. One example of this is plasma turbulence, which affects reactor performance as it effectively increases the mobility of the plasma across equilibrium magnetic field lines. In many MCF designs, including the front-running device, the tokamak, turbulence is often the dominant cross-field transport mechanism, and thus the greatest factor influencing $nT\tau_E$. Understanding the causes and consequences of plasma turbulence is therefore of great importance for commercial fusion power plants (and is the main focus of this work).

Before discussing plasma turbulence, I first describe some basic magnetised plasma phenomena. This is not intended to be an exhaustive catalogue, but covers some concepts which will recur throughout this thesis.

1.2 Properties of magnetised plasmas

1.2.1 Definition of a plasma

A definition that describes fusion plasmas well is given by Chen [9]: "*A plasma is a quasi-neutral gas of charged and neutral particles which exhibits collective behaviour.*" "Quasi-neutral" means that the net electrical charge of any small parcel of plasma is very close to zero and thus large electrostatic potentials do not exist in the plasma. The characteristic length scale above which the plasma is quasi-neutral is the Debye length, λ_D, given by [9]:

$$\lambda_D = \sqrt{\frac{\epsilon_0 k_B T_e}{n e^2}}, \tag{1.2.1}$$

where k_B is Boltzmann's constant, T_e the electron temperature, n the electron number density and e the fundamental unit of electronic charge. It can be shown [9] that the plasma is quasi-neutral on length scales $L > \lambda_D$ provided that the number of particles N_D within the Debye sphere (a sphere of radius λ_D) is large. N_D is sometimes referred to as the "plasma parameter".

"Collective behaviour" means that the dominant mechanisms affecting particle trajectories are long-range and nonlocal, such that many particles interact simultaneously. In the case of plasma, particle dynamics are governed by electromagnetic fields; each particle interacts with a large number of nearby particles via the electromagnetic force. This differs from a conventional gas, in which the trajectory of each particle is dominated by local, short-range collisions. The requirement that plasma exhibits collective behaviour can be formalised as a requirement that the timescale of plasma phenomena (say, an oscillation with frequency ω) is less than the typical timescale over which collisions randomise particle trajectories τ_c.

Thus, the definition encompasses three conditions for a gas to be considered a plasma:

$$\lambda_D \ll L \tag{1.2.2}$$

$$N_D \equiv \frac{4}{3}\pi\lambda_D^3 n \gg 1 \tag{1.2.3}$$

$$\omega\tau_c > 1, \tag{1.2.4}$$

where L is the length scale of the system. Eq. (1.2.2) states that the Debye length is very small compared to the typical length scales in the plasma; eq. (1.2.3) states that there are a very large number of particles within the Debye sphere; eq. (1.2.4) states that collisions do not dominate particle interactions.

1.2.2 Definition of a magnetised plasma

For simplicity, consider a particle with mass m and charge q in a uniform magnetic field $\mathbf{B} = B\hat{\mathbf{z}}$ in the absence of any other forces. Inserting eq. (1.1.4) into Newton's second law gives

$$m\frac{\mathrm{d}\mathbf{v}}{\mathrm{d}t} = m\begin{pmatrix}\mathrm{d}v_x/\mathrm{d}t\\ \mathrm{d}v_y/\mathrm{d}t\\ \mathrm{d}v_z/\mathrm{d}t\end{pmatrix} = q\mathbf{v}\times\mathbf{B} = q\begin{pmatrix}v_x\\ v_y\\ v_z\end{pmatrix}\times\begin{pmatrix}0\\ 0\\ B\end{pmatrix} = q\begin{pmatrix}Bv_y\\ -Bv_x\\ 0\end{pmatrix}. \tag{1.2.5}$$

Since $\mathrm{d}v_z/\mathrm{d}t = 0$, this magnetic field has no effect on the parallel velocity. The coupled equations in **x** and **y** can be solved to give

$$\frac{\mathrm{d}^2 v_{x(y)}}{\mathrm{d}t^2} = -\frac{q^2 B^2}{m^2} v_{x(y)}, \tag{1.2.6}$$

which describes harmonic motion, known as a "Larmor motion" or "gyromotion", with frequency $\Omega_{\text{gyro}} = \frac{qB}{m}$. The Larmor radius or gyro-radius, ρ_{gyro}, is simply

$$\rho_{\text{gyro}} = \left|\frac{v_\perp}{\Omega_{\text{gyro}}}\right|, \tag{1.2.7}$$

where $v_\perp$ is the perpendicular particle speed. The typical spatial scale of the Larmor motion is characterised by the thermal Lamor radius $\rho_{\text{gyro},th} \equiv |v_{th}/\Omega_{\text{gyro}}|$ where v_{th} is the thermal velocity. This implies $\rho_{\text{gyro},th} \propto m^{-1/2}$; less massive particles have bigger gyrofrequencies but smaller gryro-radii.

A plasma may be considered "strongly magnetised" if the particle motion is determined, to leading order, by gyromotion i.e. if gyromotion is faster than any other physical behaviour of interest:

$$\left|\frac{\Omega_{\text{gyro}}}{\omega}\right| \gg 1, \tag{1.2.8}$$

where again, ω is the frequency of some physical phenomenon (say, a plasma oscillation.) All plasmas considered in this work satisfy eq. (1.2.8).

1.2.3 Conserved quantities and the "mirror force"

It can be shown that the total particle energy and the particle magnetic moment $\mu \equiv mv_\perp^2/2B$ are conserved as a particle moves in an electromagnetic field, provided that:

1. The electric and magnetic fields are static and approximately constant over ρ_{gyro}
2. The particle does not undergo any collisions (since collisions allow the particle to exchange energy and momentum with other particles)
3. The non-relativistic limit is taken, such that (for example) the cyclotron radiation of gyrating particles is neglected.

To show energy is conserved, one combines the Lorentz force law (1.1.4) with Newton's second law of motion and dots with **v**:

$$m\frac{\mathrm{d}\mathbf{v}}{\mathrm{d}t} = q(\mathbf{E} + \mathbf{v} \times \mathbf{B}) \tag{1.2.9}$$

$$m\mathbf{v} \cdot \frac{\mathrm{d}\mathbf{v}}{\mathrm{d}t} = \frac{m}{2}\frac{\mathrm{d}v^2}{\mathrm{d}t} = q(\mathbf{v} \cdot \mathbf{E} + \underbrace{\mathbf{v} \cdot (\mathbf{v} \times \mathbf{B})}_{=0}). \tag{1.2.10}$$

Rewriting $\mathbf{v} \cdot \mathbf{E}$ as the convective derivative of the electrostatic potential ϕ:

$$\mathbf{v} \cdot \mathbf{E} = -\mathbf{v} \cdot \boldsymbol{\nabla}\phi = -\frac{\partial \mathbf{x}}{\partial t} \cdot \frac{\partial \phi}{\partial \mathbf{x}} = -\left(\frac{\mathrm{d}\phi}{\mathrm{d}t} - \cancel{\frac{\partial \phi}{\partial t}}\right) \tag{1.2.11}$$

and inserting into (1.2.10) yields

$$\frac{\mathrm{d}}{\mathrm{d}t}\left(\frac{1}{2}mv^2 + q\phi\right) = 0, \tag{1.2.12}$$

which expresses that the total energy is conserved.

A fairly straightforward proof of magnetic moment conservation is presented by Wesson [8], the key point being that μ is an adiabatic invariant, i.e. is conserved provided that B varies slowly along the trajectory of the particle. The conservation of energy and magnetic moment gives rise to an important physical effect known as the "mirror force". As a particle travels from a region of weak to strong B, $|v_\perp|$ increases to conserve μ. Since $(v_\parallel^2 + v_\perp^2)$ is also conserved (in the absence of an electric field), $|v_\parallel|$ falls; the particle experiences a force in the parallel direction. If the change in B from the weak field region (with $B = B_-$ and $v_\perp = v_{\perp -}$) to the strong field region (with $B = B_+$) is such that

$$\frac{v^2}{B_+} < \frac{{v_{\perp}}_{-}^{2}}{B_-}, \tag{1.2.13}$$

then the particle cannot enter the stronger field region because E and μ cannot simultaneously be conserved. This leads to particles becoming *trapped* in regions of weak magnetic field. Trapped particles can have important effects in MCF plasmas.

1.2.4 Particle drifts

Another important feature of magnetised plasmas is particle drifts, which typically arise from electric fields in the plasma or from an inhomogeneous magnetic field.

A starting point for this is to consider a particle in a uniform, constant magnetic field $\mathbf{B} = B_z\hat{\mathbf{e}}_z$

in the presence of a uniform force perpendicular to **B** ($\mathbf{F} = F_x\hat{\mathbf{e}}_x + F_y\hat{\mathbf{e}}_y$). The perpendicular velocity can be decomposed into $\mathbf{v} = \mathbf{v}_{\text{gyro}} + \mathbf{v}_1$ (where $\mathbf{v}_{\text{gyro}}$ is gyromotion) and the equation of motion becomes

$$m\frac{\mathrm{d}\cancel{\mathbf{v}_{\text{gyro}}} + \mathbf{v}_1}{\mathrm{d}t} = \mathbf{F} + q(\cancel{\mathbf{v}_{\text{gyro}}} + \mathbf{v}_1) \times \mathbf{B}, \tag{1.2.14}$$

and if $\mathbf{v}_1$ is assumed time-independent, the left hand side (LHS) vanishes. Crossing with **B** and rearranging, one finds

$$\mathbf{v}_{1\perp} = \frac{\mathbf{F} \times \mathbf{B}}{qB^2}. \tag{1.2.15}$$

Eq. (1.2.15) reveals that, in a magnetised plasma, a force **F** perpendicular to **B** will result in the particle drifting at a constant velocity in a direction mutually perpendicular to **F** and **B**. A physical picture for this behaviour is that the particle Larmor orbits are slightly deformed by **F**: ρ_{gyro} grows over half of the gyroperiod (when $\mathbf{v}_{\text{gyro}} \cdot \mathbf{F} > 0$ since $v_\perp$ increases) and shrinks over the other half. These nonuniform orbits give rise to a net drift superimposed on normal gyromotion. For a given force, the drift is mass-independent (more massive particles are less readily accelerated, but this is compensated by larger ρ_{gyro}).

Replacing **F** in (1.2.15) with the force arising from an electric field $\mathbf{F} = q\mathbf{E}$ reveals the $\mathbf{E} \times \mathbf{B}$ drift:

$$\mathbf{V}_{\mathbf{E}\times\mathbf{B}} = \frac{\mathbf{E} \times \mathbf{B}}{B^2}, \tag{1.2.16}$$

which is independent of the particle charge, mass and velocity (provided $q \neq 0$, $m \neq 0$, $v \neq 0$). If one considers a curved magnetic field and replaces **F** with a centrifugal force $\mathbf{F} = \frac{mv_\parallel^2}{R_C}\mathbf{R}_C$ (where $\mathbf{v} \cdot \mathbf{B}/B = v_\parallel$ and R_C is the radius of curvature), one finds the *curvature drift* $\mathbf{V}_C$:

$$\mathbf{V}_C = \frac{mv_\parallel^2}{qB^2}\frac{\mathbf{R}_C \times \mathbf{B}}{R_C^2}, \tag{1.2.17}$$

which is perpendicular to the field curvature and is charge-, mass- and velocity-dependent (although, for thermal particles, the drift appears mass-independent since $v_{\parallel,th} \propto m^{-1/2}$).

The final drift I derive is called the $\boldsymbol{\nabla}B$ drift, arising from a change in magnetic field strength perpendicular to **B**. If one assumes the length scale of the variation in B is much greater than the ρ_{gyro},

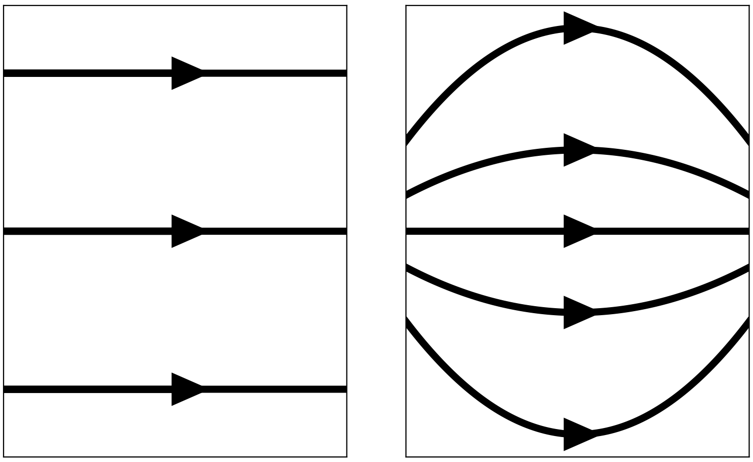

Figure 1.1: Left: a uniform magnetic field. Particles are not confined parallel to the field. Right: a "magnetic mirror". Most particles are confined by the "magnetic mirror" force, but a particular region of velocity space is unconfined, and this region is constantly repopulated from the rest of velocity space by collisions.

one can Taylor expand **B** around the guiding center. Inserting into Newton's law and considering the $\hat{\mathbf{e}}_x$ component gives

$$m\frac{\partial v_x}{\partial t} = qBv_y = qv_y\left(B_0 + \frac{v_\perp}{\Omega_{\text{gyro}}}\cos\bigl(\Omega_{\text{gyro}}t\bigr)\frac{\partial B}{\partial y}\right). \tag{1.2.18}$$

Taking $v_y = v_\perp\cos\bigl(\Omega_{\text{gyro}}t\bigr)$ and averaging over a single gyro-orbit, one finds

$$m\frac{\partial \bar{v}_x}{\partial t} = q\frac{v_\perp^2}{2\Omega_{\text{gyro}}}\frac{\partial B}{\partial y}. \tag{1.2.19}$$

Repeating the analysis for $\hat{\mathbf{e}}_y$, one arrives at an expression for $\mathbf{V}_{\boldsymbol{\nabla}B}$:

$$\mathbf{V}_{\boldsymbol{\nabla}B} = \frac{v_\perp}{2\Omega_{\text{gyro}}}\frac{\mathbf{B}\times\boldsymbol{\nabla}\mathbf{B}}{B^2}, \tag{1.2.20}$$

which is charge-dependent through Ω_{gyro} but, like $\mathbf{V}_C$, mass-independent for thermal particles.

1.3 MCF devices

A strong magnetic field ensures that particles are, to leading order, confined perpendicular to the field. The first challenge of an MCF device is therefore to confine the motion parallel to the field; a uniform magnetic field, such as shown in figure 1.1a, does not confine the plasma in the parallel direction.

One approach to this is the "magnetic mirror" concept (figure 1.1b), in which parallel motion is

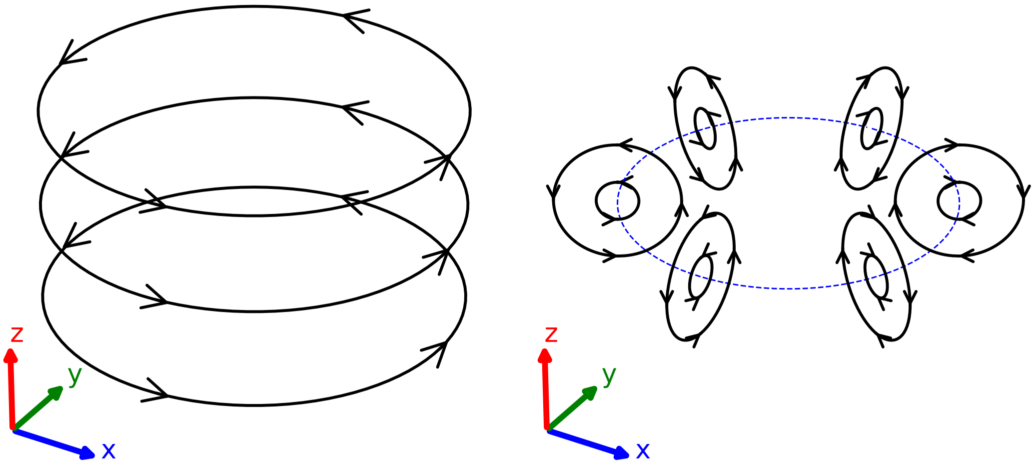

Figure 1.2: Left: A circular magnetic field (i.e. a toroidal plasma with $q = \infty$). Confinement is limited by particle drifts and the $1/R$ force. Right: A ring of closed magnetic loops (i.e. a toroidal plasma with a safety factor $q = 0$). Confinement is limited by the $1/R$ force, the Hoop force and plasma instabilities.

confined by a gradient in B. The varying field strength gives rise to the mirror force, trapping the particles in the region of low field. This concept has been explored fairly thoroughly (for a review see [10]) and is still the subject of research (e.g. [11]), but is currently not a front-running fusion MCF concept. A principal issue is that particles with sufficiently high $v_{\|}/v_{\perp}$ (i.e. sufficiently small μ) will escape from the ends of the magnetic trap. Since collisions act to randomise the velocity distribution of the particles, the region of phase space for which particles are not confined is continually being repopulated. Thus, confinement in mirror systems tends to be uncompetitively low.

A more promising approach is to shape the magnetic field into a closed volume, for example a circle, such that particles travelling along the field line remain in a fixed volume (such as shown in figure 1.2). This confines the plasma to leading order.

The next challenge is to confine the perpendicular motion to higher order. For example, a simple circular magnetic field (figure 1.2, left) gives rise to charge-dependent curvature drifts. Since these are charge-dependent, they establish a vertical electric field, and hence an outward $\mathbf{E} \times \mathbf{B}$ drift. The plasma is confined on the timescale of thermal streaming ($\mathcal{O}(1\mu\text{s})$ for a hypothetical device of size 1m with plasma temperature of 10keV) but not on the scale of particle drifts ($\mathcal{O}(100\mu\text{s})$ for this hypothetical device, assuming a magnetic field of 1T and a curvature radius and $\boldsymbol{\nabla} B$ length scale of 1m). An additional problem in this configuration is that the magnetic field, and hence magnetic pressure, is greater on the inboard side (i.e. at smaller radii) than on the outboard side. This results in a net force (sometimes called the "$1/R$" force [12]) which pushes the plasma outwards and also leads to a loss of confinement.

A ring of closed magnetic loops generated by driving a current toroidally in the plasma, such as figure 1.2b, also shows poor confinement. In this case, as well as the $1/R$ force, a force known as the “Hoop force” [12], arising from the interaction of the current with its induced magnetic field, also pushes the plasma outwards. Furthermore, this configuration is unstable to kink instabilities which cause the plasma to quickly deform and lose confinement [8].

Several decades of research into optimal confinement (for a review, see [13]) have led to several classes of device being widely accepted as plausible energy-producing MCF reactor concepts. In this thesis, I focus on the two currently most popular of these: the tokamak and the stellarator.

1.3.1 The tokamak

The tokamak is currently the most widely adopted MCF design (for an early, contemporaneous description see [14]; for an extensive review, see [8]). The principle of the tokamak is to confine a torus-shaped plasma using an axisymmetric helical magnetic field, such as is shown in figure 1.3. The magnetic field is symmetric about the axis of rotation of the torus, which I refer to as the “symmetry axis”. The magnetic field lines form nested surfaces about an axis known as the “magnetic axis”.

The helical magnetic field is established mostly by a combination of large magnets surrounding the plasma vessel which produce a toroidal field, and a toroidal current in the plasma which generates a poloidal magnetic field. The toroidal current can be achieved in several ways; a defining feature of the tokamak is a central solenoid which induces a secondary current in the plasma. Other sources of toroidal current include neutral beam injection, microwaves and self-driven currents from the plasma itself. The poloidal magnetic field overcomes the issue of particle drifts described in the previous section by connecting different vertical locations in the plasma such that a vertical electric field is not established. The toroidal field is necessary to avoid large-scale plasma instabilities.

The helical field is described by the *safety factor* q (or its inverse, the rotational transform ι), defined as the number of toroidal turns of the magnetic field required to make a full poloidal rotation:

$$q = \frac{2\pi}{\iota} \equiv \frac{\#.\ \text{toroidal turns}}{1\ \text{poloidal turn}}, \tag{1.3.1}$$

which roughly corresponds to the slope of the field line; $q = 0$ corresponds to zero toroidal field (i.e. figure 1.2 b), and $q = \infty$ to zero poloidal field (i.e. figure 1.2 a). Magnetic field lines with $q = 3$

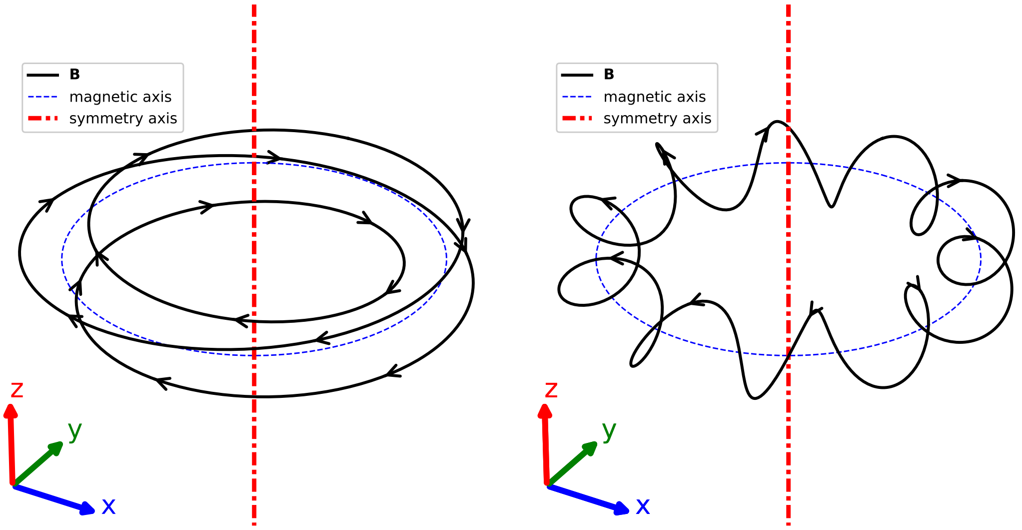

Figure 1.3: Examples of magnetic field lines in tokamak. Left: Magnetic field with $q = 3$. Right: Magnetic field with $q = 0.1$.

and $q = 0.1$ are shown in figure 1.3.

Experimental and theoretical tokamak research has shown their potential for energy production. The tokamak JET ("Joint European Torus"), for example, ran a DT campaign in 1997 which set the record for peak fusion power (16.1MW) and the total fusion energy of a single shot (21.7MJ) [15]. The latest DT campaign at JET achieved in December 2021 posted a record energy output of 59MJ from a single shot lasting five seconds, with $Q \equiv (\text{fusion power}/\text{external heating power}) = 0.33$ [16]. The next generation of conventional tokamaks include ITER [17] and DEMO [18], which aim to produce net energy ($Q > 1$) and, in the case of DEMO, a net supply of electricity.

A challenge facing the commercial viability of these machines is their large size, which makes the capital cost high and presents engineering challenges. An alternative class of tokamak design which may generally reduce the machine size is the *spherical tokamak*.

1.3.1.1 The spherical tokamak

The spherical tokamak, or spherical torus (ST), is characterised by a small machine aspect ratio $A \equiv R/r$, where R (called the major radius) is the distance from the symmetry axis of the torus to the magnetic axis and r is the distance from the magnetic axis to the vessel wall in the horizontal plane (called the minor radius). Conventional tokamaks (CTs) have $A \geq 2.5$, whereas STs typically have $A \sim 1.5$ [19]; the poloidal cross sections of two example plasmas with $A = 3$ and $A = 1.5$ are shown in figure 1.4 (left).

Lower A reduces the space around the symmetry axis available for magnets. As a result, the

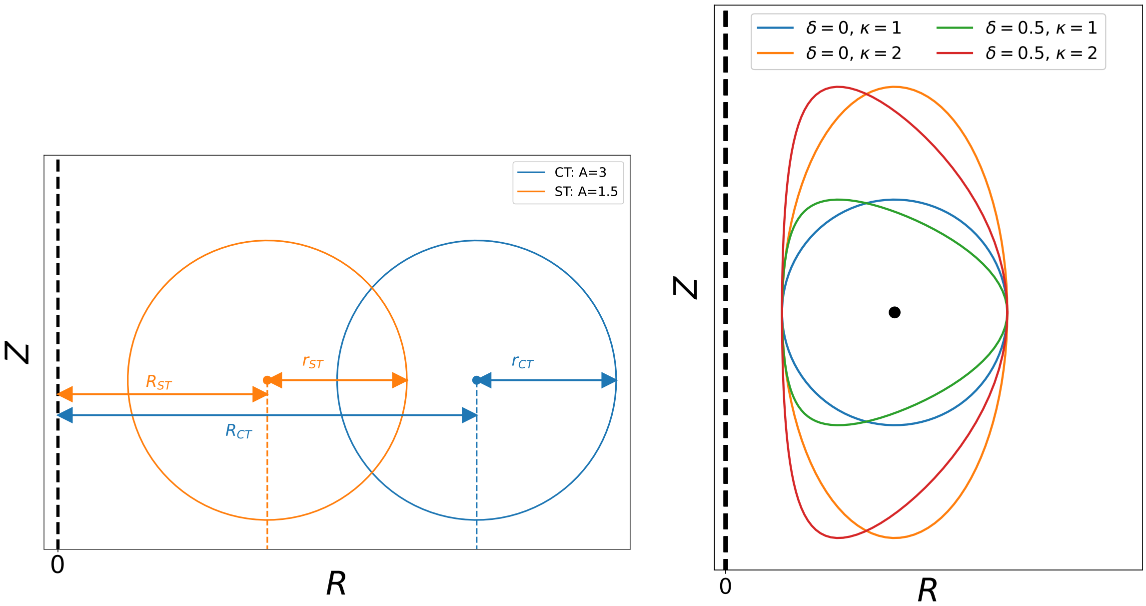

Figure 1.4: Left: poloidal cross sections of conventional and spherical tokamak with zero triangularity ($\delta = 0$) and unity elongation ($\kappa = 1$). Right: spherical tokamak poloidal cross sections with constant major and minor radius and varying (δ, κ).

strength of the achievable magnetic field in STs is more limited. In order to operate at a given pressure, STs must therefore operate at a higher plasma β, defined as the ratio of plasma pressure to magnetic pressure:

$$\beta \equiv \frac{p}{B^2/(2\mu_0)}, \tag{1.3.2}$$

where p is the plasma pressure. Economically speaking, higher β is generally desirable, since it implies a higher plasma pressure (and hence higher $nT\tau_E$ and more fusion power, since $P_\alpha \propto n^2T^2 \propto p^2$) for a given magnetic field, or a lower magnetic field (and hence lower capital and operating costs) for fixed p. Commercially viable ST power plants must operate at relatively high β due to the comparatively low field, with β around an order of magnitude greater than CTs ($\mathcal{O}(0.1)$ compared to $\mathcal{O}(0.01)$ [8].)

The reason for higher attainable β in STs is the strong shaping of the plasmas, which improve some plasma stability properties [20, 21]. The shaping typically consists of elongating the plasma vertically and making the plasma more "pointy" on the outboard side (known as triangularity). Some examples of different elongation κ and triangularity δ are shown in figure 1.4 (right). The maximum achievable β for a tokamak is usually limited by magnetohydrodynamic instabilities, which gave rise to a semi-empirical β limit devised by Troyon *et al.* [22] :

$$\beta_N \equiv \frac{\beta_T R B_{T0}}{I_p} < 0.028, \tag{1.3.3}$$

where β_N is the normalised β_T, $\beta_T \equiv 2\mu_0 \langle p \rangle / B_{T0}^2$ B_{T0} is the toroidal magnetic field on the magnetic axis, I_p the total plasma current and $\langle p \rangle$ the volume-averaged pressure. However, this limit is routinely exceeded by STs, and further studies by Menard *et al.*[23] show that this is due to improved magnetohydrodynamic stability in small-A, strongly shaped devices. The favourable properties of the ST has led to considerable investment, including the planned building STEP ("Spherical Tokamak for Energy Production") [5], a proof-of-principle energy-producing ST reactor in the UK.

1.3.1.2 Flux surfaces

It is worth noting here that if q is irrational, the magnetic field will never join back up with itself, and will instead ergodically sample a toroidal surface. Due to the high mobility of particles along the magnetic field, certain quantities (such as density and temperature) become constant on this surface (this is shown in the derivation presented in chapter 2). One such quantity is the enclosed poloidal magnetic flux $\psi = \int \mathbf{B} \cdot d\mathbf{S}$, where the integral is taken over the surface $\mathbf{S}$ which goes from the magnetic axis to the toroidal surface while keeping the toroidal angle fixed. As a result, these nested toroidal surfaces are referred to as "flux surface" and can be labelled by ψ.

1.3.2 The stellarator

Similar to the tokamak, stellarators also confine a toroidal plasma using a magnetic field. A key difference in design is how the rotational transform ι is achieved. Rather than driving a current in the plasma, stellarators principally use the magnetic coils to achieve the transform; either by elongating the plasma flux surfaces and making them rotate poloidally as the toroidal angle changes, or by making the magnetic axis non-planar [24]. Diagrams of the field coils and plasma for a tokamak and stellarator are shown in figure 1.6. It is clear that the stellarator lacks the toroidal symmetry of the tokamak and is an inherently three-dimensional configuration. The stellarator shown in figure 1.6 (Wendelstein 7-X) consists of five identical "field periods" connected to make a full toroidal rotation, resulting in five-fold rotational invariance.

A number of differences exist between tokamaks and stellarators. By eliminating the challenge of continually driving a toroidal current in the plasma, the stellarator is an inherently more steady-state device than the tokamak. In addition, the zero or very small toroidal currents make the plasma less susceptible to current-driven plasma instabilities [25]. On the other hand, the bespoke field coil designs make the stellarator more difficult and expensive to build[24]. An additional major difference is the "neoclassical" transport in stellarators, arising from the collisionless trajectories of particles. This is briefly described in the following section.

1.3.2.1 Neoclassical transport in tokamaks and stellarators

Since B is not uniform along magnetic field lines in tokamaks and stellarators, a subset of particles are trapped in regions of weak magnetic field. When combined with the magnetostatic drifts in tokamaks (which are largely up-down symmetric), this gives rise to "banana orbits" as shown schematically in figure 1.5 (left). These orbits remain local to a particular surface owing to a symmetry of the magnetic drifts with respect to the magnetic well.

Trapped particle trajectories in stellarators are rather more complicated. In particular, multiple magnetic wells exist along the field line, which result in a subset of particle orbits secularly departing from their original surface. A simplified 2D picture to illustrate the general point is shown in figure 1.5 (right). However, it should be noted that since stellarator plasmas are not toroidally symmetric, describing the dynamics with respect to a single poloidal cross section is unrealistic.

There are ways in which this neoclassical transport can be minimised by carefully optimising the equilibrium field to have particular symmetry properties [26–28]. Such configurations are currently the subject of theoretical and experimental investigation, most notably in the optimised stellarator Wendelstein 7-X [29] in Greifswald, Germany. In addition to reducing neoclassical transport to around the level of tokamaks, optimised stellarators also show remarkable properties with respect to microinstabilities [30–32] (see section 1.4.3). I examine this topic in chapter 7.

1.4 Plasma equilibrium, instabilities and turbulence

1.4.1 Equilibrium

The typical density of an MCF plasma is $\mathcal{O}(10^{-8} - 10^{-7})\mathrm{kg} \cdot \mathrm{m}^{-3}$, but the typical magnitude of the forces in an MCF device is large (for a typical magnetic field of 1T and a plasma current of 1MA in a volume of $100\mathrm{m}^3$, the typical force density is $\mathbf{f} = \mathbf{j} \times \mathbf{B} \sim \frac{I}{V} B = \mathcal{O}(10^4)\mathrm{N} \cdot \mathrm{m}^{-3}$). A small imbalance of forces will therefore lead to large bulk acceleration of the plasma and a rapid loss of confinement [8]. For this reason, a necessary (but not sufficient) condition for an MCF plasma to

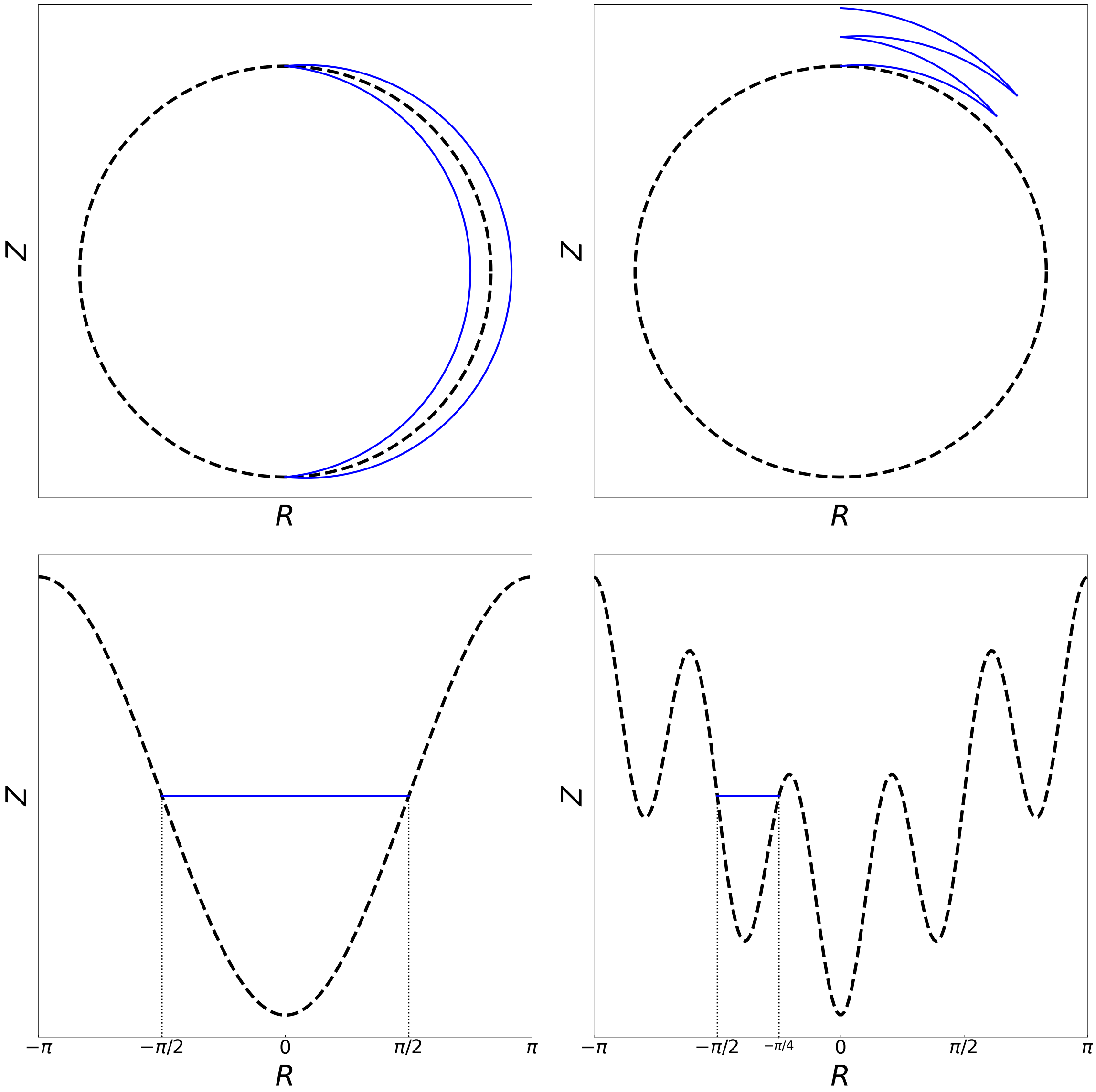

Figure 1.5: Schematic diagram of banana orbits in a tokamak (left) and stellarator (right) plasma about a circular flux surface. Upper: trajectory of a single trapped particle (solid blue line) on a circular flux surface (black dashed line). Lower: trajectory (solid blue) and magnetic field strength (solid black) as a function of poloidal angle.

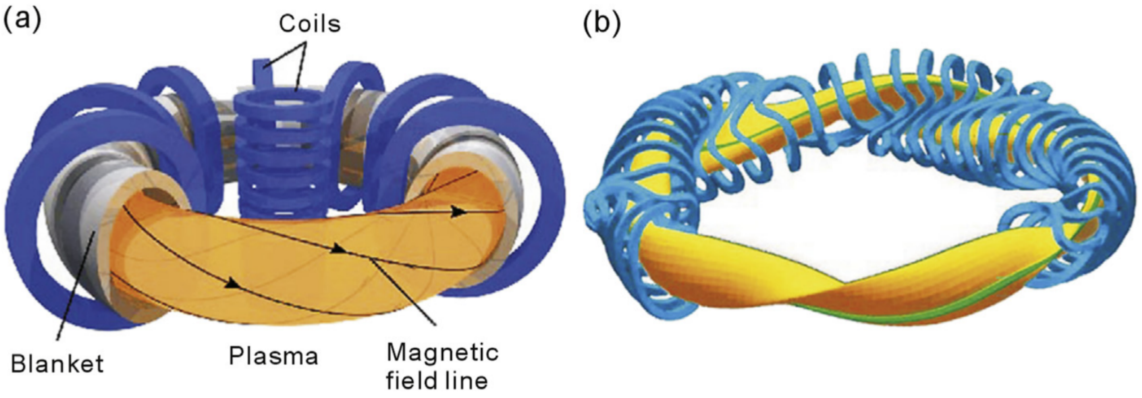

Figure 1.6: Schematic of (left) tokamak with conventional aspect ratio and (right) a stellarator, showing the plasma (yellow/orange) and magnetic field coils (blue). Figure reproduced from [25].

be well-confined it that the net force acting on each plasma element is zero. A plasma which is net force-free everywhere is said to be in equilibrium.

The question of equilibrium is usually addressed using the theoretical framework of magnetohydrodynamics (MHD) (discussed more in chapter 4). For axisymmetric devices such as the tokamak, this leads to the Grad-Shafranov equation [33]. Equilibrium in axially asymmetric devices such as the stellarator is rather more involved, although simplified models (again starting from MHD theory) have been developed [34]. Since fusion performance is determined by the properties of the equilibrium, finding high-performance equilibria (i.e. those which maximise $nT\tau_E$) is essential for the commercial viability of fusion power plants.

1.4.2 Instabilities

Unfortunately, the requirement for a plasma to be in MHD equilibrium is not a sufficient condition for the plasma to be well-confined; one must also consider plasma stability, that is, whether a small perturbation from the equilibrium causes the system to return to equilibrium or depart further [35]. In the latter case, the equilibrium is said to be unstable since instabilities (seeded by small random fluctuations) will cause the plasma to stray away from equilibrium in a short amount of time. An analogous system is a ball resting on a surface, say, the apex of a hill or the base of a valley. The former case is unstable (it being energetically favourable for the ball to roll down the hill, away from the apex) and the latter is stable. A ball resting on a (locally) level surface is an example of marginal stability, since an initial displacement of the ball will neither grow nor diminish.

The largest and most violent instabilities in an MCF plasma are rapidly-growing machine-size ("macroscopic") instabilities, in which the magnitude of fluctuation (in density, current or temperature) relative to the equilibrium quantities is order unity. The worst of these can terminate the plasma in a disruption event, by displacing the entire volume into the vessel wall, where it quickly cools and recombines. Slightly less severe are large Edge-Localised Modes (ELMs) [36, 37]. In these large-scale instabilities, the plasma loses a significant fraction of its energy, which is undesirable both for fusion performance and the longevity of plasma-facing components, which are damaged by transient high heat loads. For devices such as ITER, where heat loads on plasma-facing components are challenging even in steady state, large instabilities are considered unacceptable [38]. These instabilities have important consequences for the viability of fusion devices, but are not the subject of this thesis.

1.4.3 Microinstabilities and turbulence

Another class of instabilities are so-called microinstabilities, which have a spatial scale comparable to the ion or electron Larmor radius. Rather than causing large-scale disruptions, these grow, interact nonlinearly with each other and eventually saturate, resulting in small-scale turbulence (small both in terms of fluctuation amplitude and spatial size). The overall effect of this turbulence, which is sometimes referred to as microturbulence, is to enhance transport across the equilibrium magnetic field, which affects performance in several ways.

Firstly, the enhanced transport reduces the energy confinement time τ_E in the fusion triple product $nT\tau_E$, degrading performance; the fuel cannot self-heat as efficiently. Secondly, the turbulence tends to grow strongly above some critical threshold, and so the n and T profiles become "stiff": the equilibrium becomes regulated by turbulence and cannot be pushed beyond some critical parameter (e.g. a critical gradient in n, T or p) [39, 40]. Clearly, the gradients determine the volume-averaged n and T so optimising equilibria to raise these gradients is desirable. A third consideration is the transport of impurities; it is generally desirable to expel impurities (such as helium "ash" or material eroded from the plasma-facing components) from the core to avoid dilution of the hydrogenic ions and radiative cooling of the plasma. Plasma turbulence is a mechanism for impurity transport, so the "right kind" of turbulence may be beneficial.

Thus, in addition to an MCF plasma satisfying MHD equilibrium, it must also be stable with regards to the large-scale instabilities discussed previously, and must have sufficiently good microstability properties that turbulence does not relax the profile (without confining impurities too efficiently). Optimising MCF devices with regards to microstability is an overarching theme of this thesis.

1.5 Modelling turbulence in MCF plasmas

The previous sections have shown that a magnetically confined fusion plasma can display a wealth of interesting phenomena, spanning a huge range of spatio-temporal scales and with high dimensionality (since each individual particle occupies a particular location in six-dimensional position-velocity space, and its location varies as a function of time). This complexity presents a challenge for optimising fusion devices; it is not reasonably possible to find characteristic outputs (fusion power, wall loads, etc.) for a given set of plasma inputs (magnetic geometry, heating profile, fuelling rate, etc.) using a single physical model.

However, one may study and optimise individual aspects of fusion plasmas using non-general models. This thesis makes heavy use of gyrokinetic theory, which is particularly well-suited to studying microinstabilities and turbulence. The gyrokinetic model yields a tractable set of equations, which can be solved numerically or, in rare cases, analytically.

1.6 Structure of this thesis

This thesis is structured as follows. In this chapter, I have provided a brief background of magnetically confined thermonuclear fusion and magnetised plasma phenomena. In chapter 2, I explain the theoretical framework of gyrokinetics, and in chapter 3, how this theory is implemented in gyrokinetic software.

Next (chapter 4), I describe ideal and kinetic ballooning modes (IBMs and KBMs), the latter being an important microinstability in finite-β MCF plasmas and the former providing a useful proxy for KBM stability. I then present (in chapter 5) a study of KBMs in reactor-relevant spherical tokamak (ST) equilibria. I argue that the KBM imposes a design constraint on plasma triangularity (ST power plants likely requiring positive triangularity to be commercially viable.)

The second half of this thesis makes use of the gyrokinetic code `stella`. In chapter 6 I describe the implementation of electromagnetic fluctuations in this code and the tests and benchmarks performed. I then use `stella` to examine microstability in Wendelstein 7-X optimised stellarator plasmas (chapter 7). This work presents electrostatic results using the original implementation of `stella` and preliminary electromagnetic results using the newly developed code.

In chapter 8, I present a scheme which aims to eliminate the (sometimes restrictive) timestep constraint associated with the $\mathbf{E} \times \mathbf{B}$ nonlinearity in the gyrokinetic equation. This final piece of research contains preliminary results and describes features of the implementation which are currently poorly understood and might benefit from future work. Finally, an overall summary and outlook is given in chapter 9.

Chapter 2

Gyrokinetics: Theory

2.1 Introduction

A complete classical description of a fully ionised plasma is provided by the Lorentz-Maxwell equations (1.1.4) to (1.1.8). Simulating the motion of all particles in any reasonably sized plasma is, however, intractable; storing the $(\mathbf{x}, \mathbf{v})$ coordinates for $\mathcal{O}(10^{20})$ particles would require $\mathcal{O}(10^{20})$ bytes of memory, and updating these values once would require $\mathcal{O}(10^{20})$ floating-point operations. The first step towards a tractable theoretical framework therefore is to dispense with the individual particle picture. As an alternative, one can use a statistical approach in which the plasma is described by a distribution function $f_s(\mathbf{x}, \mathbf{v}, t)$: this describes the location of particles in a plasma in the six-dimensional phase space of position **x** and velocity **v** at time t for species s (electron, deuteron, etc.). Conceptually, f_s can be considered the density of species s over position and velocity. Indeed, the number density $n_s(\mathbf{x})$ is simply the integral of f_s over **v**:

$$n_s(\mathbf{x}) = \int d\mathbf{v} f_s(\mathbf{x}, \mathbf{v}), \tag{2.1.1}$$

where the integral is taken over all velocity space. Integrals containing f_s over velocity space are known as moments of f_s.

An entirely general expression describing the temporal evolution of f_s is given by the (microscopic) kinetic equation [35]:

$$\frac{\mathrm{d}f_s}{\mathrm{d}t} = \frac{\partial f_s}{\partial t} + \frac{\mathrm{d}\mathbf{x}}{\mathrm{d}t} \cdot \frac{\partial f_s}{\partial \mathbf{x}} + \frac{\mathrm{d}\mathbf{v}}{\mathrm{d}t} \cdot \frac{\partial f_s}{\partial \mathbf{v}} = 0, \tag{2.1.2}$$

which simply states that f_s does not change along particle trajectories. This assumes that there are no sources or sinks of particles, i.e. the number of particles in the system for each species is conserved; an assumption used throughout this thesis. Nevertheless, since this essentially contains the same information as the single-particle picture, the kinetic-Maxwell equations are also intractable in practical terms.

To simplify, it is convenient to take an ensemble average of (2.1.2), that is, to take a moving average over a small region of phase space ($\delta\mathbf{x}$, $\delta\mathbf{v}$). For an arbitrary quantity $g(\mathbf{x}, \mathbf{v})$, the ensemble average $g_{\text{ensemble}}(\mathbf{x}, \mathbf{v})$ is defined as:

$$g_{\text{ensemble}}(\mathbf{x}, \mathbf{v}) \equiv \langle g(\mathbf{x}, \mathbf{v})\rangle_{\text{ensemble}} = \frac{1}{V}\int_{\mathbf{x}-\delta\mathbf{x}}^{\mathbf{x}+\delta\mathbf{x}}\int_{\mathbf{v}-\delta\mathbf{v}}^{\mathbf{v}+\delta\mathbf{v}} d\mathbf{x}' d\mathbf{v}' g(\mathbf{x}', \mathbf{v}'), \tag{2.1.3}$$

where the angle brackets $\langle\rangle$ denote some kind of average (a notation used throughout this thesis), V is the 6D phase space volume bounded by $(\mathbf{x} - \delta\mathbf{x}, \mathbf{x} + \delta\mathbf{x})$ and $(\mathbf{v} - \delta\mathbf{v}, \mathbf{v} + \delta\mathbf{v})$ and the prime ($'$) indicates a dummy variable. $\delta\mathbf{x}$ and $\delta\mathbf{v}$ are assumed much smaller than any dynamically relevant spatial or velocity scale of the system, such that the plasma dynamics are not affected by the ensemble average. The ensemble average serves two purposes:

1. It ensures that the distribution function $f_{s,\text{ensemble}}$ is smooth, and thus amenable to a greater range of mathematical analysis; f_s, by contrast, is pathologically jagged down to the classical limit.

2. By averaging over phase space, $f_{s,\text{ensemble}}$ effectively removes particle labelling; swapping the phase space location of two identical particles changes f_s but not $f_{s,\text{ensemble}}$. $f_{s,\text{ensemble}}$ therefore removes redundant information about the particles; a particular $f_{s,\text{ensemble}}$ describes a set of microscopically unique but macroscopically (i.e. on any scale of physical interest) equivalent plasmas.

Ensemble averaging eq. (2.1.2) yields

$$\frac{\mathrm{d}f_{s,\text{ensemble}}}{\mathrm{d}t} = \frac{\partial f_{s,\text{ensemble}}}{\partial t} + \frac{\mathrm{d}\mathbf{x}}{\mathrm{d}t}\cdot\frac{\partial f_{s,\text{ensemble}}}{\partial\mathbf{x}} + \frac{\mathrm{d}\mathbf{v}}{\mathrm{d}t}\cdot\frac{\partial f_{s,\text{ensemble}}}{\partial\mathbf{v}} = \left(\frac{\partial f_{s,\text{ensemble}}}{\partial t}\right)_c \equiv C[f_{s,\text{ensemble}}], \tag{2.1.4}$$

which I refer to as “the ensemble-averaged kinetic equation”. (Various names are given to equation (2.1.4) in literature [35, 41, 42], usually based upon the form of the collision operator.) The RHS describes the effect of close-range interactions, or Coulomb collisions, occurring on spatial scales much smaller than the Debye scale. The distinction between long-range interactions described by the LHS of eq. (2.1.4) and the Coulomb collisions on the RHS is as follows. The latter happen over very short spatio-temporal scales, and are able to cause large changes in particle velocities. Since the timescale of the interaction is too small to be reasonably simulated, Coulomb collisions are taken to occur instantaneously, and this causes $f_{s,\text{ensemble}}$ to change discontinuously in velocity space. As a result, $f_{s,\text{ensemble}}$ is no longer conserved along its trajectory, and so $\left(\frac{\partial f_{s,\text{ensemble}}}{\partial t}\right)_c$ can be considered a source/sink term which redistributes $f_{s,\text{ensemble}}$ over velocity space. By contrast, the forces arising on the LHS are smoothly behaving over a 6D volume element, and $f_{s,\text{ensemble}}$ is conserved. It is often convenient to represent the RHS as $C[f_{s,\text{ensemble}}]$ where C is a *collision operator*. As shall be seen, one consequence of $C[f_{s,\text{ensemble}}]$ is to drive the equilibrium $f_{s,\text{ensemble}}$ towards a Maxwellian distribution.

Eq. (2.1.4) is also, alas, intractable for any reasonably sized plasma. It is therefore necessary to dispense with generalities and adopt a particular set of physical assumptions to address specific plasma behaviours.

The gyrokinetic framework seeks to accurately describe gyro-radius scale low-frequency (compared with the gyrofrequency) plasma instabilities and the turbulence these instabilities give rise to. The low-frequency assumption allows the governing equations to be averaged over the particle gyrophase ("gyroaveraging"). Gyroaveraging replaces $f_{s,\text{ensemble}}$ with $\langle f_{s,\text{ensemble}}\rangle_{\mathbf{X}_s}$: the distribution function of "rings" of charged particles of species s, with guiding centre $\mathbf{X}_s$ and velocity distribution specified by $(v_{||}, v_\perp)$. This helpfully eliminates one of the velocity dimensions and thus the resulting system of equations is five-dimensional. It also eliminates the fast timescale of gyration, making numerical analysis more practical.

A concise derivation of a gyrokinetic framework is presented in the next section. A summary is as follows. I first define a small parameter, ρ_*, then use this to express $f_{s,\text{ensemble}}$ as an asymptotic series and mathematically define the ordering assumptions. I then define a new coordinate system, well-suited to gyroaveraging, and write eq. (2.1.4) in this coordinate system, using the expansion of $f_{s,\text{ensemble}}$. This yields a set of equations ordered in ρ_*. The gyrokinetic equation is obtained by taking the gyroaverage of the piece of the $\mathcal{O}(\rho_*^2\Omega_s f_{s,\text{ensemble}})$ equation which fluctuates on turbulent spatio-temporal scales.

This derivation is presented using the SI formulation of electromagnetism. It is also relatively common in gyrokinetics for the Gaussian convention to be used, the only difference being a factor of c (the speed of light) in **B** in the Lorentz equation and a factor of $c/(4\pi\mu_0)$ in Ampére's law (eq.

(1.1.8)). This derivation takes the same basic approach as Abel *et al.* [42] and Hazeltine and Meiss [35].

2.2 Concise derivation of the gyrokinetic equation

2.2.1 Gyrokinetic orderings

I begin by formally defining ρ_*, which is taken to be the ratio of the thermal Larmor radius of a species s to the plasma minor radius $a = r$:

$$\rho_* \equiv \frac{\rho_s}{a} \ll 1, \tag{2.2.1}$$

where $\rho_s \equiv |v_{th,s}/\Omega_s|$ and $v_{th,s} = \sqrt{2T_s/m_s}$. The choice of r in defining ρ_* is somewhat arbitrary; it is chosen because it usually represents the spatial scale over which the equilibrium varies. It should be noted that where this does not hold, one should pay careful attention to whether the assumptions underpinning gyrokinetics are satisfied. In "high confinement mode" (H-mode) [43] plasmas for example, the equilibrium changes over a relatively small region of the plasma known as the pedestal. One may then wish to define $\rho_* \equiv \rho_s/w_{ped}$ where w_{ped} is the pedestal width. However, in experimental conditions ρ_s/w_{ped} is not necessarily much less than 1 and so may violate (2.2.1).

It is also worth noting that ρ_* is species-specific via ρ_s. For example, assuming a main ion species i and an electron species e at the same temperature, $\rho_{*,i} > \rho_{*,e}$ (e.g. $\rho_{*,i}/\rho_{*,e} = 60$ for a deuterium plasma.) Clearly, $\rho_{*,e} \ll 1$ is automatically satisfied by requiring that $\rho_{*,i} \ll 1$. However, very massive or very fast particles, such as impurity ions or fusion α particles respectively, risk violating (2.2.1). For the ordering of the fields (which are species-independent) to be consistent, I take ρ_* to be the same order for all species e.g. $\rho_{*,e} \sim \mathcal{O}(\rho_{*,i})$.

To distinguish between the pieces of the distribution function which fluctuate on turbulent spatio-temporal scales and those which do not, the distribution function is written as $f_{s,\text{ensemble}} = F_s + \delta f_s$, where F_s represents the turbulence-independent, or non-fluctuating, piece of the distribution function and δf_s represents the fluctuating piece (I have dropped the subscript $_{\text{ensemble}}$ for convenience). These satisfy:

$$\langle F_s \rangle_{\text{fluc}} = F_s \tag{2.2.2}$$

$$\langle \delta f_s \rangle_{\text{fluc}} = 0, \tag{2.2.3}$$

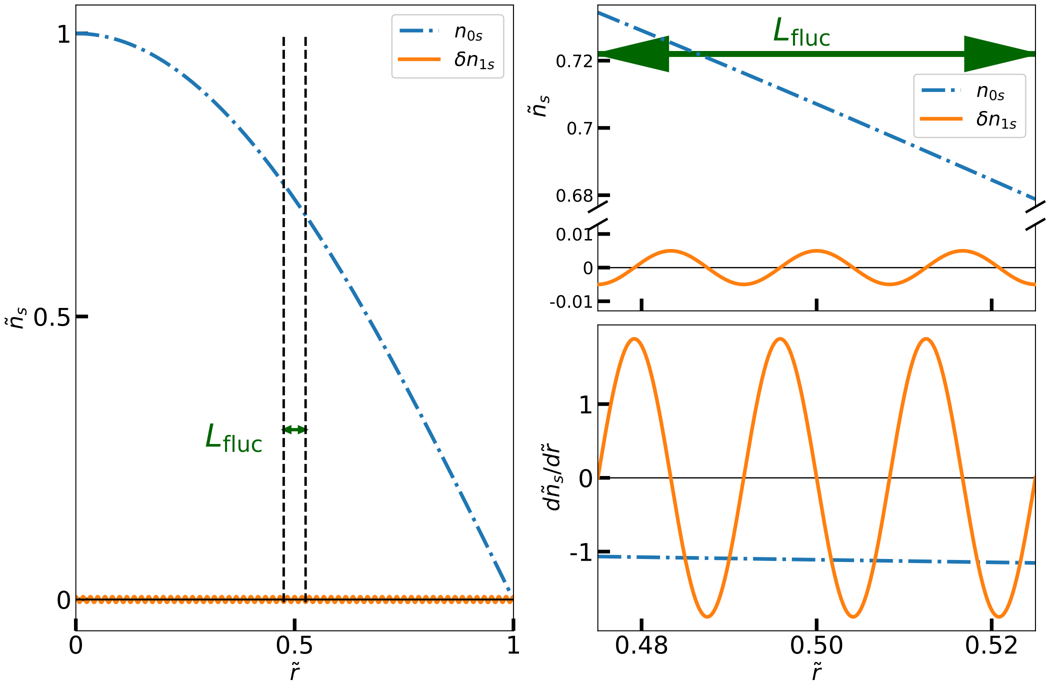

Figure 2.1: Illustration of the separation of scales in a plasma. Left: hypothetical density profiles of n_{0s} and δn_{1s} across the plasma at some given poloidal angle (which is modelled simplistically as sinusoidal). Right, upper: n_{0s} and δn_{1s} in the domain L_{fluc}. δn_{1s} varies on the scale of ρ_s and vanishes when averaged over L_{fluc}. Lower: gradients $\frac{\partial}{\partial r}$ of n_{0s} and δn_{1s}. In this example, $L_{\text{fluc}}/a = 0.05$ and $\rho_* = 0.005$. All densities are normalised to n_{0s} at $r = 0$ and all distances normalised to a, taken as r at the last closed flux surface.

where $\langle g \rangle_{\text{fluc}}$ is the quantity g averaged over some "turbulence spatio-temporal scale" $(L_{\text{fluc}}, t_{\text{fluc}})$, which sits between (but is asymptotically separated from) the Larmor and equilibrium scales: $\rho_s \ll L_{\text{fluc}} \ll a$, $\Omega_s \ll t_{\text{fluc}} \ll t_{eq}$ [42]. With L_{fluc} being much larger than the size of turbulent features and t_{fluc} much greater than the timescale of the fluctuations, $\langle\rangle_{\text{fluc}}$ can be thought of as an "average over the turbulence". An illustration of the distinction between equilibrium and fluctuating quantities is shown in figure 2.1.

2.2.1.1 Scale assumptions

Given these definitions, the assumptions underpinning this derivation can be expressed mathematically:

1. That the amplitude of the turbulent fluctuations of f_s are small ($\mathcal{O}(\rho_*)$) compared with the equilibrium amplitude of f_s. Thus, f_s is expanded as follows:

$$f_s = (F_{0s} + F_{1s} + F_{2s} + \delta f_{1s} + \delta f_{2s} + \ldots)\,, \tag{2.2.4}$$

with

$$\frac{F_{1s}}{F_{0s}} \sim \frac{\delta f_{1s}}{F_{0s}} \sim \frac{\delta f_{2s}}{\delta f_{1s}} \sim \ldots \sim \mathcal{O}(\rho_*). \tag{2.2.5}$$

F_{0s} is the largest component of f_s and represents the lowest order equilibrium distribution function. Higher-order non-fluctuating components $(F_{1s}, F_{2s}, \ldots)$ represent spatially large-scale corrections to equilibrium, and are known as neoclassical corrections. δf_{1s} represents the leading order turbulent fluctuations, which is to be solved for in subsequent chapters.

The electromagnetic fields are also asymptotically expanded:

$$\mathbf{E} = \mathbf{E}_0 + \mathbf{E}_1 + \mathbf{E}_2 + \ldots \tag{2.2.6}$$

$$\mathbf{B} = \mathbf{B}_0 + \mathbf{B}_1 + \mathbf{B}_2 + \ldots \tag{2.2.7}$$

$$\frac{E_1}{E_0} \sim \frac{E_2}{E_1} \sim \frac{B_1}{B_0} \sim ... \sim \mathcal{O}(\rho_*). \tag{2.2.8}$$

The size of the electric and magnetic fields are related to one another by

$$E_\alpha \sim v_{th,s} B_\alpha. \tag{2.2.9}$$

In other words, the force from the electric field $\mathbf{E}_\alpha$ is equal to the typical force arising from the magnetic field $\mathbf{B}_\alpha$ for each component α.

2. That $\mathbf{E}_0 = 0$. This is known as drift-ordering [35], or the low-flow limit, since this assumption implies the maximum $\mathbf{E} \times \mathbf{B}$ velocity has a magnitude:

$$\mathbf{v}_E \sim \frac{\mathbf{E}_1 \times \mathbf{B}_0}{B_0^2} \sim \frac{E_1}{B_0} \sim \rho_* v_{th,s}. \tag{2.2.10}$$

If one allows $\mathbf{E}_0 \neq 0$ (the high-flow limit, or MHD ordering), then $\mathbf{v}_E \sim v_{th,s}$ (i.e. sonic flows) are permitted. This may be the case in tokamak plasmas, but rather complicates the picture, since equilibrium flows and flow shear affect the turbulence (the reader is directed to Abel *et al.* [42] for more details). This thesis exclusively uses the low-flow formulation of gyrokinetics.

3. That the timescale of turbulent fluctuations is much greater ($\mathcal{O}(1/\rho_*)$) than the gyro period, but much less (at least $\mathcal{O}(\rho_*)$) than the timescale over which the equilibrium evolves. In this work the non-fluctuating timescale is taken to be $\mathcal{O}(\rho_*^3)$ smaller than the gyro-period (known

as transport ordering [35, 42]), that is

$$\left.\frac{\partial}{\partial t}\right|_{\text{non-fluc}} \sim \rho_*^3 \Omega_s; \qquad \left.\frac{\partial}{\partial t}\right|_{\text{fluc}} \sim \omega \sim \rho_* \Omega_s, \tag{2.2.11}$$

where $\left.\frac{\partial}{\partial t}\right|_{\text{fluc (non-fluc)}}$ represents the derivative of either a turbulent-fluctuating quantity (such as δf_s) or a non-fluctuating quantity (such as F_s).

4. That the spatial scale for the turbulent features which are perpendicular to $\mathbf{B}_0$ is similar to the gyro-radius, but the scale parallel to $\mathbf{B}_0$ is similar to the equilibrium length scale. Thus:

$$\left.\boldsymbol{\nabla}_{\|}\right|_{\text{non-fluc}} \sim \left.\boldsymbol{\nabla}_{\perp}\right|_{\text{non-fluc}} \sim \left.\boldsymbol{\nabla}_{\|}\right|_{\text{fluc}} \sim \frac{1}{a}; \qquad \left.\boldsymbol{\nabla}_{\perp}\right|_{\text{non-fluc}} \sim \frac{1}{\rho_s}, \tag{2.2.12}$$

where I define the parallel ($\|$) and perpendicular ($\perp$) directions with respect to $\mathbf{B}_0$. An illustration of perpendicular spatial derivatives is shown in figure 2.1.

2.2.1.2 Electrostatic and magnetic potentials

The fields can be written in terms of the electrostatic and magnetic vector potentials (φ, $\mathbf{A}$):

$$\mathbf{B} = \boldsymbol{\nabla} \times \mathbf{A}; \qquad \mathbf{E} = -\boldsymbol{\nabla}\varphi - \frac{\partial \mathbf{A}}{\partial t}. \tag{2.2.13}$$

The Coulomb gauge is chosen, so that $\boldsymbol{\nabla} \cdot \mathbf{A} = 0$. I also asymptotically expand $\mathbf{A}$ and φ; $\mathbf{A} = \mathbf{A}_0 + \mathbf{A}_1 + ...$ and $\varphi = \varphi_0 + \varphi_1 + ...$ where

$$\frac{e\varphi_1}{T_s} \sim \frac{e v_{th,s} A_1}{T_s} \sim \rho_*. \tag{2.2.14}$$

Note that the magnitude of a field arising from a given potential depends on the length or time scale over which the potential varies. For example, splitting φ_1 into a fluctuating piece $\delta\varphi_1$ and a non-fluctuating piece Φ_1, it is clear that

$$\boldsymbol{\nabla}\Phi_1 \sim \frac{\varphi_1}{a} \sim \boldsymbol{\nabla}_{\|}\delta\varphi_1 \sim \rho_* \boldsymbol{\nabla}_{\perp}\delta\varphi_1. \tag{2.2.15}$$

Thus, Φ_1 contributes to $\mathbf{E}_2$, whereas $\delta\varphi_1$ contributes to $\mathbf{E}_2$ in the parallel direction and $\mathbf{E}_1$ in the perpendicular direction.

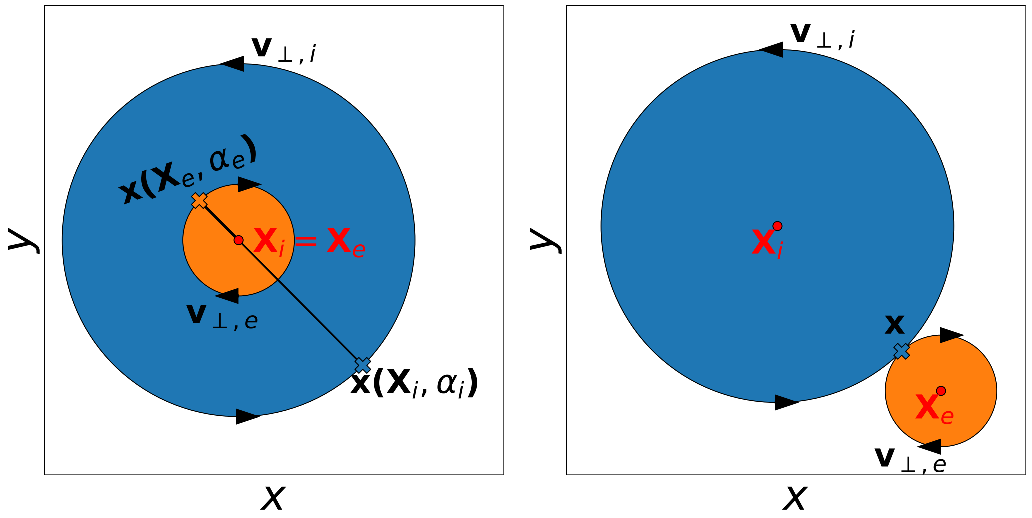

Figure 2.2: Illustration of guiding centres. Left: gyro-orbits of an ion (blue) and an electron (orange), with identical guiding centre $\mathbf{X}_s = \mathbf{X}_i = \mathbf{X}_e$. Crosses indicate the spatial position of each at gyrophase $\alpha_s = \alpha_i = \alpha_e$. Right: gyro-orbits of an ion and an electron with identical spatial position $\mathbf{x}$ and identical gyrophase, but different guiding centres. For clarity I have set $\rho_e = \rho_i/\sqrt{10}$, which is equivalent to increasing the electron mass to $m_i/10$.

2.2.2 Choice of coordinates

Anticipating the gyroaveraging, I select a particular set of coordinates well-suited to gyroaveraging. These are: the guiding centre $\mathbf{X}_s \equiv \mathbf{x} - \boldsymbol{\rho}_s$ (where $\boldsymbol{\rho}_s = \Omega_s^{-1}\mathbf{b} \times \mathbf{v}$ and $\mathbf{b} \equiv \mathbf{B}_0/B_0$ is the unit vector parallel to $\mathbf{B}_0$); the parallel velocity $v_\parallel = \mathbf{v} \cdot \mathbf{b}$; the magnetic moment with respect to the equilibrium magnetic field $\mu_s = \frac{mv_\perp^2}{2B_0}$; the gyrophase angle α_s (defined implicitly by $\mathbf{v}_\perp = v_\perp(\cos(\alpha_s)\hat{\mathbf{e}}_2 - \sin(\alpha_s)\hat{\mathbf{e}}_1)$ where $\hat{\mathbf{e}}_1$ and $\hat{\mathbf{e}}_2$ are unit vectors perpendicular to $\mathbf{b}$ such that $(\mathbf{b}, \hat{\mathbf{e}}_1, \hat{\mathbf{e}}_2)$ form an orthonormal set of basis vectors). The distinction between $\mathbf{x}$ and $\mathbf{X}_s$ is illustrated in figure 2.2.

With this choice of coordinates, eq. (2.1.4) becomes

$$\frac{\mathrm{d}f_s}{\mathrm{d}t} = \frac{\partial f_s}{\partial t} + \frac{\mathrm{d}\mathbf{X}}{\mathrm{d}t} \cdot \frac{\partial f_s}{\partial \mathbf{X}} + \frac{\mathrm{d}v_\parallel}{\mathrm{d}t} \cdot \frac{\partial f_s}{\partial v_\parallel} + \frac{\mathrm{d}\mu_s}{\mathrm{d}t} \cdot \frac{\partial f_s}{\partial \mu_s} + \frac{\mathrm{d}\alpha_s}{\mathrm{d}t} \cdot \frac{\partial f_s}{\partial \alpha_s} = C[f_s] \tag{2.2.16}$$

(where the subscript $_{\text{ensemble}}$) is dropped for convenience).

2.2.3 Calculation of terms

I now insert (2.2.4) into (2.2.16), and order the terms by ρ_*. The first three orders of the equation (the $\mathcal{O}(\rho_*^0\Omega_s F_{0s})$, $\mathcal{O}(\rho_*^1\Omega_s F_{0s})$ and $\mathcal{O}(\rho_*^2\Omega_s F_{0s})$ equation) will then be studied. The first step is to calculate $\frac{\mathrm{d}}{\mathrm{d}t}$ of $\mathbf{X}_s$, $v_\parallel$, μ_s and α_s.

2.2.3.1 Calculation of $\frac{\mathrm{d}}{\mathrm{d}t}(\mathbf{X}_s, v_{\|}, \mu_s, \alpha_s)$

$\frac{\mathrm{d}\mathbf{X}_s}{\mathrm{d}t}$ can be written as

$$\frac{\mathrm{d}\mathbf{X}_s}{\mathrm{d}t} = \frac{\mathrm{d}\mathbf{x}}{\mathrm{d}t} \cdot \left.\frac{\partial \mathbf{X}_s}{\partial \mathbf{x}}\right|_{t,\mathbf{v}} + \frac{\mathrm{d}\mathbf{v}}{\mathrm{d}t} \cdot \left.\frac{\partial \mathbf{X}_s}{\partial \mathbf{v}}\right|_{t,\mathbf{x}}, \tag{2.2.17}$$

$$= \mathbf{v} \cdot \frac{\partial \mathbf{X}_s}{\partial \mathbf{x}} + \frac{Z_s e}{m}(\mathbf{E} + \mathbf{v} \times \mathbf{B}) \cdot \frac{\partial \mathbf{X}_s}{\partial \mathbf{v}}. \tag{2.2.18}$$

Writing $\mathbf{v} = \mathbf{v}_{\|} + \mathbf{v}_{\perp}$ and using the asymptotic expansions for the fields gives

$$\frac{\mathrm{d}\mathbf{X}_s}{\mathrm{d}t} = \underbrace{\mathbf{v}_{\|}}_{\mathcal{O}(v_{th})} + \underbrace{\mathbf{v}_E + \Omega_s^{-1}\left[\mathbf{v} \times (\mathbf{v} \cdot \boldsymbol{\nabla}\mathbf{b}) - \frac{1}{B_0}\mathbf{v} \times \mathbf{b}\,((\mathbf{v} \cdot \boldsymbol{\nabla} B_0)\right] - \frac{1}{B_0}\mathbf{b} \times (\mathbf{v} \times \mathbf{B}_1)}_{\mathcal{O}(\rho_* v_{th})} + \mathcal{O}(\rho_*^2 v_{th}), \tag{2.2.19}$$

where

$$\mathbf{v}_E = \frac{\mathbf{E}_1 \times \mathbf{B}_0}{B_0^2}. \tag{2.2.20}$$

$\frac{\mathrm{d}\mathbf{X}_s}{\mathrm{d}t}$ can be interpreted as the velocity of the guiding centres at fixed $(v_{\|}, \mu_s, \alpha_s)$. The physical significance of the terms in (2.2.19) are as follows. The first term ($\mathbf{v}_{\|}$) is “parallel streaming” of guiding centres along the equilibrium magnetic field, and is unaffected by gyroaveraging. The second term ($\mathbf{v}_{\mathbf{E}}$) is the $\mathbf{E} \times \mathbf{B}$ drift arising from electric field $\mathbf{E}_1$, and is predominantly electrostatic (i.e. arising from Φ_0 and φ_1), with a higher-order electromagnetic correction from $\frac{\partial \mathbf{A}_1}{\partial t}$. The terms appearing in the square brackets, upon gyroaveraging, will turn into the curvature and $\boldsymbol{\nabla} B$ drifts described in section 1.2.4. The final explicit term relates to Larmor motion arising from the perturbed magnetic field. Upon gyroaveraging, this will create fluctuating magnetic drifts arising from the fluctuating magnetic field $\mathbf{B}_1$.

It is also worth emphasising that streaming is the dominant term (the only term entering at $\mathcal{O}(v_{th})$); guiding centres stream quickly along the equilibrium field lines and drift slowly across them.

Likewise, $\frac{\mathrm{d}v_{\|}}{\mathrm{d}t}$ can be written as

$$\frac{\mathrm{d}v_{\|}}{\mathrm{d}t} = \mathbf{v} \cdot (\mathbf{v} \cdot \boldsymbol{\nabla}\mathbf{b}) + \frac{Z_s e}{m_s}\mathbf{E}_1 \cdot \mathbf{b} + \frac{Z_s e}{m_s c}(\mathbf{v} \times \mathbf{B}_1) \cdot \mathbf{b}, \tag{2.2.21}$$

where the first and third terms are $\mathcal{O}(\rho_* \Omega_s v_{th})$, but the parallel electric field term is $\mathcal{O}(\rho_*^2 \Omega_s v_{th})$. $\frac{\mathrm{d}\mu_s}{\mathrm{d}t}$

can be written as

$$\frac{\mathrm{d}\mu_s}{\mathrm{d}t} = -\frac{\mu_s}{B_0}\mathbf{v}\cdot\boldsymbol{\nabla}B_0 - \frac{m_s v_{\|}}{B_0}\mathbf{v}_{\perp}\cdot(\mathbf{v}\cdot\boldsymbol{\nabla}\mathbf{b}) + \frac{Z_s e}{B_0}\left(\mathbf{E}_1\cdot\mathbf{v}_{\perp} + \frac{1}{c}(\mathbf{v}_{\|}\times\mathbf{B}_1)\cdot\mathbf{v}_{\perp}\right). \tag{2.2.22}$$

Since the motion perpendicular to the field is gyromotion to leading order, $\frac{\mathrm{d}\alpha_s}{\mathrm{d}t}$ can be written as

$$\frac{\mathrm{d}\alpha_s}{\mathrm{d}t} = \Omega_s + \mathcal{O}(\rho_*\Omega_s) + \ldots \tag{2.2.23}$$

As shall be seen, it is not necessary to calculate the terms in $\frac{\mathrm{d}\alpha_s}{\mathrm{d}t}$ beyond leading order.

2.2.3.2 Gyroaveraging

In order to eliminate the gyrophase α_s, I will take the gyroaverage of the expanded kinetic equation, where the gyroaveraging operator is defined as

$$\langle g\rangle_{\mathbf{X}_s} \equiv \left.\left(\frac{1}{2\pi}\int_0^{2\pi} g d\alpha_s\right)\right|_{\mathbf{X}_s, v_{\|}, \mu_s, t}, \tag{2.2.24}$$

where g is an arbitrary quantity. Naturally the coordinates $(\mathbf{X}_s, v_{\|}, \mu_s)$ will be invariant with respect to gyroaveraging (e.g. $\langle v_{\|}\rangle_{\mathbf{X}_s} = v_{\|}$), as will quantities which do not fluctuate over the spatial scale ρ_s (e.g. $\langle F_{0s}\rangle_{\mathbf{X}_s} = F_{0s}$). However, quantities which do fluctuate over ρ_s will have some (undetermined) gyrophase dependency, e.g. $\langle \delta f_{1s}\rangle_{\mathbf{X}_s} \neq \delta f_{1s}$. The expressions for $\frac{\mathrm{d}}{\mathrm{d}t}$, together with the definition of the gyroaverage (2.2.24), are now used to examine different orders of the ensemble-averaged kinetic equation.

2.2.4 The expanded ensemble-averaged kinetic equation: zeroth order ($\mathcal{O}(\rho_*^0\Omega_s F_{0s})$)

Only the $\frac{\mathrm{d}\alpha_s}{\mathrm{d}t}\frac{\partial F_{0s}}{\partial\alpha_s}$ term contributes to this order, which gives

$$\Omega_s\frac{\partial F_{0s}}{\partial\alpha_s} = 0. \tag{2.2.25}$$

Thus F_{0s} is gyrophase-independent.

2.2.5 The expanded ensemble-averaged kinetic equation: The first order ($\mathcal{O}(\rho_*\Omega_s F_{0s})$)

Considering the $\mathcal{O}(\rho_*^1\Omega_s F_{0s})$ component, one finds

$$\begin{aligned}
&\mathbf{v}_\parallel \cdot \frac{\partial F_{0s}}{\partial \mathbf{X}} \\
&+ \left(\mathbf{v}\cdot(\mathbf{v}\cdot\boldsymbol{\nabla}\mathbf{b}) + \frac{Z_s e}{m_s c}(\mathbf{v}\times\mathbf{B}_1)\cdot\mathbf{b}\right)\frac{\partial F_{0s}}{\partial v_\parallel} \\
&+ \left[-\frac{\mu_s}{B_0}\mathbf{v}\cdot\boldsymbol{\nabla}B_0 - \frac{m_s v_\parallel}{2B_0}\mathbf{v}_\perp\cdot(\mathbf{v}\cdot\boldsymbol{\nabla}\mathbf{b}) + \frac{Z_s e}{B_0}\left(\mathbf{E}_1\cdot\mathbf{v}_\perp + \frac{1}{c}(\mathbf{v}_\parallel\times\mathbf{B}_1)\cdot\mathbf{v}_\perp\right)\right]\frac{\partial F_{0s}}{\partial \mu_s} \\
&+ \Omega_s\frac{\partial}{\partial \alpha_s}(F_{1s}+\delta f_{1s}) = C[F_{0s}]. \qquad (2.2.26)
\end{aligned}$$

Gyroaveraging gives

$$\mathbf{v}_\parallel \cdot \frac{\partial F_{0s}}{\partial \mathbf{X}} - \frac{\mu_s}{m_s}\mathbf{b}\cdot\boldsymbol{\nabla}B_0\frac{\partial F_{0s}}{\partial v_\parallel} = C[F_{0s}] \qquad (2.2.27)$$

It is useful here to make a change of variables $(\mathbf{X}_s, v_\parallel, \mu_s, \alpha_s) \to (\mathbf{X}_s, \varepsilon_s, \mu_s, \alpha_s)$ where $\varepsilon_s \equiv m_s v^2/2$ is the particle kinetic energy. The derivative $\frac{\partial F_{0s}}{\partial \mathbf{X}}$ can be written as:

$$\begin{aligned}
\left.\frac{\partial F_{0s}}{\partial \mathbf{X}_s}\right|_{v_\parallel,\mu_s,\alpha_s} &= \left.\frac{\partial \mathbf{X}_s}{\partial \mathbf{X}_s}\right|_{v_\parallel,\mu_s,\alpha_s}\cdot\left.\frac{\partial F_{0s}}{\partial \mathbf{X}_s}\right|_{\varepsilon_s,\mu_s,\alpha_s} + \left.\frac{\partial \varepsilon_s}{\partial \mathbf{X}_s}\right|_{v_\parallel,\mu_s,\alpha_s}\cdot\left.\frac{\partial F_{0s}}{\partial \varepsilon_s}\right|_{\mathbf{X}_s,\mu_s,\alpha_s} \\
&\quad + \overbrace{\cancel{\left.\frac{\partial \mu_s}{\partial \mathbf{X}_s}\right|_{v_\parallel,\mu_s,\alpha_s}}}^{=0}\cdot\left.\frac{\partial F_{0s}}{\partial \mu_s}\right|_{\mathbf{X}_s,\varepsilon_s,\alpha_s} + \overbrace{\cancel{\left.\frac{\partial \alpha_s}{\partial \mathbf{X}_s}\right|_{v_\parallel,\mu_s,\alpha_s}}}^{=0}\cdot\left.\frac{\partial F_{0s}}{\partial \alpha_s}\right|_{\mathbf{X}_s,\varepsilon_s,\mu_s} \qquad (2.2.28) \\
&= \left.\frac{\partial F_{0s}}{\partial \mathbf{X}_s}\right|_{\varepsilon_s,\mu_s,\alpha_s} + \left.\frac{\partial}{\partial \mathbf{X}_s}\right|_{v_\parallel,\mu_s,\alpha_s}\left(\frac{1}{2}m_s v_\parallel^2 + \mu_s B_0\right)\left.\frac{\partial F_{0s}}{\partial \varepsilon_s}\right|_{\mathbf{X}_s,\mu_s,\alpha_s} \qquad (2.2.29) \\
&= \left.\frac{\partial F_{0s}}{\partial \mathbf{X}_s}\right|_{\varepsilon_s,\mu_s,\alpha_s} + \mu_s\frac{\partial B_0}{\partial \mathbf{X}_s}\left.\frac{\partial F_{0s}}{\partial \varepsilon_s}\right|_{\mathbf{X}_s,\mu_s,\alpha_s} \qquad (2.2.30)
\end{aligned}$$

Likewise, $\frac{\partial F_{0s}}{\partial v_\parallel}$ can be written:

$$\begin{aligned}
\left.\frac{\partial F_{0s}}{\partial v_\parallel}\right|_{\mathbf{X}_s,\mu_s,\alpha_s} &= \overbrace{\cancel{\left.\frac{\partial \mathbf{X}_s}{\partial v_\parallel}\right|_{\mathbf{X}_s,\mu_s,\alpha_s}}}^{=0} \cdot \left.\frac{\partial F_{0s}}{\partial \mathbf{X}_s}\right|_{\varepsilon_s,\mu_s,\alpha_s} + \left.\frac{\partial \varepsilon_s}{\partial v_\parallel}\right|_{\mathbf{X}_s,\mu_s,\alpha_s} \left.\frac{\partial F_{0s}}{\partial \varepsilon_s}\right|_{\mathbf{X}_s,\mu_s,\alpha_s} \\
&\quad + \overbrace{\cancel{\left.\frac{\partial \mu_s}{\partial v_\parallel}\right|_{\mathbf{X}_s,\mu_s,\alpha_s}}}^{=0} \left.\frac{\partial F_{0s}}{\partial \mu_s}\right|_{\mathbf{X}_s,\varepsilon_s,\alpha_s} + \overbrace{\cancel{\left.\frac{\partial \alpha_s}{\partial v_\parallel}\right|_{\mathbf{X}_s,\mu_s,\alpha_s}}}^{=0} \left.\frac{\partial F_{0s}}{\partial \alpha_s}\right|_{\mathbf{X}_s,\varepsilon_s,\mu_s} && (2.2.31) \\
&= m_s v_\parallel \left.\frac{\partial F_{0s}}{\partial \varepsilon_s}\right|_{\mathbf{X}_s,\mu_s,\alpha_s} && (2.2.32)
\end{aligned}$$

Inserting (2.2.30) and (2.2.32) into (2.2.27) gives

$$\begin{aligned}
\text{LHS} &= \mathbf{v}_\parallel \cdot \frac{\partial F_{0s}}{\partial \mathbf{X}} - \frac{\mu_s}{m_s}\mathbf{b}\cdot\boldsymbol{\nabla} B_0 \frac{\partial F_{0s}}{\partial v_\parallel} && (2.2.33) \\
&= \mathbf{v}_\parallel \cdot \left(\left.\frac{\partial F_{0s}}{\partial \mathbf{X}_s}\right|_{\varepsilon_s,\mu_s,\alpha_s} + \mu_s \frac{\partial B_0}{\partial \mathbf{X}_s} \left.\frac{\partial F_{0s}}{\partial \varepsilon_s}\right|_{\mathbf{X}_s,\mu_s,\alpha_s} \right) - \frac{\mu_s}{m_s}\mathbf{b}\cdot\boldsymbol{\nabla} B_0 \left(m_s v_\parallel \left.\frac{\partial F_{0s}}{\partial \varepsilon_s}\right|_{\mathbf{X}_s,\mu_s,\alpha_s} \right) && (2.2.34) \\
&= \mathbf{v}_\parallel \cdot \left.\frac{\partial F_{0s}}{\partial \mathbf{X}}\right|_{\varepsilon_s,\mu_s,\alpha_s} = C[F_{0s}] && (2.2.35)
\end{aligned}$$

Multiplying by $(1 + \ln F_{0s})$ and integrating over $\mathbf{x}$ and $\mathbf{v}$, one can show that

$$\int d^3\mathbf{x} d^3\mathbf{v} \ln F_{0s} C[F_{0s}] = 0. \tag{2.2.36}$$

By Boltzmann's H-theorem, this implies F_{0s} is a Maxwellian [42]. As a consequence, $C[F_{0s}] = 0$ and so

$$\mathbf{v}_\parallel \cdot \left.\frac{\partial F_{0s}}{\partial \mathbf{X}}\right|_{\varepsilon} = 0. \tag{2.2.37}$$

In other words, F_{0s} is constant along field lines. If the field lines form nested tori, as in tokamaks, this demonstrates that F_{0s} is a flux surface quantity in (ε_s, μ_s) coordinates.

Thus, an explicit expression for F_{0s} is

$$F_{0s} = n_s \left[\frac{m_s}{2\pi T_s}\right]^{3/2} \exp\left(\frac{-\varepsilon_s}{T_s}\right) = n_s \left[\frac{m_s}{2\pi T_s}\right]^{3/2} \exp\left(\frac{-m_s v^2}{2T_s}\right) \tag{2.2.38}$$

$$= n_s \left[\frac{m_s}{2\pi T_s}\right]^{3/2} \exp\left(\frac{-m_s v_\parallel^2}{2T_s} - \frac{\mu_s B_0}{T_s}\right). \tag{2.2.39}$$

2.2.5.1 The Boltzmann Response

Eq. (2.2.39) is now substituted into (2.2.26), enabling the properties of F_{1s} and δf_{1s} to be examined. After making a series of cancellations, this yields

$$\frac{Z_s e}{T_s}\mathbf{v}_\perp \cdot (\boldsymbol{\nabla}\varphi_1)\, F_{0s} = -\Omega_s \frac{\partial}{\partial \alpha_s}(F_{1s} + \delta f_{1s}) + \mathcal{O}(\rho_*^2 \Omega_s f_s). \tag{2.2.40}$$

Using the identity $\Omega_s \left.\frac{\partial g}{\partial \alpha_s}\right|_{\mathbf{X}} = \mathbf{v}_\perp \cdot \boldsymbol{\nabla} g + \Omega_s \left.\frac{\partial g}{\partial \alpha_s}\right|_{\mathbf{x}}$, this becomes

$$\frac{Z_s e}{T_s} F_{0s} \Omega_s \frac{\partial \varphi_1}{\partial \alpha_s} = -\Omega_s \frac{\partial}{\partial \alpha_s}(F_{1s} + \delta f_{1s}) + \mathcal{O}(\rho_*^2 \Omega_s f_s). \tag{2.2.41}$$

Eq. (2.2.41) contains both fluctuating and non-fluctuating terms. Since they vary over different scales, one can consider the mean (non-fluctuating) part of the equation and the fluctuating part separately; both must be independently satisfied. The non-fluctuating part is simply:

$$\frac{\partial F_{1s}}{\partial \alpha_s} = 0, \tag{2.2.42}$$

demonstrating that F_{1s} is independent of gyrophase. The fluctuating components are

$$\frac{-Z_s e}{T_s} F_{0s} \frac{\partial \varphi_1}{\partial \alpha_s} = \frac{\partial(\delta f_{1s})}{\partial \alpha_s}, \tag{2.2.43}$$

which can be integrated with respect to α_s to yield

$$\delta f_{1s} = \frac{-Z_s e \varphi_1}{T_s} F_{0s} + h_s, \tag{2.2.44}$$

where h_s is a constant of integration and hence gyrophase-independent. The first term on the RHS of (2.2.44) describes the gyrophase-dependent part of δf_{1s} and is called the Boltzmann response. The equation determining h_s is the gyrokinetic equation, which is obtained from the next order of (2.2.16).

2.2.6 The expanded ensemble-averaged kinetic equation: The second order ($\mathcal{O}(\rho_*^2\Omega_s F_{0s})$)

The $\mathcal{O}(\rho_*^2\Omega_s F_{0s})$ components of eq. (2.2.16) contain terms arising from F_{0s}, F_{1s}, δf_{1s} (about which some of the information is known), but unfortunately also contains the terms ($\Omega_s\frac{\partial F_{2s}}{\partial\alpha_s}$, $\Omega_s\frac{\partial\delta f_{2s}}{\partial\alpha_s}$). These relate to F_{2s} and δf_{2s}, which at this point are entirely unknown quantities. Fortunately, these contributions are eliminated by taking the gyroaverage. Moreover, by only considering the fluctuating components, several terms relating to F_{0s} and F_{1s} are eliminated (equilibrium magnetic drifts acting on F_{0s}, for example).

The gyroaveraged fluctuating $\mathcal{O}(\rho_*^2\Omega_s F_{0s})$ piece of (2.2.16) can be written as

$$\begin{aligned}
&\left\langle\left(\frac{\mathrm{d}\mathbf{X}}{\mathrm{d}t}\cdot\frac{\partial F_s}{\partial\mathbf{X}}+\frac{\mathrm{d}v_\|}{\mathrm{d}t}\frac{\partial F_s}{\partial v_\|}+\frac{\mathrm{d}\mu_s}{\mathrm{d}t}\frac{\partial F_s}{\partial\mu_s}+\frac{\mathrm{d}\alpha_s}{\mathrm{d}t}\frac{\partial F_s}{\partial\alpha_s}\right)_{\text{fl},\,\mathcal{O}(\epsilon^2\Omega_s f_s)}\right\rangle_{\mathbf{X}_s}\\
&+\left\langle\frac{\partial h_s}{\partial t}+\left(\frac{\mathrm{d}\mathbf{X}}{\mathrm{d}t}\cdot\frac{\partial h_s}{\partial\mathbf{X}}+\frac{\mathrm{d}v_\|}{\mathrm{d}t}\frac{\partial h_s}{\partial v_\|}+\frac{\mathrm{d}\mu_s}{\mathrm{d}t}\frac{\partial h_s}{\partial\mu_s}+\frac{\mathrm{d}\alpha_s}{\mathrm{d}t}\frac{\partial h_s}{\partial\alpha_s}\right)_{\mathcal{O}(\epsilon^2\Omega_s f_s)}\right\rangle_{\mathbf{X}_s}\\
&-\left\langle\left(\frac{Z_s e}{T_s}\frac{\mathrm{d}}{\mathrm{d}t}\left(\varphi_1 F_{0s}\right)\right)_{\mathcal{O}(\epsilon^2\Omega_s f_s)}\right\rangle_{\mathbf{X}_s}=0,
\end{aligned}\tag{2.2.45}$$

where for convenience I have ignored collisions. Inserting the expressions for $\frac{\mathrm{d}}{\mathrm{d}t}(\mathbf{X}_s, v_\|, \mu_s)$ and performing some manipulations, one arrives at the (collisionless) *gyrokinetic equation*:

$$\frac{\partial h_s}{\partial t}+\left(\mathbf{v}_\|+\mathbf{v}_{Ms}+\langle\mathbf{v}_\chi\rangle_{\mathbf{X}_s}\right)\cdot\boldsymbol{\nabla}_{\mathbf{X}_s}h_s-\frac{\mu_s}{m_s}\mathbf{b}\cdot\boldsymbol{\nabla}B_0\frac{\partial h_s}{\partial v_\|}+\langle\mathbf{v}_\chi\rangle_{\mathbf{X}_s}\cdot\boldsymbol{\nabla}\Big|_\epsilon F_{0s}-\frac{Z_s e}{T_s}F_{0s}\frac{\partial\langle\chi\rangle_{\mathbf{X}_s}}{\partial t}=0,\tag{2.2.46}$$

where

$$\langle\chi\rangle_{\mathbf{X}_s}=\langle\varphi_1\rangle_{\mathbf{X}_s}-v_\|\left\langle A_{1\|}\right\rangle_{\mathbf{X}_s}-\langle\mathbf{v}_\perp\cdot\mathbf{A}_{1\perp}\rangle_{\mathbf{X}_s},\tag{2.2.47}$$

$$\langle\mathbf{v}_\chi\rangle_{\mathbf{X}_s}=-\frac{1}{B_0}\boldsymbol{\nabla}_{\mathbf{X}_s}\langle\chi\rangle_{\mathbf{X}_s}\times\mathbf{b}.\tag{2.2.48}$$

$\langle\chi\rangle_{\mathbf{X}_s}$ is known as the gyrokinetic potential and is comprised of fluctuating electric and magnetic potentials. $\langle\mathbf{v}_\chi\rangle_{\mathbf{X}_s}$ can be considered a generalised $\mathbf{E}\times\mathbf{B}$ drift, arising from a combination of an electrostatic drift given by φ_1 and the motion of guiding centres along perturbed field lines.

2.3 Maxwell's equations in the gyrokinetic framework

The fluctuating electromagnetic fields are determined by quasi-neutrality and Ampére's law. Applying quasi-neutrality to fluctuating $\mathcal{O}(\rho_* n_s)$ quantities gives

$$\sum_s Z_s e \delta n_s = 0, \tag{2.3.1}$$

which can be written in terms of h_s as

$$\sum_s Z_s e \int d^3\mathbf{v} \delta f_{1s} = \sum_s Z_s e \int d^3\mathbf{v} \left(h_s - \frac{Z_s e}{T_s} F_{0s} \varphi_1 \right) = 0. \tag{2.3.2}$$

Ampére's law in the non-relativistic limit, applied to fluctuating $\mathcal{O}(\mathbf{B}_1)$ quantities can be written as

$$\boldsymbol{\nabla} \times \delta\mathbf{B} = \mu_0 \delta\mathbf{j}_1. \tag{2.3.3}$$

$\delta\mathbf{B}$ can be written as $\delta\mathbf{B} = \boldsymbol{\nabla}_\perp A_{1||} \times \mathbf{b} + B_{1||}\mathbf{b}$ [44]; to obtain an expression for $B_{1||}$, eq. (2.3.3) is crossed with $\mathbf{b}$ and then dotted with $\boldsymbol{\nabla}$ to obtain

$$\boldsymbol{\nabla} \cdot (\mathbf{b} \times (\boldsymbol{\nabla} \times \delta\mathbf{B})) = \mu_0 \sum_s Z_s e \int d^3\mathbf{v} \boldsymbol{\nabla} \cdot (\delta f_{1s} (\mathbf{b} \times \mathbf{v}_\perp)) \tag{2.3.4}$$

$$= \boldsymbol{\nabla}^2 B_{1||} = \boldsymbol{\nabla}_\perp^2 B_{1||} = \mu_0 \sum_s Z_s e \int d^3\mathbf{v} \boldsymbol{\nabla} \cdot (h_s (\mathbf{b} \times \mathbf{v}_\perp)), \tag{2.3.5}$$

where the Boltzmann response has been eliminated since it will vanish when integrated over $\mathbf{v}_\perp$. To find an expression for $A_{1||}$, eq. (2.3.3) is dotted with $\mathbf{b}$ to obtain

$$-\boldsymbol{\nabla}_\perp^2 A_{1||} = \mu_0 \sum_s Z_s e \int d^3\mathbf{v} v_{||} \delta f_{1s} \tag{2.3.6}$$

$$= \mu_0 \sum_s Z_s e \int d^3\mathbf{v} v_{||} h_s, \tag{2.3.7}$$

where the Boltzmann response has been eliminated since it is symmetric in $v_{||}$, and so will vanish when multiplied by $v_{||}$ and integrated over $v_{||}$.

It should also be emphasised that these field equations are evaluated at a fixed position $\mathbf{x}$ rather than $\mathbf{X}_s$, since the fields $\mathbf{E}$ and $\mathbf{B}$ are functions of $\mathbf{x}$.

2.4 Some properties of the gyrokinetic-Maxwell equations

Having derived the physical equations, it is useful to enumerate some of their properties:

1. The system of equations is five-dimensional ($\mathbf{X}_s$, $v_\parallel$ and μ_s). The model equations consist of the three field equations (2.3.2), (2.3.5), (2.3.7), and the gyrokinetic equation (2.2.46) for each species.

2. The system of equations is multiscale in space. This is because the parallel spatial scale is always the system scale a (fast streaming forbids fluctuating quantities from varying quickly), but there are a mixture of perpendicular length scales: turbulent quantities vary on the scale ρ_s and non-fluctuating quantities vary on scale a. This disparity often results in gyrokinetic codes treating parallel and perpendicular spatial dimensions differently. Local gyrokinetics, for example, exploits this scale separation by only simulating a small perpendicular spatial extent ($\sim \mathcal{O}(L_{\text{fluc}})$) but large parallel spatial extents ($\sim \mathcal{O}(a)$). This is discussed in greater detail in chapter 3.

3. Although all terms in the GKE are the same size in ρ_*, the system of equations may be multiscale in the magnitude of terms, due to the difference in mass between ion and electron species. The reason for this is that some, but not all, of the terms in (2.2.46) have a dependence on species mass. For example, consider a turbulent feature with a perpendicular spatial scale approximately that of the ion Larmor radius ρ_i. Since the ions and electrons are coupled by the fields, both h_i and h_e will have this spatial scale, such that $\boldsymbol{\nabla}_\perp h_i \sim h_i/\rho_i$, $\boldsymbol{\nabla}_\perp h_e \sim h_e/\rho_i$. Examining the streaming and drift terms for ions and electrons reveals:

$$\text{ion parallel streaming: } \mathbf{v}_\parallel \cdot \boldsymbol{\nabla}_{\mathbf{X}_s} h_i \sim \frac{v_{th,i}}{a} h_i, \tag{2.4.1}$$

$$\text{ion magnetostatic drifts: } \mathbf{v}_{Ms} \cdot \boldsymbol{\nabla}_{\mathbf{X}_s} h_i \sim \frac{\rho_i}{a} v_{th,i} \frac{h_i}{\rho_i} \sim \frac{v_{th,i}}{a} h_i, \tag{2.4.2}$$

$$\text{electron parallel streaming: } \mathbf{v}_\parallel \cdot \boldsymbol{\nabla}_{\mathbf{X}_s} h_e \sim \frac{v_{th,e}}{a} h_e, \tag{2.4.3}$$

$$\text{electron magnetostatic drifts: } \mathbf{v}_{Ms} \cdot \boldsymbol{\nabla}_{\mathbf{X}_s} h_e \sim \frac{\rho_e}{a} v_{th,e} \frac{h_e}{\rho_i} \sim \frac{\rho_e}{\rho_i} \frac{v_{th,e}}{a} h_e. \tag{2.4.4}$$

   In the ion GKE the streaming and magnetostatic drift terms are of the same magnitude. However, in the electron GKE the drift term is naturally smaller than the streaming term by a factor of $\frac{\rho_e}{\rho_i} \sim \sqrt{m_e/m_i} \sim 1/60$ for deuterium ions.

   This multiscale-ness can be either favourable or unfavourable. On one hand, it may introduce numerical difficulties by mixing terms of differing magnitudes. On the other hand, it can allow simplifications; taking the limit $\sqrt{m_e/mi} \ll 1$, most terms in the electron GKE become small for ion-scale features, so that h_e can be calculated without solving the electron GKE (the "adiabatic" or "Boltzmann" treatment of electrons [45]). A similar simplification can be applied to the ion GKE if one considers electron-scale features, such that the temporal scale is that of the electron transit timescale; $\frac{\partial}{\partial t} \sim v_{th,e}/a$. In the limit $\sqrt{m_e/mi} \ll 1$, the $\frac{\partial h_i}{\partial t}$ term is much greater than all the other terms, and so to leading order $\frac{\partial h_i}{\partial t} = 0$.

4. The system of equations is integro-differential, with integrals over $(v_{\|}, \mu_s, s)$ required to evaluate the fields.

5. The system of equations is nonlinear in h_s, due to the $\langle \mathbf{v}_\chi \rangle_{\mathbf{X}_s} \cdot \boldsymbol{\nabla}_{\mathbf{X}_s} h_s$ term in the GKE (since $\langle \mathbf{v}_\chi \rangle_{\mathbf{X}_s}$ is a function of h_s). The physical interpretation of the nonlinearity is as follows. In the absence of this term, the GKE-Maxwell system of equations is linear i.e.

$$\frac{\partial h_s}{\partial t} = \mathcal{L}(h_s), \tag{2.4.5}$$

where $\mathcal{L}$ is a linear (integro-differential) operator. Being linear, the general solution takes the form

$$h_s = h_s(t=0)\exp(-i\Omega t), \tag{2.4.6}$$

where $\Omega = \omega + i\gamma$ is the complex mode frequency, ω the real frequency and γ the growth rate. Solving (2.4.5)("linear gyrokinetics") thus yields information about microinstabilities in the plasma, which will grow or decay exponentially so long as the nonlinear term is negligible. This provides valuable insights into the physics underlying the instabilities. When the nonlinear term is included and becomes non-negligible, nonlinear interactions cause the linear features to couple, and deviate from the exponential behaviour. This may cause the turbulence to saturate, i.e. reach some statistically steady-state amplitude. Saturated turbulence is observed experimentally, so it is reassuring that a physical mechanism exists for this within gyrokinetics (although it should be noted that flow shear can also play a role in turbulence saturation). It is also worth emphasising that gyrokinetics can be used to consider plasmas which are not experimentally attainable. Thus, the observation of saturation in experimental plasmas does not guarantee that hypothetical gyrokinetic plasmas should reach turbulence saturation.

6. Since I include electrostatic and magnetic fluctuations, equations (2.2.46), (2.3.2), (2.3.5), (2.3.7) may be described as the *electromagnetic* gyrokinetic-Maxwell set of equations. If one forbids fluctuations in the magnetic field i.e. $\delta \mathbf{B}_1 = 0$, one recovers the gyrokinetic-Poisson equations:

$$\frac{\partial h_s}{\partial t} + (\mathbf{v}_{\|} + \mathbf{v}_{Ms} + \mathbf{v}_E) \cdot \boldsymbol{\nabla}_{\mathbf{X}_s} h_s - \frac{\mu_s}{m_s} \mathbf{b} \cdot \boldsymbol{\nabla}_{\mathbf{X}_s} B_0 \frac{\partial h_s}{\partial v_{\|}} + \mathbf{v}_E \cdot \frac{\partial F_{0s}}{\partial \mathbf{X}} - \frac{Z_s e}{T_s} F_{0s} \frac{\partial \langle \varphi_1 \rangle_{\mathbf{X}_s}}{\partial t} = 0 \tag{2.4.7}$$

$$\sum_s Z_s e \int d^3\mathbf{v} \delta f_{1s} = \sum_s Z_s e \int d^3\mathbf{v} \left(h_s - \frac{Z_s e}{T_s} F_{0s} \varphi_1 \right) = 0. \tag{2.4.8}$$

(NB eq. (2.4.8) is identical to (2.3.2) and (2.4.7) has simply applied $\chi \to \varphi_1$ to (2.2.46)).

The parameter determining the importance of magnetic fluctuations is the plasma β. This can be shown by applying the gyrokinetic orderings to (2.3.3). The LHS is ordered like

$$\boldsymbol{\nabla} \times \delta \mathbf{B} \sim \frac{\delta B}{\rho_x}, \tag{2.4.9}$$

where ρ_x is the gyro-radius of a "typical" species. The RHS is ordered like

$$\mu_0 \delta \mathbf{j} = \mu_0 \sum_s \int \mathbf{v}^3 \mathbf{v} h_s \tag{2.4.10}$$

$$\sim \mu_0 \sum_s v_{th,s} \rho_* n_s \tag{2.4.11}$$

$$\sim \mu_0 v_{th,x} \rho_* n_x. \tag{2.4.12}$$

Combining the LHS and RHS and rearranging, one finds

$$\delta B_1 \sim \frac{n_x T_x}{B_0^2/\mu_0} \rho_* B_0, \tag{2.4.13}$$

$$\sim \beta_x \rho_* B_0, \tag{2.4.14}$$

where $\beta_x = n_x T_x/(B_0^2/\mu_0)$; the plasma β for the "typical" species x. Eq. (2.4.14) shows that, as expected, δB_1 is ordered like ρ_*. However, it will also tend to scale with β; at high β, the equilibrium magnetic field (for some fixed plasma pressure) is weaker, so turbulent fluctuations can more readily perturb the magnetic field.

2.5 Solving the gyrokinetic-Maxwell equations

The computational cost of finding solutions to the gyrokinetic-Maxwell set of equations is highly variable, depending on the exact "flavour" of gyrokinetic theory used and code implementation choices. The full-f global code GT5D, for example, has reported results of nonlinear simulations, taking $\sim 10^5$CPU-hours and memory consumption $\sim$ 750GB[46]. Such simulations are valuable as they capture the greatest amount of physics, but are too expensive for routine simulations; one may wish, for example, to simulate many equilibria, under different conditions, to find ways of optimising transport. Relatively inexpensive codes have been developed to this end by making further physical approximations.

A simplification, already discussed, is to use a δf formulation rather than full-f; this is usually reasonable in the core and edge, though not in the scrape-off layer, where fluctuations can have approximately the same magnitude as the equilibrium [47]. Another approximation, which greatly reduces computational time, is the *local approximation*, which takes advantage of the short length scale perpendicular to the equilibrium magnetic field.

This thesis makes heavy use of two local δf gyrokinetic codes; `stella` and `GS2`. In the following chapter I describe how the simulation equations for these codes are derived from the physical equations (2.2.46) (2.3.2), (2.3.5), (2.3.7), and how they are solved computationally.

2.6 Concluding remarks

This chapter describes and derives the gyrokinetic system using an asymptotic expansion in $\rho_* = \rho_s/a$. This reduces the entirely general kinetic-Maxwell equations to a five-dimensional set of equations, and eliminates timescales which are either much faster (e.g. gyro-motion) or much slower (e.g. equilibrium variation) than that of the turbulent fluctuations. This represents an enormous improvement in tractability. However, the gyrokinetic system is five-dimensional, multiscale, integro-differential and nonlinear and therefore still far from trivial to solve, often requiring computational calculation. This is done using gyrokinetic codes which are the subject of the next chapter.

Chapter 3

Local gyrokinetics: `stella` and `GS2`

3.1 Introduction

Chapter 2 derived the gyrokinetic-Maxwell equations eqs. (2.2.46), (2.3.2), (2.3.5) and (2.3.7), describing microinstabilities and turbulence in magnetically confined fusion plasmas. This chapter describes how these equations are translated into gyrokinetic software.

3.1.1 `stella` and `GS2`

This thesis presents results from two gyrokinetic codes, `stella` [45, 48] and `GS2` [49]. These are similar in that both spectrally solve the δf gyrokinetic system in the local limit using time-marching schemes. The physical model (and thus, the regime of validity) is the same between the two codes. Both are capable of simulating either tokamaks and stellarators: `GS2` was extended to simulate non-axisymmetric plasmas by Baumgaertel *et al.* [50] and `stella` was built with non-axisymmetric plasmas in mind and has been benchmarked against several other gyrokinetic codes in stellarator geometry [51, 52].

A significant difference between `stella` and `GS2` is their choice coordinates used to describe velocity space. `GS2` uses (ε_s, μ_s), which makes the mirror force implicit in the GKE. This enables the linear terms to be advanced reasonably straightforwardly using an implicit numerical scheme (see section 3.10). By contrast `stella` uses $(v_\parallel, \mu_s)$ coordinates which introduces a $\frac{\partial}{\partial v_\parallel}$ operator. Solving the linear system implicitly would become rather complicated, but is made possible using a flexible operator splitting scheme. This has the additional benefit of giving `stella` greater freedom in the choice of numerical scheme (numerical schemes can be "mixed and matched" to suit the problem at hand, and different schemes can be easily compared).

Another important difference is that the main branch of `stella`, as of today, is electrostatic. For this reason, the code `GS2` is used in chapter 5 to study electromagnetic instabilities in spherical tokamaks. Incorporating electromagnetic effects in `stella` is presented in chapter 6 in order to study electromagnetic instabilities in stellarators. An advantage of `stella` over `GS2` in the context of stellarator simulations is that `stella` is under active development with the needs of stellarator simulations firmly in mind.

For definiteness, in this chapter I describe the electrostatic implementation of `stella` in flux tube geometry. However, I will also make reference to (electromagnetic) `GS2` where there is a significant divergence between the codes.

Advancing from eqs. (2.2.46), (2.3.2), (2.3.5) and (2.3.7) to (electrostatic) `stella` consists of the following steps:

1. Taking the electrostatic limit; $A_{1\|} = B_{1\|} = 0$ (which corresponds to the limit $\beta \to 0$).
2. Applying the *local approximation*, which allows the simulation domain to be a "flux tube" rather than a full plasma, and for a 2D Fourier transform to be applied perpendicular to the equilibrium field.
3. Changing variable from h_s to $g_s \equiv h_s - \frac{Z_s e}{T_s} F_{0s} \left\langle \varphi_1 \right\rangle_{\mathbf{X}_s}$.
4. Normalisation, such that simulation variables are order unity.
5. Operator splitting, which allows different terms in the gyrokinetic equation to be separated and solved by different numerical schemes.
6. Discretisation in $(k_x, k_y, z, v_\|, \mu_s, t)$.

The electrostatic limit simply replaces gyrokinetic-Maxwell equations with the gyrokinetic-Poisson, or gyrokinetic-quasi-neutral system of equations (equations (2.4.7) and (2.4.8)). The other steps are discussed in greater detail in the following sections.

3.2 The local approximation

The local approximation in gyrokinetics takes advantage of the separation of spatial scales by assuming that, since $L_{\text{fluc}} \ll a$, the value of equilibrium quantities (e.g. $F_{0s}, \mathbf{B}_0$) are fixed over the perpendicular simulation domain L_{fluc}. Thus, properties of the equilibrium field, such as $\boldsymbol{\nabla} B_0$, are only a function of the parallel coordinate z. Note that although equilibrium quantities are assumed fixed over L_{fluc}, it is consistent to treat their gradients as finite (illustrated pictorially in figure 2.1).

Another benefit of the local approximation is that, if the perpendicular spatial domain is taken to be large enough that the turbulence is statistically decorrelated across the domain, a 2D Fourier transform can be applied in the perpendicular directions; the simulation equations become spectral in perpendicular dimensions x and y. The local field-aligned coordinate system and the spectral treatment are described in the following sections.

3.2.1 Local coordinates (x, y, z)

The local field-aligned coordinates are described well by Highcock [53]; a brief summary is provided here. Firstly, a coordinate system is defined using the basis vectors $(\hat{\psi} \equiv \boldsymbol{\nabla}\psi/|\boldsymbol{\nabla}\psi|, \hat{\alpha} \equiv \boldsymbol{\nabla}\alpha/|\boldsymbol{\nabla}\alpha|, \mathbf{b} \equiv \mathbf{B}_0/B_0)$, where ψ is the poloidal flux function and α is a scalar quantity satisfying

$$\mathbf{B}_0 = \boldsymbol{\nabla}\alpha \times \boldsymbol{\nabla}\psi \tag{3.2.1}$$

(NB this is known as the Clebsch representation and by definition ensures $\boldsymbol{\nabla} \cdot \mathbf{B}_0 = 0$). α can be written as [54]:

$$\alpha = \phi + q(\psi)\theta + \nu(\phi, \theta, \psi), \tag{3.2.2}$$

where ϕ is the toroidal angle, θ is the poloidal angle and ν is a function which is periodic in ϕ and θ. On a given surface, α is constant along a field line so can be considered a "field line label" (just as ψ can be considered a "flux surface label"). It is worth noting that $\hat{\psi}$ and $\hat{\alpha}$ are, by definition, perpendicular to $\mathbf{b}$, but not to one another in the presence of finite magnetic shear as $\hat{\alpha}$ contains a term like $\theta\boldsymbol{\nabla}q \propto \hat{\psi}$.

Local coordinates (i.e. local to a particular field line labelled by ψ_0 and α_0) x and y can be defined as

$$x = \frac{\partial x}{\partial \psi}(\psi - \psi_0) \tag{3.2.3}$$

$$y = \frac{\partial y}{\partial \alpha}(\alpha - \alpha_0), \tag{3.2.4}$$

and parallel coordinate z (discussed in section 3.2.2). The local basis is $(\hat{\mathbf{x}} \equiv \boldsymbol{\nabla}x/|\boldsymbol{\nabla}x|, \hat{\mathbf{y}} \equiv \boldsymbol{\nabla}y/|\boldsymbol{\nabla}y|, \mathbf{b})$. NB since y is defined by α, it is a function of x and z ($y = y(x, z)$), and $\hat{\mathbf{y}}$ is not, in general, perpendicular to $\hat{\mathbf{x}}$.

3.2.2 The parallel coordinate z

In tokamak simulations, it is common to use a poloidal angle-like variable as the parallel coordinate z (for this reason, `GS2` refers to the parallel coordinate as θ or `theta`). There are several choices of definition for z. One example is what I will refer to as "geometric z", equal to $\arctan\left(\frac{Z-Z_0}{R-R_0}\right)$, where (R, Z) are cylindrical coordinates and (R_0, Z_0) is the geometric centre of the flux surface, with the sign and phase appropriately chosen to span from 0 to 2π. Another choice is θ_{Miller}, which is used in the local analytic model for flux surfaces derived by Miller *et al.* [55] (this is discussed in section 5.5.1.1). In all of these definitions, $z = 0$ corresponds to the outboard midplane by convention.

In stellarator simulations in `stella` the parallel domain is defined by the number of field periods the user chooses to include. Hence, the parallel coordinate is related to the toroidal angle ζ, but is normalised to the range $-\pi \leq z \leq \pi$. NB if the number of field periods simulated is equal to the number of field periods in the device (e.g. 5 in W7-X) multiplied by q, then z can again be interpreted as the poloidal angle.

3.2.3 Spectral representation of the gyrokinetic system

I now perform a Fourier transform of the gyrokinetic-Maxwell equations in x and y. A complex 2D Fourier transform represents an arbitrary quantity $f(x, y)$ in the range ($-L_x/2 \leq x \leq L_x/2$, $-L_y/2 \leq y \leq L_y/2$) as [56]:

$$f(x, y) = \sum_{r=-\infty}^{\infty} \sum_{s=-\infty}^{\infty} \hat{f}_{r,s} \exp i \left(\frac{2\pi r x}{L_x} + \frac{2\pi s y}{L_y} \right), \tag{3.2.5}$$

where $k_x \equiv \frac{2r\pi}{L_x}$ and $k_y \equiv \frac{2s\pi}{L_y}$ are the Fourier wavenumbers of the system. In local gyrokinetics, fluctuating quantities are represented on a discrete, finite grid of (k_x, k_y); an arbitrary quantity f can be written as [45]:

$$f(x, y, z, v_\parallel, \mu_s, t) = \sum_{-k_{x,\text{max}}}^{k_{x,\text{max}}} \sum_{-k_{y,\text{max}}}^{k_{y,\text{max}}} \hat{f}_{k_x,k_y}(z, v_\parallel, \mu_s, t) \exp i(k_x x + k_y y), \tag{3.2.6}$$

where k_x and k_y have a user-defined spacing Δk_x and Δk_y respectively. $k_{x(y),\text{max}}$ defines the spatial resolution in $x(y)$, and $\Delta k_{x(y)}$ determines the largest spatial scale simulated (i.e. the perpendicular size of the flux tube, or "box size"). The distribution function and fields are required to be purely real, which is satisfied by imposing $\hat{f}_{k_x,k_y} = \hat{f}^*_{-k_x,-k_y}$, where * denotes the complex conjugate. For this reason, `stella` and `GS2` do not simulate negative k_y values since they can be calculated trivially from the positive k_y modes.

Thus, an arbitrary gyrophase-independent quantity $g(\mathbf{X}_s)$ (such as h_s) can be written as:

$$\begin{aligned} g(\mathbf{X}_s, v_\parallel, \mu_s, t) &= g(\mathbf{x}, \alpha_s, v_\parallel, \mu_s, t) && (3.2.7) \\ &= \sum_{k_x,k_y} \hat{g}'_{k_x,k_y}(\alpha_s, z, v_\parallel, \mu_s, t) \exp i(xk_x + yk_y) && (3.2.8) \\ &= \sum_{k_x,k_y} \hat{g}_{k_x,k_y}(z, v_\parallel, \mu_s, t) \exp i((\mathbf{X}_s \cdot \hat{\mathbf{x}})k_x + (\mathbf{X}_s \cdot \hat{\mathbf{y}})k_y), && (3.2.9) \end{aligned}$$

where the prime ($'$) is used to denote that the Fourier coefficients in (3.2.8) and (3.2.9) are different; (3.2.8) is a straightforward application of (3.2.6), and (3.2.9) takes advantage of the gyrophase-independence of g (such that $\hat{g}_{k_x,k_y}$ is not a function of α). The formulation (3.2.9) is used exclusively which ensures that $\hat{g}_{k_x,k_y}$ are unaffected by gyroaveraging at fixed $\mathbf{X}_s$ for gyrophase-independent quantities:

$$\left\langle g(\mathbf{X}_s, v_\parallel, \mu_s, t)\right\rangle_{\mathbf{X}_s} = g(\mathbf{X}_s, v_\parallel, \mu_s, t) = \sum_{k_x,k_y} \hat{g}_{k_x,k_y}(z, v_\parallel, \mu_s, t) \exp i(\mathbf{X}_s \cdot (k_x\hat{\mathbf{x}} + k_y\hat{\mathbf{y}})). \quad (3.2.10)$$

The fields $\varphi, A_{1\parallel}, B_{1\parallel}$, which are a function of **x** but not **v**, can be written as

$$f(\mathbf{x}, t) = \sum_{k_x,k_y} f_{k_x,k_y}(z, t) \exp i(k_x x + k_y y), \quad (3.2.11)$$

where $f = \left\{\varphi, A_{1\parallel}, B_{1\parallel}\right\}$. Calculating the gyroaverage of f at fixed $\mathbf{X}_s$ (as required by the GKE) is done using the identity $\mathbf{x} = \mathbf{X}_s + \boldsymbol{\rho}_s$:

$$f(\mathbf{x}, \mathbf{v}, t) = f(\mathbf{x}, v_\|, \mu_s, t) = \sum_{k_x, k_y} \hat{f}_{k_x,k_y}(z, v_\|, \mu_s, t) \exp i(\mathbf{x} \cdot (k_x\hat{\mathbf{x}} + k_y\hat{\mathbf{y}})) \tag{3.2.12}$$

$$\langle f(\mathbf{x}, \mathbf{v}, t)\rangle_{\mathbf{X}_s} = \left\langle \sum_{k_x,k_y} \hat{f}_{k_x,k_y}(z, v_\|, \mu_s, t) \exp i(\mathbf{X}_s \cdot (k_x\hat{\mathbf{x}} + k_y\hat{\mathbf{y}})) \exp i(\boldsymbol{\rho}_s \cdot (k_x\hat{\mathbf{x}} + k_y\hat{\mathbf{y}})) \right\rangle_{\mathbf{X}_s} \tag{3.2.13}$$

$$= \sum_{k_x,k_y} \hat{f}_{k_x,k_y}(z, v_\|, \mu_s, t) \exp i(\mathbf{X}_s \cdot (k_x\hat{\mathbf{x}} + k_y\hat{\mathbf{y}})) \left\langle \exp i(\boldsymbol{\rho}_s \cdot (k_x\hat{\mathbf{x}} + k_y\hat{\mathbf{y}}))\right\rangle_{\mathbf{X}_s} \tag{3.2.14}$$

$$= \sum_{k_x,k_y} \hat{f}_{k_x,k_y}(z, v_\|, \mu_s, t) \exp i(\mathbf{X}_s \cdot (k_x\hat{\mathbf{x}} + k_y\hat{\mathbf{y}})) J_0(\gamma_s), \tag{3.2.15}$$

where $\gamma_s = \frac{k_\perp v_\perp}{\Omega_s}$, $k_\perp^2 = k_x^2|\boldsymbol{\nabla} x|^2 + k_y^2|\boldsymbol{\nabla} y|^2 + 2k_xk_y\boldsymbol{\nabla} x \cdot \boldsymbol{\nabla} y$ and I have used the identity

$$J_n(x) = \frac{1}{2\pi}\int_{-\pi}^{\pi} \exp i(x \sin\tau - n\tau)d\tau, \tag{3.2.16}$$

where $J_n(x)$ is an ordinary Bessel function of the first kind. Similarly, the field equations for φ_1 and $A_{1\|}$ require integrating h_s (or some other gyrophase-independent quantity g) over $d^3\mathbf{v}$ at fixed $\mathbf{x}$, which can be written as:

$$g(\mathbf{X}, v_\|, \mu_s, t) = \sum_{k_x,k_y} \hat{g}_{k_x,k_y}(z, v_\|, \mu_s, t) \exp i(\mathbf{x} \cdot (k_x\hat{\mathbf{x}} + k_y\hat{\mathbf{y}})) \exp i(-\boldsymbol{\rho}_s \cdot (k_x\hat{\mathbf{x}} + k_y\hat{\mathbf{y}})) \tag{3.2.17}$$

$$\int d^3\mathbf{v} g(\mathbf{X}, v_\|, \mu_s, t) = \int dv_\| dv_\perp^2 d\alpha_s g(\mathbf{X}, v_\|, \mu_s, t) \tag{3.2.18}$$

$$= \int dv_\| \left(\frac{B_0}{m_s}\right) d\mu_s d\alpha_s \sum_{k_x,k_y} \hat{g}_{k_x,k_y}(z, v_\|, \mu_s, t) \exp i(\mathbf{x} \cdot (k_x\hat{\mathbf{x}} + k_y\hat{\mathbf{y}})) \exp i(-\boldsymbol{\rho}_s \cdot (k_x\hat{\mathbf{x}} + k_y\hat{\mathbf{y}})) \tag{3.2.19}$$

$$= \int dv_\| \left(\frac{B_0}{m_s}\right) d\mu_s \sum_{k_x,k_y} \hat{g}_{k_x,k_y}(z, v_\|, \mu_s, t) \exp i(\mathbf{x} \cdot (k_x\hat{\mathbf{x}} + k_y\hat{\mathbf{y}})) \cdot 2\pi J_0(\gamma_s). \tag{3.2.20}$$

To obtain $B_{1\|}$ requires integrating $\boldsymbol{\nabla} \cdot (h_s(\mathbf{b} \times \mathbf{v}_\perp))$ over $d^3\mathbf{v}$ (see equation (2.3.5)). This can be written as:

$$\int d^3\mathbf{v}\boldsymbol{\nabla}\cdot\left(h_s(\mathbf{X},v_\parallel,\mu_s,t)(\mathbf{b}\times\mathbf{v}_\perp)\right)=\int dv_\parallel\left(\frac{B_0}{m_s}\right)d\mu_s d\alpha_s\boldsymbol{\nabla}\cdot\left(h_s(\mathbf{b}\times\mathbf{v}_\perp)\right) \tag{3.2.21}$$

$$=\int dv_\parallel\left(\frac{B_0}{m_s}\right)d\mu_s d\alpha_s\boldsymbol{\nabla}\cdot\sum_{k_x,k_y}\hat{h}_{s,k_x,k_y}(z,v_\parallel,\mu_s,t)\exp i(\mathbf{x}\cdot\mathbf{k})\exp i(-\boldsymbol{\rho}_s\cdot\mathbf{k})(\mathbf{b}\times\mathbf{v}_\perp) \tag{3.2.22}$$

$$=\int dv_\parallel\left(\frac{B_0}{m_s}\right)d\mu_s d\alpha_s\cdot\sum_{k_x,k_y}\hat{h}_{s,k_x,k_y}(z,v_\parallel,\mu_s,t)\exp i(\mathbf{x}\cdot\mathbf{k})\exp i(-\boldsymbol{\rho}_s\cdot\mathbf{k})i\mathbf{k}\cdot(\mathbf{b}\times\mathbf{v}_\perp) \tag{3.2.23}$$

$$=\int dv_\parallel\left(\frac{B_0}{m_s}\right)d\mu_s d\alpha_s\cdot\sum_{k_x,k_y}\hat{h}_{s,k_x,k_y}\exp i(\mathbf{x}\cdot\mathbf{k})\exp i(\gamma_s\sin(\alpha_s))(-k_\perp v_\perp)\left(e^{i\alpha_s}-e^{-i\alpha_s}\right) \tag{3.2.24}$$

$$=\int dv_\parallel\left(\frac{B_0}{m_s}\right)d\mu_s d\alpha_s\cdot\sum_{k_x,k_y}\hat{h}_{s,k_x,k_y}\exp i(\mathbf{x}\cdot\mathbf{k})k_\perp v_\perp 2\pi J_1(\gamma_s), \tag{3.2.25}$$

where use has been made of the identity $J_{-n}(x)=(-1)^n J_n(x)$.

3.2.4 Benefits of spectral codes

Spectral codes have several advantages:

1. Perpendicular gradients ($\boldsymbol{\nabla}_\perp$) of fluctuating quantities can be evaluated spectrally, which is cheaper and more accurate than finite difference schemes.
2. The gyroaverage is easily calculated.
3. Excluding the nonlinear term, the GKE-Maxwell equations are linear in g_s; thus, each spectral coefficient $\hat{g}_{k_x,k_y}$ is independent and can be considered separately (subject to the boundary condition in z, discussed in section 3.6). This effectively eliminates two spatial dimensions from the linear system of equations (dependence on x and y is prescribed) and provides physics insight by separating the spatial scales of fluctuations. The nonlinear source term mixes different (k_x,k_y) so requires a grid of $\mathbf{k}$ to be constructed. However, the linear source terms can still be calculated spectrally and the nonlinear term calculated pseudo-spectrally (as discussed in section 3.5).

3.3 Choice of distribution function variable

`stella`'s choice of distribution variable $g_s \equiv h_s - \frac{Z_s e}{T_s} F_{0s} \left\langle \varphi_1 \right\rangle_{\mathbf{X}_s}$ eliminates the $\left(\frac{\partial \langle \varphi_1 \rangle_{\mathbf{X}_s}}{\partial t} \right)$ term from the GKE, such that only g_s appears in a temporal derivative. This makes `stella`'s operator splitting more straightforward as well as simplifying the source terms when using explicit numerical schemes. `GS2` also uses g_s in electrostatic simulations, but in electromagnetic simulations uses the variable

$$g_{s,\texttt{GS2}} \equiv h_s - \frac{Z_s e}{T_s} F_{0s} \left(\langle \varphi_1 \rangle_{\mathbf{X}_s} - \langle \mathbf{v}_\perp \cdot \mathbf{A}_{1\perp} \rangle_{\mathbf{X}_s} \right), \tag{3.3.1}$$

such that $B_{1\|}$ is also included in the distribution function [57][1]. With this definition, a term like $\left(\frac{\partial A_{1\|}}{\partial t} \right)$ appears in the GKE, but because the operator splitting in `GS2` is different, the problems encountered by `stella` are avoided.

3.4 Normalisations

It is natural and convenient for gyrokinetic codes to normalise all quantities to ensure they are near to unity. This helps avoid computational issues associated with computing very large or very small numbers, and makes the simulation equations dimensionless. The fundamental normalising quantities used are: the mass, temperature and number density of a "reference" species m_r, T_r n_r, a reference value of magnetic field strength B_r and a reference macroscopic scale length a. Z_r could also be used as a normalising quantity but for consistency with Barnes *et al.* [45] I take $Z_r = 1$. With these, the following compound normalising quantities can be constructed:

$$v_{th,r} = \sqrt{\frac{2T_r}{m_r}}, \qquad \Omega_r = \frac{eB_r}{m_r}, \qquad \rho_r = \frac{v_{th,r}}{\Omega_r}, \tag{3.4.1}$$

the thermal velocity, Larmor frequency and thermal Larmor radius of the reference species, respectively. With these, `stella` normalises the terms in the gyrokinetic-Maxwell equations as follows

---

[1] A possible source of confusion is that in the `GS2` code the non-adiabatic piece of the distribution function is labelled g_s and the modified distribution function is labelled h_s i.e. the opposite of `stella`. So that this thesis is self-consistent, I will refer to `GS2`'s modified distribution function as $g_{s,\texttt{GS2}}$

[45]:

$$\tilde{t} = t v_{th,r}/a, \qquad \tilde{T}_s = T_s/T_r, \qquad \tilde{v}_\parallel = v_\parallel / v_{th,s}, \tag{3.4.2}$$

$$\tilde{\boldsymbol{\nabla}}_\parallel = a\boldsymbol{\nabla}_\parallel, \qquad \tilde{\mu}_s = \mu_s \frac{B_r}{2T_s}, \qquad \tilde{B}_0 = B/B_r, \tag{3.4.3}$$

$$\tilde{v}_s = v/v_{th,s}, \qquad \tilde{n}_s = n_s/n_r, \qquad \tilde{k}_x = k_x \rho_r, \tag{3.4.4}$$

$$\tilde{k}_y = k_y \rho_r, \qquad \tilde{\varphi}_{1\mathbf{k}} = \frac{e\varphi_{1\mathbf{k}}}{T_r}\frac{a}{\rho_r}, \qquad \tilde{g}_{\mathbf{k},s} = \hat{g}_{k_x,k_y}\frac{e^{-\tilde{v}_s^2}}{F_{0s}}\frac{a}{\rho_r}, \tag{3.4.5}$$

where the tilde ($\tilde{}$) indicates a normalised quantity. `GS2`'s normalisation is very similar [53]. One notable difference is that `GS2`'s distribution function is normalised $\tilde{g}_{\texttt{GS2},\mathbf{k},s} = (\hat{g}_{\texttt{GS2},k_x,k_y}/F_{0s})\frac{a}{\rho_r}$ (i.e. missing $e^{-\tilde{v}_s^2}$). `stella`'s choice is necessary to ensure $|\tilde{g}_{\mathbf{k},s}| \to 0$ as $\tilde{v}_\parallel \to \pm\infty$ so that a zero-incoming boundary condition can be used in $\tilde{v}_\parallel$ in `stella`.

3.5 Simulation equations in `stella`

Taking the above points in mind one arrives at the simulation equations solved by the gyrokinetic codes. For `stella`, these are:

$$\begin{aligned} \text{GKE:} \quad & \frac{\partial \tilde{g}_{\mathbf{k},s}}{\partial \tilde{t}} + \overbrace{\tilde{v}_{th,s}\tilde{v}_\parallel(\mathbf{b}\cdot\tilde{\boldsymbol{\nabla}}z)\left(\frac{\partial \tilde{g}_{\mathbf{k},s}}{\partial z} + \frac{Z_s}{\tilde{T}_s}\frac{\partial J_0(\gamma_s)\tilde{\varphi}_{1\mathbf{k}}}{\partial z}e^{-\tilde{v}_s^2}\right)}^{\text{streaming}} - \overbrace{\tilde{v}_{th,s}\tilde{\mu}_s\mathbf{b}\cdot\tilde{\boldsymbol{\nabla}}\tilde{B}_0\frac{\partial \tilde{g}_{\mathbf{k},s}}{\partial \tilde{v}_\parallel}}^{\text{mirror}} \\ & + \underbrace{i\omega_{d,\mathbf{k},s}\left(\tilde{g}_{\mathbf{k},s} + \frac{Z_s}{\tilde{T}_s}J_0(\gamma_s)\tilde{\varphi}_{1\mathbf{k}}e^{-\tilde{v}_s^2}\right)}_{\text{drifts}} + \underbrace{i\omega_{*,\mathbf{k},s}J_0(\gamma_s)\tilde{\varphi}_{1\mathbf{k}}}_{\text{diamagnetic}} + \underbrace{\mathcal{N}_{\mathbf{k},s}}_{\mathbf{E}\times\mathbf{B}\text{ nonlinearity}} = 0 \end{aligned} \tag{3.5.1}$$

$$\text{Quasi-neutrality:} \quad \sum_s Z_s \tilde{n}_s \left(\frac{2\tilde{B}_0}{\sqrt{\pi}}\int_{-\infty}^{\infty} d\tilde{v}_\parallel \int_0^\infty d\tilde{\mu}_s J_0(\gamma_s)\tilde{g}_{\mathbf{k},s} + \frac{Z_s}{\tilde{T}_s}(\Gamma_0(b_s)-1)\tilde{\varphi}_{1\mathbf{k}}\right) = 0, \tag{3.5.2}$$

where

$$\omega_{d,\mathbf{k},s} = \frac{\tilde{T}_s}{Z_s\tilde{B}_0}\left(\tilde{v}_\parallel^2\mathbf{v}_\kappa + \tilde{\mu}_s\mathbf{v}_{\boldsymbol{\nabla}B}\right)\cdot\left(\tilde{k}_y\boldsymbol{\nabla}y + \tilde{k}_x\boldsymbol{\nabla}x\right) \tag{3.5.3}$$

$$\omega_{*,\mathbf{k},s} = \frac{\tilde{k}_y}{2}aB_r\frac{dy}{d\alpha}e^{-\tilde{v}_s^2}\frac{d\ln F_{0s}}{\psi}, \tag{3.5.4}$$

$$\mathcal{N}_{\mathbf{k},s} = \frac{B_r}{2}\frac{dy}{d\alpha}\frac{dx}{d\psi}\mathcal{F}_\mathbf{k}\left[\mathcal{F}_\mathbf{k}^{-1}\left[i\tilde{k}_yJ_0(\gamma_s)\tilde{\varphi}_{1\mathbf{k}}\right]\mathcal{F}_\mathbf{k}^{-1}\left[i\tilde{k}_x\tilde{g}_{\mathbf{k},s}\right] - \mathcal{F}_\mathbf{k}^{-1}\left[i\tilde{k}_xJ_0(\gamma_s)\tilde{\varphi}_{1\mathbf{k}}\right]\mathcal{F}_\mathbf{k}^{-1}\left[i\tilde{k}_y\tilde{g}_{\mathbf{k},s}\right]\right], \tag{3.5.5}$$

$\Gamma_0(b_s) = e^{-b_s}I_0(b_s)$ where I_0 is a modified Bessel function of the first kind, $b_s = k_\perp^2\rho_s^2/2$, $\mathbf{v}_\kappa = \mathbf{b}\times\left(\mathbf{b}\cdot\tilde{\boldsymbol{\nabla}}\mathbf{b}\right)$, $\mathbf{v}_{\boldsymbol{\nabla}B} = \mathbf{b}\times\tilde{\boldsymbol{\nabla}}\tilde{B}_0$ and $\mathcal{F}_\mathbf{k}^{(-1)}$ indicates a(n) (inverse) Fourier transform.

I refer to all terms in the GKE except $\frac{\partial\tilde{g}_{\mathbf{k},s}}{\partial t}$ as "source terms" (since eq. (3.5.1) can be written as $\frac{\partial\tilde{g}_{\mathbf{k},s}}{\partial\tilde{t}} = \{\text{source terms}\}$). The source terms are, in order of appearance: (1) parallel streaming (i.e. advection along z with normalised velocity $\tilde{v}_\parallel$), (2) parallel acceleration (i.e. advection in $\tilde{v}_\parallel$) arising from the mirror force, (3) $\boldsymbol{\nabla}B$ and curvature magnetostatic drifts (i.e. advection in x and y), (4) a diamagnetic drift-like term arising from gradients in F_{0s}, acting on $\tilde{\varphi}_{1\mathbf{k}}$ and (5) the nonlinear $\mathbf{E}\times\mathbf{B}$ drift (nonlinear advection in x and y). Of these source terms, the diamagnetic term usually plays a dominant role in driving instabilities; physically, this is the term which "accesses" the potential energy associated with the equilibrium density and temperature gradients.

The `GS2` simulation equations are very similar in the electrostatic limit, although the mirror term is missing due to the (ε_s, μ_s) coordinates used. Electromagnetically, a term proportional to $\frac{\partial A_{1\parallel}}{\partial t}$ appears, as do the normalised field equations for $A_{1\parallel}$ and $B_{1\parallel}$. These field equations are virtually identical to the electromagnetic `stella` field equations presented in chapter 6 so are not reproduced here.

3.5.1 The nonlinear source term $\mathcal{N}_s$

In both `stella` and `GS2`, the nonlinear term is treated pseudo-spectrally: the gradients of $\tilde{\varphi}_1$ and $\tilde{g}_s$ are calculated in Fourier space, then transformed into real space, where the nonlinear term is calculated. The nonlinear term is then transformed back to Fourier space. To avoid unphysical aliasing, the number of physical gridpoints x, y are each greater by 50% than the number of Fourier modes included; the upper third of the Fourier modes in $(\tilde{k}_x, \tilde{k}_y)$ are padded with zeros. Recalling that negative k_y modes are included in the Fourier expansion but not explicitly simulated due to the reality condition (section 3.2.3) gives $n_{\tilde{k}_x} \simeq (2/3)n_x$, $n_{\tilde{k}_y} \simeq n_y/3$.

3.6 Boundary conditions in z

Physical periodicity means that all physical quantities A must be periodic in poloidal and toroidal angle:

$$A(\psi, \phi, \theta) = A(\psi, \phi + 2n\pi, \theta + 2m\phi), \tag{3.6.1}$$

for all integers n and m. Applied to the field-aligned coordinate system, this becomes a periodicity requirement in the parallel coordinate z; physical quantities must be periodic, matching the periodicity of the magnetic geometry. Assuming z represents the poloidal angle, this can be expressed as

$$A(x, y(x, z), z) = A(x, y(x, z + 2p\pi), z + 2p\pi), \tag{3.6.2}$$

where $p = n/N_p$, n is an integer and N_p is the number of field periods of the magnetic geometry (so the magnetic geometry is periodic in z with periodicity $2\pi/N_p$) (NB the non-spatial dependencies in A have been dropped for brevity). For axisymmetric devices, $N_p = 1$.

In the local limit, non-fluctuating physical quantities (e.g. magnetic geometry) are a function of z only; thus, periodicity for non-fluctuating quantities is straightforward. For fluctuating quantities, eq. (3.6.2) means that

$$\sum_{k_x,k_y} \hat{A}_{k_x,k_y}(z) \exp i(k_x x + k_y y(x, z)) = \sum_{k_x,k_y} \hat{A}_{k_x,k_y}(z + 2p\pi) \exp i(k_x x + k_y y(x, z + 2p\pi)). \tag{3.6.3}$$

When combined with the orthogonality condition of the Fourier harmonics, this means that the Fourier coefficients $\hat{A}_{k_x,k_y}$ obey

$$\hat{A}_{k_x,k_y} = \hat{A}_{k_x',k_y} \exp i \left(2p\pi k_y \frac{dy}{d\alpha} q(\psi_0) \right), \tag{3.6.4}$$

where $k_x' = k_x + 2p\pi k_y \frac{dy}{d\alpha}\frac{dq}{dx}$. In other words, each Fourier harmonic is not periodic in z (unless $\frac{dq}{dx} = 0$ or $k_y = 0$); rather, the modes have a “twist-and-shift”, or “linked”, boundary condition, whereby different values of k_x are coupled at boundary values of z, which I refer to as $\pm z_{\text{max}}$ (referred to as z_0 by Barnes *et al.* [45]). An alternative description is to write the Fourier transform as

$$A(x,y,z) = \sum_{k_x,k_y} \hat{A}_{k_x,k_y}(z) \exp i(\mathbf{k}_\perp \cdot \mathbf{x}), \tag{3.6.5}$$

where

$$\mathbf{k}_\perp = k_y\hat{\mathbf{y}} + (k_x + k_y\hat{s}z)\hat{\mathbf{x}} \equiv k_y\hat{\mathbf{y}} + k_{x,\text{eff}}\hat{\mathbf{x}} \tag{3.6.6}$$

$$k_{x,\text{eff}} = (k_x + k_y\hat{s}z) = k_y\hat{s}(z - \theta_0) \tag{3.6.7}$$

and ($\theta_0 \equiv -k_x/(k_y\hat{s})$). Thus, a particular Fourier mode $\hat{A}_{k_x,k_y}$ has a perpendicular wavenumber $\mathbf{k}_\perp$ and an "effective" k_x, which varies continuously as a function of z. The twist-and-shift boundary condition is simply that for each $\tilde{k}_y$, different $\tilde{k}_x$ modes are linked together to form extended domains in z, such that the value of $\tilde{k}_{x,\text{eff}}$ matches at the join. A zero-incoming boundary condition is applied at the extrema of the extended domains, $z = \pm z_{\text{max, ext}}$.

The requirement to form linked domains imposes a constraint in the $\tilde{k}_x$ spacing, since one requires $\left(\frac{2\tilde{k}_y\hat{s}z_{\text{max}}}{\Delta\tilde{k}_x}\right)$ to be an integer. In `stella` and `GS2` this quantity is a user-defined parameter called `jtwist`, which controls the relative spacing in $\tilde{k}_x$ and $\tilde{k}_y$. Since $\tilde{k}_{x,\text{eff}}(z)$ varies with $\tilde{k}_y$, these extended domains have, in general, different lengths; the longest extended domains occur at the minimum nonzero $\tilde{k}_y$ value (i.e. $\tilde{k}_y = \Delta\tilde{k}_y$). An illustration of extended domains, showing $\tilde{k}_{x,\text{eff}}(z)$ matching between different $\tilde{k}_x$, is shown in figure 3.1. An illustration of linked $\tilde{k}_x$ modes for different values of $\tilde{k}_y$ and `jtwist` is shown in figure 3.2 (with credit to Stephen Biggs-Fox for the inspiration).

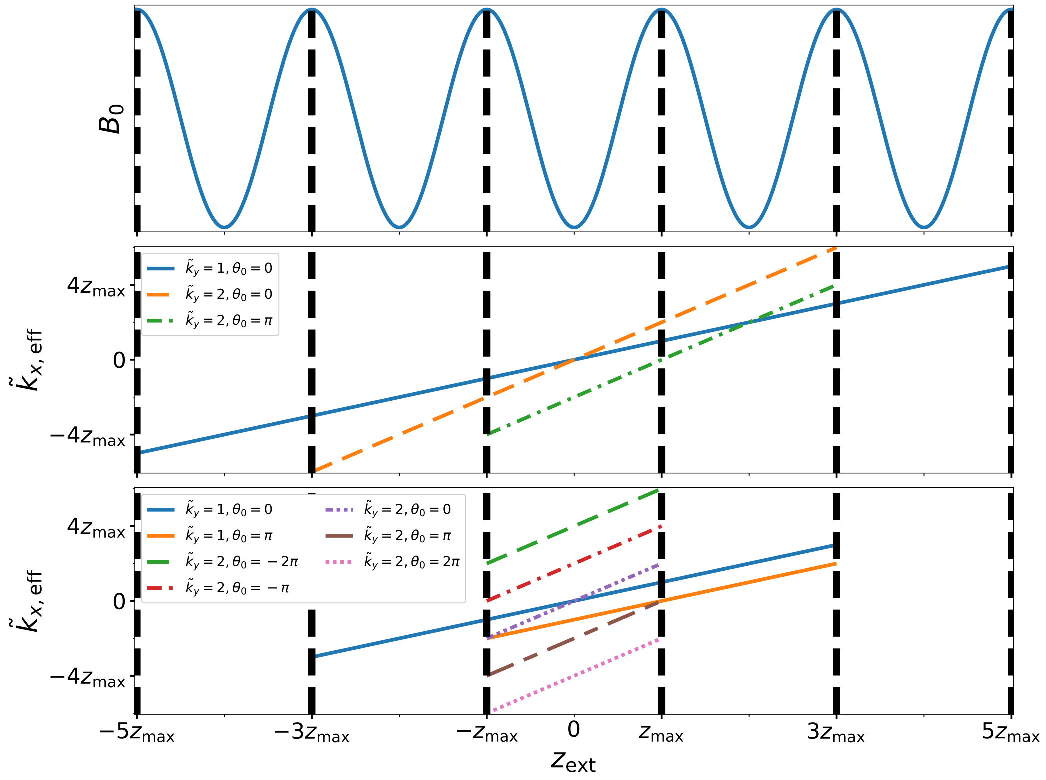

Figure 3.1: Illustration of the extended z domain for plasma with $N_p = 1$ (e.g. a tokamak plasma). Upper: equilibrium quantity B_0, which is periodic in z. Middle and lower plots: $\tilde{k}_{x,\mathrm{eff}}(z)$ for a simulation with ($\Delta\tilde{k}_y = 1$, $\hat{s} = 1$, $n_{\tilde{k}_y} = 2$, $n_{\tilde{k}_x} = 5$). Middle plot has `jtwist`$= 1$, so that $\Delta\tilde{k}_x = 2z_{\mathrm{max}}$. Lower plot has `jtwist` $= 2$, so $\Delta\tilde{k}_x = z_{\mathrm{max}}$.

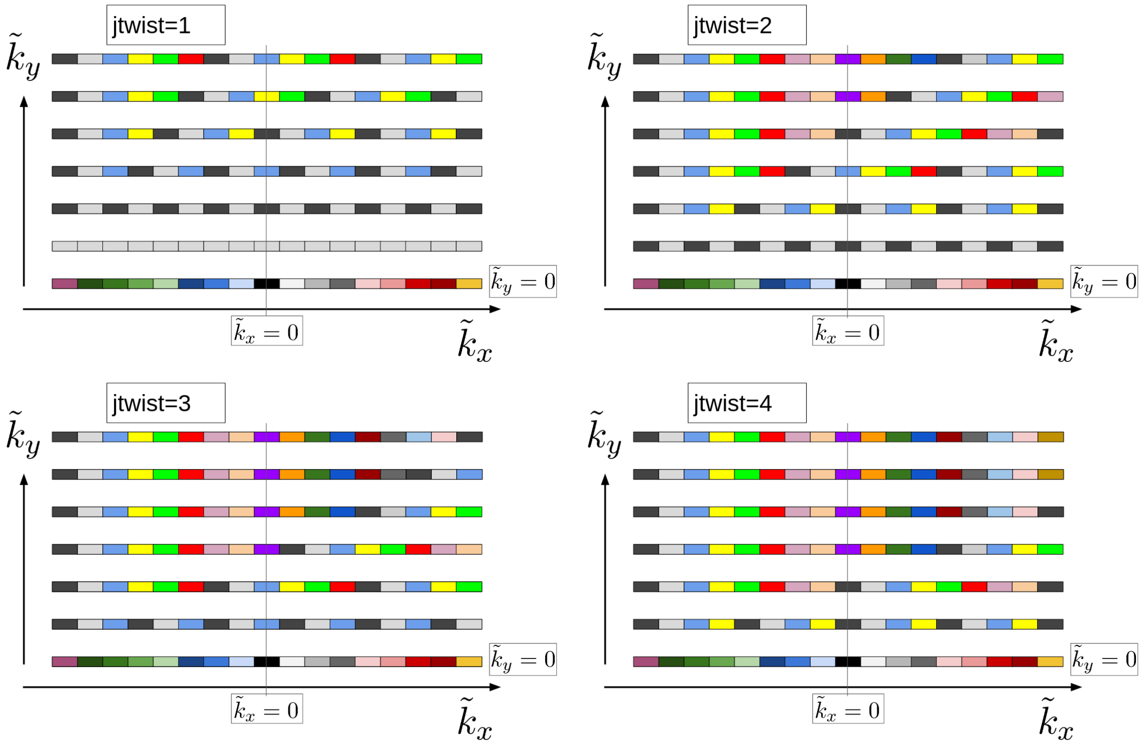

Figure 3.2: Pictorial representation of extended z domains for different values of `jtwist`. Each coloured box represents a single $(\tilde{k}_x, \tilde{k}_y)$. For each $\tilde{k}_y$, modes with the same colour are part of the same extended z domain.

The zero-incoming condition at the end of extended domains ($z = \pm z_{\text{max, ext}}$) is physically well-behaved provided that $\tilde{g}_{\mathbf{k},s} \to 0$ as $z_{\text{ext}} \to \pm z_{\text{max, ext}}$. If this is not the case, the simulation result becomes sensitive to the value of $z_{\text{max, ext}}$, which is a *non-physical* parameter, since it is a feature of the simulation but not the gyrokinetic model. Fortunately, $\tilde{g}_{\mathbf{k},s} \to 0$ as $z_{\text{ext}} \to \pm\infty$ tends to occur naturally because the argument of the Bessel function γ_s increases with z (via $k_\perp$). As $z_{\text{ext}} \to \pm\infty$, $J_0(\gamma_s) \to 0$ so the diamagnetic term in the GKE vanishes (provided that $|\tilde{\varphi}_{1\mathbf{k}}|$, which also appears in the diamagnetic term, does not grow with $|z|$ faster than $J_0(\gamma_s)$ falls). As discussed in section 3.5, the diamagnetic term is often the driving term, so as it vanishes the mode ceases to grow. A physical interpretation of this is that physical structures are “sheared apart” by the equilibrium magnetic shear: as one follows a particular feature along a magnetic field line, it deforms (becomes stretched and thinned) perpendicular to the field line due to radial variation in q (i.e. variation in magnetic pitch angle). As the perpendicular spatial size of the feature shrinks, it becomes “averaged out” by particle gyrations.

The twist-and-shift boundary condition is used in nonlinear simulations, which require the simulation of many $(\tilde{k}_x, \tilde{k}_y)$. Linear simulations simply use a zero-incoming boundary on each $(\tilde{k}_x, \tilde{k}_y)$ (unless $\tilde{k}_y = 0$ or $\hat{s} = 0$), but can extend the z domain arbitrarily far; this allows the user to extend the z domain sufficiently far to ensure that $\tilde{g}_{\mathbf{k},s} \to 0$ as $z_{\text{ext}} \to \pm z_{\text{max, ext}}$, such that a physical mode can be recovered. This is effectively the same as twist-and-shift, without explicitly defining different values of $\tilde{k}_x$.

The boundary conditions in z for $\tilde{g}_{\mathbf{k},s}$ in `stella`, imposed by physical periodicity, can thus be summarised as:

1. If $\tilde{k}_y = 0$ or $\hat{s} = 0$, $\tilde{g}_{\mathbf{k},s}$ is $2\pi/N_p$-periodic in poloidal angle ($\tilde{g}_{\mathbf{k},s}(z + 2p\pi) = \tilde{g}_{\mathbf{k},s}(z)$).
2. If $\tilde{k}_y \neq 0$ and $\hat{s} \neq 0$ but only a single mode is being considered (e.g. in linear simulations), the boundary condition is zero incoming, but the z domain can be extended arbitrarily far.
3. If $\tilde{k}_y \neq 0$ and $\hat{s} \neq 0$ and the simulation is nonlinear, the boundary condition is “twist and shift”, with different $\tilde{k}_x$ modes linking to form extended domains in the parallel coordinate, with extended z coordinate z_{ext}.
4. The boundary condition for the extrema of extended parallel domains is zero-incoming.

3.7 Boundary conditions in x, y, $\tilde{v}_{||}$, $\tilde{\mu}_s$

As previously discussed, the spectral flux tube approach implicitly imposes a periodic boundary condition in x and y. The boundary condition in $\tilde{v}_{||}$ is zero-incoming, justified provided that $\tilde{g}_{\mathbf{k},s} \to 0$ as $\tilde{v}_{||} \to \pm\tilde{v}_{||,\mathrm{max}}$, where $\tilde{v}_{||\mathrm{max}}$ is the largest value of $\tilde{v}_{||}$ in the simulation. Unlike z and $\tilde{v}_{||}$, the values of $\tilde{g}_{\mathbf{k},s}$ at different points in $\tilde{\mu}_s$ are not coupled, except by the field (i.e. there are no terms containing $\frac{\partial}{\partial\tilde{\mu}_s}$ in the GKE). Thus, no explicit boundary conditions for the μ_s grid are required. For the same reason, there is no explicit boundary condition of ε_s in `GS2`.

3.8 Temporal discretisation and choice of time-marching scheme

In general, the simulation equations eqs. (3.5.1) and (3.5.2) are not analytically soluble, and so require numerical solution. Some codes cast the linear simulation equations as an eigenvalue problem and use eigensolvers to find solutions (NB this is option in `GS2`). However, the focus here is time-marching schemes, which are applicable to both linear and nonlinear gyrokinetics. In time-marching schemes, some initial value of $\tilde{g}_{\mathbf{k},s}(\tilde{k}_x, \tilde{k}_y, z, \tilde{v}_{||}, \tilde{\mu}_s, \tilde{t} = \tilde{t}^0)$ is specified, and the simulation equations are used to advance $\tilde{g}_{\mathbf{k},s}$ in discrete time steps $(\tilde{t}^1, \tilde{t}^2, \tilde{t}^3, ...)$ until some later time $\tilde{t}^{\mathrm{final}}$ is reached. As an illustration of temporal discretisation, the general two-level scheme can be written as

$$\frac{\partial g}{\partial t} = \frac{g(t^{n+1}) - g(t^n)}{\Delta t} = \mathcal{G}_1(g(t^{n+1}), t^n + \Delta t) + \mathcal{G}_2(g(t^n), t^n), \tag{3.8.1}$$

where g is an arbitrary function (such as $\tilde{g}_{\mathbf{k},s}$), $(t^{n+1} = t^n + \Delta t)$, Δt is the timestep size and $\mathcal{G}_{1,2}$ are operators. The classification "two-level" (or equivalently "single step") refers to the fact that (3.8.1) only contains terms from two discrete points in time (t and t^{n+1}). Algorithms containing information from m time points are known as m-level methods ("multistep" if $m > 2$).

The exact form of $\mathcal{G}_x$ depends on the discretisation algorithm, or time-marching scheme, used. The choice of scheme has a large effect on the accuracy and computational cost of simulation; a detailed background is beyond the scope of this thesis, so I focus on the schemes used by `stella` and `GS2`.

Explicit numerical schemes have $\mathcal{G}_1 = 0$, and so the solution for $g(t^{n+1})$ depends only on the information from the current (and possibly previous) timestep(s), which is usually known. Examples of explicit scheme include the Runge-Kutta (an option in `stella`) and Adams-Bashforth (used in `GS2` for nonlinear term) family of algorithms [58]. Explicit schemes are usually relatively easy to implement, and have low cost per timestep. A disadvantage of explicit schemes is that they tend to have poor numerical stability properties; for example, the well-known Courant-Friedrichs-Lewy (see chapter 8 condition imposes a constraint in the timestep size Δt, beyond which non-physical solutions will grow exponentially.

Implicit numerical schemes, which have $\mathcal{G}_1 \neq 0$, often have improved numerical stability; in particular, they are less susceptible to a CFL condition, and can allow a larger timestep Δt to be taken. A disadvantage is that the cost per timestep is usually greater than for explicit schemes, since one usually solves by matrix inversion, by rearranging (3.8.1) as

$$g(t^{n+1}) = g(t^n) + \Delta t \cdot \left[\mathcal{G}_1(g(t^{n+1}), t^{n+1}) + \mathcal{G}_2(g(t^n), t^n)\right] \tag{3.8.2}$$

$$\left[\mathcal{I} - \Delta t \mathcal{G}_1\right] g(t^{n+1}) = g(t^n) + \Delta t \mathcal{G}_2(g(t^n), t^n) \tag{3.8.3}$$

$$g(t^{n+1}) = \left[\mathcal{I} - \Delta t \mathcal{G}_1\right]^{-1} \left(g(t^n) + \Delta t \mathcal{G}_2(g(t^n), t^n)\right), \tag{3.8.4}$$

where $\mathcal{I}$ is the identity operator.

A challenge for using implicit schemes in gyrokinetics is that the source terms of the GKE contain $(\tilde{\varphi}^{n+1}_{1\mathbf{k}}, \tilde{A}^{n+1}_{1\|\mathbf{k}}, \tilde{B}^{n+1}_{1\|\mathbf{k}})$, which are non-trivial integrals of $\tilde{g}^{n+1}_{\mathbf{k},s}$; the calculation and inversion of $\mathcal{G}_1$ is thus rather difficult. Fortunately, an elegant solution, in which the fields $(\tilde{\varphi}^{n+1}_{1\mathbf{k}}, \tilde{A}^{n+1}_{1\|\mathbf{k}}, \tilde{B}^{n+1}_{1\|\mathbf{k}})$ are calculated before $\tilde{g}^{n+1}_{\mathbf{k},s}$, allowing the linear GKE to be advanced implicitly at relatively low computational cost, was presented by Kotschenreuter *et al.* [59]. This is often referred to as "Kotschenreuter's implicit algorithm", and is described in section 3.10.

Before describing Kotschenreuter's algorithm, I first describe `stella`'s operator splitting, a powerful tool which allows for different terms in the GKE to be treated by different schemes.

3.9 Operator splitting in `stella`

Suppose one wishes to evolve a system governed by a differential equation:

$$\frac{\mathrm{d}g}{\mathrm{d}t} = (A + B + C)g, \tag{3.9.1}$$

where A, B and C are arbitrary non-commuting operators. The aim of splitting schemes is to treat operators (A, B, C) separately. The simplest splitting scheme is Lie-Trotter splitting, which can be written as [58]:

$$\left(\frac{\mathrm{d}g}{\mathrm{d}t}\right)_1 = Ag \tag{3.9.2}$$

$$\left(\frac{\mathrm{d}g}{\mathrm{d}t}\right)_2 = Bg \tag{3.9.3}$$

$$\left(\frac{\mathrm{d}g}{\mathrm{d}t}\right)_3 = Cg. \tag{3.9.4}$$

One can then solve eqs. (3.9.2) to (3.9.4) sequentially; one advances eq. (3.9.2) by one timestep Δt with initial value $g(t^n) \equiv g^n$ to obtain some intermediate value of g, which I call $g^\dagger$. One then uses $g^\dagger$ as the value of g^n to advance eq. (3.9.3) by Δt to obtain $g^\ddagger$. Finally, one advances $g^\ddagger$ by Δt using eq. (3.9.4) to obtain a value for $g^{n+1} \equiv g(t^n + \Delta t)$. It can be shown this scheme is first-order accurate (that is, the error ϵ in the solution for some given simulation time is proportional to Δt) for non-commuting operators, and second-order accurate ($\epsilon \propto (\Delta t)^2$) for commuting operators. The scheme extends trivially for an arbitrary number of operators.

An alternative splitting scheme is flip-flop, in which the order of operators is swapped every timestep; on (say) odd timesteps (n odd), one advances (3.9.2), then (3.9.3), then (3.9.4). On even timesteps (n even), one advances (3.9.4), then (3.9.3), then (3.9.2). This scheme can be shown to be second-order accurate for non-commuting linear operators and first-order accurate if nonlinear operators are included [58].

`stella` allows the user to select either Lie-Trotter or flip-flop splitting. By default it splits eq. (3.5.1) as follows:

$$\left(\frac{\partial \tilde{g}_{\mathbf{k},s}}{\partial \tilde{t}}\right)_1 + \tilde{v}_{th,s}\tilde{v}_{\parallel}(\mathbf{b}\cdot\tilde{\boldsymbol{\nabla}}z)\left(\frac{\partial \tilde{g}_{\mathbf{k},s}}{\partial z} + \frac{Z_s}{\tilde{T}_s}\frac{\partial J_0(\gamma_s)\tilde{\varphi}_{1\mathbf{k}}}{\partial z}e^{-\tilde{v}_s^2}\right) = 0, \tag{3.9.5}$$

$$\left(\frac{\partial \tilde{g}_{\mathbf{k},s}}{\partial \tilde{t}}\right)_2 - \tilde{v}_{th,s}\tilde{\mu}_s\mathbf{b}\cdot\tilde{\boldsymbol{\nabla}}\tilde{B}_0\frac{\partial \tilde{g}_{\mathbf{k},s}}{\partial \tilde{v}_{\parallel}} = 0, \tag{3.9.6}$$

$$\left(\frac{\partial \tilde{g}_{\mathbf{k},s}}{\partial \tilde{t}}\right)_3 + i\omega_{d,\mathbf{k},s}\left(\tilde{g}_{\mathbf{k},s} + \frac{Z_s}{\tilde{T}_s}J_0(\gamma_s)\tilde{\varphi}_{1\mathbf{k}}e^{-\tilde{v}_s^2}\right) + i\omega_{*,\mathbf{k},s}J_0(\gamma_s)\tilde{\varphi}_{1\mathbf{k}} + \mathcal{N}_{\mathbf{k},s} = 0, \tag{3.9.7}$$

and sequentially solves using Kotschenreuter's algorithm, a two-level semi-Lagrange scheme [45] (not discussed here, though semi-Lagrange schemes are described in a different context in chapter 8) and explicitly using a strong stability-preserving RK method (SSP RK2, SSP RK3 and SSP RK4 are supported). This splitting separates the dynamics of streaming (eq. (3.9.5)) and the mirror term (eq. (3.9.6)) (both of which scale with $\tilde{v}_{th,s} \sim \sqrt{1/\tilde{m}_s}$, and risk becoming large when electrons are simulated) from the dynamics of the magnetostatic drifts, diamagnetic term and nonlinear term (eq. (3.9.7)). The user also has the freedom to include the streaming and/or mirror term(s) in eq. (3.9.7); hence, running simulations fully explicitly is an option. Solving eq. (3.9.6) by matrix inversion is also an option.

3.10 Kotschenreuter's implicit algorithm

In this section I present Kotschenreuter's implicit algorithm, as used in `stella` to advance (3.9.5). Eq. (3.9.5) is discretised in $\tilde{t}$ and z as follows: derivatives in time ($\frac{\partial f}{\partial \tilde{t}}$ for arbitrary f) are given by:

$$\left(\frac{\partial f}{\partial \tilde{t}}\right)^{n*} \equiv \frac{f^{n+1} - f^n}{\Delta \tilde{t}}, \tag{3.10.1}$$

where the superscripts $^{n,n+1}$ denotes the timestep and ^{n*} indicates that the derivative is evaluated at time $\tilde{t}^{n*}$, defined as

$$\tilde{t}^{n*} \equiv \frac{1-u_t}{2}\tilde{t}^n + \frac{1+u_t}{2}\tilde{t}^{n+1}, \tag{3.10.2}$$

where u_t is the user-controlled temporal upwinding parameter, which can vary from 0 (in which case $\frac{\partial}{\partial \tilde{t}}$ is time-centered, and second-order accurate in $\Delta \tilde{t}$) to 1 (in which case $\frac{\partial}{\partial \tilde{t}}$ is fully upwinded, and is first-order accurate in $\Delta \tilde{t}$). It is usual to set u_t close to zero, although a small amount of upwinding can improve numerical stability.

All other time-dependent quantities in eq. (3.9.5) are also evaluated at t^{n*} i.e. an arbitrary time-dependent quantity f is evaluated as

$$f^{n*} = \frac{1-u_t}{2}f^n + \frac{1+u_t}{2}f^{n+1}. \tag{3.10.3}$$

Similarly, z derivatives are evaluated at z_{i*} as follows:

$$z_{i*} \equiv \frac{1 \mp u_z}{2}z_i + \frac{1 \pm u_z}{2}z_{i+1} \tag{3.10.4}$$

$$\left(\frac{\partial f}{\partial z}\right)_{i*} \equiv \frac{f_{i+1} - f_i}{\Delta z} \tag{3.10.5}$$

$$f_{i*} = \frac{1 \mp u_z}{2}f_i + \frac{1 \pm u_z}{2}f_{i+1}, \tag{3.10.6}$$

where u_z is the z centering parameter and Δz is the spacing in z ($\Delta z = z_{i+1} - z_i$). The sign preceding u_z is determined by the sign of $\tilde{v}_{\|}$; the upper is used for $\tilde{v}_{\|} > 0$ and lower for $\tilde{v}_{\|} < 0$, ensuring that the derivative is either upwinded ($u_z > 0$) or centered ($u_z = 0$) (i.e. never downwinded). The derivative is second order accurate in Δz in the centered scheme and first order accurate for the fully upwinded scheme.

Applying these discretisations to eq. (3.9.5) gives:

$$\begin{aligned}
&\frac{\left(\frac{1\mp u_z}{2}\tilde{g}_{\mathbf{k},s}^{n+1}{}_i + \frac{1\pm u_z}{2}\tilde{g}_{\mathbf{k},s}^{n+1}{}_{i+1}\right) - \left(\frac{1\mp u_z}{2}\tilde{g}_{\mathbf{k},s i}^{n} + \frac{1\pm u_z}{2}\tilde{g}_{\mathbf{k},s i+1}^{n}\right)}{\Delta\tilde{t}} \\
&+ \tilde{v}_{th,s}\tilde{v}_{\|}(\mathbf{b}\cdot\tilde{\boldsymbol{\nabla}}z)_{i*}\left[\frac{\left(\frac{1-u_t}{2}\tilde{g}_{\mathbf{k},s i+1}^{n} + \frac{1+u_t}{2}\tilde{g}_{\mathbf{k},s}^{n+1}{}_{i+1}\right) - \left(\frac{1-u_t}{2}\tilde{g}_{\mathbf{k},s i}^{n} + \frac{1+u_t}{2}\tilde{g}_{\mathbf{k},s}^{n+1}{}_{i}\right)}{\Delta z}\right. \\
&\left. + \frac{Z_s}{\tilde{T}_s}\frac{\left(\frac{1-u_t}{2}J_0(\gamma_s)_{i+1}\tilde{\varphi}_{1\mathbf{k}i+1}^{n} + \frac{1+u_t}{2}J_0(\gamma_s)_{i+1}\tilde{\varphi}_{1\mathbf{k}}^{n+1}{}_{i+1}\right) - \left(\frac{1-u_t}{2}J_0(\gamma_s)_i\tilde{\varphi}_{1\mathbf{k}i}^{n} + \frac{1+u_t}{2}J_0(\gamma_s)_i\tilde{\varphi}_{1\mathbf{k}}^{n+1}{}_i\right)}{\Delta z}e^{-\tilde{v}_s{}_{i*}^2}\right] \\
&= 0. \qquad (3.10.7)
\end{aligned}$$

To conceptually understand Kotschenreuter's algorithm one can write eq. (3.10.7) symbolically as

$$\begin{aligned}
&A_{1,i*}\tilde{g}_{\mathbf{k},s}^{n+1}{}_i + A_{2,i*}\tilde{g}_{\mathbf{k},s}^{n+1}{}_{i+1} + B_{1,i*}\tilde{g}_{\mathbf{k},s i}^{n} + B_{2,i*}\tilde{g}_{\mathbf{k},s i+1}^{n} \\
&+C_{1,i*}\tilde{\varphi}_{1\mathbf{k}}^{n+1}{}_i + C_{2,i*}\tilde{\varphi}_{1\mathbf{k}}^{n+1}{}_{i+1} + D_{1,i*}\tilde{\varphi}_{1\mathbf{k}i}^{n} + D_{2,i*}\tilde{\varphi}_{1\mathbf{k}i+1}^{n} = 0, \qquad (3.10.8)
\end{aligned}$$

where, in general, the coefficients $A - D_{\{1,2\},i*}$ are functions of $(k_y, k_x, z, v_{\|}, \mu_s)$, but are time-independent. To proceed, split g^{n+1} into a “homogeneous” piece and an “inhomogeneous” piece:

$$\tilde{g}_{\mathbf{k},s}^{n+1}{}_i = \tilde{g}_{\mathbf{k},s}^{n+1}{}_{h,i} + \tilde{g}_{\mathbf{k},s}^{n+1}{}_{inh,i} \equiv g_{h,i} + g_{inh,i}, \qquad (3.10.9)$$

(where I have temporarily dropped some of the cumbersome labels for readability), where g_{inh} satisfies

$$A_{1,i*}g_{inh,i} + A_{2,i*}g_{inh,i+1} + B_{1,i*}\tilde{g}_{\mathbf{k},s i}^{n} + B_{2,i*}\tilde{g}_{\mathbf{k},s i+1}^{n} + D_{1,i*}\tilde{\varphi}_{1\mathbf{k}i}^{n} + D_{2,i*}\tilde{\varphi}_{1\mathbf{k}i+1}^{n} = 0, \quad (3.10.10)$$

and so g_h satisfies (to be consistent with eq. 3.10.8)

$$A_{1,i*}g_{h,i} + A_{2,i*}g_{h,i+1} + C_{1,i*}\tilde{\varphi}_{1\mathbf{k}}^{n+1}{}_i + C_{2,i*}\tilde{\varphi}_{1\mathbf{k}}^{n+1}{}_{i+1} = 0. \qquad (3.10.11)$$

In other words, the inhomogeneous piece $\tilde{g}_{\mathbf{k},s}^{n+1}$ depends only on $\tilde{\varphi}_{1\mathbf{k}}$ at the old timestep ($\tilde{\varphi}_{1\mathbf{k}}^{n}$), and the homogeneous piece contains the dependency of $\tilde{g}_{\mathbf{k},s}^{n+1}$ on $\tilde{\varphi}_{1\mathbf{k}}^{n+1}$.

The inhomogeneous equation eq. (3.10.10) can be straightforwardly solved as a bidiagonal matrix equation for $g_{inh}(z)$ (upper or lower bidiagonal depending on the sign of $\tilde{v}_{\|}$). This is solved for all $(\tilde{v}_{\|}, \tilde{\mu}_s)$ (which are decoupled) to obtain $g_{inh}(z)$.

One then takes advantage of the linearity of (3.10.7) (i.e. that g_h responds linearly to $\tilde{\varphi}_{1\mathbf{k}}^{n+1}$) to calculate the updated fields $\tilde{\varphi}_{1\mathbf{k}}^{n+1}$ using a Green's function approach. This is done by writing ${\tilde{\varphi}_{1\mathbf{k}}^{n+1}}_i$ as

$$ {\tilde{\varphi}_{1\mathbf{k}}^{n+1}}_i = {\tilde{\varphi}_{1\mathbf{k}}^{n+1}}_{inh,i} + {\tilde{\varphi}_{1\mathbf{k}}^{n+1}}_{h,i} \equiv \varphi_{inh,i} + \varphi_{h,i}, \tag{3.10.12} $$

where $\varphi_{inh,i}$ is the piece of ${\tilde{\varphi}_{1\mathbf{k}}^{n+1}}_i$ which arises from inserting $g_{inh,i}$ into quasi-neutrality (3.5.2) and $\varphi_{h,i}$ arises from $g_{h,i}$ i.e.

$$ \sum_s Z_s \tilde{n}_s \left(\frac{2\tilde{B}_0}{\sqrt{\pi}} \int_{-\infty}^{\infty} d\tilde{v}_{\|} \int_0^{\infty} d\tilde{\mu}_s J_0(\gamma_s) g_{inh(h),i} + \frac{Z_s}{\tilde{T}_s} (\Gamma_0(b_s) - 1) \varphi_{inh(h),i} \right) = 0, \tag{3.10.13} $$

which can be expressed as

$$ \varphi_{inh(h),i} = \frac{\mathbf{l}_1(g_{inh(h),i})}{K_{11,i}}, \tag{3.10.14} $$

where $\mathbf{l}_1$ is an operator which integrates over velocity and sums over species, and K_{11} is time-independent. The subscripts $_1$ and $_{11}$ in $\mathbf{l}_1$ and K_{11} are used for consistency with the material presented in chapter 6. $\varphi_{inh,i}$ can be readily calculated once $g_{inh,i}$ has been found. Then, writing $g_{h,i}$ as

$$ g_{h,i} = \sum_j \left[\frac{\partial g_{h,i}}{\partial {\tilde{\varphi}_{1\mathbf{k}}^{n+1}}_j} \right] {\tilde{\varphi}_{1\mathbf{k}}^{n+1}}_j, \tag{3.10.15} $$

and substituting into (3.10.14), $\varphi_{h,i}$ can be eliminated from (3.10.12):

$$ {\tilde{\varphi}_{1\mathbf{k}}^{n+1}}_i = \varphi_{inh,i} + \frac{\mathbf{l}_1 \left(\sum_j \left[\frac{\partial g_{h,i}}{\partial {\tilde{\varphi}_{1\mathbf{k}}^{n+1}}_j} \right] {\tilde{\varphi}_{1\mathbf{k}}^{n+1}}_j \right)}{K_{11,i}} = \varphi_{inh,i} + \frac{\sum_j \mathbf{l}_1 \left(\frac{\partial g_{h,i}}{\partial {\tilde{\varphi}_{1\mathbf{k}}^{n+1}}_j} \right) {\tilde{\varphi}_{1\mathbf{k}}^{n+1}}_j}{K_{11,i}}, \tag{3.10.16} $$

where ${\tilde{\varphi}_{1\mathbf{k}}^{n+1}}_j$, having no velocity- or species-dependence, can be brought outside the operator $\mathbf{l}_1$. This can be written in matrix form as:

$$\mathcal{R}\tilde{\varphi}^{n+1}_{1\mathbf{k}}(z) = \varphi_{inh}(z), \tag{3.10.17}$$

$$\tilde{\varphi}^{n+1}_{1\mathbf{k}}(z) = \mathcal{R}^{-1}\varphi_{inh}(z), \tag{3.10.18}$$

where $\mathcal{R}$ is known as the *response matrix*, and is given by

$$\mathcal{R} = \mathcal{I} - \frac{\mathbf{l}_1\left(\frac{\partial g_h}{\partial \tilde{\varphi}^{n+1}_{1\mathbf{k}}}\right)}{K_{11}}. \tag{3.10.19}$$

Eq. (3.10.18) can be solved for $\tilde{\varphi}^{n+1}_{1\mathbf{k}}(z)$, which is finally inserted into (3.10.8) to find $\tilde{g}^{n+1}_{\mathbf{k},s}(z)$.

$\mathcal{R}$ is a dense matrix of size $N_{z,\text{ext}} \times N_{z,\text{ext}}$ for each extended domain (where $N_{z,\text{ext}}$ is the number of z gridpoints in the extended domain), but is time-independent. In `stella` it is calculated once at the start of the simulation by applying a unit impulse to $\tilde{\varphi}^{n+1}_{1\mathbf{k}}$ at every location in z and calculating $g_h(z)$ using (3.10.11). After $\mathcal{R}$ is calculated, it is LU-decomposed. On each timestep, back substitution is used to solve (3.10.18). A caveat is that $\mathcal{R}$ depends non-trivially on Δt, so if Δt changes throughout the simulation (which can happen in nonlinear simulations), $\mathcal{R}$ must be recalculated.

To summarise, Kotschenreuter's implicit algorithm for streaming in `stella` for a single timestep consists of the following steps: (1) the inhomogeneous streaming equation is solved for $g_{inh}(z)$, (2) the associated potential $\varphi_{inh}(z)$ is calculated, (3) eq. (3.10.18) is solved to find $\tilde{\varphi}^{n+1}_{1\mathbf{k}}(z)$ and (4) the full streaming equation is solved for $\tilde{g}^{n+1}_{\mathbf{k},s}$. A pseudocode representation of the steps performed by `stella` is given in appendix A.1.

3.10.1 Kotschenreuter's algorithm in `GS2`

`GS2` also employs Kotschenreuter's algorithm, but with some minor differences. Firstly, all linear terms are included, rather than just streaming. In addition, $\tilde{A}_{1\|\mathbf{k}}$ and $\tilde{B}_{1\|\mathbf{k}}$ are included in the electromagnetic version. The symbolic discretised equation is thus:

$$\begin{aligned}
&A_{1,i*}\tilde{g}^{n+1}_{\mathbf{k},s}{}_i + A_{2,i*}\tilde{g}^{n+1}_{\mathbf{k},s}{}_{i+1} + B_{1,i*}\tilde{g}^{n}_{\mathbf{k},si} + B_{2,i*}\tilde{g}^{n}_{\mathbf{k},si+1}\\
&+C_{1,i*}\tilde{\varphi}^{n+1}_{1\mathbf{k}}{}_i + C_{2,i*}\tilde{\varphi}^{n+1}_{1\mathbf{k}}{}_{i+1} + D_{1,i*}\tilde{\varphi}^{n}_{1\mathbf{k}i} + D_{2,i*}\tilde{\varphi}^{n}_{1\mathbf{k}i+1}\\
&+E_{1,i*}\tilde{A}^{n+1}_{1\|\mathbf{k}}{}_i + E_{2,i*}\tilde{A}^{n+1}_{1\|\mathbf{k}}{}_{i+1} + F_{1,i*}\tilde{A}^{n}_{1\|\mathbf{k}i} + F_{2,i*}\tilde{A}^{n}_{1\|\mathbf{k}i+1}\\
&+G_{1,i*}\tilde{B}^{n+1}_{1\|\mathbf{k}}{}_i + G_{2,i*}\tilde{B}^{n+1}_{1\|\mathbf{k}}{}_{i+1} + H_{1,i*}\tilde{B}^{n}_{1\|\mathbf{k}i} + H_{2,i*}\tilde{B}^{n}_{1\|\mathbf{k}i+1} = 0,
\end{aligned} \tag{3.10.20}$$

Parameter	Codes applicable to	Code variable	Comment
n_z	`stella`, `GS2`	`nzed` (`stella`), `ntheta` (`GS2`)	Number of z gridpoints per 2π z interval
n_{period}	`stella`, `GS2`	`nperiod` (`stella`, `GS2`)	Number of 2π z intervals in a single (non-extended) z domain
n_{fp}	`stella`	`nfield_periods`	Number of identical toroidal segments spanned by z per 2π z interval
$\Delta\tilde{t}$	`stella`, `GS2`	`code_dt`[a] (`stella`, `GS2`)	Simulation timestep
n_{step}	`stella`, `GS2`	`nstep`	Number of timesteps simulated
$n_{\tilde{v}_{\|\|}}$	`stella`	`nvgrid`	Number of $\tilde{v}_{\|\|}$ gridpoints per sign $(+/-)$ (total $\tilde{v}_{\|\|}$ gridpoints is $2n_{\tilde{v}_{\|\|}}$)
$\tilde{v}_{\|\|,\text{max}}$	`stella`	`vpa_max`	Sets the extent of the $\tilde{v}_{\|\|}$ grid
$n_{\tilde{\mu}_s}$	`stella`	`nmu`	Number of $\tilde{\mu}_s$ gridpoints
$\tilde{v}_{\perp,\text{max}}$	`stella`	`vperp_max`	Sets the extent of the $\tilde{\mu}_s$ grid
n_{gauss}	`GS2`	`ngauss`	Controls v-space resolution for trapped particles
n_E	`GS2`	`negrid`	Number of energy gridpoints
$u_{v\|\|}$	`stella`	`vpa_upwind`	Sets $\tilde{v}_{\|\|}$ upwinding in implicit schemes. $u_{v\|\|} = 0$ is fully centered, $u_{v\|\|} = 1$ is fully upwinded.
u_z	`stella`, `GS2`	`zed_upwind` (`stella`), `bakdif` (`GS2`)	Sets z upwinding in implicit schemes. $u_z = 0$ is fully centered, $u_z = 1$ is fully upwinded.
u_t, $u_{t,\text{GS2}}$	`stella`, `GS2`	`time_upwind` (`stella`), `fexpr` (`GS2`)	Sets $\tilde{t}$ upwinding in implicit schemes. $u_t = 0$ (in `stella`) or $u_{t,\text{GS2}} = 0.5$ (in `GS2`) is fully centered, $u_t, u_{t,\text{GS2}} = 1$ is fully upwinded.

Table 3.1: Description of selected non-physical parameters for `stella` and `GS2`.

---

[a] $\Delta\tilde{t}$ is set by the input parameter `delt` but used (and possibly changed) by the code as `code_dt`.

and eq. (3.10.15) becomes

$$g_{h,i} = \sum_j \left[\frac{\partial g_{h,i}}{\partial \tilde{\varphi}^{n+1}_{1\mathbf{k}\;j}} \right] \tilde{\varphi}^{n+1}_{1\mathbf{k}\;j} + \sum_j \left[\frac{\partial g_{h,i}}{\partial \tilde{A}^{n+1}_{1\|\mathbf{k}\;j}} \right] \tilde{A}^{n+1}_{1\|\mathbf{k}\;j} + \sum_j \left[\frac{\partial g_{h,i}}{\partial \tilde{B}^{n+1}_{1\|\mathbf{k}\;j}} \right] \tilde{B}^{n+1}_{1\|\mathbf{k}\;j}, \qquad (3.10.21)$$

which results in $\mathcal{R}$ having dimensions $3N_{z,\text{ext}} \times 3N_{z,\text{ext}}$. The electromagnetic algorithm is described in greater detail (in the context of `stella`) in chapter 6.

3.11 Non-physical simulation parameters

Some important variables required to describe a gyrokinetic simulation, but not appearing in the gyrokinetic model, are given in table 3.1. This is not intended to be an exhaustive list, but is intended to aid understanding in future chapters.

3.12 Concluding remarks

In this chapter I derive the simulation equations which `stella` and `GS2` seek to solve, and describe the algorithms used to "march" the distribution function and fields forwards in time. Provided that the physical assumptions are upheld, that the non-physical parameters in the simulation are well-chosen to accurately capture the physics of interest, and numerical instability can be avoided, codes such as `stella` and `GS2` can thus provide a realistic description of turbulence phenomena in MCF plasmas. This is the goal of the research presented in chapters 5 and 7.

Chapter 5 uses `GS2` to study a particular instability: the kinetic ballooning mode (KBM). Before presenting these results, it is worth describing the basic physics of this instability.

Chapter 4

Ideal and kinetic ballooning modes: theory

4.1 Introduction

The purpose of this chapter is to describe the fundamental physics and typical properties of the kinetic ballooning mode (KBM), a pressure-driven electromagnetic microinstability. Since the typical parameter space in which the KBM is unstable (particularly, plasmas with high β and/or large pressure gradients) overlaps with the parameter space for fusion reactor plasmas, managing KBM stability is likely to be an important factor when fusion power plants are designed and operated.

There are a number of ways in which KBMs can be theoretically studied beyond gyrokinetic simulation. By far the simplest model for the KBM is the $n = \infty$ ideal magnetohydrodynamic (MHD) ballooning mode (abbreviated here to "ideal ballooning mode", or IBM). Deriving from ideal MHD, the IBM ignores kinetic effects such as finite Larmor radius effects (e.g. gyroaveraging) and the effect of trapped particles. However, the IBM describes the basic physics of the instability; a competition between the stabilising effect of magnetic field line bending and the destabilising effect of a plasma pressure gradient combined with "bad" magnetic curvature. IBM stability is also easily assessed for a given plasma, and is sometimes used as a proxy for KBM stability in models such as the predictive pedestal model EPED [60–63]. For these reasons, and because IBM stability is discussed in chapter 5, I provide a background on the IBM here.

This chapter is structured as follows. I begin (section 4.2.1) by describing the linearised ideal MHD equations describing instabilities, and the "energy principle" (section 4.2.2), which is a useful and physically informative way of assessing linear stability in the ideal MHD framework. Next (section 4.2.3) I show how these general equations can be used to derive the IBM. In the limit of large n, IBM stability becomes local to each individual magnetic field line with mode structure F_0 and Ω_0^2 (where Ω_0 is the leading order mode frequency) governed by a one-dimensional second-order differential equation (a Sturm-Liouville equation). I then describe (section 4.3) how the `GS2` module `ideal_ball` assesses IBM stability of a particular field line using Newcomb's theorem. Finally I discuss the KBM as a "kinetic analogue" of the IBM (section 4.4).

4.2 Ideal MHD ballooning modes

4.2.1 The ideal MHD model

As in gyrokinetics, one can derive the ideal MHD model by applying a mathematically defined set of assumptions to the ensemble-averaged kinetic-Maxwell equations. A key difference between ideal MHD and gyrokinetics is how the distribution function of the plasma in velocity space is treated: gyrokinetics considers the equations governing the distribution function (F_{0s}, δf_s) whereas ideal MHD considers moments of the distribution function (mass, momentum, energy), which are combined to construct a set single-fluid equations.

Derivations of the ideal MHD equations are widely available in literature (see e.g. Freidberg [12]). The basic process is as follows: the first three moments of the ensemble-averaged kinetic equation (eq. (2.1.4)) are taken, to give equations describing the mass, momentum and energy of each species. These are combined with the low-frequency ($\omega \ll \omega_{pe}$), long-wavelength ($\lambda_D/k \ll 1$) and non-relativistic ($\omega/k \ll c$) forms of Maxwell's equations (where ω and k define the timescales and spatial scales of MHD phenomena) to arrive at a two-fluid set of equations. From these, a single-fluid description is derived by assuming $Z_i = 1$, $Z_e = -1$ and taking the limit $m_e \to 0$ (such that the electron response time is much faster than the timescale of MHD events).

At this point, the system of equations is unclosed (i.e. there are more unknowns than equations) since the equation for each moment contains information about a higher-order moment. The system is closed by taking the *ideal MHD limit*, consisting of (1) prescribing the equation of state:

$$\frac{\mathrm{d}}{\mathrm{d}t}\left(\frac{p}{\rho^\gamma}\right) = 0, \tag{4.2.1}$$

and (2) taking the plasma to be perfectly conducting. (1) is satisfied provided the plasma is collisionally dominated (such that the ions and electrons are described by Maxwellian distributions plus bulk flow). (2) is satisfied in the limit that $k\rho_i \to 0$ (this limit is discussed in section 4.4). The resulting ideal MHD equations are:

$$\frac{\partial \rho}{\partial t} + \boldsymbol{\nabla} \cdot (\rho \mathbf{v}) = 0 \tag{4.2.2}$$

$$\rho \frac{\mathrm{d}\mathbf{v}}{\mathrm{d}t} = \mathbf{J} \times \mathbf{B} - \boldsymbol{\nabla} p \tag{4.2.3}$$

$$\frac{\mathrm{d}}{\mathrm{d}t}\left(\frac{p}{\rho^\gamma}\right) = 0 \tag{4.2.4}$$

$$\mathbf{E} + \mathbf{v} \times \mathbf{B} = 0 \tag{4.2.5}$$

$$\boldsymbol{\nabla} \times \mathbf{E} = -\frac{\partial \mathbf{B}}{\partial t} \tag{4.2.6}$$

$$\boldsymbol{\nabla} \times \mathbf{B} = \mu_0 \mathbf{J} \tag{4.2.7}$$

$$\boldsymbol{\nabla} \cdot \mathbf{B} = 0, \tag{4.2.8}$$

where ρ is the plasma mass density, **v** the plasma flow, **J** the plasma current, p the plasma pressure, $\gamma = 5/3$ the ratio of specific heats, **E** the electric field and **B** the magnetic field. These equations describe: conservation of mass (4.2.2), Newton's second law (4.2.3), an equation of state (4.2.4), generalised form of Ohm's law ((4.2.5)) and Maxwell's equations (eqs. (4.2.6) to (4.2.8)).

Thus, ideal MHD models the plasma as a single, perfectly conducting fluid described by bulk properties (density, flow, temperature, pressure). The ideal MHD equations are three-dimensional, making the system much simpler than gyrokinetics.

4.2.2 Stability and the energy principle

To study instabilities efficiently, it is common to linearise the ideal MHD equations by means of asymptotic expansion ($A = A_0 + A_1 + A_2 + ... = A_0 + \mathcal{O}(\epsilon^1 A_0) + \mathcal{O}(\epsilon^2 A_0) + ...$ where $\epsilon \ll 1$) of all physical parameters A. Unlike gyrokinetics, the spatial scale of the perturbation is taken to be comparable to that of the equilibrium quantities ($\boldsymbol{\nabla} A_1 \sim \epsilon \boldsymbol{\nabla} A_0$). For simplicity, I assume the plasma to be in static equilibrium (i.e. $\frac{\partial A_0}{\partial t} = 0$ and $\mathbf{v}_0 = 0$). Once can then define a small plasma perturbation $\boldsymbol{\xi}$ as

$$\mathbf{v}_1 = \frac{\partial \boldsymbol{\xi}}{\partial t}, \tag{4.2.9}$$

and by considering the $\mathcal{O}(\epsilon)$ terms in equations eqs. (4.2.2) to (4.2.8), arrive at a linear system of equations describing the perturbation. The dynamical behaviour of $\boldsymbol{\xi}$ is given by the linearised form of (4.2.3):

$$\rho_0 \frac{\partial^2 \boldsymbol{\xi}}{\partial t^2} = \mathbf{F}(\boldsymbol{\xi}), \tag{4.2.10}$$

where $\mathbf{F}(\boldsymbol{\xi})$ is the *force operator*:

$$\begin{aligned} \mathbf{F}(\boldsymbol{\xi}) &\equiv \mathbf{J}_0 \times \mathbf{B}_1 + \mathbf{J}_1 \times \mathbf{B}_0 - \boldsymbol{\nabla} p_1, & (4.2.11)\\ &= \frac{1}{\mu_0}(\boldsymbol{\nabla} \times \mathbf{B}_0) \times \mathbf{B}_1 + \frac{1}{\mu_0}(\boldsymbol{\nabla} \times \mathbf{B}_1) \times \mathbf{B}_0 - \boldsymbol{\nabla} p_1, & (4.2.12) \end{aligned}$$

and $\mathbf{B}_1$ and p_1 are related to $\boldsymbol{\xi}$ by the linearised forms of equations eqs. (4.2.2) and (4.2.4):

$$\mathbf{B}_1 = \boldsymbol{\nabla} \times (\boldsymbol{\xi} \times \mathbf{B}_0) \tag{4.2.13}$$

$$p_1 = -\boldsymbol{\xi} \cdot p_0 - \gamma p_0 \boldsymbol{\nabla} \cdot \boldsymbol{\xi}. \tag{4.2.14}$$

Taking fluctuating quantities to vary as $A_1 = A_1(t=0)\exp(-i\Omega t)$, eq. (4.2.10) becomes

$$-\Omega^2 \rho_0 \boldsymbol{\xi} = \mathbf{F}(\boldsymbol{\xi}) \tag{4.2.15}$$

with stability determined by the complex frequency Ω. It can be shown (see for example Freidberg [12]) that $\mathbf{F}$ is self-adjoint, that is,

$$\int \boldsymbol{\eta} \cdot \mathbf{F}(\boldsymbol{\xi}) d\mathbf{r} = \int \boldsymbol{\xi} \cdot \mathbf{F}(\boldsymbol{\eta}) d\mathbf{r}, \tag{4.2.16}$$

for arbitrary vectors $(\boldsymbol{\eta}, \boldsymbol{\xi})$. This has the important consequence that Ω^2 is purely real; one can then assess stability of a mode $\boldsymbol{\xi}$ simply by checking the sign of Ω^2.

The energy principle [64] states that a particular plasma equilibrium is stable if and only if

$$\delta W(\boldsymbol{\xi}^*, \boldsymbol{\xi}) \equiv -\frac{1}{2} \int d\mathbf{r} \boldsymbol{\xi}^* \mathbf{F}(\boldsymbol{\xi}) \geq 0 \tag{4.2.17}$$

(where $\boldsymbol{\xi}^*$ is the complex conjugate of $\boldsymbol{\xi}$) for all allowable trial functions $\boldsymbol{\xi}$. Physically, δW represents the change in the potential energy of the system arising from a plasma perturbation $\boldsymbol{\xi}$. Whether a small departure from equilibrium grows or decays depends upon the energetic favourability (whether δW is positive or negative).

IBMs are an instability characterised by a long wavelength $k_{\|}$ parallel to $\mathbf{b}$ and a short perpendicular wavelength $k_\perp$, corresponding to high toroidal mode number n. This tends to localise the instability to a particular flux surface in order to minimise the stabilising effect of magnetic field bending (discussed shortly). For such internal, localised modes, one need only consider δW for the plasma (rather than the surrounding vacuum/wall), which can be written in an "intuitive" form [12] as

$$\begin{aligned}\delta W = \frac{1}{2\mu_0}\int [\; & \overbrace{|\mathbf{B}_{1\perp}|^2}^{\text{field line bending}} + \overbrace{B^2|\boldsymbol{\nabla}\cdot\boldsymbol{\xi}_\perp + 2\boldsymbol{\xi}_\perp\cdot\boldsymbol{\kappa}|^2}^{\text{magnetic compression}} \\ & + \underbrace{\mu_0\gamma p_0|\boldsymbol{\nabla}\cdot\boldsymbol{\xi}|^2}_{\text{plasma compression}} - \underbrace{2\mu_0(\boldsymbol{\xi}_\perp\cdot\boldsymbol{\nabla} p_0)(\boldsymbol{\xi}^*_\perp\cdot\boldsymbol{\kappa})}_{\boldsymbol{\nabla} p\text{ drive}} - \underbrace{\mu_0 J_{\|}\boldsymbol{\xi}^*_\perp\times\mathbf{b}\cdot\mathbf{Q}_\perp(\boldsymbol{\xi}_\perp)}_{J_{\|}\text{ drive}}]d\mathbf{r}.\end{aligned} \tag{4.2.18}$$

The first three terms are always positive, and therefore stabilising; these correspond to the energy required for $\boldsymbol{\xi}$ to bend the magnetic field, compress the magnetic field and compress the plasma respectively. The last two terms may be positive or negative and thus drive instabilities.

Ideal MHD ballooning modes are pressure-driven, so the penultimate term is the driving mechanism. As can be seen, the sign of this contribution depends on the sign of both $\boldsymbol{\xi}_\perp\cdot\boldsymbol{\nabla}p_0$ and $\boldsymbol{\xi}^*_\perp\cdot\boldsymbol{\kappa}$. This can be minimised (made most negative) by $\boldsymbol{\xi}$ being large in regions of "bad curvature" (where $(\boldsymbol{\xi}_\perp\cdot\boldsymbol{\nabla}p_0)(\boldsymbol{\xi}^*_\perp\cdot\boldsymbol{\kappa}) < 0$) and small in regions of "good curvature" (where $(\boldsymbol{\xi}_\perp\cdot\boldsymbol{\nabla}p_0)(\boldsymbol{\xi}^*_\perp\cdot\boldsymbol{\kappa}) > 0$). However, variation of $\boldsymbol{\xi}$ along $\mathbf{B}_0$ causes greater field-line bending (see eq. (4.2.13)), which is stabilising. Thus, the structure and stability ballooning modes are determined by a competition between these two effects.

4.2.3 The one-dimensional ideal ballooning equation

Eq. (4.2.18) is physically informative but difficult to apply as it must be solved for all trial functions $\boldsymbol{\xi}$. Fortunately, an elegant approach for assessing ballooning stability was presented by Connor, Taylor and Hastie [65]. A full description is beyond the scope of this thesis, but a summary of their procedure is as follows:

1. One considers a single Fourier mode of the form $\boldsymbol{\xi} = \boldsymbol{\xi}(\psi,\chi)\exp(in\zeta)$, where (ψ,ζ,χ) form an orthogonal coordinate system [66]. This is then decomposed into three scalars (X, U, Z), where X and U are proportional to $\xi_n = \boldsymbol{\xi}\cdot\hat{\mathbf{n}}$ and $\xi_s = \boldsymbol{\xi}\cdot\hat{\mathbf{s}}$ (where $\hat{\mathbf{n}} \equiv \boldsymbol{\nabla}\psi/|\boldsymbol{\nabla}\psi|$ and $\hat{\mathbf{s}} \equiv (\boldsymbol{\nabla}\psi\times\mathbf{b}/|\boldsymbol{\nabla}\psi|)$) respectively.

2. Z is then eliminated from eq. (4.2.18) by minimising δW with respect to $\xi_{\|}$. This is done by noting that only the third term in eq. (4.2.18) has dependence on $\xi_{\|}$. Provided the magnetic

shear is non-vanishing, it is always possible to select $\xi_{||}$ such that $\boldsymbol{\nabla} \cdot \boldsymbol{\xi} = 0$ and hence the stabilising plasma compression term vanishes (i.e. the most unstable modes are incompressible).

3. One then minimises δW with respect to U by making an expansion in $1/n \ll 1$, giving an expression for δW in terms of $X(\psi, \chi)$ only.

4. δW is then minimised with respect to X, subject to a normalisation representing the kinetic energy of the transverse motion of $\boldsymbol{\xi}$. This is done using the principle of constrained variation, yielding a (rather cumbersome) two-dimensional differential eigenvalue equation where $X(\psi, \chi)$ is the eigenfunction and $(\Omega(\psi, \chi))^2$ is the eigenvalue.

5. At this point, a difficulty arises owing to the inconsistency between the periodicity requirements of $X(\psi, \chi)$ (since X must be 2π-periodic in χ) and the effect of magnetic shear, which causes a given bundle of magnetic field lines to become non-periodic in χ [12, 41, 65]. The solution proposed by Connor *et al.* is the *ballooning transform*, in which the periodic function $X(\psi, \chi)$ is represented by an infinite sum of non-periodic "quasi-modes" $\hat{X}(\psi, l)$:

$$X(\psi, \chi) = \sum_m \exp\left(-\frac{2\pi i m \chi}{\chi_0}\right) \int_{-\infty}^{\infty} dl \exp\left(\frac{2\pi i m l}{\chi_0}\right) \hat{X}(\psi, l), \tag{4.2.19}$$

which is well-behaved provided that the $\hat{X}$ decays sufficiently quickly at large $|l|$. It can be shown that the quasi-mode $\hat{X}$ which is a solution to the two-dimensional ballooning mode equation in the infinite domain $-\infty < l < \infty$ will generate a periodic solution X with the same eigenvalue. To assess stability, one therefore only needs check the sign of Ω^2 for the most unstable quasi-mode.

6. An eikonal approach is then used to separate the rapid variation arising from large $k_\perp$ and slower variation:

$$\hat{X}(\psi, l) = F(\psi, l) \exp(iS), \tag{4.2.20}$$

where $S = n\left(\chi - \int_{l_0}^{l} \frac{\mathrm{d}\chi}{\mathrm{d}l_0} dl\right)$ (S is constant along a field line specified by (ψ, l_0) but rapidly varying across field lines) and $F(\psi, y)$ is a slowly-varying "amplitude envelope".

7. Inserting (4.2.20) into the two-dimensional equation and expanding in $n^{1/2}$ (such that $F = F_0 + F_1 + ...$), one removes all explicit dependence of F_0 on ψ. F_0 is then given by a one-dimensional equation, sometimes referred to as the $n = \infty$ ideal ballooning equation. This can

be written as [67]:

$$\overbrace{\frac{\partial}{\partial l}\left(k_\perp^2\frac{\partial F_0}{\partial l}\right)}^{\text{field line bending}}\overbrace{-2\mu_0\frac{\partial p_0}{\partial \psi}\left(\frac{\kappa_n}{|\nabla\psi|}k_n^2-\frac{\kappa_s|\nabla\psi|}{B_0}k_nk_s\right)F_0}^{\nabla p\text{ drive}}=-\Omega_0^2\left(\frac{\mu_0\rho_0}{B_0^2}k_\perp^2\right)F_0, \quad (4.2.21)$$

where $\mathbf{k}_\perp = \nabla S = k_n|\nabla\psi|\hat{\mathbf{n}} + k_sB_0/|\nabla\psi|\hat{\mathbf{s}}$, $k_\perp^2 = k_n^2|\nabla\psi|^2 + k_s^2B_0^2/|\nabla\psi|^2$ and $\boldsymbol{\kappa} \equiv \mathbf{b}\cdot\nabla\mathbf{b} = \kappa_n\hat{\mathbf{n}} + \kappa_s\hat{\mathbf{s}}$. The dependence of Ω_0 and F_0 on ψ arises only from the ψ-dependence of equilibrium quantities and thus the lowest order equation can be solved for each flux surface independently. Higher-order corrections (Ω_1, F_1) couple together these surfaces and tend to have a stabilising effect. However, one can use eq. (4.2.21) to assess the stability of $n = \infty$ ballooning modes without appealing to higher order.

8. Finally, one finds the stability of eq. (4.2.21) (i.e. the sign of Ω_0^2) using Newcomb's procedure [68]. This consists of letting $\Omega_0^2 = 0$ and solving eq. (4.2.21) for F_0. It can be shown [68] that the given field line is stable to the ballooning mode if and only if the trial function $F_0(\Omega_0^2 = 0)$ does not vanish in the interval $(-\infty < l < \infty)$.

Thus, Connor *et al.*'s approach allows one to calculate stability quickly and easily by integrating a one-dimensional differential equation (eq. (4.2.21)) for a field line specified by ψ and l_0. This has been numerically implemented in `GS2`'s module `ideal_ball`, described in the following section.

4.3 Ideal ballooning stability analysis in GS2

Converting eq. (4.3.1) to `GS2`'s field-aligned coordinates and setting $\Omega_0^2 = 0$ gives the simulation equation solved by `ideal_ball`:

$$\frac{\partial}{\partial z}\left(G(z)\frac{\partial}{\partial z}\right)F_0 + C(z)F_0 = 0, \quad (4.3.1)$$

where

$$C = -\frac{1}{2}\frac{\partial\beta}{\partial\rho}\frac{\texttt{cvdrift}}{\tilde{B}_0\cdot(\mathbf{b}\cdot\nabla z)}; \qquad G = |\tilde{\nabla}\alpha|^2\frac{(\mathbf{b}\cdot\nabla z)}{\tilde{B}_0} \quad (4.3.2)$$

$$\texttt{cvdrift} = \frac{1}{\tilde{B}_0^3}\frac{\partial\psi_N}{\partial\rho}(\mathbf{b}\times\tilde{\nabla}\beta)\cdot\tilde{\nabla}\alpha + \frac{2}{\tilde{B}_0^2}\frac{\partial\psi_N}{\partial\rho}\cdot\tilde{\nabla}\alpha, \quad (4.3.3)$$

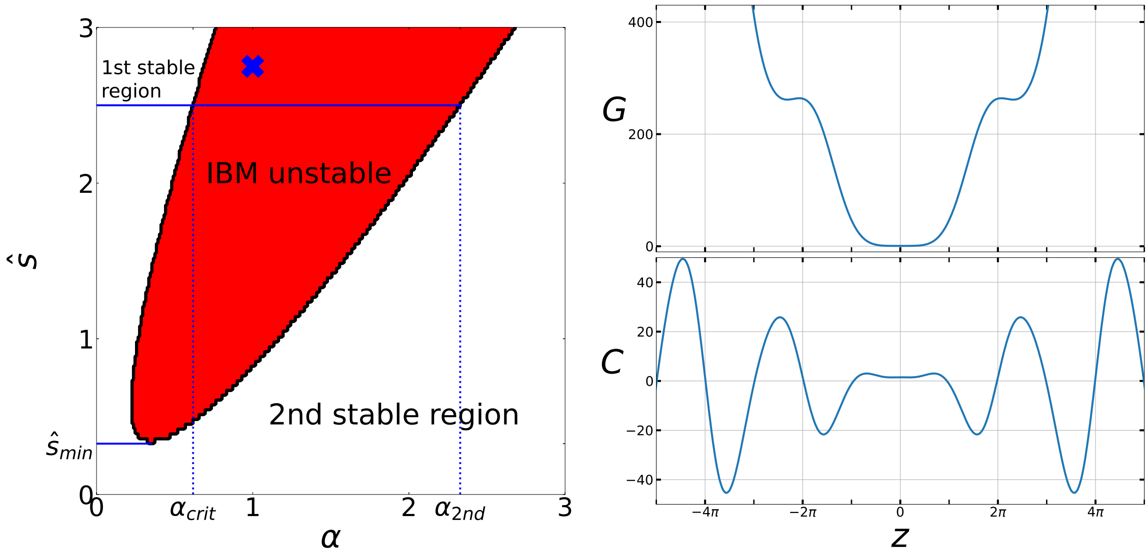

Figure 4.1: Left: IBM stability as a function of normalised pressure gradient α and magnetic shear $\hat{s}$ for the cyclone base case. Right: `ideal_ball` coefficients G and C for $\hat{s} = 2.75$, $\alpha = 1$ (marked by blue cross in left plot).

where I have used the field line selected by $\theta_0 = 0$ as this is the implementation in the main branch of the `GS2` code and is often the most unstable field line for a given surface. Computing stability for $\theta_0 \neq 0$ is implemented in the branch `feature/ideal-ball-theta0`.

`ideal_ball` has been used to study ballooning stability at low computational cost in axisymmetric fusion devices (see e.g. Patel *et al.* [69]). Besides being able to compute IBM stability for a given field line on a particular magnetic surface, `ideal_ball` can efficiently scan the normalised pressure gradient $\alpha \equiv \beta \cdot (1/p) \cdot \partial p/\partial \psi_N$ ($\psi_N \equiv \psi/\psi_{LCFS}$ will be used as the radial coordinate in the `GS2` results presented in this thesis) and magnetic shear $\hat{s} \equiv \partial q/\partial \psi_N$ for some fixed set of geometric parameters[1]. An example of IBM stability for a flux surface as a function of $(\hat{s}, \alpha)$ is shown in figure 4.1 (left), where the flux surface corresponds to the cyclone base case (CBC) [70]; a circular, finite aspect ratio flux surface. Figure 4.1 (right) shows for reference the quantities G and C corresponding to ($\alpha = 1$, $\hat{s} = 2.75$). The unstable region in figure 4.1 (left) differs slightly at low $\hat{s}$ to examples shown e.g. by Wesson [8], which specify a flux surface using a "shifted circle" model which is only strictly valid in the limit of large aspect ratio [55]. However, figure 4.1 qualitatively agrees with similar finite aspect ratio flux surfaces e.g. Greene and Chance [71].

It will be helpful in later sections to describe the structure of IBM stability in $(\hat{s}, \alpha)$ space here. One observes that for $\hat{s} > \hat{s}_{min}$, the plasma is ballooning unstable for a range of pressure gradients

---

[1] The normalised pressure gradient α is not to be confused with the binormal coordinate α. The former appears in only in this chapter and in chapter 5. The latter appears in this chapter, chapter 3 and chapter 7.

($\alpha_{crit}(\hat{s}) < \alpha < \alpha_{2nd}(\hat{s})$). The region $\hat{s} < \hat{s}_{min}$ is referred to as the second stability window, in which the plasma is stable for all α. The window size (i.e. the value of $\hat{s}_{min}$) is particularly important for spherical tokamak equilibria (e.g. [72]), since a high core β requires $\alpha(\psi_N)$ to be large, and typically $\alpha > \alpha_{crit}$ is required.

4.4 Kinetic effects and the KBM

The IBM model presented here makes several assumptions regarding the plasma. Most notably it simultaneously takes the limits: (1) $k_\perp \rho_i \ll 1$ (i.e. the mode's perpendicular scale is much greater than the Larmor radius, for ideal MHD to be applicable) and (2) $k_\perp L \gg 1$, where L is the characteristic equilibrium scale of the plasma (in order to make the high-n expansion). That is, the spatial scale of the mode is asymptotically smaller than the typical equilibrium scale but asymptotically larger than the gyro-radius. Simultaneously satisfying both requirements in a real plasma can be challenging, and thus one requires caution when applying eq. (4.2.21) to a real plasma.

The focus of this thesis is microinstabilities, which by definition are Larmor radius-scaled; in general, therefore, kinetic effects must be included, for example by using gyrokinetics. The gyrokinetic equivalent of the IBM is the kinetic ballooning mode (KBM), which shares some of the features of the IBM but is rather more complicated.

A general description of KBMs was presented by Antonsen and Lane [73] and by Tang *et al.* [74], in which the linear EM GKE is solved for h_s in terms of the fields ϕ, $A_{1\|}$, $B_{1\|}$ and the expression for h_s is inserted into the field equations. This results in three coupled, linear, integro-differential equations which may then be solved in certain limits. In particular, (4.2.21) is recovered by Tang *et al.* in the long-wavelength low frequency limit in the absence of trapped particles (the low-frequency limit is of interest since it describes IBMs near marginal stability).

However, the complexity of these equations make it difficult to assess whether kinetic effects have a net stabilising or net destabilising effect beyond simple limits. For example, Aleynokiva *et al.* [75] rigorously showed that in a strongly-driven low-β ($\beta \sim \epsilon = v_{th,i}/(\Omega^2 a^2) \ll 1$) limit (although this ordering is described as a "high β" ordering in the publication to distinguish from the ordering $\beta \sim \epsilon^2$), the KBM reduces to the IBM with a diamagnetic correction. This reduces the KBM stability boundary with respect to the IBM boundary. However, as the pressure drive is reduced, additional effects come into play which appear to have a stabilising role. Likewise, an investigation by Hastie and Hasketh [76]studying the effect of finite Larmor radius (FLR) on the KBM shows this to be weakly destabilising at long wavelength but strongly stabilising at short wavelength. Drift resonances may also provide kinetic destabilisation of the mode [73, 77], with the latter arguing that drift resonances reduce α_{crit} and that FLR effects can provide stabilisation but cannot change α_{crit} (in a large-A, low-β, $v_{th,i}/(\Omega a) < 1$ limit). Accurately describing KBMs in situations where these limits are not satisfied (such as spherical tokamaks, which have low A and high β) therefore requires gyrokinetic simulation.

4.5 Concluding remarks

The basic physics of the KBM is described by ideal MHD ballooning theory, for which stability can be quickly and easily assessed using the approach given by Connor *et al.* [65]. This approach is implemented in the `GS2` module `ideal_ball`, and the structure of IBM stability in $(\hat{s}, \alpha)$ space can be easily calculated at low computational cost ($(O)($ CPU minutes$)$). For a given geometric flux surface, scanning $(\hat{s}, \alpha)$ shows a "nose" of unstable phase space characterised by a "second stability window size" $\hat{s}_{min}$, below which the IBM is stable for all α. For $\hat{s} > \hat{s}_{min}$, stability is parametrised by $\alpha_{crit}(\hat{s})$ and $\alpha_{2nd}(\hat{s})$. The KBM is modified by kinetic effects, which have been studied analytically in the gyrokinetic framework. These approaches can make quantitative predictions for the KBM complex frequency in certain limits.

More generally, one can study KBMs numerically by performing gyrokinetic simulations, as has been widely reported (see for example [69, 78, 79]), which has the benefit that stability can be examined for realistic geometries and plasma conditions. One example of their use is to inform the design choice of fusion devices; hypothetical plasm equilibria must be sufficiently stable to KBMs to ensure good confinement, such that power can be economically produced with reasonable levels of heating and fuelling. This consideration is the subject of the next chapter.

Chapter 5

Kinetic ballooning modes as a constraint on plasma triangularity in commercial spherical tokamaks

5.1 Introduction

In this chapter, I address the stability of kinetic ballooning modes (KBMs) in spherical tokamaks (STs) as the plasma triangularity is varied (triangularity will be defined mathematically in section 5.2). These results form the basis of a publication [80], which this chapter very closely matches.

5.2 Background and motivation

As noted in section 1.3.1.1, the ST is characterised by a relatively small aspect ratio A, strong shaping and high plasma β. The reduced radial machine size lowers the capital cost, and the favourable stability properties are likely to make high-performance plasmas more readily attainable. A recent study predicted that an increase in the fusion triple product $nT\tau_E$ by a factor of 3 could be achieved in an ST compared to a conventional tokamak with similar values of fusion power and field strength but different machine size [81]. Spherical tokamaks are thus receiving significant attention in the fusion community. Several devices have recently been built or upgraded, such as NSTX-U [82], ST40 [83] and MAST-U [84]. Others are currently being designed or built, such as SMART [85] and STEP [86]. However, reactor-relevant equilibria must have sufficiently low turbulent transport to maintain their density and temperature profiles with modest heating power (equivalently, $nT\tau_E$ must be sufficiently

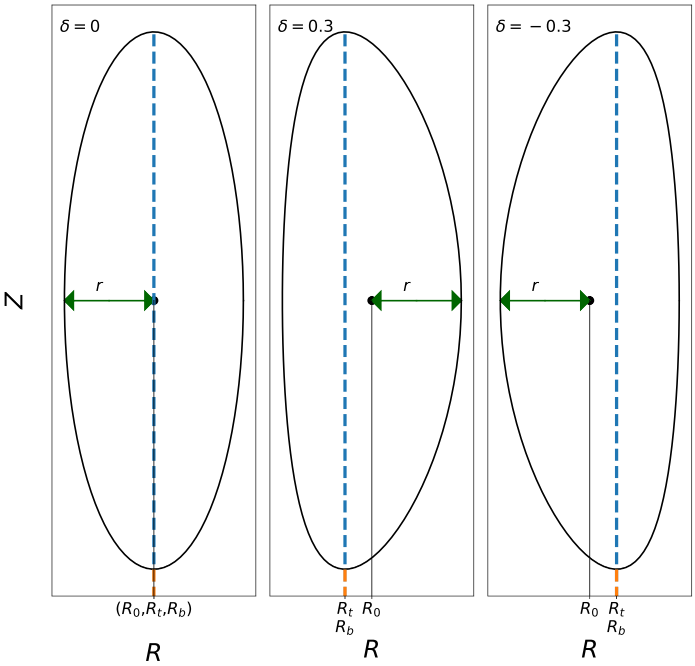

Figure 5.1: Examples of flux surface cross sections to illustrate the definition of triangularity. These cross sections have aspect ratio $A = r_{LCFS}/R = 1.67$ and elongation $\kappa = 3$. From left to right: zero triangularity ($\delta = 0$), positive triangularity ($\delta = 0.3$), negative triangularity ($\delta = -0.3$).

large). Optimising ST equilibria in this regard is an area of active research.

A novel approach to optimisation in conventional aspect ratio tokamaks (CTs) is to make the plasma triangularity (δ) negative, where δ is defined for a given flux surface as

$$\delta \equiv \frac{1}{2}\frac{2R_0 - R_t - R_b}{r}, \tag{5.2.1}$$

where $R_{t(b)}$ is the major radial location of the maximum (minimum) value of Z on the surface and R_0 the major radius (where the subscript $_0$ is used to avoid confusion with the (R, Z) coordinate system). This definition is illustrated in figure 5.1, and 3D pictorial examples of differing triangularity in CTs and STs are shown in figure 5.2. Experiments in TCV [88] and DIII-D [89] reported reduced turbulence for negative triangularity plasmas. For DIII-D, stored energy increased by 25% and electron energy confinement time by 26% compared to L-mode positive triangularity shots.

However, no L-H transition occurred for the negative triangularity discharge (which was performed in a limiter, rather than divertor, configuration), even at high heating power. This was found to coincide with the (modelled) H-mode pedestal being unstable to IBMs [90]. Saarelma *et al* [90] proposed that L-H transition in negative triangularity is only achievable when the pedestal can occupy

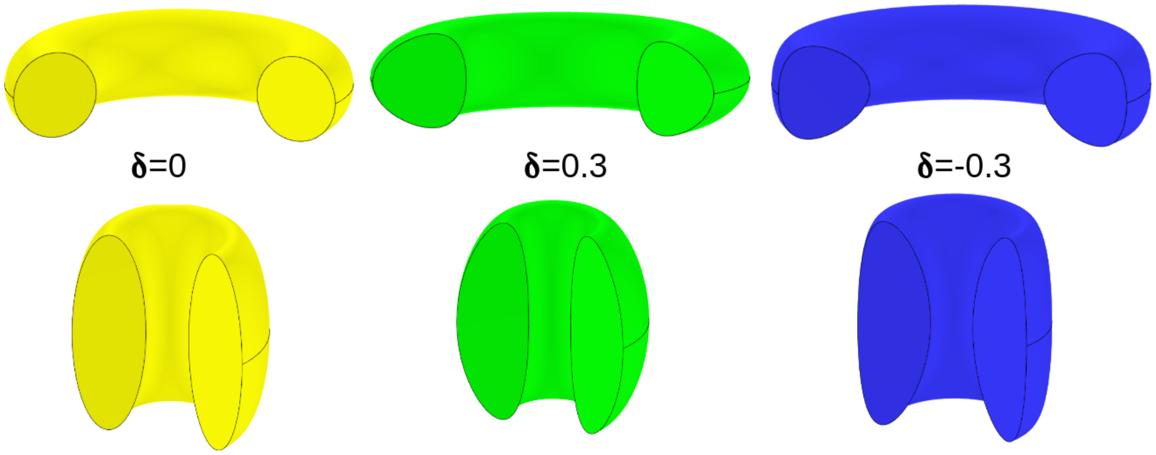

Figure 5.2: 3D visualisation of differing triangularities in tokamak plasmas. Upper row: aspect ratio $A = 3$, unity elongation ($\kappa = 1$). Lower row: aspect ratio $A = 1.67$, $\kappa = 3$. From left to right: zero triangularity ($\delta = 0$), positive triangularity ($\delta = 0.3$), negative triangularity ($\delta = -0.3$). Images generated using `paramak` [87].

the second stability window. Without second stability access, the pedestal becomes IBM-unstable as it tries to form and strong KBM-driven turbulence prevents pedestal formation: H-mode is suppressed. IBMs (and thus, presumably, KBMs) are known to be destabilised by negative triangularity [91], and this raises the question of whether negative triangularity is viable in commercial STs, which typically access second stability across the full radius [72].

This work seeks to answer two questions: (1) Do KBMs prohibit strongly negative triangularity in commercial ST reactors? (2) Are KBMs likely to be problematic in positive triangularity ST equilibria? To this end, gyrokinetic simulations with `GS2` are used to examine the ion-scale instabilities in three strongly shaped hypothetical ST equilibria, constructed with a commercial reactor in mind.

5.3 Equilibria selected

The equilibria used (which are publicly available [92]) are generated by the fixed-boundary equilibrium code SCENE [93], which simultaneously solves the Grad-Shafranov equation and the neoclassical current contributions to generate an equilibrium with self-consistent current profiles. Some important equilibria properties are shown in table 5.1 and the radial profiles of electron density n_e, electron temperature T_e, safety factor q, triangularity δ and elongation $\kappa \equiv \frac{R_t - R_b}{r}$ are plotted in figure 5.3. For simplicity $T_e = T_i$ is used throughout this work. Since fusion αs preferentially heat electrons, it is plausible that T_e would exceed T_i in practice. However, the focus of this study is ballooning modes, which are typically sensitive to the total pressure gradient rather than to the contribution of individual species.

	A	R_0	q_0	q_{LCFS}	δ_{LCFS}	κ_{LCFS}	$\langle\beta\rangle_V$	β_N	I_T (MA)	B_{T0} (T)	V (m^3)	P_H (MW)	P_{fus} (MW)
“-ve tri”	1.67	2.50	2.58	4.50	-0.300	2.80	18.1%	4.21	16.5	1.93	310	60	514
“high $q0$”	1.67	2.50	2.71	8.97	0.543	2.80	18.6%	5.47	16.5	1.83	287	60	808
“low $q0$”	1.67	2.50	1.38	9.16	0.543	2.80	18.5%	5.50	16.5	1.83	288	60	839

Table 5.1: Key equilibria quantities: aspect ratio A, magnetic axis major radius R_0, q on-axis and at LCFS, LCFS triangularity and elongation ($\delta_{LCFS}, \kappa_{LCFS}$), plasma β and normalised β (both volume-averaged), toroidal current I_T, on-axis toroidal field B_{T0}, volume V, heating power P_H and fusion power P_{fus}.

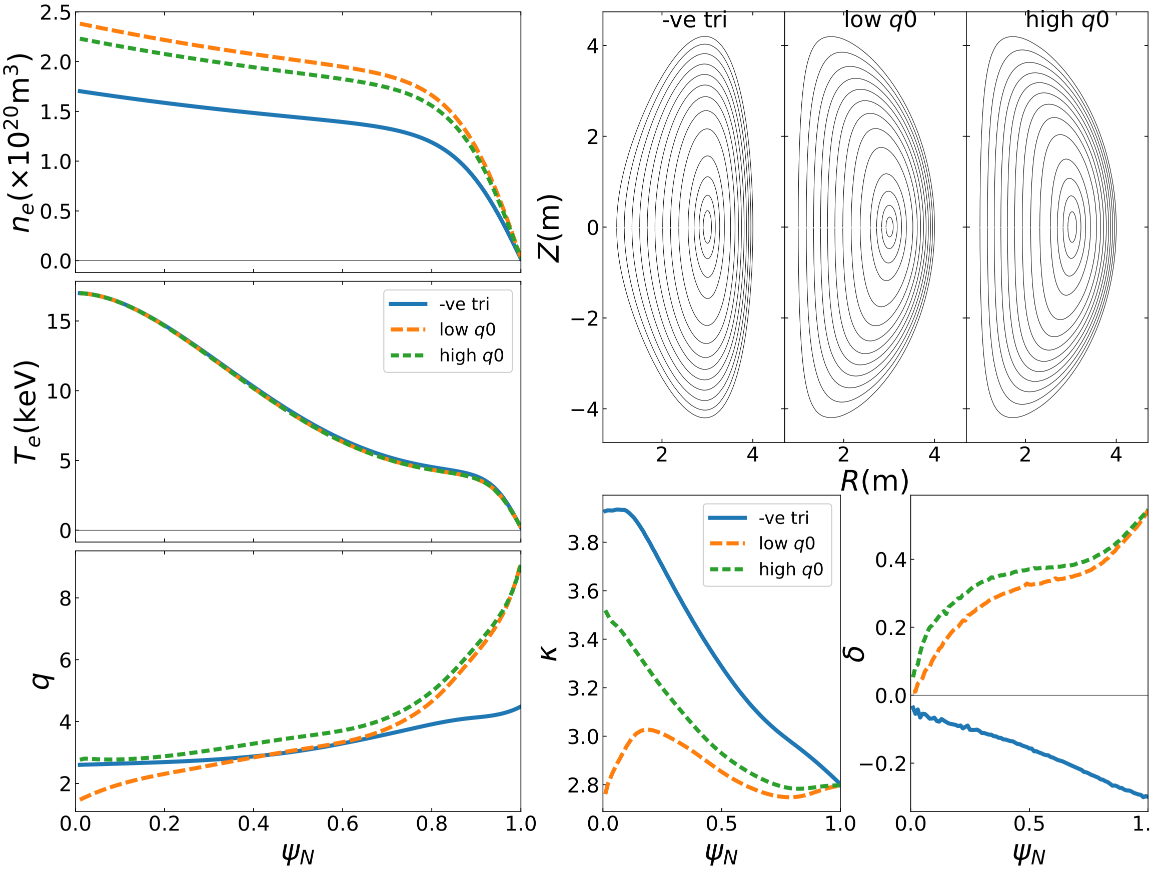

Figure 5.3: Flux surfaces and radial profiles of n_e, T_e, q, κ, δ for the three equilibria used in this study.

The equilibria are constructed with identical major radius and elongation on the last closed flux surface (LCFS), total toroidal current and auxiliary heating/current drive power. The density and temperature profiles are reasonable models but not the results of transport simulations.

Two equilibria (which I label “high $q0$” and “low $q0$”) are given strongly positive LCFS triangularity (0.543), the main difference being their on-axis safety factor q_0. The third (“-ve tri”) has LCFS triangularity of -0.3. Although this leads to a greater plasma volume, the density pedestal gradient is lower, resulting in a reduced fusion power of 40% compared to the positive triangularity cases.

5.4 Gyrokinetic analysis

I examine the KBM and other microinstabilities using `GS2`, including $A_{||}$ and $B_{||}$ fluctuations but omitting the nonlinear term. For the most part, these simulations find the complex frequency $\Omega = \omega + \mathbf{i}\gamma$ of the dominant mode as a function of $(\psi_N, \tilde{k}_y, \tilde{k}_x)$ in each equilibrium. The "reference" gyro-radius here is the proton thermal gyro-radius of the surface ($\rho_r(\psi_N) \equiv \sqrt{2T/m_p}/\Omega_p$ where m_p is the proton mass and Ω_p the proton gyrofrequency). I will also connect $k_y\rho_r$ to toroidal mode number $n = A(\psi_N)(k_y\rho_r)$ where A is a weakly varying function of ψ_N. The research presented here uses `GS2` commit `142c787` (version 8.1).

5.4.1 Effect of sheared plasma rotation

The gyrokinetic-Maxwell equations used here assume negligible plasma rotation. In reality, sheared rotation in tokamak plasmas does exist and can stabilise microinstabilities [94]. To gauge the magnitude of this effect, the Hahm-Burrel shearing rate $|\omega_{HB}|$ [94] is estimated by calculating the $\mathbf{E} \times \mathbf{B}$ flow arising from the diamagnetic flow in the equilibrium. That is, the $\mathbf{E} \times \mathbf{B}$ flow shear is estimated from the balance of electric field and pressure gradient forces in the equilibrium, in the absence of externally driven rotation (as expected for reactor-grade tokamak plasmas).

Similar to the approach used by Applegate *et. al* [95], I estimate the shearing rate as

$$\omega_{HB} = \frac{(\partial\psi/\partial r)^2}{B}\frac{\partial^2\Phi}{\partial\psi^2}, \tag{5.4.1}$$

where B is the magnetic field strength and Φ is the equilibrium electrostatic potential. Φ is estimated by taking the equilibrium force balance

$$\frac{\nabla p}{n_i e} = \mathbf{V} \times \mathbf{B} + \mathbf{E} \tag{5.4.2}$$

(where p is the ion pressure, $\eta_i = (T_i' n_i)/(T_i n_i')$, $'$ denotes a derivative with respect to ψ, $\mathbf{V}$ is the ion flow velocity and $\mathbf{E}$ the equilibrium electric field) and setting $\mathbf{V} = 0$. A little manipulation yields

$$\omega_{HB} = \frac{(\partial\psi/\partial r)^2}{B \cdot n_i e}\left(\frac{\partial^2 p}{\partial\psi^2} + \frac{1}{p \cdot (1+\eta_i)}\left(\frac{\partial p}{\partial\psi}\right)^2\right), \tag{5.4.3}$$

where B is taken as the field strength on the surface at the location of the magnetic axis.

5.4.2 Simulation parameters, species choice and collisions

The results presented here simulate a kinetic electron species and a single ion species with ($Z_i = 1$, $\tilde{m}_s = 2.5$); this effectively simulates a DT plasma with equal densities of deuterium and tritium. Collisions are ignored in this work.

The values of non-physical simulation parameters are chosen to minimise computational cost without compromising accuracy of the simulations. This choice is justified by comparing a selection of $(\psi_N, k_y\rho_r, \theta_0)$ for the three equilibria to higher-fidelity simulations. In particular, the difference in growth rate $\Delta\gamma = \gamma_0 - \gamma_{hf}$ (where γ_0 is the growth rate found with the study parameters and γ_{hf} the growth rate for a higher-fidelity simulation) is used as a figure of merit. In some cases $\gamma_{0,hf}$ is low, resulting in large fractional errors. Accordingly, the absolute error (in normalised units of $v_{th,r}/r_{LCFS}$) is reported here.

The parameters governing the parallel coordinate are $n_{\text{period}} = 3$, $n_z = 192$ (although it is sometimes necessary to adjust n_z owing to difficulties encountered in `GS2`'s `gridgen` module). $n_{\text{period}} = 3$ is insufficient to resolve extended micro-tearing structures which have been seen in high-β equilibria [69], but is sufficient to resolve KBMs. Preliminary research did not reveal any (dominant) extended structures at long wavelength. Comparing $n_{\text{period}} = 3$ to $n_{\text{period}} = 5$, I find $\texttt{max}(|\Delta\gamma|) = 4\text{E}{-3}$ with rms value $\Delta\gamma_{rms} \equiv \sqrt{\sum_N (\Delta\gamma)_N^2/N} = 4\text{E}{-4}$. Increasing $n_z = 192$ to $n_z = 394$ results in $\Delta\gamma_{rms} = 5\text{E}{-3}$ for $\psi_N <= 0.9$ and $\Delta\gamma_{rms} = 0.02$ for $\psi_N > 0.9$, reflecting a difficulty in the calculation of geometric quantities in `GS2` for strongly-shaped numerically-prescribed surfaces.

The equilibrium data provides profiles for the density $n(\psi_N)$ of electrons, the main ion species, helium ash and two impurity species: tungsten (with typical density $n_W/n_e \sim 10^{-5}$) and xenon ($n_{Xe}/n_e \sim 10^{-4}$) (both assumed fully ionised). Lacking simulated temperature profiles, it is assumed that $T(\psi_N)$ is identical for all species (the effect of fast α particles could be an interesting area of future research.) Comparing simulations with the five kinetic species to the "reduced" simulation with two kinetic species (in which $n_i = n_e$ is set to ensure quasi-neutrality) results in a difference of $\Delta\gamma_{rms} = 0.02$.

Collisions are ignored in the results presented here. Comparing collisionless to collisional simulations found $\Delta\gamma_{rms} = 0.01$ for $\psi_N \leq 0.9$ and $\Delta\gamma_{rms} = 0.09$ for $\psi_N > 0.9$ (consistent with the lower temperatures, and hence increased collisionality, near the edge).

To summarise, the tests described above find that these simulations present a realistic picture for $k_y\rho_r <\sim 1$ over most of the plasma ($\psi_N <\sim 0.9$). Near the edge ($\psi_N > 0.9$) collisionality becomes

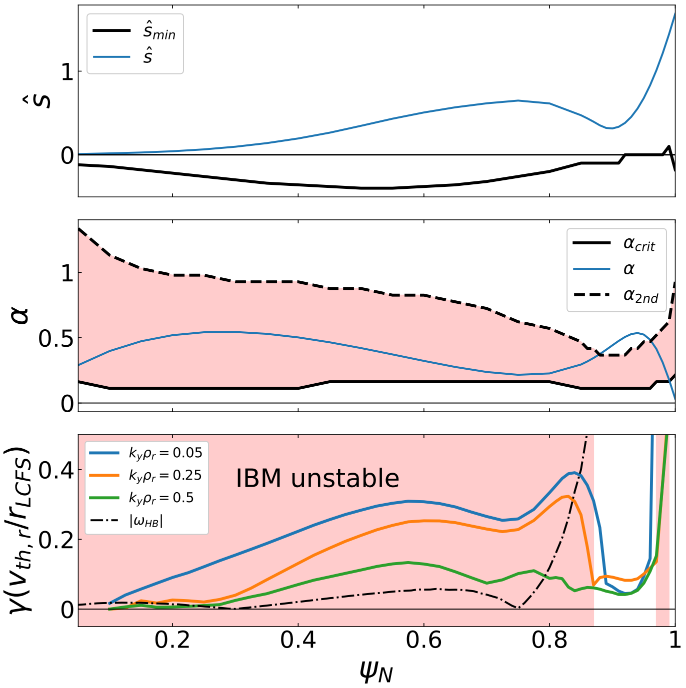

Figure 5.4: "-ve tri" equilibrium stability properties vs ψ_N. Upper: Equilibrium shear ($\hat{s}$) and second stability "window size" ($\hat{s}_{min}$). Middle: Equilibrium pressure gradient (α), marginally IBM-unstable α ($\alpha_{crit}, \alpha_{2nd}$); shaded region indicates IBM-unstable plasma parameters. Lower: Gyrokinetic growth rate ($\gamma(\psi_N)$) for several $k_y\rho_r$ and $\theta_0 = 0$ (solid lines). Dashed line indicates estimated Hahm-Burrel shearing rate $|\omega_{HB}|$.

more important and the strong shaping presents challenges to the calculation of `GS2`'s z grid; these edge results should therefore be interpreted qualitatively, rather than quantitatively. Suprathermal α particles are included in the equilibrium calculations, but in the gyrokinetic simulation they are incorporated into the ion species by increasing n_i and ensuring the kinetic profiles matched the prescribed pressure gradient while maintaining $n_i = n_e$ and $T_i = T_e$.

5.5 Stability properties of the negative triangularity equilibrium

In the "-ve tri" equilibrium, second stability is blocked across the entire plasma ($\hat{s}_{min} < 0$) and $\alpha(\psi) > \alpha_{crit}(\psi)$ (shown in figure 5.4). As a result, the equilibrium is ideal MHD ballooning unstable over the core. In the pedestal, α strays into the second stable region ($\alpha > \alpha_{2nd}$), coinciding with a sharp drop in the normalised gyrokinetic growth rate $\gamma(\psi_N)$ (lower plot). This supports the picture (validated in section 5.7.1) that, where the plasma is IBM-unstable, long-wavelength KBMs are the dominant instability. It should be noted that the gyrokinetic growth rate γ is normalised to the thermal velocity associated with the flux surface, so the absolute growth rates have a different (but qualitatively similar) trend.

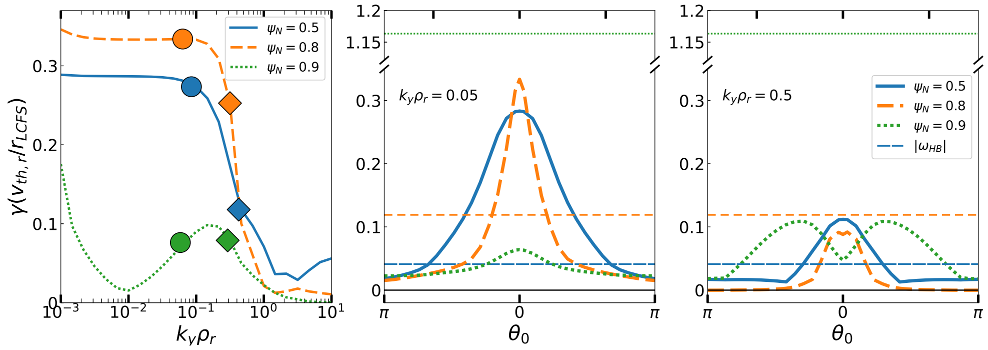

Figure 5.5: Gyrokinetic growth rate γ for several flux surfaces for "-ve tri" equilibrium. Left: $\gamma(k_y\rho_r)$ for $\theta_0 = 0$, ($n = 10$ and $n = 50$ marked with filled circles and diamonds respectively). Middle and right: $\gamma(\theta_0)$ for $k_y\rho_r = 0.05$ and 0.5. Estimated Hahm-Burrel shearing rate $|\omega_{HB}|$ for each surface shown with thin lines.

At $\psi_N >\sim 0.97$, there are strongly growing instabilities, as the equilibrium again becomes ballooning-unstable. However, the estimated $|\omega_{HB}|$ is high in this region, so flow shear (as well as collisions) would likely need be included in simulations to give a realistic picture of stability.

Figure 5.5 shows $\gamma(k_y\rho_r, \theta_0)$ for several values of ψ_N. For $\psi_N = 0.5, 0.8$, the instability spans a wide range of low $k_y\rho_r$, suggestive of an "ideal" KBM, largely governed by ideal MHD physics [75, 96]. These KBMs are also wide in θ_0, and thus less easily stabilised by flow shear. $\psi_N = 0.9$ shows the KBM being less unstable for modes with $k_y\rho_r <\sim 0.1$, before the onset of a negative-frequency tearing parity mode at $k_y\rho_r <\sim 0.01$. At such low $k_y\rho_r$, the validity of the local approximation as applied to this equilibrium becomes questionable. However, some discussion is given to the instability in section 5.7.1.

Although nonlinear gyrokinetic simulations would be needed to calculate the turbulent fluxes of particles and energy, these linear results indicate that those fluxes would be large in the core, since the linear growth rate is moderately large over a wide range of $(k_y\rho_r, \theta_0)$. It has previously been reported that turbulent fluxes (in particular, the electron heat flux) increase strongly as β exceeds the marginally stable value for the KBM [97], which is clearly the case here. It should be noted that reliable nonlinear results may be difficult to obtain, since electromagnetic nonlinear simulations often fail to saturate, for reasons which may be physical (e.g. [98]) or non-physical. Electromagnetic nonlinear stellarator simulations reported by McKinney *et al.* [99], for example, only saturate when the lowest-k_y modes are linearly stable to KBMs. Given the wide range of KBM-unstable k_y values, this condition would not be satisfied here.

5.5.1 Second stability access in the negative triangularity regime

Section 5.5 supports a simple picture: KBM growth rates tracking IBM stability, and are likely unacceptably high for steady-state operation. This prompts the question: is the closing of second stability a general feature of negative triangularity STs, or could a configuration exist with second stability access?

To test this, the $\psi_N = 0.5$ surface from the negative triangularity equilibrium is Miller-parametrised. The triangularity and elongation are then varied in isolation, to elucidate the underlying causes of reduced stability and to investigate whether the destabilising effect of negative triangularity can be compensated by tuning other plasma parameters. A description of the parametrisation process is given in the following section.

5.5.1.1 Miller parametrisation

Miller *et al.*'s finite-A equilibrium model [55] describes each surface by nine dimensionless parameters: aspect ratio A, elongation κ, triangularity δ, the radial derivatives of major radius, elongation and triangularity s_κ, s_δ, $\partial R_0/\partial\psi_N$, the safety factor q, normalised magnetic shear $\hat{s} \equiv \partial q/\partial\psi_N$, and normalised pressure gradient $\alpha \equiv -\partial\beta/\partial\psi_N$. These specify the shape of the flux surface and its poloidal magnetic field:

$$R = R_0 + r\cos[\theta_M + x\sin\theta_M], \tag{5.5.1}$$

$$Z = \kappa r\sin\theta_M, \tag{5.5.2}$$

$$B_p = \frac{(\partial\psi/\partial r)\kappa^{-1}R^{-1}\left[\sin^2(\theta_M + x\sin\theta_M)(1 + x\cos\theta_M)^2 + \kappa^2\cos^2\theta_M\right]^{1/2}}{\cos\left(x\sin\theta_M\right) + (\partial R_0/\partial r)\cos\theta_M + [s_\kappa - s_\delta\cos\theta_M + (1 + s_\kappa)x\cos\theta_M]\sin\theta_M\sin\left(\theta_M + x\sin\theta_M\right)}, \tag{5.5.3}$$

where R and Z are cylindrical coordinates (with the magnetic axis located at $Z = 0$), B_p the poloidal magnetic field and θ_M a poloidal coordinate ranging from 0 to 2π and $x = \sin^{-1}(\delta)$. (NB $\hat{s}$ and α do not appear in equations (5.5.1) to (5.5.3) so can be freely chosen for a given (R, Z, B_p).)

Miller parameters for the numerical SCENE flux surface data are found as follows. Firstly, the numerical values of R, Z and B_p for the flux surface of interest are extracted from the SCENE data. R and Z are used to construct θ_{geo}, a poloidal coordinate defined by $\theta_{geo} = \arctan((Z - Z_{maxis})/(R - R_{maxis}))$, where (R_{maxis}, Z_{maxis}) is the location of the magnetic axis, and is taken from the SCENE equilibrium. Splines of $R(\theta_{geo})$ and $Z(\theta_{geo})$ are used to upsample R and Z, and from this calculate the values for A, r, κ, δ and construct Miller's poloidal

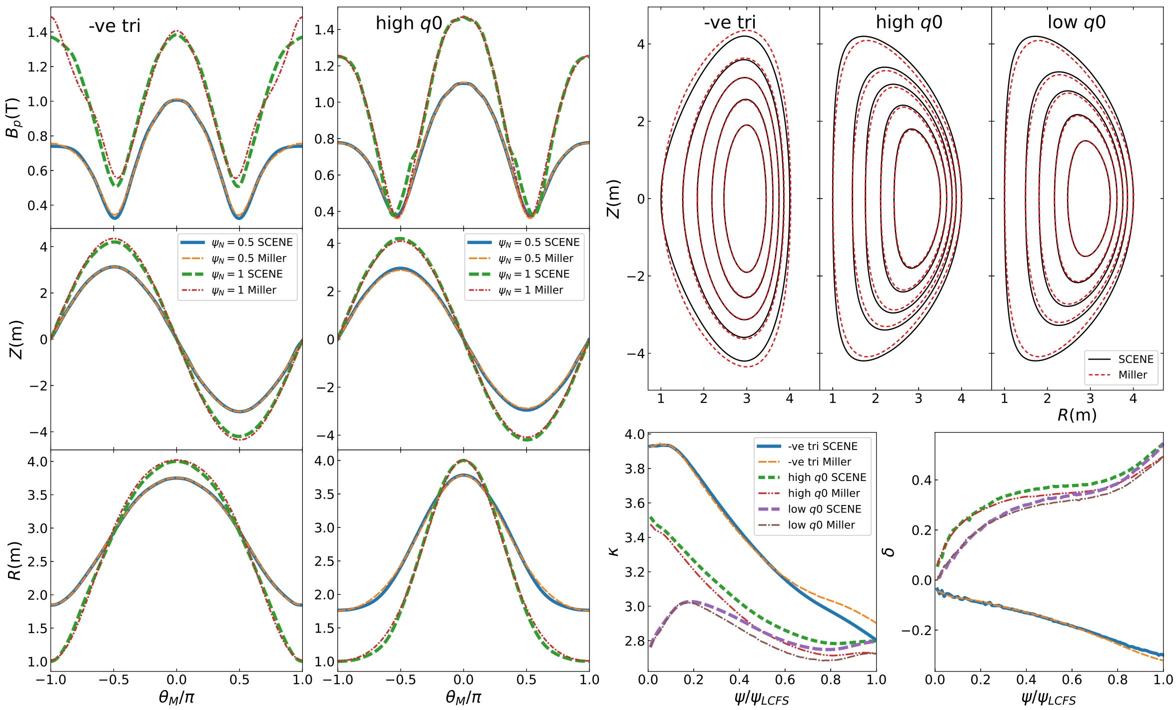

Figure 5.6: Comparison of numerical equilibria data generated by SCENE to Miller parametrisation. Left: R, Z, B_p as a function of poloidal coordinate θ_M. Right, upper: flux surface shape for $\psi_N = (0.15, 0.3, 0.5, 0.7, 1)$. Right, lower: elongation (κ) and triangularity (δ) vs ψ_N; calculated directly from SCENE data and Miller parametrised.

coordinate by defining

$$\theta_M \equiv \arcsin((Z - Z_{maxis})/(\kappa r)). \tag{5.5.4}$$

$B_p(\theta_M)$ is then constructed and fitted to (5.5.3), with fitting parameters s_κ, s_δ, $\partial_r R_0$, $\partial\psi/\partial r$ (the latter determining q).

The above process yields an estimate of the Miller parameters describing a particular surface. However, it treats the parameters (A, r, κ, δ) on a different footing to (s_κ, s_δ, $\partial_r R_0$, q); calculating the former from R and Z does not guarantee an optimal fit of B_p, or indeed of (R,Z) (since most of the R, Z points are ignored.) Therefore, having fitted these values, I apply an additional step of simultaneously fitting ($R_M(\theta_M)$, $Z_M(\theta_M)$, $B_{pM}(\theta_M)$) to ($R(\theta_M)$, $Z(\theta_M)$, $B_p(\theta_M)$), allowing all 8 parameters to vary freely. The previously calculated values are used as initial guesses. This method ensures that B_p is treated on the same footing as R and Z, at the expense of allowing (A, r, κ, δ) to deviate from their geometric values. Finally, the values of $\hat{s}$ and α are selected. A caveat of the scheme presented above is that for reasons of convenience, I use the numerical equilibrium value of q rather than the value derived from $\partial_r R_0$.

Plots of the Miller parametrisation for several flux surfaces for each equilibrium are shown in

Miller quantity	“-ve tri” $\psi_N = 0.5$	“high $q0$” $\psi_N = 0.5$	“low $q0$” $\psi_N = 0.5$
A	2.94	2.67	2.79
κ	3.28	2.85	2.79
δ	-0.154	0.340	0.305
s_κ	-1.99	-0.936	-0.673
s_δ	-0.359	0.145	0.220
`shift`$\equiv \partial R_0/\partial r$	-0.462	-0.508	-0.482
q	3.05	3.50	3.09
$\hat{s}$	0.583	0.536	0.644
α	0.791	1.15	1.13

Table 5.2: Miller parameters for the $\psi_N = 0.5$ surfaces of each equilibria.

figure 5.6. $R, Z, B_p(\theta_M)$ and (R, Z) show good agreement between the SCENE data and the Miller fit in the core, with slightly worse agreement towards the edge; in particular, the fitted B_p for the “-ve tri” has a tendency to artificially peak on the inboard side. Another systematic feature is that the κ tends to be underestimated for the positive triangularity cases and overestimated for “-ve tri” with the effect becoming more exaggerated at higher ψ_N.

5.5.1.2 Results of parametrisation investigation

The role of reducing δ is to reduce both $\hat{s}_{min}$ and α_{crit} i.e. to close the second stability window and shrink the first stability region. For negative δ, the effect of increasing κ is to increase α_{crit} but reduce $\hat{s}_{min}$. These results are illustrated in figure 5.7.

It should be noted that the other Miller parameters, such as q, also affect $\hat{s}_{min}$. A general study of the parametric dependencies of the IBM is beyond the scope of this work, but it is found that that relatively large changes to the Miller parameters of this surface are required to open second stability at fixed (δ, κ). As an example, achieving $\hat{s}_{min} > 0$ for the “-ve tri” $\psi_N = 0.5$ surface requires increasing q from 3.0 to 5.4 with all other parameters kept fixed.

I also explore the effect of adjusting the local Shafranov shift parameter, $|\partial R_0/\partial\psi_N|$. This is generally higher in the positive triangularity equilibria than for negative triangularity (e.g. “high $q0$” has 10% greater shift than “-ve tri” at $\psi_N = 0.5$), probably due to the reduced core pressure in the latter. Scanning $|\partial R_0/\partial\psi_N|$ shows that $\hat{s}_{min}$ decreases (i.e. became more negative) as the magnitude of $|\partial R_0/\partial\psi_N|$ increases from its original Miller-fitted value. Whilst this is not exactly the same as recalculating the global equilibrium with an increased core β_N, this suggests that attempting to operate at higher β is unlikely to alleviate the problem of second stability access.

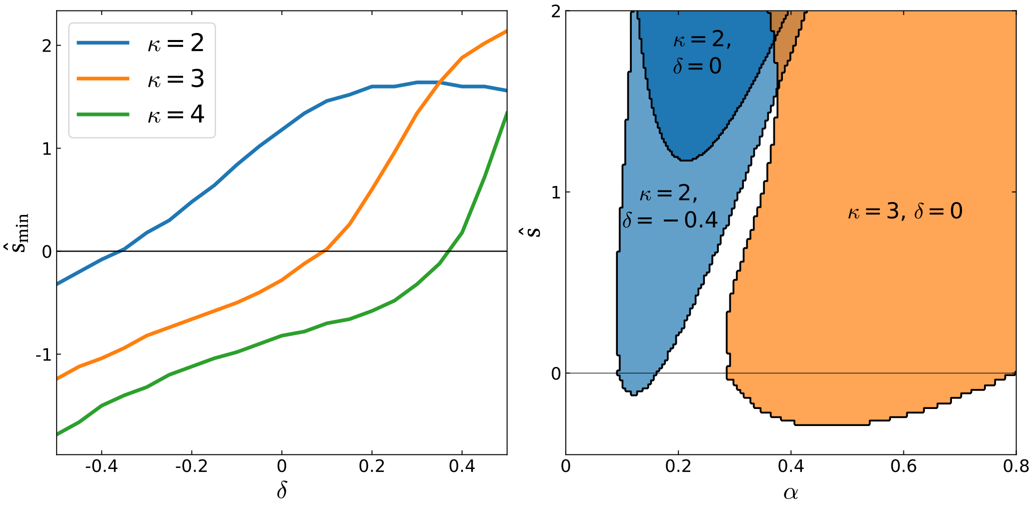

Figure 5.7: Left: dependence of second stability access window ($\hat{s}_{min}$) on elongation (κ) and triangularity (δ) for the $\psi_N = 0.5$ surface of "-ve tri" equilibrium. Right: IBM unstable regions for $(\kappa, \delta) = (2, -0.4)$ (light blue), $(2, 0)$ (dark blue), $(3, 0)$ (orange).

5.5.2 β limits for negative triangularity

These results indicate that $\delta < 0$ is not an attractive option with respect to IBMs, unless β is sufficiently low that the equilibrium remains in the first stable region. However, as can be seen by figure 5.4 (middle), the first stable region is small; a normalised pressure profile confined to this region ($\alpha(\psi_N) = \alpha_{crit}(\psi_N)$) would reduce α by a factor of $\sim$ 2-3 over most of the plasma. The volume-averaged plasma β would consequently fall by a similar amount.

For fixed plasma size and plasma pressure (to ensure the same fusion power), a low-β device would require a large magnetic field, which is difficult to achieve in STs due to the reduced centre column space. High temperature superconductors may provide a possible pathway but present engineering challenges.

5.6 Stability properties of positive triangularity equilibria

`ideal_ball` simulations of the positive triangularity equilibria reveal better IBM stability, with $\hat{s}_{min} > 0$ everywhere (this is shown in figure 5.8). Despite this, the "low $q0$" equilibrium is unstable near the magnetic axis ($\psi_N <\sim 0.5$), illustrating the importance of current distribution (via its effect on q) on ballooning stability. A "high $q0$" is achieved with a hollow current profile, and this is IBM-stable across the plasma. Plots of IBM stability for flux surfaces $\psi_N = 0.1$ and $\psi_N = 0.9$ for all 3 equilibria are shown in figure 5.9.

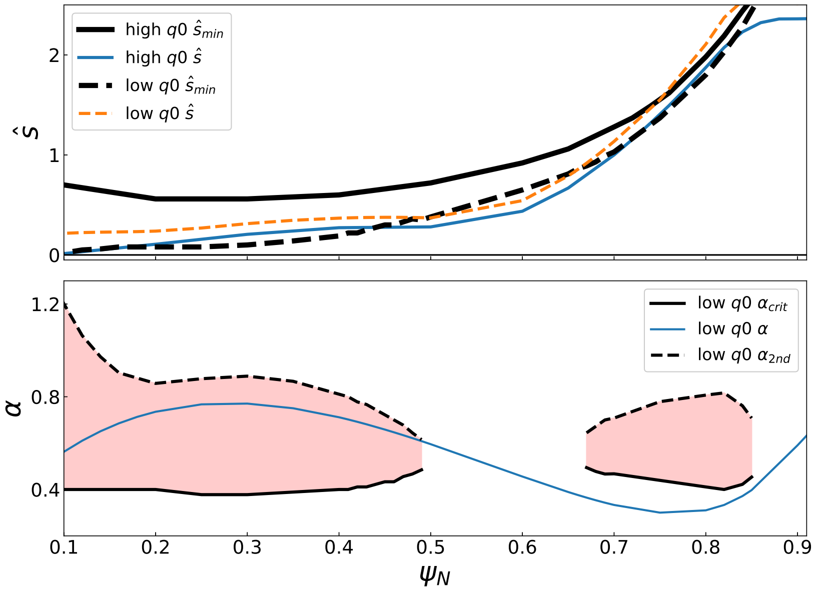

Figure 5.8: Upper: $\hat{s}$ and $\hat{s}_{min}$ for the positive triangularity equilibria. Lower: α, α_{crit} and α_{2nd} for the "low $q0$" equilibrium. NB for "high $q0$", $\hat{s} < \hat{s}_{min}$ for all values of ψ_N, so α_{crit} and α_{2nd} is undefined.

The gyrokinetic $\gamma(\psi_N)$ (shown in figure 5.10) show similar behaviour between "high $q0$" and "low $q0$" for $\psi_N >\sim 0.5$ (consistent with the similarity of q, κ, δ). In this region, instabilities with shorter wavelengths ($k_y\rho_r \sim 0.5$) are dominant for $\theta_0 = 0$, peaking near the pedestal top. However, as shown in figure 5.11, $\gamma(\theta_0)$ is very narrow, and hence highly susceptible to $\mathbf{E}\times\mathbf{B}$ shear stabilisation.

However, $\gamma(\psi_N)$ differs in the core ($\psi_N <\sim 0.5$), coinciding with differences in IBM stability. "low $q0$" exhibits a long-wavelength "ideal" KBM ($\gamma(k_y\rho_r)$ shown in figure 5.11), arising because the plasma is on or over the ideal ballooning boundary. "high $q0$" has small but finite γ at long wavelength. Identification of these dominant instabilities is discussed in the following section.

For both equilibria, $\gamma(\psi_N)$ is lower than for "-ve tri", unstable over a smaller range of $k_y\rho_r$ (figure 5.11) and of similar magnitude to $|\omega_{HB}|$ over much of the plasma. This represents a dramatic improvement in microstability, as a direct result of making the triangularity positive.

5.7 Instability identification

5.7.1 Negative triangularity

The goal of this section is to identify the core and pedestal instabilities in the "-ve tri" equilibrium, by considering ($k_y\rho_r = 0.05, \theta_0 = 0$) for the $\psi_N = 0.5$ (core) and $\psi_N = 0.9$ (pedestal) flux surfaces.

I first verify that the dominant instability tracks the IBM stability boundary in $\hat{s} - \alpha$ space (as

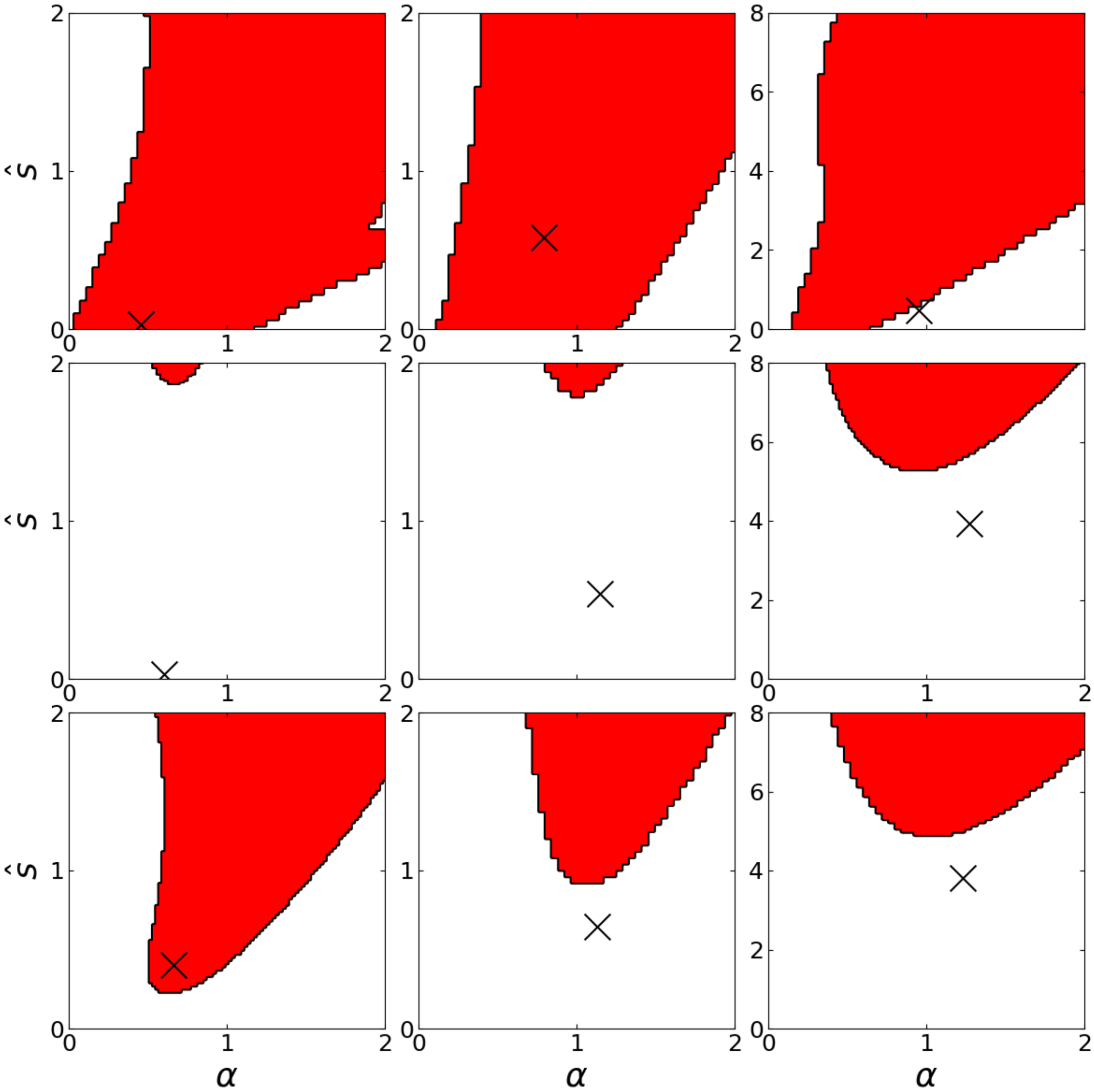

Figure 5.9: IBM stability for three sample flux surfaces for each equilibria. Rows, from top to bottom, are ("-ve tri", "high $q0$", "low $q0$"). Columns, from left to right, are ($\psi_N = 0.1, 0.5, 0.9$). Crosses marks equilibrium values of $\hat{s}$, α.

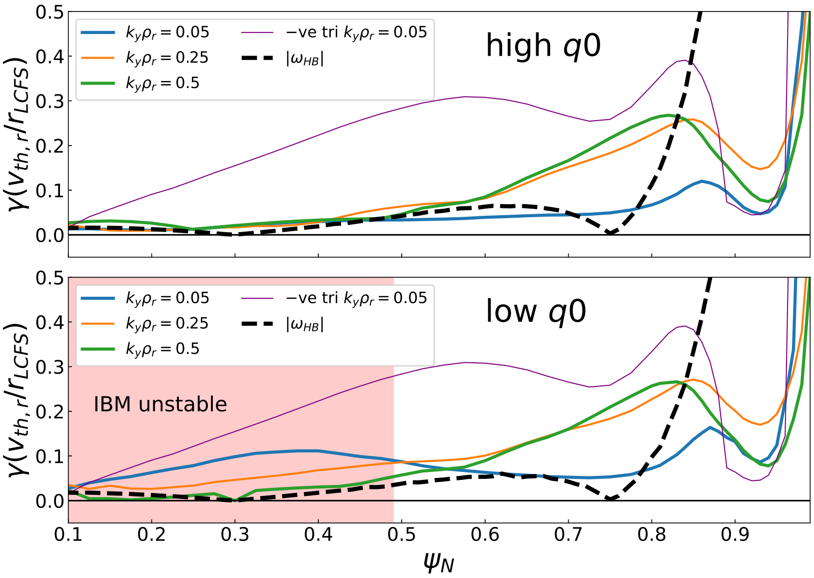

Figure 5.10: $\gamma(\psi_N, k_y\rho_r)$ for "high $q0$" (upper) and "low $q0$" (lower) with $\theta_0 = 0$. "-ve tri" ($k_y\rho_r = 0.05$) shown for comparison (thin purple line). All growth rates normalised to $v_{th,r}/r_{LCFS}$ for their own flux surface and equilibria. Dashed black line indicates approximate magnitude of Hahm-Burrel shearing rate $|\omega_{HB}|$. Shaded region indicates ideal MHD ballooning unstable surfaces.

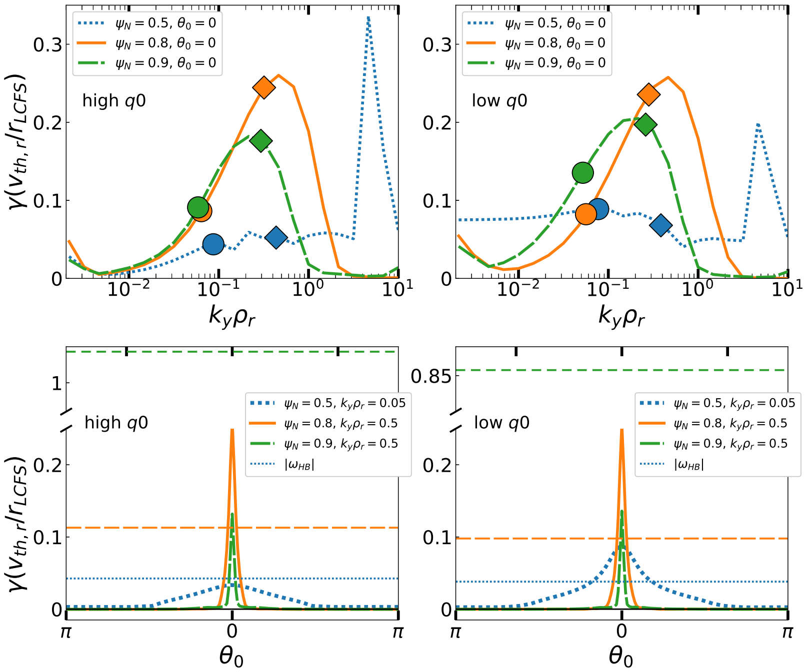

Figure 5.11: Upper row: $\gamma(k_y\rho_r)$ for "high $q0$ (left) and "low $q0$" (right) for several ψ_N, $\theta_0 = 0$. $n = 10$ and $n = 50$ marked with filled circles and diamonds respectively. Lower row: $\gamma(\theta_0)$ for selected ψ_N, $k_y\rho_r$ for "high $q0$" (left) and "low $q0$" (right). Estimated Hahm-Burrel shearing rate $|\omega_{HB}|$ shown with thinner horizontal lines.

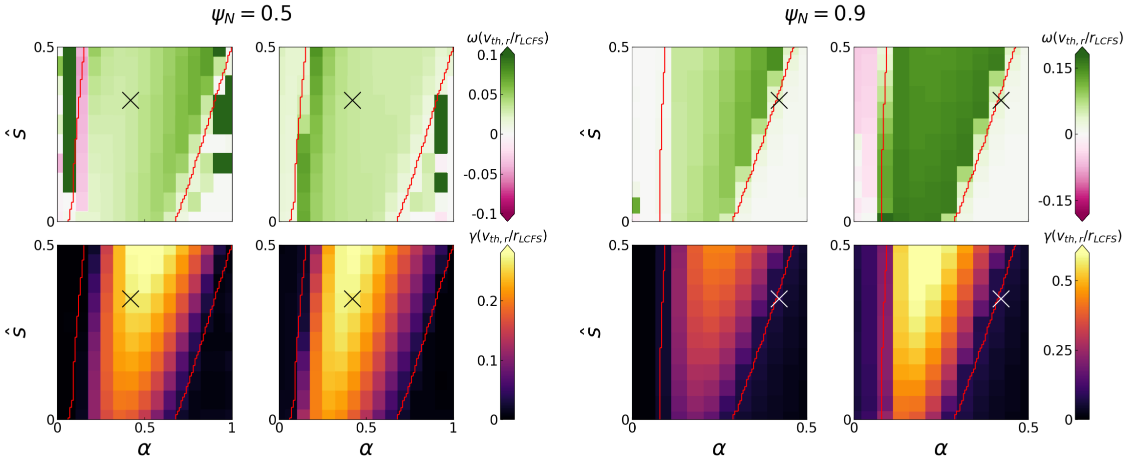

Figure 5.12: Gyrokinetic $\hat{s} - \alpha$ plot for the $\psi_N = 0.5$ (left 4 plots) surface of "-ve tri" equilibrium ($k_y\rho_r = 0.05, \theta_0 = 0$) and $\psi_N = 0.9$ (right 4 plots). Top row shows mode frequency ω and lower shows growth rate γ. Left column: fixed β. Right column: fixed gradients. Crosses mark equilibrium $\hat{s}$, α.

shown in figure 5.12). For both surfaces, the complex frequency Ω tracks the IBM boundary fairly well; γ is high across the unstable region and the frequency is smooth and in the ion diamagnetic direction. To self-consistently change α, one must scale the simulation value of β and/or the normalised kinetic gradients ($n'_{i,e}/n_{i,e}$, $T'_{i,e}/T_{i,e}$). Both of these choices are shown in figure 5.12.

Given that the KBM is expected to be sensitive to α, the next test is to examine the dependence of the instability on ($\partial T/\partial\psi_N$, $\partial n/\partial\psi$, β). This is done by scanning $f \equiv \beta \cdot (1/T) \cdot (\partial T/\partial\psi_N)$, in three cases:

1. Scaling $(1/T) \cdot (\partial T/\partial\psi_N)$ at fixed β, adjusting $(1/n) \cdot (\partial n/\partial\psi_N)$ to keep α constant.
2. Scaling $(1/T) \cdot (\partial T/\partial\psi_N)$ at fixed β but keeping $\eta \equiv (n \cdot \partial T/\partial\psi_N)/(T \cdot \partial n/\partial\psi_N)$ fixed (such that f changes α, with $f = 0$ corresponding to $\alpha = 0$).
3. Keeping the gradients constant but scaling β.

In all cases, the magnetic geometry is kept fixed (i.e. not changed to be consistent with α). Figure 5.13 (left) shows that $\Omega(f)$ and the parallel electric field $\mathtt{max}(E_{||}(\theta))(f) \equiv \mathtt{max}(-\partial\phi/\partial\theta - \partial A_{||}/\partial t)$ (normalised to the electrostatic potential ϕ) are constant when α is fixed (case 1) for the $\psi_N = 0.5$ surface. Cases (2) and (3) demonstrate that the kinetic gradients and β are approximately interchangeable in driving the mode (provided $\beta > 0$). Moreover, the normalised mode structures ($|\hat{\phi}(\theta)|$, $|\hat{A}_{||}(\theta)|$, $|\hat{B}_{||}(\theta)|$) (figure 5.13 (right)) are virtually identical when f is scanned at fixed α. This confirms the mode is indeed driven by α. These same features are observed for the ($\psi_N = 0.9$, $k_y\rho_r = 0.05$) instability (figures 5.14 (left) and 5.15 (left)), although the mode structures show some variation.

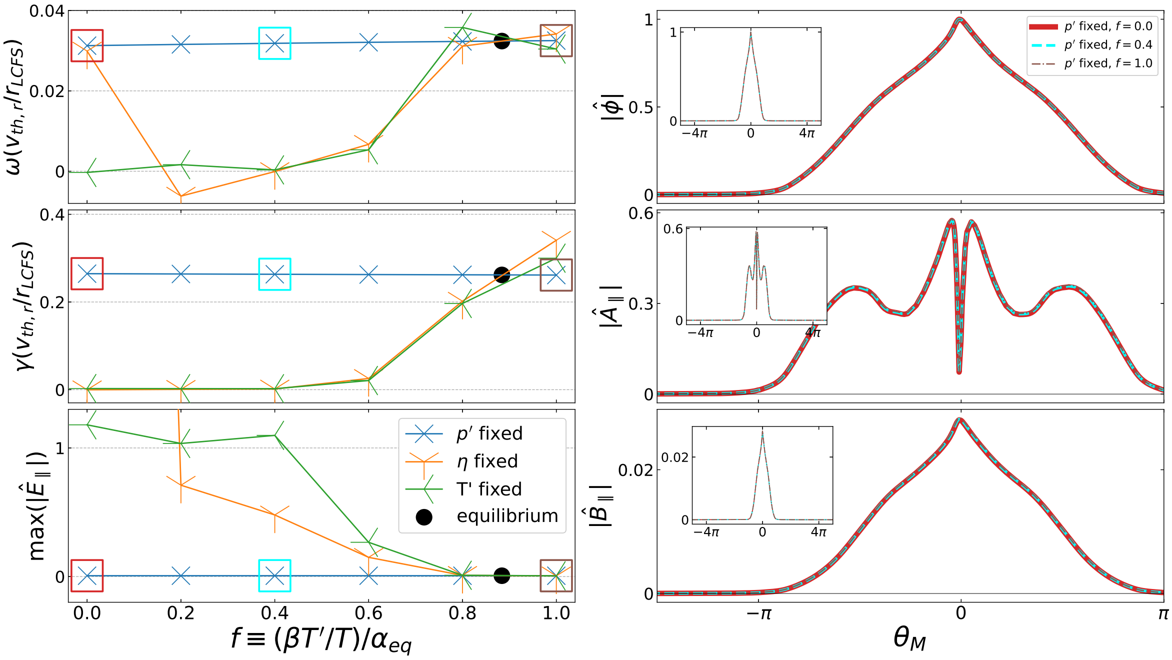

Figure 5.13: Left: $\Omega(f)$ and normalised $E_{\|}(f)$ where $f \equiv \beta \cdot (1/T) \cdot (\partial T/\partial \psi_N)$ for (1) fixed α and β (blue crosses), (2) fixed η and β (orange Y), (3) fixed gradients (green Y) for the "$-$ve tri" equilibrium with $\psi_N = 0.5, k_y\rho_r = 0.05, \theta_0 = 0$. Equilibrium value of f shown as black filled circle. Right: $\tilde{\varphi}_{1\mathbf{k}}(\theta_M)$, $\tilde{A}_{1\|\mathbf{k}}(\theta_M)$, $\tilde{B}_{1\|\mathbf{k}}(\theta_M)$ for varying f at fixed α and β (corresponding to the unfilled squares in left plot).

Finally, I attempt to classify the negative-frequency tearing-parity mode observed at very long wavelength on the $\psi_N = 0.9$ surface (shown in figure 5.5) by repeating this analysis for $\tilde{k}_y = 0.0021$. The results, shown in figures 5.14 (right) and 5.15 (right), show that this mode is also sensitive to pressure gradient, with Ω and mode structure insensitive to n', T' at fixed p'. It is possible that this is a tearing-parity KBM (TKBM), which has been previously reported by McKinney *et al.* [99]. The dependence of the mode on β at fixed α is investigated by doubling β and halving the kinetic gradients (mode structure shown in 5.15, right); the dominant instability in this case has positive frequency and tearing parity mode. This mode has a with a 10% larger growth rate then the suspected TKBM, so it is possible that the latter is indeed driven by α, but is obscured by a more unstable mode. The tearing parity of the "TKBM" may be connected to the fact that $\theta_0 = 0$ is not the most unstable mode, i.e. the KBM "wants" to peak at $\theta_M \neq 0$.

To conclude, the instability observed across the core is an "ideal MHD"-like KBM, with the following features:

1. γ tracks the ideal MHD boundary well.

2. The frequency is in the ion diamagnetic direction.

3. The mode has a low parallel electric field $E_{\|}(\theta)$, indicative of MHD-like modes [96].

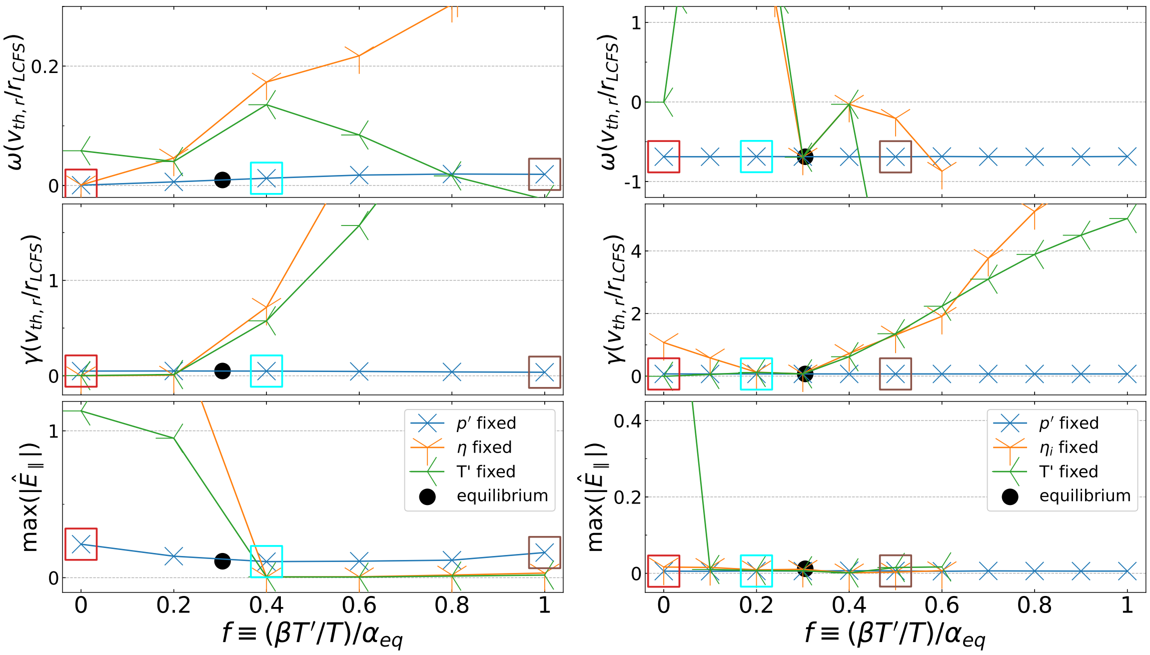

Figure 5.14: $\Omega(f)$ and normalised $E_\parallel(f)$ for "$-$ve tri" equilibrium with $\psi_N = 0.9$, $\theta_0 = 0$. Left: $k_y\rho_r = 0.05$. Right: $k_y\rho_r = 0.0021$.

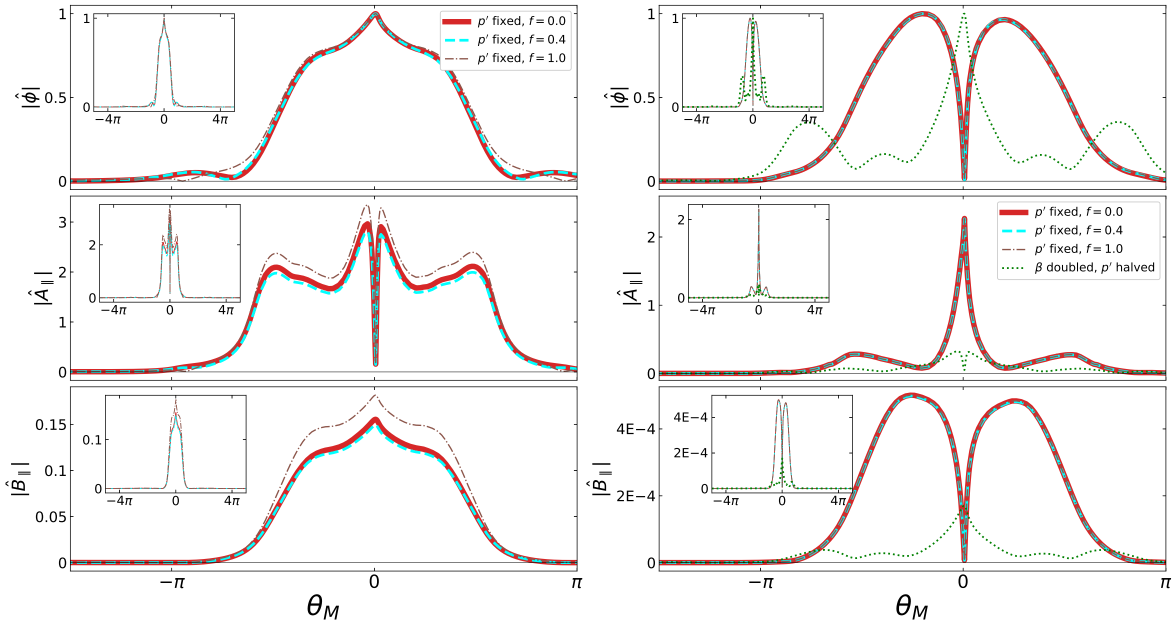

Figure 5.15: $\tilde{\varphi}_{1\mathbf{k}}(\theta_M)$, $\tilde{A}_{1\parallel\mathbf{k}}(\theta_M)$, $\tilde{B}_{1\parallel\mathbf{k}}(\theta_M)$ for varying f at fixed α and β for "$-$ve tri" equilibrium with $\psi_N = 0.9$, $\theta_0 = 0$ (corresponding to the unfilled squares in figure 5.14). Left: $k_y\rho_r = 0.05$. Right: $k_y\rho_r = 0.0021$.

4. The mode amplitude is greatest in the bad curvature region and has twisting parity.
5. The mode preferentially occurs at long wavelength.
6. The mode structure and complex frequency are sensitive to α but not to kinetic gradients or β individually.

The $k_y\rho_r = 0.05$ instability found in the pedestal has all of these above properties, although γ is more sensitive to $(k_y\rho_r)$ at long wavelength (shown in figure 5.5). I speculate that this is a "non-ideal" KBM, destabilised by some kinetic effect(s), allowing it to slightly exceed the ideal boundary. The very-long wavelength ($k_y\rho_r = 0.0021$) mode is also pressure-driven and may be a TKBM.

5.7.2 Positive triangularity

This analysis is repeated for $(\psi_N = 0.5, k_y\rho_r = 0.05, \theta_0 = 0)$ for the "high $q0$" and "low $q0$" equilibria. Departures from the ideal MHD stability boundary are seen in $\hat{s} - \alpha$ space (figure 5.16), with the KBM smoothly extending across the IBM boundary into the second stability window. This smooth transition, is confirmed by a fine scan in $\hat{s}$ at fixed α (shown in figure 5.17).

Like the KBMs discussed in 5.7.1, the mode has a frequency in the ion diamagnetic direction and twisting parity. $E_{\|}$ is low, but rises smoothly as $\hat{s}$ leaves the IBM unstable region. Scanning $f \equiv \beta \cdot (1/T) \cdot (\partial T/\partial \psi_N)$ for "high $q0$" (shown in figure 5.18), again shows the mode to be α-driven. These features are also found for other flux surfaces sampled across the core, and for $k_y\rho_r = 0.5$ (f scan for $(\psi_N = 0.8, k_y\rho_r = 0.5)$ shown in figure 5.18). These observations support the conclusion that, although ideal ballooning stable, the dominant long-wavelength instability in these equilibria is a "non-ideal" KBM.

5.8 Sensitivity to $B_{1\|}$ fluctuations

An additional phenomenon common to "-ve tri" and the positive triangularity equilibria is that the KBMs are strongly stabilised by omitting $B_{1\|}$ fluctuations from the simulation ($B_{1\|} = 0$). This is illustrated by a gyrokinetic $(\hat{s} - \alpha)$ scan at fixed $\beta = 0.11$ (corresponding to the equilibrium β value) of the "high $q0$ $\psi_N = 0.5$ flux surface shown in figure 5.16 (bottom row): even over a wide range of $(\hat{s}, \alpha)$ the instability growth rate drops to $\gamma < 0.02$ and the dominant instability no longer tracks the IBM boundary. It is possible that the KBM is weakly unstable in these simulations, but the growth rate is reduced by an at least around an order of magnitude at the equilibrium $(\hat{s}, \alpha)$ compared with

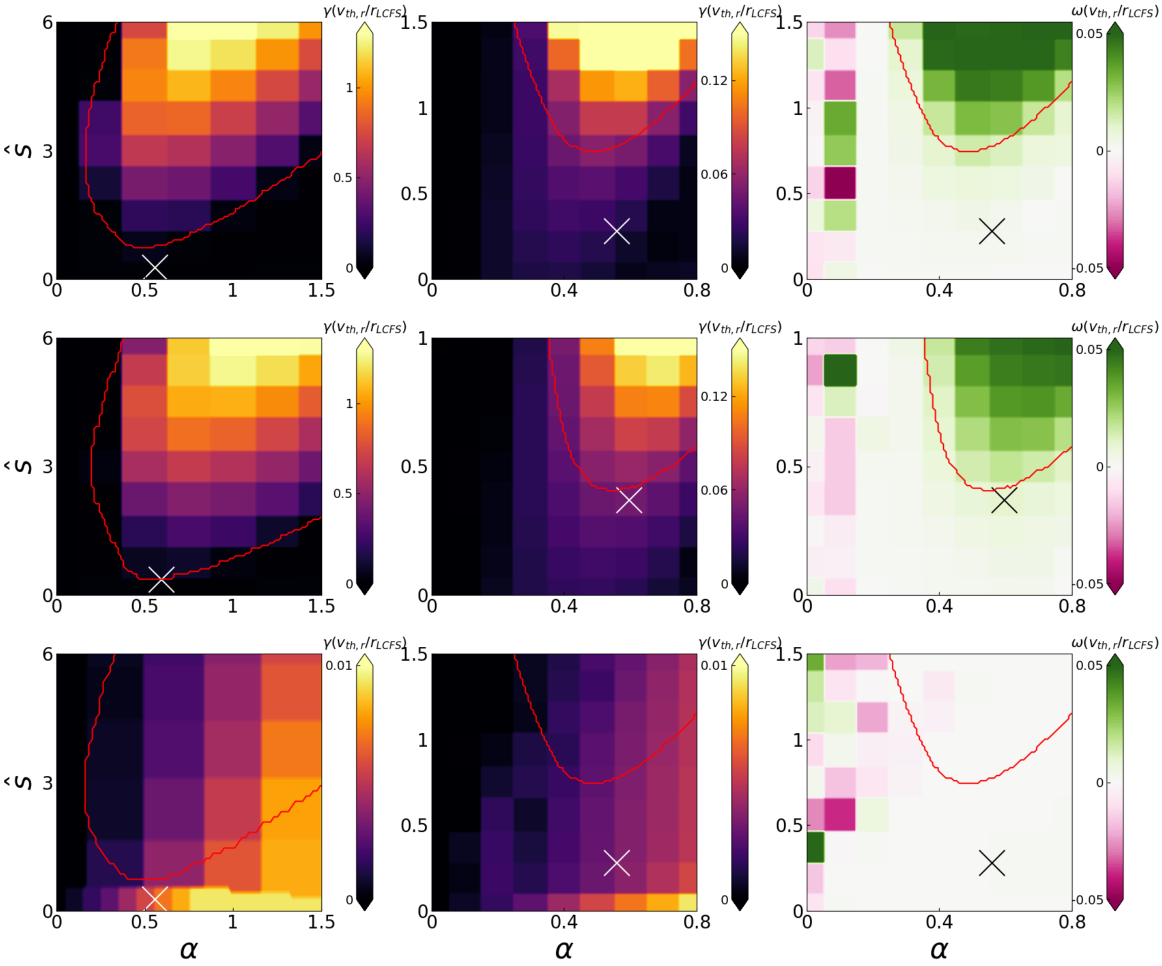

Figure 5.16: Gyrokinetic $\hat{s}-\alpha$ plots for the $\psi_N = 0.5$ surface for $k_y\rho_r = 0.05$, $\theta_0 = 0$ at fixed β. Left column shows $\gamma(\hat{s},\alpha)$ over a large range, middle column shows $\gamma(\hat{s},\alpha)$ over a small range and right column shows $\omega(\hat{s},\alpha)$ over a small range. Top row: "high $q0$". Middle row: "low $q0$"; $\gamma(\hat{s},\alpha)$. Bottom row: "high $q0$", but with $B_{1\parallel} = 0$ (note different colour scale). Simulations performed at fixed β. Crosses indicate equilibrium $\hat{s}$, α. Red contour shows IBM stability boundary.

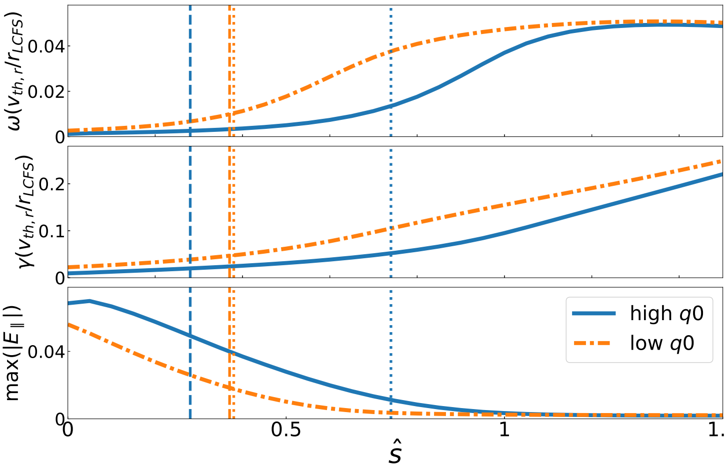

Figure 5.17: Upper: ω, γ, $\max(|\hat{E}_\parallel|)$ for the $\psi_N = 0.5$ flux surface for "high $q0$" and "low $q0$" ($k_y\rho_r = 0.05$, $\theta_0 = 0$) as $\hat{s}$ is scanned. Equilibrium $\hat{s}$ shown by vertical dashed lines and IBM marginal stability by vertical dotted lines.

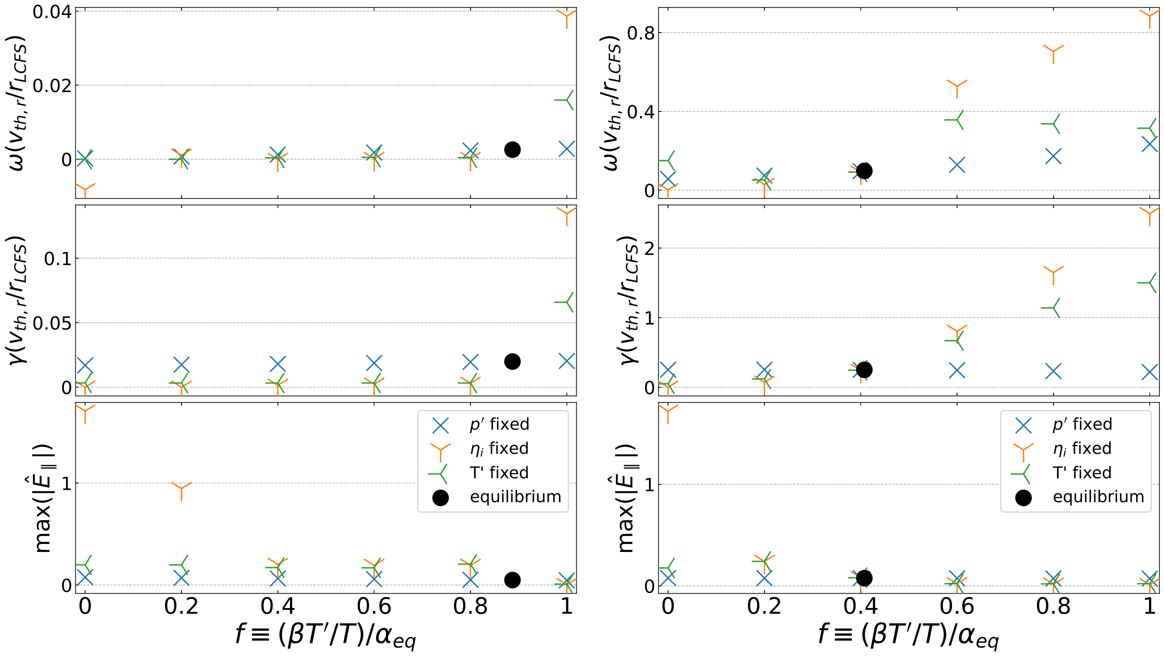

Figure 5.18: "high $q0$" equilibrium; ω, γ, $|\hat{E}_{\parallel}|$ as $f \equiv \beta \cdot (1/T) \cdot (\partial T/\partial \psi_N)$ is scanned. Left: $\psi_N = 0.5$, $k_y \rho_r = 0.05, \theta_0 = 0$. Right: $\psi_N = 0.8$, $k_y \rho_r = 0.5, \theta_0 = 0$.

the $B_{1\parallel} \neq 0$ scans. In these simulations, the geometry, including the magnetic drifts, retain finite-β corrections i.e. are the same between the $B_{1\parallel} = 0$ and $B_{1\parallel} \neq 0$ cases. The stabilising effect of $B_{1\parallel} = 0$ on KBMs is also demonstrated by Aleynikova *et al.* [79].

A reason for $B_{1\parallel} = 0$ having a stabilising effect for MHD-like modes is presented by Graves *et al.* [100] by considering its role in the "magnetic compression" term in δW (see eq. (4.2.18)). If $B_{1\parallel}$ is ignored then this term is minimised incorrectly which has a stabilising effect on pressure-driven modes. Graves *et al.* show this for IBMs in the analytic case of large A and small β, concluding the effect is small. However, these ST equilibria operate at low A, high β; by performing investigations with the cyclone base case (CBC) at varying β, I find that the stabilising effect of neglecting $B_{1\parallel}$ is greater at higher β. Thus, including $B_{1\parallel}$ fluctuations in simulations is important when modelling KBM stability in STs. This is worth emphasising since, as noted by Graves *et al.*, a number of gyrokinetic codes do not calculate $B_{1\parallel}$.

5.9 Concluding remarks

IBM stability is studied for three hypothetical ST equilibria, constructed with a commercial power-producing reactor in mind. In each equilibrium, α is sufficiently large that it exceeds the first stable region in $\hat{s} - \alpha$ space; the equilibrium is either in the unstable region or in the second stability window. In the negative triangularity case, the second stability window does not exist at positive magnetic shear, meaning the plasma is ideal ballooning unstable across the core; this coincides with strongly growing KBMs and indicates that this is unlikely to be a feasible equilibrium in the context of transport. By testing the dependency of second stability access on shaping parameters using a Miller fit, it is shown that second stability may be obtained either by making triangularity more positive, or reducing the elongation, but the latter requires a fairly extreme change to make $\hat{s}_{min} > 0$ (changing $\kappa = 3.3$ to $\kappa < 2$ for the $\psi_N = 0.5$ surface). Similarly, for the $\psi_N = 0.5$ surface the safety factor would need to increase from $q = 3.0$ to $q = 5.4$ to recover $\hat{s}_{min} > 0$. Tokamaks are able to achieve negative magnetic shear across regions of the core [101], but since $\hat{s}_{min} < 0$ across the entire plasma, tokamaks with reversed shear would be unable to alleviate the problem.

These results suggest that the KBM prohibits negative triangularity as an option in commercial STs unless they can be stabilised by flow shear. However, the amount of flow shear required for stabilisation is likely much larger than the diamagnetic level of flow shear, and would unlikely be achieved by external momentum injection in a commercial reactor.

The positive triangularity equilibria show better stability properties. In these, IBM second stability access exists across the plasma and, provided the on-axis safety factor is not too low, the equilibrium occupies the second stability window. Microinstability growth rates are correspondingly low. However, there remains a weakly growing instability with KBM-like properties, namely: pressure-driven, twisting parity, smoothly connecting to the “ideal MHD” KBM, low parallel electric field and, in some cases, the modes are pervasive at long wavelength. I speculate that the KBM is destabilised by kinetic effects. Being weakly growing, these could feasibly be stabilised by flow shear or may impose a soft β limit on STs. Identifying these effects would be an interesting area of future work, and may be necessary if one wished to build a predictive model of ST H-mode pedestals in a similar manner to EPED. Finally I note the importance of including $B_{1\|}$ fluctuations when studying microinstabilities in STs.

Chapter 6

Implementing and testing electromagnetic effects linearly in the `stella` code

6.1 Introduction

Chapter 5 illustrates the value of linear electromagnetic (EM) gyrokinetic simulations for informing the design of fusion power plants. Such simulations have huge potential for the optimisation of fusion plasmas.

However, several challenges face the gyrokinetic community. An unavoidable problem is the large number of instabilities which exist in fusion plasmas, many of which are not fully understood and may be difficult to capture in simulations. An example of this is a branch of the micro-tearing mode (MTM) which has a very extended structure along the field line [69, 102] and hence can be challenging to resolve.

Another issue is numerical difficulties which may be encountered in gyrokinetic codes, affecting their consistency, convergence, accuracy or numerical stability. A general feature of explicit codes for example is the Courant-Friedrichs-Lewy (CLF) condition [103]. This limits the timestep $\Delta\tilde{t}$ for explicit time-marching schemes, beyond which numerical instabilities cause the solution to unphysically blow up. The fluctuating magnetic field introduces additional terms into the EM GKE scaling with the species thermal velocity $v_{th,s} \sim m_s^{-1/2}$, which tends to make the CFL condition more restrictive in EM simulations (in which kinetic electrons are vital since they have the dominant contribution to δB).

More subtle numerical problems can be difficult to diagnose and remedy, since in general the gyrokinetic system of equations is five-dimensional, multiscale, integro-differential and nonlinear. Having a range of codes which can be applied to particular problems can therefore increase the robustness of the physical conclusions. If new codes are able to reduce the computational cost of simulation without loss of accuracy, so much the better.

To this end, I seek to implement electromagnetic effects in the code `stella` using both implicit and explicit numerical schemes. This provides a new tool by which electromagnetic turbulence in tokamaks and stellarators can be studied, and enables cross-code validation. `stella` is also ideally suited to experimenting with different numerical algorithms by virtue of its operator splitting scheme, which enables very flexible use of time-marching schemes. An additional benefit is that `stella` was designed (and is regularly used) to perform simulations for both axisymmetric and non-axisymmetric geometries. Relatively few other codes can perform electromagnetic stellarator simulations. These include `EUTERPE` [104], `GKV-X` [105], `GENE` [106], `Gkeyll` [107] and `GS2` [50]; the last three of these report electromagnetic results.

This code development falls into two categories. The first, the focus of this chapter, is to implement and benchmark linear EM effects in `stella`. I describe the simulation equations in section 6.2 and their implementation in section 6.3. I then perform a set of tests and benchmarks to verify and validate the code. These tests also give an indication of the computational cost of the different approaches. Some preliminary investigations of EM instabilities in the Wendelstein 7-X stellarator are presented in chapter 7.

The second is to treat the $\mathbf{E}\times\mathbf{B}$ nonlinearity using a semi-Lagrange scheme, in order to eliminate the CFL timestep constraint in nonlinear simulations. This is described in chapter 8.

6.2 Simulation Equations

6.2.1 Formulation in $\bar{g}_s$

The (collisionless) EM gyrokinetic equation (GKE) is eq. (2.2.46), reproduced here for convenience:

$$\frac{\partial h_s}{\partial t} + \left(\mathbf{v}_\parallel + \mathbf{v}_{Ms} + \langle \mathbf{v}_\chi \rangle_{\mathbf{X}_s}\right) \cdot \boldsymbol{\nabla}_{\mathbf{X}_s} h_s - \frac{\mu_s}{m_s} \mathbf{b} \cdot \boldsymbol{\nabla} B_0 \frac{\partial h_s}{\partial v_\parallel} + \langle \mathbf{v}_\chi \rangle_{\mathbf{X}_s} \cdot \boldsymbol{\nabla}\Big|_\epsilon F_{0s} - \frac{Z_s e}{T_s} F_{0s} \frac{\partial \langle \chi \rangle_{\mathbf{X}_s}}{\partial t} = 0. \tag{6.2.1}$$

In the electrostatic case, the term $\frac{Z_s e}{T_s} F_{0s} \frac{\partial \langle \varphi_1 \rangle_{\mathbf{X}_s}}{\partial t}$ is eliminated by defining a new distribution function $g_s \equiv h_s - \frac{Z_s e}{T_s} F_{0s} \langle \varphi_1 \rangle_{\mathbf{X}_s}$ (see section 3.3). Analogously, one could avoid $\frac{Z_s e}{T_s} F_{0s} \frac{\partial \langle \chi \rangle_{\mathbf{X}_s}}{\partial t}$ from explicitly appearing in the EM GKE by defining

$$\bar{g}_s \equiv h_s - \frac{Z_s e}{T_s} F_{0s} \langle \chi \rangle_{\mathbf{X}_s}, \tag{6.2.2}$$

(where $\langle \chi \rangle_{\mathbf{X}_s}$ is the gyrokinetic potential defined in eq. (2.2.47)) and writing the GKE in terms of $\bar{g}_s$:

$$\begin{aligned} &\frac{\partial \bar{g}_s}{\partial t} + v_{\parallel}(\mathbf{b} \cdot \boldsymbol{\nabla} z) \left(\frac{\partial \bar{g}_s}{\partial z} + \frac{Z_s e}{T_s} F_{0s} \frac{\partial \langle \chi \rangle_{\mathbf{X}_s}}{\partial z} \right) + \mathbf{v}_{Ms} \cdot \boldsymbol{\nabla}_{\mathbf{X}_s} \left(\bar{g}_s + \frac{Z_s e}{T_s} F_{0s} \langle \chi \rangle_{\mathbf{X}_s} \right) \\ &+ \langle \mathbf{v}_\chi \rangle_{\mathbf{X}_s} \cdot \boldsymbol{\nabla}_{\mathbf{X}_s} \bar{g}_s + \langle \mathbf{v}_\chi \rangle_{\mathbf{X}_s} \cdot \boldsymbol{\nabla} \Big|_{\epsilon} F_{0s} - \frac{\mu_s}{m_s} \mathbf{b} \cdot \boldsymbol{\nabla} B_0 \frac{\partial \bar{g}_s}{\partial v_{\parallel}} - \frac{\mu_s}{m_s} \mathbf{b} \cdot \boldsymbol{\nabla} B_0 \frac{Z_s e}{T_s} F_{0s} \left\langle A_{1\parallel} \right\rangle_{\mathbf{X}_s} = 0. \end{aligned} \tag{6.2.3}$$

The advantage of eq. 6.2.3 is that it allows the GKE to be split into equations of the form

$$\left(\frac{\partial \bar{g}_s}{\partial t} \right)_m + \mathcal{S}_m \left(\bar{g}_s, \langle \varphi_1 \rangle_{\mathbf{X}_s}, \left\langle A_{1\parallel} \right\rangle_{\mathbf{X}_s}, \left\langle B_{1\parallel} \right\rangle_{\mathbf{X}_s} \right) = 0, \tag{6.2.4}$$

where $\mathcal{S}_m$ is a source term with no explicit time dependence. This approach is implemented in `stella`, but is found to have slow convergence with n_z (i.e. parallel resolution) at moderate β when benchmarked against `GS2`.

An example of this behaviour is shown in figure 6.1. In this fully electromagnetic benchmark, β is scanned at fixed geometry (with $\beta' = 0$ used in the calculation of geometric quantities) for the cyclone base case (CBC) [70] for wavenumber $\tilde{k}_x = 0$, $\tilde{k}_y = 0.5$. The left plot of figure 6.1 shows the normalised complex frequency ($\tilde{\Omega}(\beta) \equiv \Omega a / v_{th,r}$) for two `GS2` simulations (differing only in parallel fidelity) and a range of parallel resolutions for the `stella` implementation (all of which evaluate the source terms using the SSP RK3 algorithm). All scans show the usual ITG-KBM transition seen elsewhere (e.g. [78]). In the right plot, $\tilde{\Omega}$ values for all simulations are compared with the higher-fidelity `GS2` simulation, which is used as a fiducial simulation.

Figure 6.1 (right) shows the `GS2` simulation to be reasonably converged in (n_{period}, n_z) for values ($n_{\text{period}} = 2$, $n_z = 32$), with $\tilde{\omega}$ and $\tilde{\gamma}$ changing by $\leq 10\%$ and $\leq 2\%$ respectively as fidelity is increased (and by $\Delta\tilde{\omega} \leq 2\%$ and $\Delta\tilde{\gamma} \leq 0.5\%$ for $\beta \geq 0.02$). In contrast, `stella` shows serious disagreement in the KBM region for the same parallel simulation parameters (with $\Delta\tilde{\gamma} \geq 20\%$ in the KBM region). Good agreement is recovered in the limit that n_z becomes large, but it is surprising that such high resolution is required for the CBC geometry (which is a circular, large-aspect ratio flux surface).

I argue the reason for this slow convergence is as follows. Examining the mass- and β-dependence of terms in eq. (6.2.1), one finds

$$\begin{aligned}
&\overbrace{\frac{\partial h_s}{\partial t}}^{\sim\tilde{m}_s^0} + (\overbrace{\mathbf{v}_\parallel}^{\sim\tilde{m}_s^{-1/2}} + \overbrace{\mathbf{v}_{Ms}}^{\sim\tilde{m}_s^0} + \overbrace{\langle \mathbf{v}_\chi \rangle_{\mathbf{X}_s}}^{\sim\tilde{m}_s^{-1/2}\beta}) \cdot \overbrace{\nabla_{\mathbf{X}_s} h_s}^{\sim\tilde{m}_s^0} - \overbrace{\frac{\mu_s}{m_s}\mathbf{b}\cdot\nabla B_0 \frac{\partial h_s}{\partial v_\parallel}}^{\sim\tilde{m}_s^{-1/2}} \\
&+ \overbrace{\langle \mathbf{v}_\chi \rangle_{\mathbf{X}_s} \cdot \nabla\Big|_\epsilon F_{0s}}^{\sim\tilde{m}_s^{-1/2}\beta} - \overbrace{\frac{Z_s e}{T_s} F_{0s} \frac{\partial \langle \chi \rangle_{\mathbf{X}_s}}{\partial t}}^{\sim\tilde{m}_s^{-1/2}\beta} = 0, \qquad (6.2.5)
\end{aligned}$$

where the β-related terms arise from the $A_{1\parallel}$ component of $\langle \chi \rangle_{\mathbf{X}_s}$: $(-v_\parallel \langle A_{1\parallel} \rangle_{\mathbf{X}_s}) \sim \beta v_{th,s} \sim \beta \tilde{m}_s^{-1/2}$, where the scaling $A_{1\parallel} \sim \beta$ is based on the heuristic argument given in section 2.4. Here, the most extreme mass scaling is $\tilde{m}_s^{-1/2}$. In the $\bar{g}_s$ formulation, $\bar{g}_s \sim (\tilde{m}_s^{-1/2}\beta)$ from the $A_{1\parallel}$ term and so the electromagnetic components of eq. (6.2.3) scale as:

$$\begin{aligned}
&\overbrace{\frac{\partial \bar{g}_s}{\partial t}}^{\sim\tilde{m}_s^{-1/2}\beta} + \overbrace{v_\parallel (\mathbf{b}\cdot\nabla z) \frac{\partial \bar{g}_s}{\partial z}}^{\tilde{m}_s^{-1}\beta} + \overbrace{v_\parallel (\mathbf{b}\cdot\nabla z) \frac{Z_s e}{T_s} F_{0s} \frac{\partial \langle \chi \rangle_{\mathbf{X}_s}}{\partial z}}^{\tilde{m}_s^{-1}\beta} \\
&+ \overbrace{\mathbf{v}_{Ms} \cdot \nabla_{\mathbf{X}_s} \left(\bar{g}_s + \frac{Z_s e}{T_s} F_{0s} \langle \chi \rangle_{\mathbf{X}_s} \right)}^{\sim\tilde{m}_s^{-1/2}\beta} + \overbrace{\langle \mathbf{v}_\chi \rangle_{\mathbf{X}_s} \cdot \nabla_{\mathbf{X}_s} \bar{g}_s}^{\sim\tilde{m}_s^{-1}\beta} + \overbrace{\langle \mathbf{v}_\chi \rangle_{\mathbf{X}_s} \cdot \nabla\Big|_\epsilon F_{0s}}^{\sim\tilde{m}_s^{-1/2}\beta} \\
&- \overbrace{\frac{\mu_s}{m_s}\mathbf{b}\cdot\nabla B_0 \frac{\partial \bar{g}_s}{\partial v_\parallel}}^{\sim\tilde{m}_s^{-1}\beta} - \overbrace{\frac{\mu_s}{m_s}\mathbf{b}\cdot\nabla B_0 \frac{Z_s e}{T_s} F_{0s} \langle A_{1\parallel} \rangle_{\mathbf{X}_s}}^{\sim\tilde{m}_s^{-1}\beta} = 0, \qquad (6.2.6)
\end{aligned}$$

where terms in blue have a mass scaling of $\tilde{m}_s^{-1}$. By making the change of variable $h_s \to \bar{g}_s$, artificial large terms are introduced into the GKE; terms in blue become unphysically large when electrons are simulated and β is sufficiently large. One then requires all $\sim \tilde{m}_s^{-1}$ terms to cancel to leading order, leaving behind terms of size $\sim \tilde{m}_s^{-1/2}$. However, these terms contain finite difference derivatives (over $z, v_\parallel$) which, for reasons of numerical stability, are not all computed in the same way. This leads to inexact numerical cancellation and hence inaccuracy in the solution, which becomes worse with increasing β. Convergence at high resolution is achieved as the derivatives become more accurate.

The slowness of convergence with n_z increases computational cost in two ways. Firstly, increasing n_z increases the cost per timestep since more points are simulated. Secondly, if the parallel

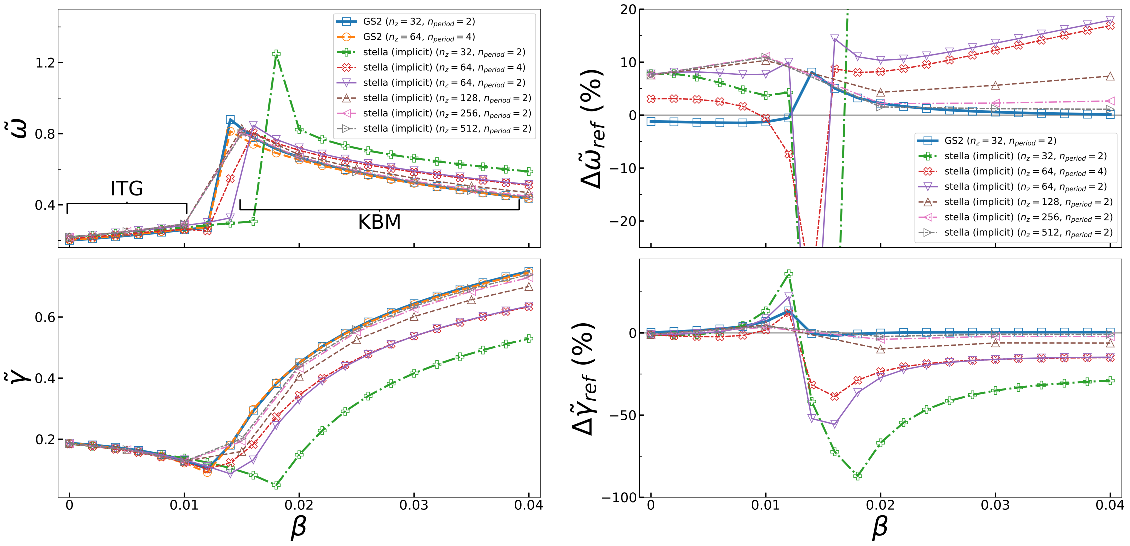

Figure 6.1: Benchmark of electromagnetic `stella` implementation with the source terms formulated in $\tilde{\bar{g}}_{\mathbf{k},s}$ (eq. (6.2.3). Left: frequency $\tilde{\omega}$ and growth rate $\tilde{\gamma}$ for CBC β scan at fixed geometry with $k_y\rho_i = 0.5$ Left: . Right: $\%$ difference in $\tilde{\omega}, \tilde{\gamma}$ compared to the `GS2` simulation with higher n_z, n_{period} (see table 3.1 for definitions of n_z, n_{period}).

streaming source term is calculated explicitly, increasing n_z makes the CFL condition more restrictive (since Δz is reduced). If this forces a smaller timestep, n_{step} must increase for a given amount of simulation time.

The shortfalls of the "$\bar{g}_s$ formulation" motivate an alternative approach, which is described in the next section.

6.2.2 A "mixed" formulation in $\bar{g}_s$ and h_s

This approach uses $\bar{g}_s$ to remove $\frac{\partial\langle\chi\rangle_{\mathbf{X}_s}}{\partial t}$ but keeps the remaining source terms in h_s:

$$\overbrace{\frac{\partial \bar{g}_s}{\partial t}}^{\sim\tilde{m}_s^{-1/2}\beta} + (\overbrace{\mathbf{v}_\parallel}^{\sim\tilde{m}_s^{-1/2}} + \overbrace{\mathbf{v}_{Ms}}^{\sim\tilde{m}_s^{0}} + \overbrace{\langle \mathbf{v}_\chi\rangle_{\mathbf{X}_s}}^{\sim\tilde{m}_s^{-1/2}\beta}) \cdot \overbrace{\boldsymbol{\nabla}_{\mathbf{X}_s} h_s}^{\sim\tilde{m}_s^{0}} - \overbrace{\frac{\mu_s}{m_s}\mathbf{b}\cdot\boldsymbol{\nabla}B_0\frac{\partial h_s}{\partial v_\parallel}}^{\sim\tilde{m}_s^{-1/2}}$$
$$+ \underbrace{\langle \mathbf{v}_\chi\rangle_{\mathbf{X}_s}\cdot\boldsymbol{\nabla}\Big|_\epsilon F_{0s}}_{\sim\tilde{m}_s^{-1/2}\beta} = 0 \tag{6.2.7}$$

(for which no terms scale like $\tilde{m}_s^{-1}$). Applying the Fourier transform and normalisations, the simulation GKE is

$$\frac{\partial \tilde{\bar{g}}_{\mathbf{k},s}}{\partial \tilde{t}} + \tilde{v}_{\parallel}\tilde{v}_{th,s}(\mathbf{b}\cdot\tilde{\boldsymbol{\nabla}} z)\frac{\partial \tilde{h}_{\mathbf{k},s}}{\partial z} + i\tilde{\omega}_{ds\mathbf{k}}\tilde{h}_{\mathbf{k},s} + \mathcal{N}_{\mathbf{k},\mathrm{EM}} + i\omega_{*k}\left\langle \tilde{\chi}_{\mathbf{k}} \right\rangle_{\mathbf{X}_s} - \tilde{v}_{th,s}\tilde{\mu}_s\left(\mathbf{b}\cdot\tilde{\boldsymbol{\nabla}}\tilde{B}_0\right)\frac{\partial \tilde{h}_{\mathbf{k},s}}{\partial \tilde{v}_{\parallel}} = 0, \tag{6.2.8}$$

where

$$\tilde{\bar{g}}_{\mathbf{k},s} = \frac{\bar{g}_{\mathbf{k},s}}{F_{0s}}\exp\left(-\tilde{v}_s^2\right)\frac{a}{\rho_r} = \tilde{h}_{\mathbf{k},s} - \frac{Z_s}{\tilde{T}_s}\exp\left(-\tilde{v}_s^2\right)\left\langle \tilde{\chi}_{\mathbf{k}} \right\rangle_{\mathbf{X}_s}, \tag{6.2.9}$$

$$\left\langle \tilde{\chi}_{\mathbf{k}} \right\rangle_{\mathbf{X}_s} = \left[J_0(\gamma_s)\tilde{\varphi}_{1\mathbf{k}} - 2\tilde{v}_{\parallel}\tilde{v}_{th,s}J_0(\gamma_s)\tilde{A}_{1\parallel\mathbf{k}} - 4\tilde{\mu}_s\frac{\tilde{T}_s}{Z}\frac{J_1(\gamma_s)}{\gamma_s}\tilde{B}_{1\parallel\mathbf{k}} \right], \tag{6.2.10}$$

$$\tilde{A}_{1\parallel\mathbf{k}} = A_{1\parallel\mathbf{k}}\frac{a}{B_r\rho_r^2} = A_{1\parallel\mathbf{k}}\frac{1}{B_r\rho_*\rho_r} \tag{6.2.11}$$

$$\tilde{B}_{1\parallel\mathbf{k}} = B_{1\parallel\mathbf{k}}\frac{a}{B_r\rho_r} = B_{1\parallel\mathbf{k}}\frac{1}{B_r\rho_*}, \tag{6.2.12}$$

$$\begin{aligned}\mathcal{N}_{\mathbf{k},\mathrm{EM}} = \frac{B_r}{2}\frac{dy}{d\alpha}\frac{dx}{d\psi}\mathcal{F}_{\mathbf{k}}\Big[&\mathcal{F}_{\mathbf{k}}^{-1}\left[i\tilde{k}_y\left\langle \tilde{\chi}_{\mathbf{k}} \right\rangle_{\mathbf{X}_s}\right]\mathcal{F}_{\mathbf{k}}^{-1}\left[i\tilde{k}_x\tilde{h}_{\mathbf{k},s}\right] \\ &- \mathcal{F}_{\mathbf{k}}^{-1}\left[i\tilde{k}_x\left\langle \tilde{\chi}_{\mathbf{k}} \right\rangle_{\mathbf{X}_s}\tilde{\varphi}_{1\mathbf{k}}\right]\mathcal{F}_{\mathbf{k}}^{-1}\left[i\tilde{k}_y\tilde{h}_{\mathbf{k},s}\right]\Big].\end{aligned} \tag{6.2.13}$$

(NB the implementation and testing of the EM nonlinearity $\mathcal{N}_{\mathbf{k},\mathrm{EM}}$ is still in progress). It is worth noting that there is a factor 2 difference in the normalisation of $\tilde{A}_{1\parallel\mathbf{k}}$ between `stella` and `GS2`. In the benchmarking results later shown, $\tilde{A}_{1\parallel\mathbf{k}}$ is reported using `stella`'s normalisation.

6.2.3 Field equations

As shall be seen, implementing eq. (6.2.8) using implicit numerical schemes requires the field solve calculations to be performed when the distribution function is expressed in either $\tilde{\bar{g}}_{\mathbf{k},s}$ (to update the fields after $\tilde{\bar{g}}_{\mathbf{k},s}$ is updated explicitly) or $\tilde{h}_{\mathbf{k},s}$ (to update the fields in implicit schemes, before $\tilde{\bar{g}}_{\mathbf{k},s}$ is updated). The simulation field equations in $\tilde{\tilde{g}}_{\mathbf{k},s}$ are:

Quasi-neutrality:

$$\sum_s Z_s\tilde{n}_s\left(\frac{2\tilde{B}_0}{\sqrt{\pi}}\int d\tilde{v}_\parallel d\tilde{\mu}_s J_0(\gamma_s)\tilde{\tilde{g}}_{\mathbf{k},s}+\frac{Z_s}{\tilde{T}_s}(\Gamma_0(b_s)-1)\tilde{\varphi}_{1\mathbf{k}}+\frac{1}{\tilde{B}_0}\Gamma_1(b_s)\tilde{B}_{1\parallel\mathbf{k}}\right)=0, \tag{6.2.14}$$

Parallel Ampére's law:

$$\left(1-\frac{\beta}{(k_\perp\rho_r)^2}\sum_s\frac{Z_s^2\tilde{n}_s}{\tilde{m}_s}\Gamma_0(b_s)\right)\tilde{A}_{1\parallel\mathbf{k}}=-\frac{\beta}{(k_\perp\rho_r)^2}\frac{2}{\sqrt{\pi}}\tilde{B}_0\sum_s Z_s\tilde{n}_s\tilde{v}_{th,s}\int d\tilde{v}_\parallel d\tilde{\mu}_s J_0(\gamma_s)\tilde{v}_\parallel\tilde{\tilde{g}}_{\mathbf{k},s}, \tag{6.2.15}$$

Perpendicular Ampére's law:

$$\left(\frac{\beta}{2\tilde{B}_0}\sum_s Z_s\tilde{n}_s\Gamma_1(b_s)\right)\tilde{\varphi}_{1\mathbf{k}}+\left(1+\frac{\beta}{2\tilde{B}_0}\sum_s Z_s\tilde{n}_s\tilde{T}_s\Gamma_2(b_s)\right)\tilde{B}_{1\parallel\mathbf{k}}=$$
$$\frac{-4\beta\tilde{B}_0}{\sqrt{\pi}}\sum_s\tilde{n}_s\tilde{T}_s\int d\tilde{v}_\parallel d\tilde{\mu}_s\tilde{\mu}_s\frac{J_1(\gamma_s)}{\gamma_s}\tilde{\tilde{g}}_{\mathbf{k},s}, \tag{6.2.16}$$

where $\Gamma_0(b_s)=I_0(b_s)e^{-b_s}$, $\Gamma_1(b_s)=(I_0(b_s)-I_1(b_s))e^{-b_s}$, $I_{0,1}$ are modified Bessel functions of the first kind (these identities are given by Howes *et al.* [108]), $b_s=\tilde{k}_\perp^2/2$ and I define $\beta=\frac{8\pi n_r T_r}{B_r^2}$. The simulation field equations in $\tilde{h}_{\mathbf{k},s}$ are:

$$\text{Quasi-neutrality: }\sum_s Z_s\tilde{n}_s\left(\frac{2\tilde{B}_0}{\sqrt{\pi}}\int d\tilde{v}_\parallel d\tilde{\mu}_s J_0(\gamma_s)\tilde{h}_{\mathbf{k},s}-\frac{Z_s}{\tilde{T}_s}\tilde{\varphi}_{1\mathbf{k}}\right)=0, \tag{6.2.17}$$

$$\text{Parallel Ampére's law: }\tilde{A}_{1\parallel\mathbf{k}}=-\frac{\beta}{(k_\perp\rho_r)^2}\frac{2}{\sqrt{\pi}}\tilde{B}_0\sum_s Z_s\tilde{n}_s\tilde{v}_{th,s}\int d\tilde{v}_\parallel d\tilde{\mu}_s J_0(\gamma_s)\tilde{v}_\parallel\tilde{h}_{\mathbf{k},s}, \tag{6.2.18}$$

$$\text{Perpendicular Ampére's law: }\tilde{B}_{1\parallel\mathbf{k}}=\frac{-4\beta\tilde{B}_0}{\sqrt{\pi}}\sum_s\tilde{n}_s\tilde{T}_s\int d\tilde{v}_\parallel d\tilde{\mu}_s\tilde{\mu}_s\frac{J_1(\gamma_s)}{\gamma_s}\tilde{h}_{\mathbf{k},s}. \tag{6.2.19}$$

Like GS2, the field equations for $\tilde{\varphi}_{1\mathbf{k}}$ and $\tilde{B}_{1\parallel\mathbf{k}}$ are coupled in the $\tilde{\tilde{g}}_{\mathbf{k},s}$ simulation equations.

6.3 Implementation details

The implementation described here (and results presented) correspond to the `stella` commit `f5355ba`.

6.3.1 Field solve

Firstly, I implement the subroutines required to solve the normalised field equations. eqs. (6.2.14) to (6.2.16) can be symbolically written as a matrix equation:

$$\begin{pmatrix} K_{11} & 0 & K_{13} \\ 0 & K_{22} & 0 \\ K_{31} & 0 & K_{33} \end{pmatrix} \begin{pmatrix} \tilde{\varphi}_{1\mathbf{k}} \\ \tilde{A}_{1\|\mathbf{k}} \\ \tilde{B}_{1\|\mathbf{k}} \end{pmatrix} \equiv \underline{\underline{K}}\mathbf{f} = \begin{pmatrix} l_1(\tilde{\bar{g}}_{\mathbf{k},s}) \\ l_2(\tilde{\bar{g}}_{\mathbf{k},s}) \\ l_3(\tilde{\bar{g}}_{\mathbf{k},s}) \end{pmatrix} \equiv \mathbf{l}(\tilde{\bar{g}}_{\mathbf{k},s}), \tag{6.3.1}$$

where

$$\mathbf{f} = \begin{pmatrix} \tilde{\varphi}_{1\mathbf{k}} \\ \tilde{A}_{1\|\mathbf{k}} \\ \tilde{B}_{1\|\mathbf{k}} \end{pmatrix}. \tag{6.3.2}$$

K_{XX} represents a time-independent integral over velocity and species, and $l_X(\tilde{\bar{g}}_{\mathbf{k},s})$ represents an integral of $\tilde{\bar{g}}_{\mathbf{k},s}$ over velocity and species. This can be solved as

$$\mathbf{f} = \underline{\underline{K}}^{-1}\mathbf{l}(\tilde{\bar{g}}_{\mathbf{k},s}) \equiv \underline{\underline{J}}\mathbf{l}(\tilde{\bar{g}}_{\mathbf{k},s}), \tag{6.3.3}$$

or, explicitly,

$$\tilde{\varphi}_{1\mathbf{k}} = \frac{l_1(\tilde{\bar{g}}_{\mathbf{k},s}) - (K_{13}/K_{33}) \cdot l_3(\tilde{\bar{g}}_{\mathbf{k},s})}{K_{11} - (K_{13} \cdot K_{31}/K_{33})} \tag{6.3.4}$$

$$\tilde{A}_{1\|\mathbf{k}} = \frac{l_2(\tilde{\bar{g}}_{\mathbf{k},s})}{K_{22}} \tag{6.3.5}$$

$$\tilde{B}_{1\|\mathbf{k}} = \frac{l_3(\tilde{\bar{g}}_{\mathbf{k},s}) - (K_{31}/K_{11}) \cdot l_1(\tilde{\bar{g}}_{\mathbf{k},s})}{K_{33} - (K_{13} \cdot K_{31}/K_{11})}, \tag{6.3.6}$$

where

$$K_{11} = \sum_s \frac{Z_s^2 \tilde{n}_s}{\tilde{T}_s} \cdot \frac{2\tilde{B}_0}{\sqrt{\pi}} \int d\tilde{v}_\parallel d\tilde{\mu}_s \left(\exp\left(-\tilde{v}_s^2\right) \left[1 - J_0(\gamma_s)^2\right]\right) \tag{6.3.7}$$

$$K_{13} = -4 \sum_s Z_s \tilde{n}_s \cdot \frac{2\tilde{B}_0}{\sqrt{\pi}} \int d\tilde{v}_\parallel d\tilde{\mu}_s \left(\exp\left(-\tilde{v}_s^2\right) \tilde{\mu}_s J_0(\gamma_s) \frac{J_1(\gamma_s)}{\gamma_s}\right) \tag{6.3.8}$$

$$K_{22} = \tilde{k}_\perp^2 + 2\beta_0 \sum_s \frac{Z_s^2 \tilde{n}_s}{\tilde{m}_s} \cdot \frac{2\tilde{B}_0}{\sqrt{\pi}} \int d\tilde{v}_\parallel d\tilde{\mu}_s \left(\exp\left(-\tilde{v}_s^2\right) \tilde{v}_\parallel^2 J_0(\gamma_s)^2\right) \tag{6.3.9}$$

$$K_{31} = 2\beta_0 \sum_s Z_s \tilde{n}_s \cdot \frac{2\tilde{B}_0}{\sqrt{\pi}} \int d\tilde{v}_\parallel d\tilde{\mu}_s \left(\exp\left(-\tilde{v}_s^2\right) \tilde{\mu}_s J_0(\gamma_s) \frac{J_1(\gamma_s)}{\gamma_s}\right) \tag{6.3.10}$$

$$K_{33} = 1 + 8\beta_0 \sum_s \tilde{T}_s \tilde{n}_s \cdot \frac{2\tilde{B}_0}{\sqrt{\pi}} \int d\tilde{v}_\parallel d\tilde{\mu}_s \left(\exp\left(-\tilde{v}_s^2\right) \tilde{\mu}_s^2 \left(\frac{J_1(\gamma_s)}{\gamma_s}\right)^2\right) \tag{6.3.11}$$

$$l_1(\tilde{\bar{g}}_{\mathbf{k},s}) = \sum_s Z_s \tilde{n}_s \cdot \frac{2\tilde{B}_0}{\sqrt{\pi}} \int d\tilde{v}_\parallel d\tilde{\mu}_s \left(\bar{g}_{\mathbf{k},s} J_0(\gamma_s)\right) \tag{6.3.12}$$

$$l_2(\tilde{\bar{g}}_{\mathbf{k},s}) = \beta_0 \sum_s Z_s \tilde{n}_s \tilde{v}_{th,s} \cdot \frac{2\tilde{B}_0}{\sqrt{\pi}} \int d\tilde{v}_\parallel d\tilde{\mu}_s \left(\tilde{\bar{g}}_{\mathbf{k},s} \tilde{v}_\parallel J_0(\gamma_s)\right) \tag{6.3.13}$$

$$l_3(\tilde{\bar{g}}_{\mathbf{k},s}) = -2\beta_0 \sum_s \tilde{n}_s \tilde{T}_s \cdot \frac{2\tilde{B}_0}{\sqrt{\pi}} \int d\tilde{v}_\parallel d\tilde{\mu}_s \left(\tilde{\bar{g}}_{\mathbf{k},s} \tilde{\mu}_s \frac{J_1(\gamma_s)}{\gamma_s}\right). \tag{6.3.14}$$

K_{XX} are time-independent and are calculated once, at the start of the simulation. $l_X(\tilde{\bar{g}}_{\mathbf{k},s})$ are calculated each time the field solve subroutine (`advance_fields`) is called.

It should be noted that the $\tilde{\bar{g}}_{\mathbf{k},s}$ formulation risks a well-known cancellation problem at long wavelengths, known as the Ampére cancellation problem [107]. The cause of this can be seen from comparing equations (6.2.15) and (6.2.18); the second term on the LHS of (6.2.15) should cancel with the $\frac{Z_s}{\tilde{T}_s} \exp\left(-\tilde{v}_s^2\right) \langle \tilde{\chi}_\mathbf{k} \rangle_{\mathbf{X}_s}$ term appearing in the integral on the RHS to reduce to (6.2.18). However, this term becomes much larger than the first term on the LHS when $\tilde{k}_\perp$ is small, and so small errors from inexact cancellation lead to a large error in $\tilde{A}_{1\parallel\mathbf{k}}$. However, promisingly, large errors in the $\tilde{\bar{g}}_{\mathbf{k},s}$ field solve at long wavelength are not observed in the field solve tests.

The field equations in $\tilde{h}_{\mathbf{k},s}$ in `stella` notation are:

$$\underline{\underline{K}}_h \mathbf{f} = \mathbf{l}(\tilde{h}_{\mathbf{k},s}), \tag{6.3.15}$$

or, explicitly:

$$\tilde{\varphi}_{1\mathbf{k}} = \frac{l_1(\tilde{h}_{\mathbf{k},s})}{K_{11,h}} \tag{6.3.16}$$

$$\tilde{A}_{1\|\mathbf{k}} = \frac{l_2(\tilde{h}_{\mathbf{k},s})}{K_{22,h}} \tag{6.3.17}$$

$$\tilde{B}_{1\|\mathbf{k}} = \frac{l_3(\tilde{h}_{\mathbf{k},s})}{K_{33,h}} \tag{6.3.18}$$

where

$$K_{11,h} = \sum_s \frac{Z_s^2 \tilde{n}_s}{\tilde{T}_s} \cdot \frac{2\tilde{B}_0}{\sqrt{\pi}} \int d\tilde{v}_{\|} d\tilde{\mu}_s \exp\bigl(-\tilde{v}_s^2\bigr); \qquad K_{22,h} = \tilde{k}_\perp^2; \qquad K_{33,h} = 1, \tag{6.3.19}$$

where the integral required to calculate $K_{11,h}$ is performed numerically (rather than analytically) to ensure consistency with the calculation of K_{11}.

6.3.2 Explicit source terms

The implementation of the source terms explicitly in `stella` is relatively straightforward, with code changes falling into two categories:

1. The replacement of the distribution function $\tilde{g}_{\mathbf{k},s}$ with $\tilde{h}_{\mathbf{k},s}$. These changes are:
   1.1. Making the replacement $\frac{\partial \tilde{g}_{\mathbf{k},s}}{\partial z} + \frac{Z}{T} e^{-\tilde{v}_s^2} \frac{\partial \tilde{\varphi}_{1\mathbf{k}}}{\partial z} \rightarrow \frac{\partial \tilde{h}_{\mathbf{k},s}}{\partial z}$ in the parallel streaming source term.
   1.2. Making the replacement $\tilde{g}_{\mathbf{k},s} + \frac{Z}{T} e^{-\tilde{v}_s^2} \tilde{\varphi}_{1\mathbf{k}} \rightarrow \tilde{h}_{\mathbf{k},s}$ in the magnetic drift source term.
   1.3. Making the replacement $\frac{\partial \tilde{g}_{\mathbf{k},s}}{\partial \tilde{v}_{\|}} \rightarrow \frac{\partial \tilde{h}_{\mathbf{k},s}}{\partial \tilde{v}_{\|}}$ in the mirror term.
2. Making the replacement $\langle \tilde{\varphi}_{1\mathbf{k}} \rangle_{\mathbf{X}_s} \rightarrow \langle \tilde{\chi}_{\mathbf{k}} \rangle_{\mathbf{X}_s}$ in the driving (diamagnetic-like) term and the nonlinear term.

6.3.3 Implicit streaming and mirror terms

A fully explicit implementation is sufficient, but the timestep is restricted by the Courant-Friedrichs-Lewy (CFL) condition (discussed in greater detail in section 8.2) for each source term. To partially circumvent this, I implement implicit schemes for the streaming and mirror terms, which are found to have the most restrictive timestep constraint in the CBC benchmarking simulations. To treat the streaming and mirror terms implicitly, (6.2.8) is split as follows:

$$\left(\frac{\partial \tilde{\bar{g}}_{\mathbf{k},s}}{\partial \tilde{t}}\right)_1 + \tilde{v}_\parallel \tilde{v}_{th,s}(\mathbf{b}\cdot\tilde{\boldsymbol{\nabla}} z)\frac{\partial \tilde{h}_{\mathbf{k},s}}{\partial z} = 0, \tag{6.3.20}$$

$$\left(\frac{\partial \tilde{\bar{g}}_{\mathbf{k},s}}{\partial \tilde{t}}\right)_2 - \tilde{v}_{th,s}\tilde{\mu}_s\left(\mathbf{b}\cdot\tilde{\boldsymbol{\nabla}}\tilde{B}_0\right)\frac{\partial \tilde{h}_{\mathbf{k},s}}{\partial \tilde{v}_\parallel} = 0, \tag{6.3.21}$$

$$\left(\frac{\partial \tilde{\bar{g}}_{\mathbf{k},s}}{\partial \tilde{t}}\right)_3 + i\tilde{\omega}_{ds\mathbf{k}}\tilde{h}_{\mathbf{k},s} + \mathcal{N}_{\mathbf{k},\mathrm{EM}} + i\omega_{*k}\left\langle\tilde{\chi}_{\mathbf{k}}\right\rangle_{\mathbf{X}_s} = 0. \tag{6.3.22}$$

Compared to the implicit streaming algorithm described in section 3.10, the EM implicit streaming algorithm requires all three fields to be included in the response matrix calculation (similar to that done in `GS2`). This is described in section 6.3.3.1.

One also requires a response matrix approach for the electromagnetic mirror term, since the simulation equation with source term in $\tilde{h}_{\mathbf{k},s}$ (eq. (6.3.21)) is no longer simple advection; the updated fields are required to update $\tilde{\bar{g}}_{\mathbf{k},s}$. This is described briefly in section 6.3.3.2.

Making the remaining terms in the GKE implicit would be a relatively straightforward piece of future work. In the benchmarking simulations presented in section 6.4.3, the CFL constraint arising from these terms is found to restrict $\Delta\tilde{t}$ by around an order of magnitude between simulations with $n_{\text{period}} = 2$ and $n_{\text{period}} = 4$ (the latter being more restrictive as $k_\perp$ increases with z), so the savings realised by this could be significant when a large parallel simulation domain is required.

6.3.3.1 The electromagnetic implicit streaming algorithm

Beginning with the streaming equation:

$$\frac{\partial \tilde{\bar{g}}_{\mathbf{k},s}}{\partial \tilde{t}} + \tilde{v}_\parallel \tilde{v}_{th,s}(\mathbf{b}\cdot\tilde{\boldsymbol{\nabla}} z)\frac{\partial \tilde{h}_{\mathbf{k},s}}{\partial z} = 0, \tag{6.3.23}$$

I replace $\tilde{g}_{\mathbf{k},s} \rightarrow \tilde{h}_{\mathbf{k},s} - \frac{Z}{T}e^{-\tilde{v}_s^2}\left\langle\tilde{\chi}_{\mathbf{k}}\right\rangle_{\mathbf{X}_s}$ and temporally discretise to arrive at

$$\frac{\tilde{h}^{n+1}_{\mathbf{k},s} - \tilde{h}^{n}_{\mathbf{k},s} - \frac{Z}{T}e^{-\tilde{v}_s^2}\left(\left\langle\tilde{\chi}_{\mathbf{k}}\right\rangle^{n+1}_{\mathbf{X}_s} - \left\langle\tilde{\chi}_{\mathbf{k}}\right\rangle^{n}_{\mathbf{X}_s}\right)}{\Delta\tilde{t}} + \tilde{v}_{\|}\tilde{v}_{th,s}(\mathbf{b}\cdot\tilde{\boldsymbol{\nabla}}z)\left(\frac{\partial\tilde{h}^{n*}_{\mathbf{k},s}}{\partial z}\right) = 0 \tag{6.3.24}$$

$$\tilde{h}^{n+1}_{\mathbf{k},s} - \tilde{h}^{n}_{\mathbf{k},s} - \frac{Z}{T}e^{-\tilde{v}_s^2}\left(\Delta\left\langle\tilde{\chi}_{\mathbf{k}}\right\rangle_{\mathbf{X}_s}\right) + \Delta\tilde{t}\tilde{v}_{\|}\tilde{v}_{th,s}(\mathbf{b}\cdot\tilde{\boldsymbol{\nabla}}z)\left(\frac{\partial\tilde{h}^{n*}_{\mathbf{k},s}}{\partial z}\right) = 0 \tag{6.3.25}$$

$$\tilde{h}^{n+1}_{\mathbf{k},s} - \tilde{h}^{n}_{\mathbf{k},s} - \frac{Z}{T}e^{-\tilde{v}_s^2}\left(\Delta\left\langle\tilde{\chi}_{\mathbf{k}}\right\rangle_{\mathbf{X}_s}\right) + \Delta\tilde{t}\tilde{v}_{\|}\tilde{v}_{th,s}(\mathbf{b}\cdot\tilde{\boldsymbol{\nabla}}z)\left(\frac{1+u_t}{2}\frac{\partial\tilde{h}^{n+1}_{\mathbf{k},s}}{\partial z} + \frac{1-u_t}{2}\frac{\partial\tilde{h}^{n}_{\mathbf{k},s}}{\partial z}\right) = 0, \tag{6.3.26}$$

where, as before (see section 3.10), the superscripts ${}^{n}, {}^{n+1}, {}^{n*}$ denote evaluation at time $\tilde{t}^n, \tilde{t}^{n+1}, \tilde{t}^{n*}$ respectively,

$$\tilde{t}^{n*} \equiv \frac{1-u_t}{2}\tilde{t}^n + \frac{1+u_t}{2}\tilde{t}^{n+1}, \tag{6.3.27}$$

and $0 \leq u_t \leq 1$ is the user-specified temporal upwinding parameter. I have also defined:

$$\Delta\left\langle\tilde{\chi}_{\mathbf{k}}\right\rangle_{\mathbf{X}_s} \equiv \left\langle\tilde{\chi}_{\mathbf{k}}\right\rangle^{n+1}_{\mathbf{X}_s} - \left\langle\tilde{\chi}_{\mathbf{k}}\right\rangle^{n}_{\mathbf{X}_s} \tag{6.3.28}$$

$$= \left[J_0(\gamma_s)\Delta\tilde{\varphi}_{1\mathbf{k}} - 2\tilde{v}_{\|}\tilde{v}_{th,s}J_0(\gamma_s)\Delta\tilde{A}_{1\|\mathbf{k}} - 4\tilde{\mu}_s\frac{\tilde{T}_s}{Z}\frac{J_1(\gamma_s)}{\gamma_s}\Delta\tilde{B}_{1\|\mathbf{k}}\right]. \tag{6.3.29}$$

I then write $\tilde{h}^{n+1}_{\mathbf{k},s} = \tilde{h}_{\mathbf{k},s,\text{inh}} + \tilde{h}_{\mathbf{k},s,\text{hom}}$, where $\tilde{h}_{\mathbf{k},s,\text{inh}}$ and $\tilde{h}_{\mathbf{k},s,\text{hom}}$ are the inhomogeneous and homogeneous pieces of $\tilde{h}^{n+1}_{\mathbf{k},s}$, defined as

$$\tilde{h}_{\mathbf{k},s,\text{inh}} - \tilde{h}^{n}_{\mathbf{k},s} + \Delta\tilde{t}\tilde{v}_{\|}\tilde{v}_{th,s}(\mathbf{b}\cdot\tilde{\boldsymbol{\nabla}}z)\left(\frac{1+u_t}{2}\frac{\partial\tilde{h}_{\mathbf{k},s,\text{inh}}}{\partial z} + \frac{1-u_t}{2}\frac{\partial\tilde{h}^{n}_{\mathbf{k},s}}{\partial z}\right) = 0 \tag{6.3.30}$$

$$\tilde{h}_{\mathbf{k},s,\text{hom}} + \Delta\tilde{t}\tilde{v}_{\|}\tilde{v}_{th,s}(\mathbf{b}\cdot\tilde{\boldsymbol{\nabla}}z)\frac{1+u_t}{2}\frac{\partial\tilde{h}_{\mathbf{k},s,\text{hom}}}{\partial z} - \frac{Z}{T}e^{-\tilde{v}_s^2}\Delta\left\langle\tilde{\chi}_{\mathbf{k}}\right\rangle_{\mathbf{X}_s} = 0. \tag{6.3.31}$$

The inhomogeneous equation, eq. 6.3.30, does not depend on $\Delta\left\langle\tilde{\chi}_{\mathbf{k}}\right\rangle_{\mathbf{X}_s}$ so can be solved straightforwardly.

To calculate the change in the fields $\Delta\mathbf{f}$, I use the familiar response matrix approach. Each field (e.g. $\tilde{\varphi}_{1\mathbf{k}}$) can be updated at each z location z_i by splitting $\Delta\tilde{\varphi}_{1\mathbf{k},i}$ as follows:

$$\Delta\tilde{\varphi}_{1\mathbf{k},i} \equiv \tilde{\varphi}^{n+1}_{1\mathbf{k},i} - \tilde{\varphi}^{n}_{1\mathbf{k},i} = \Delta\tilde{\varphi}_{1\mathbf{k},\text{inh},i} + \Delta\tilde{\varphi}_{1\mathbf{k},\text{hom},i}, \tag{6.3.32}$$

where

$$\Delta\tilde{\varphi}_{1\mathbf{k},\text{inh},i} = \frac{l_1(\tilde{h}_{\mathbf{k},s,\text{inh},i}) - l_1(\tilde{h}^n_{\mathbf{k},s,i})}{K_{11h,i}} \tag{6.3.33}$$

$$\Delta\tilde{\varphi}_{1\mathbf{k},\text{hom},i} = \frac{l_1(\tilde{h}_{\mathbf{k},s,\text{hom},i})}{K_{11h,i}} \tag{6.3.34}$$

$$= \frac{1}{K_{11h,i}} l_1 \left(\sum_j \frac{\partial \tilde{h}_{\mathbf{k},s,\text{hom},i}}{\partial \Delta\tilde{\varphi}_{1\mathbf{k},j}} \Delta\tilde{\varphi}_{1\mathbf{k},j} + \sum_j \frac{\partial \tilde{h}_{\mathbf{k},s,\text{hom},i}}{\partial \Delta\tilde{A}_{1\|\mathbf{k},j}} \Delta\tilde{A}_{1\|\mathbf{k},j} + \sum_j \frac{\partial \tilde{h}_{\mathbf{k},s,\text{hom},i}}{\partial \Delta\tilde{B}_{1\|\mathbf{k},j}} \Delta\tilde{B}_{1\|\mathbf{k},j} \right). \tag{6.3.35}$$

Using vector notation this can be written compactly for all z and the three fields as

$$\Delta\mathbf{f} = \Delta\mathbf{f}_{\text{inh}} + \Delta\mathbf{f}_{\text{hom}} = \underline{\underline{K}}_h^{-1} \left(\mathbf{l}(\tilde{h}_{\mathbf{k},s,\text{inh}}) - \mathbf{l}(\tilde{h}_{\mathbf{k},s}{}^{n}) \right) + \underline{\underline{K}}_h^{-1} \mathbf{l}(\tilde{h}_{\mathbf{k},s,\text{hom}}) \tag{6.3.36}$$

$$= \Delta\mathbf{f}_{\text{inh}} + \underline{\underline{K}}_h^{-1} \mathbf{l} \left(\left[\frac{\partial \tilde{h}_{\mathbf{k},s,\text{hom}}}{\partial \Delta\mathbf{f}} \right] \Delta\mathbf{f} \right) \tag{6.3.37}$$

$$= \Delta\mathbf{f}_{\text{inh}} + \underline{\underline{K}}_h^{-1} \mathbf{l} \left(\left[\frac{\partial \tilde{h}_{\mathbf{k},s,\text{hom}}}{\partial \Delta\mathbf{f}} \right] \right) \Delta\mathbf{f}, \tag{6.3.38}$$

which can be rearranged to give

$$\underline{\underline{R}} \Delta\mathbf{f} = \left(\underline{\underline{I}} - \underline{\underline{K}}_h^{-1} \mathbf{l} \left(\left[\frac{\partial \tilde{h}_{\mathbf{k},s,\text{hom}}}{\partial \Delta\mathbf{f}} \right] \right) \right) \Delta\mathbf{f} = \Delta\mathbf{f}_{\text{inh}}, \tag{6.3.39}$$

and solved for $\Delta\mathbf{f}$ by inverting $\underline{\underline{R}}$:

$$\Delta\mathbf{f} = \underline{\underline{R}}^{-1} \Delta\mathbf{f}_{\text{inh}}. \tag{6.3.40}$$

Once $\Delta\mathbf{f}$ is known, eq. (6.3.26) can finally be solved for $\tilde{h}^{n+1}_{\mathbf{k},s}$. The full fields $\mathbf{f}^{n+1}$ are calculated and used to make the conversion $\tilde{h}^{n+1}_{\mathbf{k},s} \to \tilde{g}^{n+1}_{\mathbf{k},s}$.

As in the electrostatic case, $\underline{\underline{R}}$ is time-independent. It is calculated once at the beginning of the simulation, by applying a unit impulse in $\Delta\mathbf{f}$ for every field and every z location. $\underline{\underline{R}}$ is then *LU*-decomposed. On each simulation timestep, back substitution is used to calculate $\Delta\mathbf{f}$ from $\Delta\mathbf{f}_{\text{inh}}$. A pseudocode description of how `stella` implements this algorithm is given for completeness in appendix A.2.

6.3.3.2 The electromagnetic implicit mirror algorithm

The mirror equation,

$$\frac{\partial \tilde{g}_{\mathbf{k},s}}{\partial \tilde{t}} - \tilde{v}_{th,s}\tilde{\mu}_s \left(\mathbf{b}\cdot\tilde{\boldsymbol{\nabla}}\tilde{B}_0\right)\frac{\partial \tilde{h}_{\mathbf{k},s}}{\partial \tilde{v}_{\|}} = 0, \tag{6.3.41}$$

has a very similar form to the streaming equation (eq. (6.3.23)), and the algorithm used to implicitly advance the mirror equation is virtually identical to that used for the streaming. One noteworthy difference is that in eq. (6.3.41) different z locations are decoupled, but $\tilde{v}_{\|}$ gridpoints are coupled by the $\frac{\partial}{\partial \tilde{v}_{\|}}$ operator. A consequence of this is that the response matrix **R** has a total size $(n_z \times \texttt{nfields} \times \texttt{nfields})$ (a square matrix of order `nfields`) for each $(\tilde{k}_y, \tilde{k}_x)$, rather than $(n_z^2 \times \texttt{nfields}^2)$ for the streaming response matrix (a square matrix of order $(\texttt{nfields} \times n_z)$) for each $(\tilde{k}_y, \tilde{k}_x)$.

For completeness, the algorithm is described in appendix B. An interesting feature of this scheme is that $\Delta\tilde{\varphi}_{1\mathbf{k},\mathrm{inh},i}$ and $\Delta\tilde{B}_{1\|\mathbf{k},\mathrm{inh},i}$ are approximately zero because the inhomogeneous equation is advection of $\tilde{h}_{\mathbf{k},s}$ in $\tilde{v}_{\|}$-space. This could plausibly create numerical problems in extremely high-fidelity simulations, but nothing of this kind has been observed so far.

6.3.4 Centering of the derivative $\frac{\partial}{\partial z}$

The benchmarking studies find that the `stella` simulations with implicit streaming are sensitive to the value of u_z, which controls the centering of spatial derivatives (see section 6.4.2). It is usual to set u_z to a small value ($u_z = 0.02$ by default) in electrostatic (ES) simulations, which introduces a small amount of numerical dissipation but generally improves numerical stability. However, in the simulations presented here I set $u_z = 0$ unless otherwise stated.

Given the sensitivity of the implicit implementation to z upwinding, one may wonder whether the same is true when streaming is evaluated explicitly. The original version of `stella` calculates this this derivative using a third-order upwinded scheme. To allow centering to vary whilst still allowing the option of the original scheme, I implement an ad-hoc way of calculating the derivative:

$$\left(\frac{\partial}{\partial z}\right)_{\text{EM }\texttt{stella}\text{, expl}} = u_{z,\texttt{exp}}\left(\frac{\partial}{\partial z}\right)_{\text{3}^{\text{rd}}\text{ order upw.}} + (1-u_{z,\texttt{exp}})\left(\frac{\partial}{\partial z}\right)_{\text{2}^{\text{nd}}\text{ order cent.}}, \tag{6.3.42}$$

which linearly mixes the third-order upwinded scheme and the second-order centered scheme. By default I set $u_{z,\texttt{exp}} = 0.1$ (i.e. an almost-centered scheme), since numerical instability is observed for $u_{z,\texttt{exp}} = 0$ in some cases.

6.4 Tests and Benchmarks

Here I present benchmarks of the electromagnetic implementation of `stella`. I first verify that the field calculations to obtain $\tilde{\varphi}_{1\mathbf{k}}$, $\tilde{A}_{1\|\mathbf{k}}$ and $\tilde{B}_{1\|\mathbf{k}}$ are correctly implemented. `stella` is then benchmarked against `GS2` in an unsheared slab geometry. Finally, `stella` is compared with `GS2` using the CBC geometry. The effect of varying non-physical simulation parameters is tested, and the reader is referred to table 3.1 for the meaning of these parameters.

An electrostatic benchmark is also performed between the electromagnetic implementation of `stella` and the original `stella` implementation with stellarator geometry. However, since the geometry and instabilities are not introduced until the next chapter, the description of this benchmark is delayed until section 7.6.2.

6.4.1 Testing the field solve

6.4.1.1 $\tilde{v}_{\|}$-symmetric $\tilde{h}_{\mathbf{k},s}$

The field solve subroutines are tested by initialising the distribution function ($\tilde{h}_{\mathbf{k},s}$ or $\tilde{\bar{g}}_{\mathbf{k},s}$), such that the fields ($\tilde{\varphi}_{1\mathbf{k}}$, $\tilde{A}_{1\|\mathbf{k}}$, $\tilde{B}_{1\|\mathbf{k}}$) have an analytic form. I first selected the distribution function to be either

$$\tilde{h}_{\mathbf{k},s} = Z_s \exp^{-\tilde{v}_s^2} J_0(\gamma_s), \tag{6.4.1}$$

or

$$\tilde{\bar{g}}_{\mathbf{k},s} = Z_s \exp^{-\tilde{v}_s^2} J_0(\gamma_s), \tag{6.4.2}$$

and selected physical parameters ($Z_i = 1$, $Z_e = -1$, $\tilde{T}_i = \tilde{T}_e = \tilde{n}_i = \tilde{n}_e = 1$). The solution for variables appearing in the field solve equations are

$$l_1(\tilde{h}_{\mathbf{k},s}) = \Gamma_0(b_i) + \Gamma_0(b_e), \quad l_2(\tilde{h}_{\mathbf{k},s}) = 0, \quad l_3(\tilde{h}_{\mathbf{k},s}) = \frac{-2\beta}{\tilde{B}_0}(\Gamma_1(b_e) - \Gamma_1(b_i)) \tag{6.4.3}$$

$$K_{11,h} = 2, \qquad K_{22,h} = \tilde{k}_\perp^2, \qquad K_{22} = \tilde{k}_\perp^2 - \beta\left(\frac{\Gamma_0(b_i)}{\tilde{m}_i} + \frac{\Gamma_0(b_e)}{\tilde{m}_e}\right), \tag{6.4.4}$$

$$K_{11} = 2 - (\Gamma_0(b_i) + \Gamma_0(b_e)), \qquad K_{13} = \frac{1}{\tilde{B}_0}(\Gamma_1(b_e) - \Gamma_1(b_i)), \tag{6.4.5}$$

$$K_{31} = \frac{\beta}{\tilde{B}_0}(\Gamma_1(b_i) - \Gamma_1(b_e)), \qquad K_{33} = 1 + \frac{\beta}{\tilde{B}_0}(\Gamma_1(b_i) - \Gamma_1(b_e)), \tag{6.4.6}$$

where I have used identities given by Howes *et al.* [108]. The fields are calculated using `stella` for a range of velocity space resolution parameters using species masses $\tilde{m}_i = 1$, $\tilde{m}_e = 2.8 \times 10^{-4}$ and $\tilde{k}_\perp = 1$. Firstly, $\tilde{v}_\perp$ parameters are set to a high-fidelity value ($\tilde{v}_{\perp,\text{max}} = 5.0$, $n_{\tilde{\mu}_s} = 144$) and the $\tilde{v}_{||}$ resolution parameters ($\tilde{v}_{||,\text{max}}$, $n_{\tilde{v}_{||}}$) are varied. Next, $\tilde{v}_{||}$ parameters are fixed ($\tilde{v}_{||,\text{max}} = 5.0$, $n_{\tilde{v}_{||}} = 144$) and $\tilde{v}_{\perp,\text{max}}$ and $n_{\tilde{\mu}_s}$ are varied.

These results are shown in figures 6.2 and 6.3. For both the $\tilde{h}_{\mathbf{k},s}$ and $\tilde{\bar{g}}_{\mathbf{k},s}$ formulations, $\tilde{A}_{1||\mathbf{k}}$ is zero to within a small (approximately machine precision) tolerance, and is insensitive to **v**-space fidelity. This is likely due to the symmetry in the distribution function between positive and negative values of $\tilde{v}_{||}$, which cancel to within machine precision.

$\tilde{\varphi}_{1\mathbf{k}}$ and $\tilde{B}_{1||\mathbf{k}}$ show the following general trend in all but one scenario. For low values of $\tilde{v}_{||,\text{max}}$ or $\tilde{v}_{\perp,\text{max}}$ ($\lesssim 2$), the dominant source of error is the truncation of the integral, and so the result is insensitive to the number of gridpoints used. For $\tilde{v}_{||,\text{max}}, \tilde{v}_{\perp,\text{max}} > 2$, there is a dependence on the number of gridpoints for $n_{\tilde{\mu}_s} \lesssim 10$ and $n_{\tilde{v}_{||}} \lesssim 20$ as this becomes the dominant error source. The exception to this trend is the calculation of $\tilde{\varphi}_{1\mathbf{k}}$ using the $\tilde{h}_{\mathbf{k},s}$ formulation of the field solve, for which low error ($\sim 10^{-12}\%$) is observed for all values of ($\tilde{v}_{||,\text{max}}$, $n_{\tilde{v}_{||}}$). This is presumably caused by compensating truncation errors in $l_1(\tilde{h}_{\mathbf{k},s})$ and $K_{11,h}$, which ensure that $\tilde{v}_{||}$-related parameters are not dominant.

6.4.1.2 $\tilde{v}_{||}$-antisymmetric $\tilde{h}_{\mathbf{k},s}$

To test the field solve for $\tilde{A}_{1||\mathbf{k}}$, the distribution function is set to

$$\tilde{h}_{\mathbf{k},s} = Z_s \tilde{v}_{||} \exp^{-\tilde{v}_s^2} J_0(\gamma_s), \tag{6.4.7}$$

or

$$\tilde{\bar{g}}_{\mathbf{k},s} = Z_s \tilde{v}_{||} \exp^{-\tilde{v}_s^2} J_0(\gamma_s), \tag{6.4.8}$$

for which, using ($Z_i = 1$, $Z_e = -1$, $\tilde{T}_i = \tilde{T}_e = \tilde{n}_i = \tilde{n}_e = 1$), the values of K_{XX} are the same as the previous test, but the $l_X(\tilde{h}_{\mathbf{k},s})$ values are:

$$l_1(\tilde{h}_{\mathbf{k},s}) = l_3(\tilde{h}_{\mathbf{k},s}) = 0, \qquad l_2(\tilde{h}_{\mathbf{k},s}) = \frac{\beta}{2}\left(\frac{\Gamma_0(b_i)}{\sqrt{\tilde{m}_i}} + \frac{\Gamma_0(b_e)}{\sqrt{\tilde{m}_e}}\right), \tag{6.4.9}$$

As in the tests for $\tilde{\varphi}_{1\mathbf{k}}$ and $\tilde{B}_{1||\mathbf{k}}$, a comparison with the analytic result is made as v-space fidelity parameters are varied. I also test the effect of changing $\tilde{k}_\perp$ at fixed v-space resolution.

The results are shown in figure 6.4. As $\tilde{v}_{||}$-related parameters are varied, the same behaviour as was seen for $\tilde{\varphi}_{1\mathbf{k}}$ and $\tilde{B}_{1||\mathbf{k}}$ tests is observed: the truncation error from $\tilde{v}_{||,\max}$ dominates, except for $\tilde{v}_{||,\max} \gtrsim 3$, for which $n_{\tilde{v}_{||}}$ dominates the error at low $n_{\tilde{v}_{||}}$. For $\tilde{v}_\perp$ variation, the dominant error is set by $\tilde{v}_{\perp,\max}$ for $\tilde{v}_{||,\max} \lesssim 3$. Beyond this, there is a dependence on $n_{\tilde{\mu}_s}$, but this is not always with the expected trend ($\Delta\tilde{A}_{1||\mathbf{k}} \downarrow$ as $n_{\tilde{\mu}_s} \uparrow$). This may be peculiar to this particular test, for which "accidental" good agreement occurs at low $n_{\tilde{\mu}_s}$. The dependence of $\tilde{A}_{1||\mathbf{k}}$ on $\tilde{k}_\perp$ shows an opposite trend for the $\tilde{h}_{\mathbf{k},s}$ formulation (in which the error falls roughly log-linearly with increasing $\tilde{k}_\perp$) and the $\tilde{\bar{g}}_{\mathbf{k},s}$ formulation (in which the error tends to increase with $\tilde{k}_\perp$).

It should be emphasised that the test is not a like-for-like comparison of the field solves in $\tilde{h}_{\mathbf{k},s}$ and $\tilde{\bar{g}}_{\mathbf{k},s}$, since the form of the distribution function is fixed between the tests rather than the fields being fixed. For example, $\tilde{A}_{1||\mathbf{k}}$ becomes large at low $\tilde{k}_\perp$ in the $\tilde{h}_{\mathbf{k},s}$ field test, but this does not occur in the $\tilde{\bar{g}}_{\mathbf{k},s}$ test (shown in figure 6.5). A comparison in which the field is the same between the $\tilde{h}_{\mathbf{k},s}$ and $\tilde{\bar{g}}_{\mathbf{k},s}$ would be a useful piece of additional work.

For brevity, results for $\tilde{\varphi}_{1\mathbf{k}}$ and $\tilde{B}_{1||\mathbf{k}}$ in this test are not shown, but these are found to be small (in agreement with expectation from the analytic theory that $\tilde{\varphi}_{1\mathbf{k}} = \tilde{B}_{1||\mathbf{k}} = 0$).

Based on the above tests, I conclude that a choice of $n_{\tilde{v}_{||}} = 20$, $n_{\tilde{\mu}_s} = 10$, $\tilde{v}_{||,\max} = 3.0$, $\tilde{v}_{\perp,\max} = 3.0$ is sufficient to calculate the fields for these particular forms of distribution function with an error of less than 0.1%. Increasing $\tilde{v}_{||,\max}$ to 4.0 reduces this error to $< 10^{-4}\%$. Of course, these parameters are not guaranteed to resolve the fields for an arbitrary distribution function, and also do not inform the resolution required to accurately advance the GKE. However, this provides a starting point for convergence tests.

6.4.2 The unsheared slab

The next test is performed in an "unsheared slab" geometry, representing an equilibrium magnetic field which is spatially uniform and straight in Cartesian coordinates. I also set the kinetic gradients in the plasma to zero, which removes the driving term. In this case, the Fourier-transformed `stella`-normalised linear GKE in $\tilde{h}_{\mathbf{k},s}$ reduces to

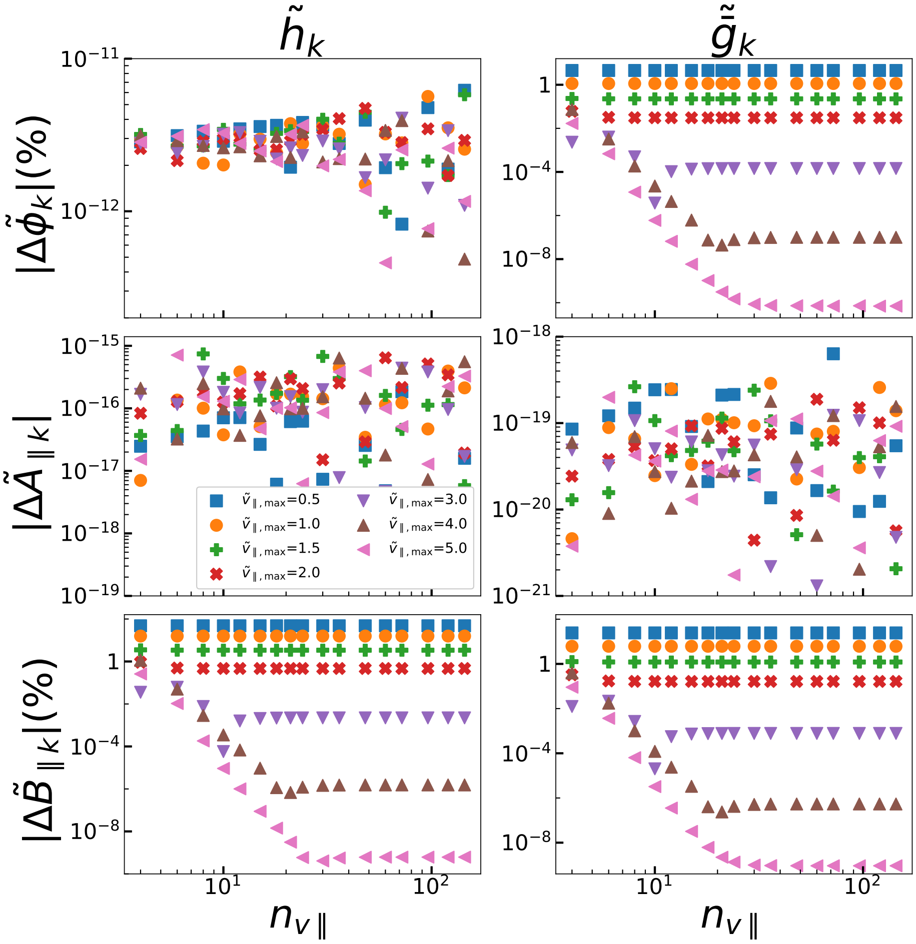

Figure 6.2: Error in field solve calculations for $\tilde{v}_\parallel$-symmetric distribution function with $\tilde{k}_\perp = 1, \beta = 1$ with varying $\tilde{v}_\parallel$ fidelity. Left column: fields calculated for a prescribed $\tilde{h}_{\mathbf{k},s}$. Right column: fields calculated for a prescribed $\tilde{\bar{g}}_{\mathbf{k},s}$.

$$\frac{\partial \tilde{h}_{\mathbf{k},s}}{\partial \tilde{t}} + \tilde{v}_\parallel \tilde{v}_{th,s}(\mathbf{b}\cdot\tilde{\nabla} z)\left(\frac{\partial \tilde{h}_{\mathbf{k},s}}{\partial z}\right) - \frac{Z}{\tilde{T}_s}\exp\left(-\tilde{v}_s^2\right)\frac{\partial \left\langle \tilde{\chi}_{\mathbf{k}}\right\rangle_{\mathbf{X}_s}}{\partial t} = 0, \tag{6.4.10}$$

where $(\mathbf{b}\cdot\tilde{\nabla} z)$ is a constant which is set to 1, and a periodic boundary condition is imposed in z. This setup allows linearisation in z, such that one can consider each mode $\tilde{h}_{\mathbf{k},k_z,s}(\tilde{k}_x,\tilde{k}_y,z,t) = \tilde{h}_{\mathbf{k},s}(\tilde{k}_x,\tilde{k}_y)\exp(ik_z z)\exp\left(-i\tilde{\Omega}\tilde{t}\right)$ independently. Eq. (6.4.10) can be solved for $\tilde{h}_{\mathbf{k},k_z,s}$ to give

$$-i\tilde{\Omega}\tilde{h}_{\mathbf{k},k_z,s} + \tilde{v}_\parallel\tilde{v}_{th,s}(ik_z)\tilde{h}_{\mathbf{k},k_z,s} - \frac{Z}{\tilde{T}_s}\exp\left(-\tilde{v}_s^2\right)\left(-i\tilde{\Omega}\left\langle\tilde{\chi}_{\mathbf{k}}\right\rangle_{\mathbf{X}_s}\right) = 0 \tag{6.4.11}$$

$$\tilde{h}_{\mathbf{k},k_z,s} = \frac{Z_s}{\tilde{T}_s}\exp\left(-\tilde{v}_s^2\right)\frac{\left\langle\tilde{\chi}_{\mathbf{k}}\right\rangle_{\mathbf{X}_s}}{1-\frac{\tilde{v}_{th,s}\tilde{v}_\parallel k_z}{\tilde{\Omega}}}. \tag{6.4.12}$$

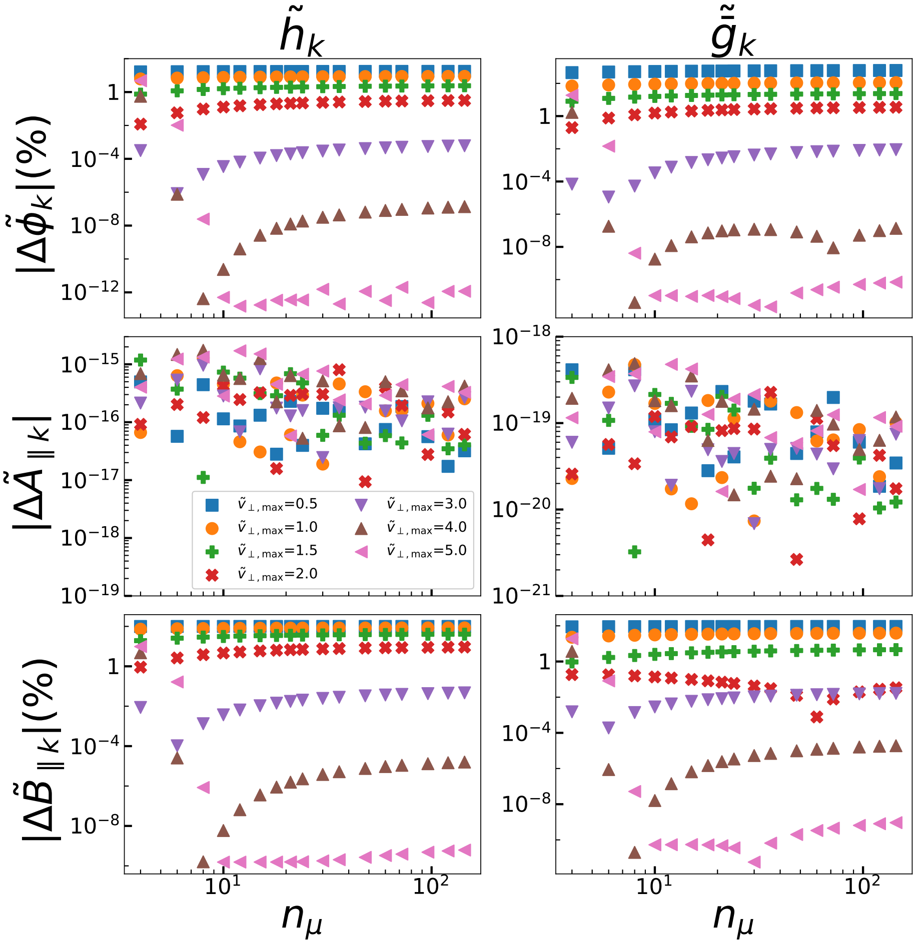

Figure 6.3: Error in field solve calculations for $\tilde{v}_{\|}$-symmetric distribution function with $\tilde{k}_\perp = 1, \beta = 1$ with varying $\tilde{v}_\perp$ fidelity. Left column: fields calculated for a prescribed $\tilde{h}_{\mathbf{k},s}$. Right column: fields calculated for a prescribed $\tilde{\tilde{g}}_{\mathbf{k},s}$.

Eq. 6.4.12 for ions and electrons together with the field equations form a set of five simultaneous equations describing the plasma. This system is rather difficult to solve in the general case but gives rise to a plasma wave known as the kinetic shear Alfvén wave (KSAW) [109], a kinetic analogue of the ideal MHD shear Alfvén wave.

Here I simulate a plasma with ($\beta = 1$, $\tilde{k}_y = 1$) in `GS2` and `stella`. The real part of the distribution function in each case is normalised to

$$\tilde{\tilde{g}}_{\mathbf{k},s} = -Z_s \exp^{-\tilde{v}_s^2} \cos(z), \tag{6.4.13}$$

and in `GS2`:

$$\tilde{g}_{\mathtt{GS2},\mathbf{k},s} = -Z_s \cos(z). \tag{6.4.14}$$

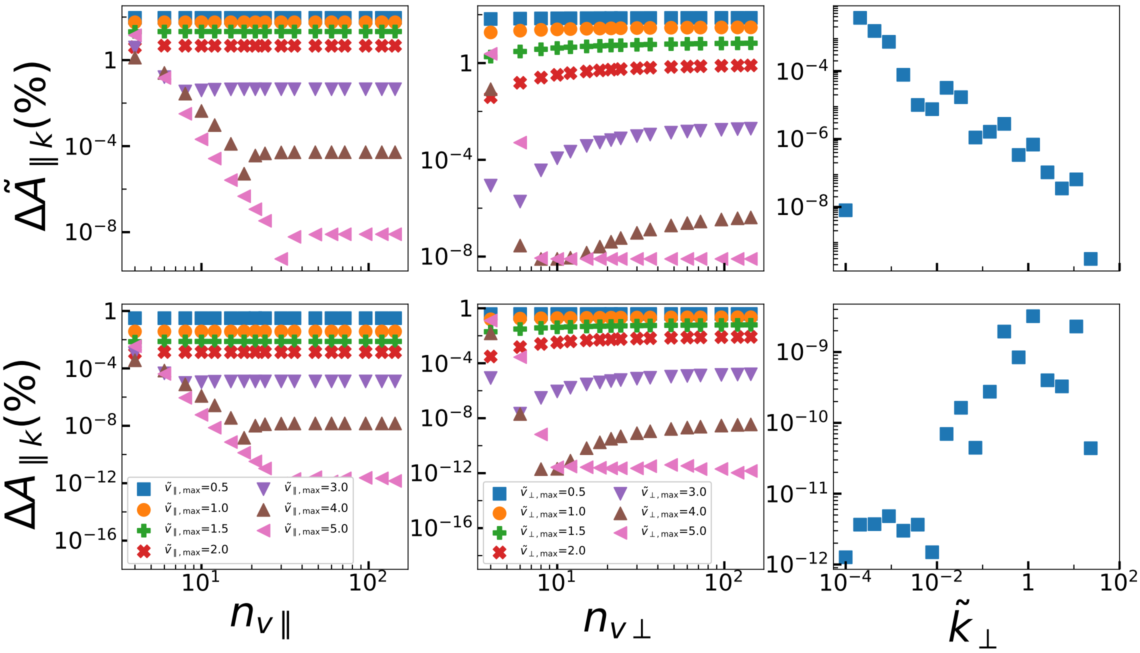

Figure 6.4: Error in $\tilde{A}_{1\|\mathbf{k}}$ field solve calculation for $\tilde{v}_\parallel$-antisymmetric distribution function with $\beta = 1$ with varying $\tilde{v}_\parallel$ fidelity, $\tilde{v}_\perp$ fidelity and $\tilde{k}_\perp$. Upper row: fields calculated for a prescribed $\tilde{h}_{\mathbf{k},s}$. Lower row: fields calculated for a prescribed $\tilde{\tilde{g}}_{\mathbf{k},s}$.

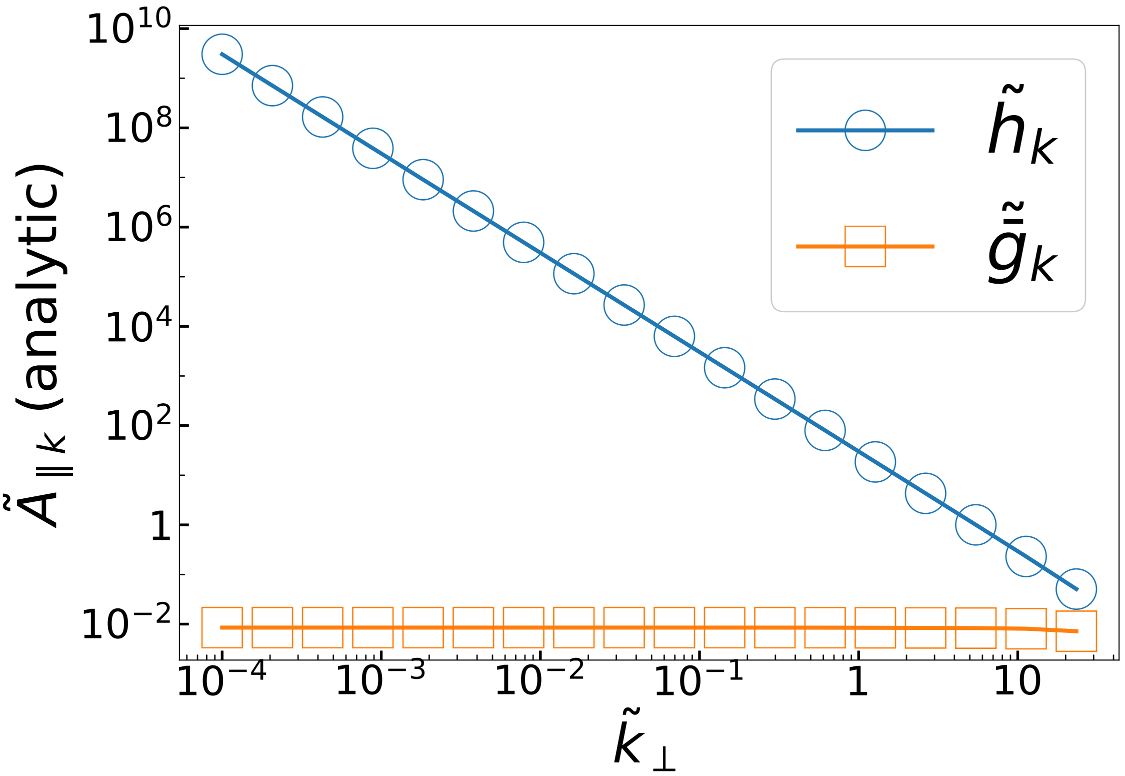

Figure 6.5: $\tilde{A}_{1\|\mathbf{k}}(\tilde{k}_\perp)$ for $\tilde{v}_\parallel$-antisymmetric field solve test.

Note that since the normalisation of $\tilde{g}_{\texttt{GS2},\mathbf{k},s}$ contains an extra factor of $\exp\bigl(-\tilde{v}_s^2\bigr)$ and symmetry in $\tilde{v}_{\|}$ implies $\tilde{A}_{1\|\mathbf{k}} = 0$, equations (6.4.13) and (6.4.14) correspond to the same initialisation of $\tilde{h}_{\mathbf{k},s}$.

Simulations are run using `GS2`, `stella` (using RK3 scheme) and `stella` (using implicit streaming) with physical parameters ($\beta = 1$, $\tilde{k}_y = 1$, $\tilde{T}_i = \tilde{T}_e = \tilde{m}_i = 1$, $\tilde{m}_e = 2.8 \times 10^{-4}$) and a fiducial set of non-physical parameters (given in appendix C). The fields at the final timestep (normalised to have equal amplitudes), shown in figure 6.6 (left), show a box-scale mode with a $\pi/2$ phase difference between ($\tilde{\varphi}_{1\mathbf{k}}, \tilde{B}_{1\|\mathbf{k}}$) and $\tilde{A}_{1\|\mathbf{k}}$ with excellent agreement between implementations. Figure 6.6 (right) plots $\tilde{\varphi}_{1\mathbf{k}}(z = 0, \tilde{t})$ for each simulation, showing a damped oscillation in each case. However, there is a clear difference in damping rate between `stella` and `GS2`.

The frequency and damping rate are calculated by fitting

$$\tilde{\varphi}_{1\mathbf{k}}(z = 0, \tilde{t}) = A \exp\bigl(\tilde{\gamma}\tilde{t}\bigr) \sin\bigl(B + \tilde{\omega}\tilde{t}\bigr), \tag{6.4.15}$$

where (A, $\tilde{\gamma}$, B, $\tilde{\omega}$) are free parameters. These simulations are then repeated with varying non-physical parameters. The results are summarised in table 6.1. `GS2` shows very little change in $\tilde{\omega}$ for all simulations. There is very little change in $\tilde{\gamma}$ when n_z is varied ($< 1\%$), a small change when the $\tilde{t}$ and z derivatives are centered or when the timestep is reduced ($\sim 7\%$ in both cases), and a larger change when the velocity-space resolution is increased from ($n_{\text{gauss}} = 12$, $n_E = 16$) to ($n_{\text{gauss}} = 24$, $n_E = 36$) ($\sim 15\%$). Increasing further to ($n_{\text{gauss}} = 48$, $n_E = 72$) results in only a small change in $\tilde{\gamma}$ ($\sim 1\%$).

$\tilde{\gamma}$ for `stella` is insensitive to $\Delta\tilde{t}$ and n_z but sensitive to the centering of derivates. Numerical instability is observed when u_z departs from its fiducial value of zero in the implicit scheme. $\tilde{\Omega}$ is in good agreement between the implicit and RK3 schemes when derivatives are fully centered in the former and $\frac{\partial}{\partial z}$ is fully centered in the latter ($\Delta\tilde{\Omega} < 2\%$) which is promising, though $\tilde{\gamma}$ is $\geq 50\%$ lower than all `GS2` simulations.

To conclude, there is persistent disagreement between the codes `GS2` and `stella` for this high-β benchmarking test, indicating that at least one of the codes is inaccurate at large β ($\beta \sim \mathcal{O}(1)$). Given that `GS2` is well-established, a reasonable assumption is that `stella` is inaccurate. However, an additional benchmark against the `GENE` code (performed with a single set of simulation parameters informed by the fiducial `GS2` simulation) has reported a (renormalised) complex frequency of $\tilde{\Omega} = 1.128 - i0.0184$, which better matches the `stella` results [110]. A valuable piece of future work would be comparing these codes against a simple analytic KSAW result.

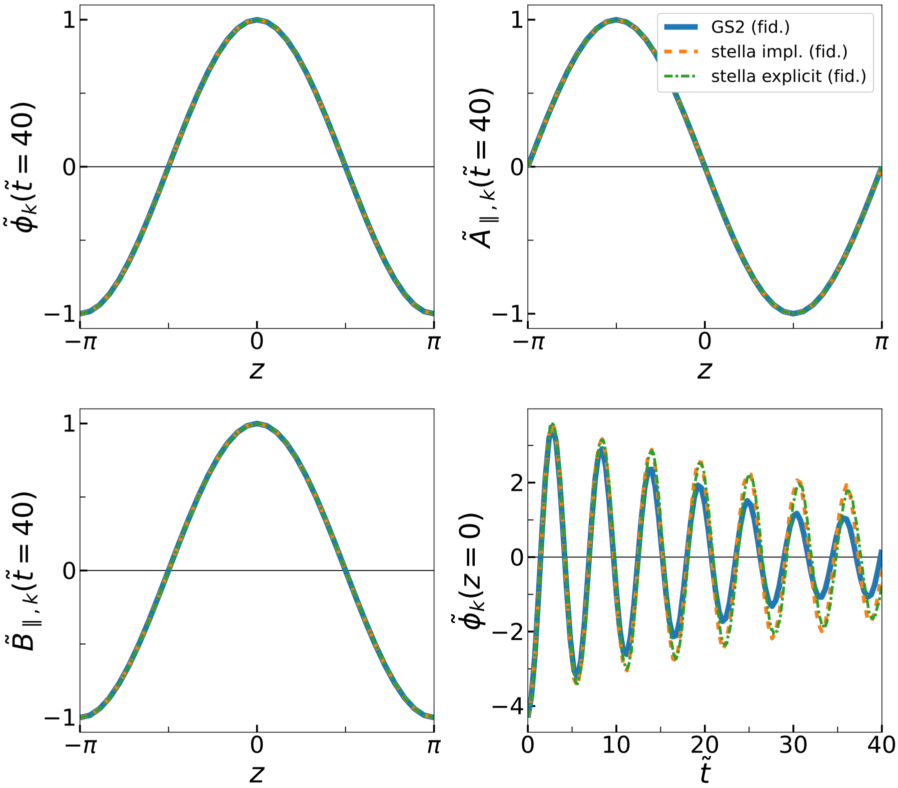

Figure 6.6: Upper row and bottom left: the real parts of fields $(\tilde{\varphi}_{1\mathbf{k}}, \tilde{A}_{1\|\mathbf{k}}, \tilde{B}_{1\|\mathbf{k}})(z)$ at $\tilde{t} = 40$, all normalised to have a maximum amplitude of 1. Bottom right: $\tilde{\varphi}_{1\mathbf{k}}(z = 0, \tilde{t})$ (not renormalised).

Code	**Simulation notes**	$\tilde{\omega}$	$\Delta\tilde{\omega}(\%)$	$\tilde{\gamma}$	$\Delta\tilde{\gamma}(\%)$
`GS2`	Fiducial	1.1412	$5\text{E}-4$	-0.0385	$5\text{E}-4$
`GS2`	$\Delta\tilde{t} = 4\text{E}-4$	1.1417	$5\text{E}-4$	-0.0359	$5\text{E}-4$
`GS2`	$u_z = 0, u_{t,\texttt{GS2}} = 0.5$	1.1414	$5\text{E}-4$	-0.0358	$5\text{E}-4$
`GS2`	$n_z = 72$	1.1390	$5\text{E}-4$	-0.0384	$5\text{E}-4$
`GS2`	$n_E = 36$	1.1407	$3\text{E}4$	-0.0329	$3\text{E}-4$
`GS2`	$n_E = 72$	1.1403	$3\text{E}4$	-0.0333	$3\text{E}-4$
`stella`	Fiducial, implicit	1.1362	$3\text{E}-4$	-0.0209	$3\text{E}-4$
`stella`	$\Delta\tilde{t} = 4\text{E}-4$	1.1364	$3\text{E}-4$	-0.0209	$3\text{E}-4$
`stella`	$u_t = 0.02$	1.1363	$3\text{E}-4$	-0.0215	$3\text{E}-4$
`stella`	$u_t = 0.1$	1.1363	$3\text{E}-4$	-0.0236	$3\text{E}-4$
`stella`	$u_z = 0.02$	n/a (blowup)	n/a	n/a	n/a
`stella`	$n_z = 72$	1.1342	$3\text{E}-4$	-0.0209	$3\text{E}-4$
`stella`	$n_{\tilde{v}_\parallel} = 48, n_{\tilde{\mu}_s} = 24$	1.1290	$3\text{E}-4$	-0.0206	$3\text{E}-4$
`stella`	Fiducial, explicit	1.1286	$1\text{E}-4$	-0.0225	$1\text{E}-4$
`stella`	$u_{z,\text{exp}} = 0$	1.1280	$1\text{E}-4$	-0.0205	$1\text{E}-4$
`stella`	$u_{z,\text{exp}} = 0.5$	1.1309	$2\text{E}-4$	-0.0305	$2\text{E}-4$
`stella`	$u_{z,\text{exp}} = 1$	1.1338	$2\text{E}-4$	-0.0406	$2\text{E}-4$

Table 6.1: Fitted frequency and damping rates for unsheared slab simulations. Fiducial parameters are given in appendix C. Errors $\Delta\tilde{\omega}, \Delta\tilde{\gamma}$ correspond to the fitting error. For `GS2`, $u_z = 0$ and $u_{t,\texttt{GS2}} = 0.5$ correspond to centered derivatives (equivalent to $u_z = 0$ and $u_t = 0$ in `stella`) (see table 3.1.

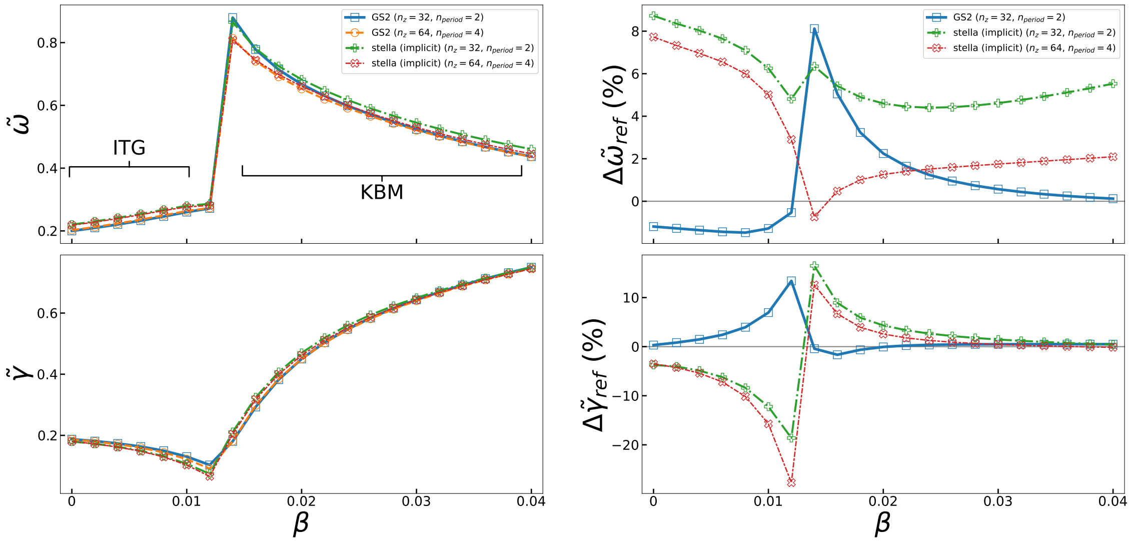

Figure 6.7: CBC β scan at fixed geometry with $k_y\rho_i = 0.5$ Left: $\tilde{\omega}(\beta)$ and $\tilde{\gamma}(\beta)$. Right: $\%$ difference in $\tilde{\omega}, \tilde{\gamma}$ compared with the `GS2` simulation with parallel fidelity.

6.4.3 The cyclone base case

I next test the linear simulations using the CBC as a realistic tokamak test case with $k_y\rho_i = 0.5$ (NB this is the same test as presented in section 6.2.1. β is scanned at fixed geometry, including fixing the geometric parameter $\frac{\partial\beta}{\partial\psi}$, which is set to zero. `GS2` and `stella` are tested for two different resolutions of z-coordinate (($n_{\text{period}} = 2$, $n_z = 32$) and ($n_{\text{period}} = 4$, $n_z = 64$)), with the `stella` simulations treating streaming and mirror terms implicitly. Simulation parameters are given in appendix C. The simulation cost per timestep is similar (within 20%) between `stella` and `GS2` with these simulation parameters.

$\tilde{\Omega}(\beta)$ (figure 6.7) shows good agreement between codes across the full range of β with typical differences below 10%. Mode structure comparisons at $\beta = 0$ (figure 6.8) and $\beta = 0.04$ (figure 6.9) are produced interpolating the fields onto a common z grid and renormalising such that $\texttt{max}(|\tilde{\varphi}_{1\mathbf{k}}|) = 1$. These also show good cross-code agreement and agreement between implicit and explicit `stella` implementations, although the fractional error becomes large where the field amplitudes are small. Whether even better agreement between `stella` and `GS2` can be obtained by adjusting other non-physical parameters remains an open question.

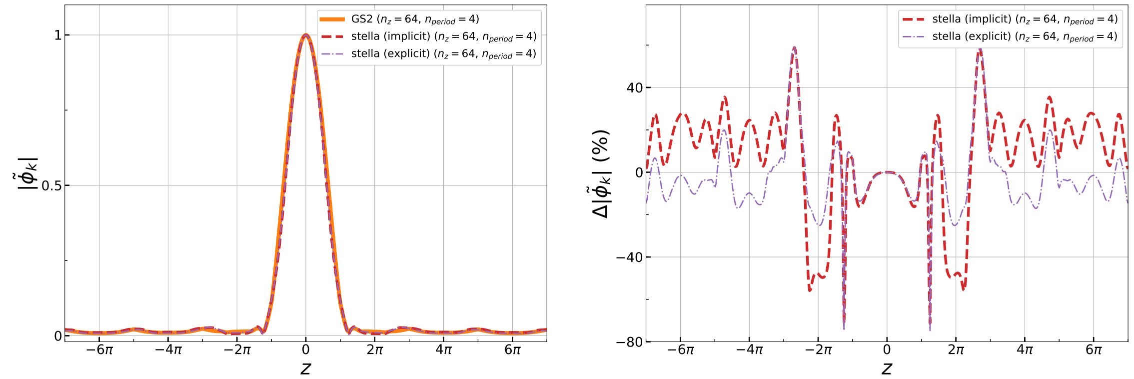

Figure 6.8: Left: $|\tilde{\varphi}_{1\mathbf{k}}|(z)$ for $\beta = 0$, normalised such that $\mathtt{max}(|\tilde{\varphi}_{1\mathbf{k}}|) = 1$. Right: Difference in $|\tilde{\varphi}_{1\mathbf{k}}|(z)$ compared with `GS2` simulation.

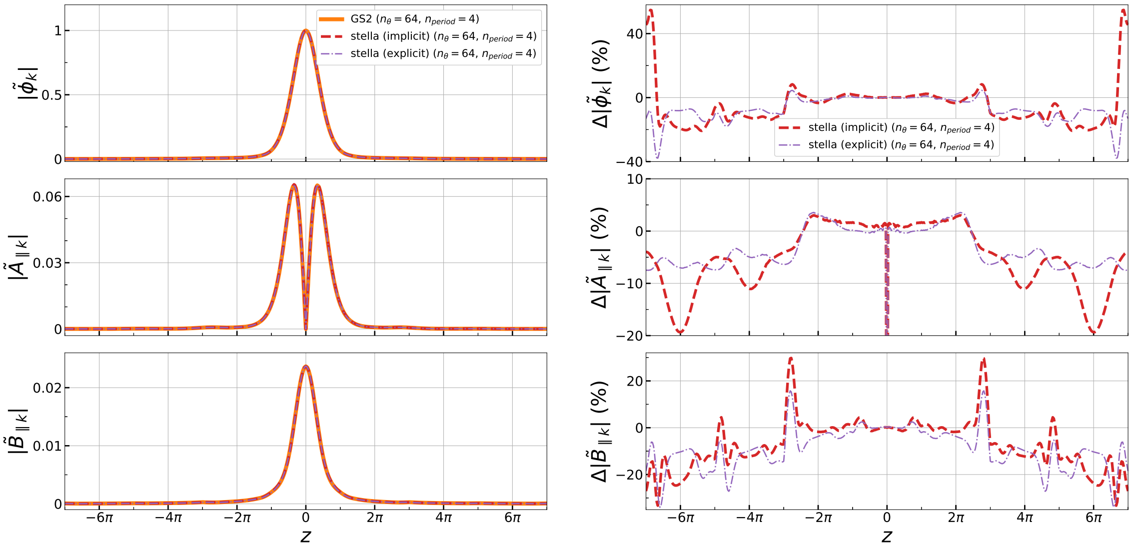

Figure 6.9: Left: $|\tilde{\varphi}_{1\mathbf{k}}, \tilde{A}_{1\|\mathbf{k}}, \tilde{B}_{1\|\mathbf{k}}|(z)$ for $\beta = 0.04$, normalised such that $\mathtt{max}(|\tilde{\varphi}_{1\mathbf{k}}|) = 1$. Right: Difference compared with `GS2` simulation.

6.5 Concluding remarks

Electromagnetic field effects ($A_{1\|}$ and $B_{1\|}$) are implemented linearly in the gyrokinetic code `stella` using a scheme which mixes distribution functions $\tilde{h}_{\mathbf{k},s}$ and $\tilde{\bar{g}}_{\mathbf{k},s} = \tilde{h}_{\mathbf{k},s} - \frac{Z_s}{\tilde{T}_s} \exp\left(\tilde{v}_s^2\right) \langle\tilde{\chi}_{\mathbf{k}}\rangle_{\mathbf{X}_s}$. This enables Lie-Trotter and flip-flop operator splitting, without unphysically large terms appearing in the GKE (as happens in a $\tilde{\bar{g}}_{\mathbf{k},s}$-only approach, which shows slow convergence with n_z as a result). All source terms can be evaluated explicitly (using any of the SSP RK2, SSP RK3 and SSP RK4 schemes). In addition, the streaming and mirror terms are implemented implicitly using an electromagnetic Greens function approach (Kotschenreuter's algorithm). It would be fairly straightforward to implement the remaining linear terms implicitly, allowing linear simulations to be performed without timestep constraint.

Analytic field solve tests and linear fully electromagnetic gyrokinetic benchmarking against `GS2` is performed. The former show convergence as velocity-space fidelity increases. In the latter, good agreement is found for the CBC (which exhibits the ITG at low β and the KBM at high β) at reasonable resolution. Slab simulations observe the KSAW, for which the frequency matches well between codes but the damping rate differs by order unity. With centered derivatives, the implicit and SSP RK3 implementations of `stella` are in agreement on $\tilde{\omega}$ and $\tilde{\gamma}$ to $< 2\%$ for fiducial parameters. Comparison with an analytic result for the KSAW to elucidate differences between `stella` and `GS2` would be a valuable area of future research.

The implementation of the electromagnetic nonlinear term is in progress. This is a particularly important piece of ongoing work which would pave the way towards a fully implicit nonlinear EM local δf gyrokinetic implementation (together with the material presented in chapter 8).

Whilst there are currently some unexplained features of the EM `stella` implementation, it appears that accurate results can be obtained at reasonable simulation resolution. This is put to use in the following chapter where electromagnetic instabilities in the Wendelstein 7-X stellarator are preliminarily explored.

Chapter 7

A study of the stability valley in the Wendelstein 7-X stellarator

7.1 Introduction

Although the stellarator concept has existed for over seventy years [111], studies of their transport have tended to focus on neoclassical transport, rather than turbulence, since the former has been historically dominant in experiments. This high neoclassical transport arises from the trajectories of particles "trapped" in regions of weak field [112, 113] by the magnetic mirror force, for which the bounce-averaged radial magnetic drift is nonzero in general. Trapped particles secularly drifting away from their original flux surface gives rise to high transport compared with neoclassical transport in tokamaks, or with turbulent transport. For this reason, stellarator microstability and turbulence research is still in relative infancy.

However, several decades of study have arrived at "optimised" stellarator configurations, in which trapped particle trajectories remain (almost) local to a flux surface (i.e. the bounce-averaged radial drift nearly vanishes). This property is known as omnigeneity [114], and includes several classes of magnetic topology, such as quasi-axisymmetry, quasi-helical symmetry and quasi-isodynamicity. Modelled neoclassical transport levels in omnigenous or near-omnigenous stellarators is similar to that of tokamaks, and comparable to or lower than estimated turbulent transport. The relative importance of turbulence in such optimised stellarators behooves the study of their microstability.

The largest optimised stellarator in the world is Wendelstein 7-X (W7-X), a large, HELIAS-type [115], nearly quasi-isodynamic stellarator. A primary goal of W7-X is to demonstrate long ($\geq$ 1800s) pulses with fusion-relevant plasma conditions, though without DT fuel [116]. W7-X began operating in 2015 [116], and has been able to sustain long (up to $\sim$ 100s), stable pulses with good core conditions and low neoclassical transport [116–119]. High-performance shots in W7-X have reported plasma densities of $1 - 4.5 \times 10^{19}\mathrm{m}^{-3}$, electron temperatures of $5 - 10$keV and the highest ever stellarator fusion triple product ($nT_i\tau_E = 6.5 \times 10^{19}$keV·m^{-3}s) [29, 118].

Regarding microstability, theoretical studies of quasi-isodynamic stellarators in general [120–122] and W7-X in particular [32, 121] indicate novel microstability properties arising from their complex magnetic geometry. An example in W7-X, and the focus of this research, is the so-called "stability valley" [32, 121], in which instability growth rates are suppressed when the temperature and density gradient length scales are approximately equal. This could plausibly enable plasmas to sustain large kinetic gradients with low heating and fuelling; a highly desirable regime for economically viable fusion reactors.

In this chapter, I use the code `stella` to investigate the electrostatic stability valley in W7-X plasmas. I first provide a brief background on neoclassical optimisation in stellarators, W7-X and the stability valley. I then describe the magnetic geometries and simulation parameters used in my study (section 7.3), followed by an exploration of the stability valley using linear simulations (sections 7.4 and 7.5). Conclusions, including a discussion of the validity and limitations of this research, are presented in section 7.7.

7.1.1 Acknowledgements

This research was performed in collaboration with the CIEMAT group in Madrid, in particular, with Dr José-Manuel García-Regaña, Hanne Thienpondt and Antonio González-Jerez. All results presented here are my own, but interpretation and discussion makes reference to additional research performed by the CIEMAT group. This research is acknowledged and, where possible, cited. This research collaboration was tangentially useful to a study of impurity transport in W7-X by García-Regaña *et al.*[123], although that is not the focus of this chapter.

7.2 Omnigeneity in stellarator plasmas

In order to study neoclassical transport in 3D equilibria, it is instructive to consider a simplified model in which collisions, instabilities and turbulence are ignored. Thus, the dynamics of charged particles are determined only by the equilibrium magnetic and electric fields, and transport can be explored by considering trajectories of single particles. In the material presented here (based heavily on Helander

[114]), arguments about stellarator optimisation are made using a Lagrangian formulation for the guiding centre trajectories and making an asymptotic expansion in $\rho_* \equiv \rho_s/a$.

Using the coordinate system (ψ, α, z) described in section 3.2.1, one can write the Lagrangian L for the guiding centre of a charged particles as

$$\begin{aligned} L = T - V &= \frac{m\left(\mathbf{b}\cdot\frac{\partial \mathbf{X}_s}{\partial t}\right)^2}{2} + Z_s e\mathbf{A}\cdot\frac{\partial \mathbf{X}_s}{\partial t} - \mu_s B - Z_s e\varphi && (7.2.1)\\ &= \frac{m}{2}\left[\frac{\partial z}{\partial t} + \mathbf{b}\cdot\left(\frac{\partial \mathbf{X}_s}{\partial \psi}\frac{\partial \psi}{\partial t} + \frac{\partial \mathbf{X}_s}{\partial \alpha}\frac{\partial \alpha}{\partial t}\right)\right]^2 - Z_s e\alpha\frac{\partial \psi}{\partial t} - \mu_s B - Z_s e\varphi, && (7.2.2) \end{aligned}$$

and the Hamiltonian H as

$$\begin{aligned} H &= \mathbf{P}\cdot\frac{\partial \mathbf{X}_s}{\partial t} - L && (7.2.3)\\ &= \frac{mv_\parallel^2}{2} + \mu_s B + Z_s e\varphi, && (7.2.4) \end{aligned}$$

(equal to the total energy of the guiding centre), where

$$\mathbf{P} = \frac{\partial L}{\partial\left(\frac{\partial \mathbf{X}_s}{\partial t}\right)}. \qquad (7.2.5)$$

Eq. (7.2.4) can be rearranged to provide an expression for $v_\parallel$:

$$v_\parallel = \pm\sqrt{\frac{2(H - \mu_s B - Z_s e\varphi)}{m}}. \qquad (7.2.6)$$

Then, using the Euler-Lagrange equations one can arrive at

$$\frac{\mathrm{d}}{\mathrm{d}t}\left(\psi + \frac{mv_\parallel}{Z_s e}\mathbf{b}\cdot\frac{\partial \mathbf{X}_s}{\partial \alpha}\right) = \frac{m_s v_\parallel}{Z_s e}\left.\frac{\partial v_\parallel}{\partial \alpha}\right|_{H,mu_s,\psi,z}. \qquad (7.2.7)$$

$\frac{\mathrm{d}\psi}{\mathrm{d}t}$ represents the leading order radial drift velocity of a guiding centre (which is $\mathcal{O}(\rho_* v_{th,s})$).

To examine the confinement of the particles, one can consider the radial drift $\Delta\psi$ between two points z_1 and z_2:

$$\Delta\psi \equiv \int_{z_1}^{z_2} \frac{\partial\psi}{\partial t} dt = \int_{z_1}^{z_2} \frac{m_s v_\|}{Z_s e} \left.\frac{\partial v_\|}{\partial\alpha}\right|_{H,mu_s,\psi,z} \frac{dz}{v_\|} \tag{7.2.8}$$

$$= \frac{m_s}{Z_s e} \int_{z_1}^{z_2} \left.\frac{\partial v_\|}{\partial\alpha}\right|_{H,mu_s,\psi,z} dz \tag{7.2.9}$$

$$= \frac{1}{Z_s e} \left.\frac{\partial\mathcal{J}}{\partial\alpha}\right|_{H,\mu_s,\psi,z}, \tag{7.2.10}$$

where $\mathcal{J}$ is defined:

$$\mathcal{J}(\psi, \alpha, \varepsilon, \mu) \equiv \int_{z_1}^{z_2} m v_\| \mathrm{d}z. \tag{7.2.11}$$

It is possible to show [113] that for passing particles, $\Delta\psi = 0$ when the arc length $z_2 - z_1$ is large (i.e. in the limit that many toroidal turns are taken). Thus, passing particles are well-confined to first order in ρ_*.

Trapped particles present a greater challenge, since $\Delta\psi$ taken between two successive bounce points (z_1, z_2) is nonzero unless $\frac{\partial\mathcal{J}}{\partial\alpha}\big|_{H,\mu_s,\psi,z} = 0$. This condition can be met in several ways. One way is to ensure that the magnetic field strength is (locally) independent of α i.e. $B = B(\psi, z)$; thus $v_\|$ and hence $\mathcal{J}$ are independent of α and so $\Delta\psi = 0$. It can be shown [114] that this requires the magnetic field be expressible as $B = B(\psi, M\theta_B - N\phi_B)$ for a single value of (M, N), where θ_B and ϕ_B are poloidal and toroidal Boozer coordinates [124]. Depending on the values on M and N, this is known as quasi-axisymmetry (QAS) ($N = 0$), quasi-poloidal symmetry (QPS) ($M = 0$) or quasi-helical symmetry (QHS) ($M \neq 0$, $N \neq 0$). The prefix “quasi” is used because B is independent of α but other properties of the magnetic geometry are not; a QAS stellarator is not fully axisymmetric, unlike the magnetic geometry of a tokamak.

It is possible for a plasma to satisfy omnigeneity without being quasi-symmetric. A particular example of this is for the plasma to be quasi-isodynamic (QID), in which the magnetic field strength *cannot* be written $B = B(\psi, z)$, but nevertheless, contours of B on each surface are poloidally closed. QID configurations are of particular interest since they also minimise the bootstrap current [28]. Unfortunately, it has been shown that it is impossible for stellarators to achieve exact QAS, QHS, QPD or QID [125, 126], although plasmas can very closely approximate QAS, QHD and QID [113]. Landreman and Paul [127] have recently reported near-perfect computer-generated QAS and QHS equilibria with deviations from quasisymmetry reduced to as low as $\delta B/B_{0,0} \leq 5 \times 10^{-5}$, where δB is the deviation and $B_{0,0}$ the mean magnetic field.

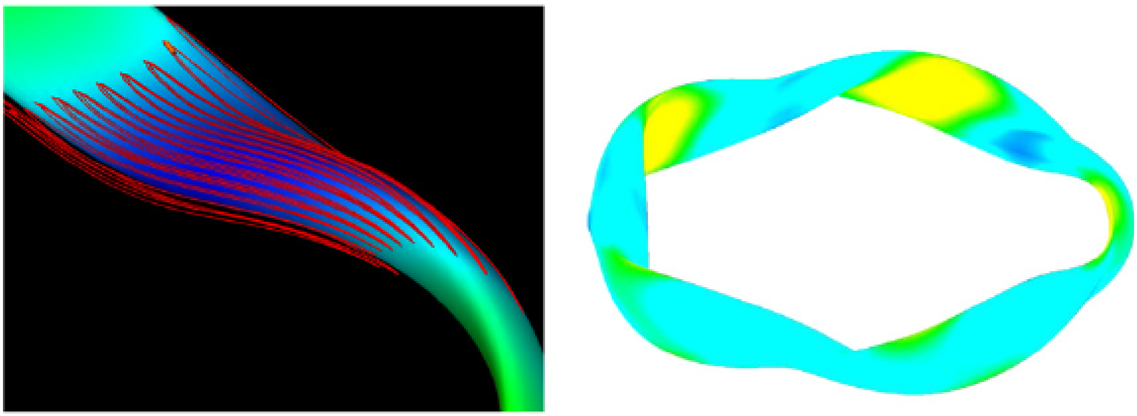

Figure 7.1: Left: Trapped particle orbits in W7-X, precessing poloidally on a flux surface. Right: Magnetic field strength on the outermost flux surface of W7-X. Reproduced from [28]

A final point to note for omnigenous plasmas is that $\frac{\partial \mathcal{J}}{\partial \alpha}\big|_{H,\mu_s,\psi,z} = 0$ implies that $\mathcal{J}$ is a flux surface quantity, and is conserved (and is referred to as the second, or parallel, adiabatic invariant).

7.2.1 Wendelstein 7-X equilibria

Since the deficiencies of “classical stellarators” have been known, theoretical research on stellarator optimisation has been performed in tandem with experiment [128]. The first “advanced stellarator” was the partially-optimised stellarator W7-AS [129]. Its successor, W7-X, was designed using a “unified” optimisation procedure [128] which sought to minimise the neoclassical transport and maximise the confinement of collisionless fast α particles, subject to a constraint of small bootstrap current.

An example of a W7-X equilibrium is given in figure 7.1. The left plot shows a trapped particle trajectory, which is confined to a region of weak B and precesses poloidally around the flux surface, without net radial transport. The right plot shows the magnetic field strength B of a surface in W7-X. W7-X is “max-$\mathcal{J}$” configuration, meaning that $\mathcal{J}$ is maximum on the magnetic axis [120]. Having $\frac{\partial \mathcal{J}}{\partial \psi} < 0$ has been shown to bestow favourable microstability properties with regards to the interchange instability [130].

7.3 Simulation details and convergence tests

The work presented here considers three W7-X reference magnetic geometries, referred to in literature as EIM (“standard”), KJM (“high mirror”) and FTM/FSM (“high iota”) configurations [131]. In the electrostatic studies, I use the vacuum field (i.e. $\beta = 0$) equilibria. In each, I select the $s = \psi_{\text{tor}}/\psi_{\text{tor},LCFS} = 0.49$ surface for study, where ψ_{tor} is the toroidal flux function. This corresponds to a radius of $r/a = 0.7$ (where r is the flux surface minor radius and a is the device minor radius).

Measurements of (n, T_i, T_e) profiles reported by Carralero *et al.* [119] for an EIM configuration, reproduced in figure 7.2, are used to estimate the experimentally relevant ranges of these values. These discharges are split into 3 categories: (1) discharges heated entirely by Electron Cyclotron Resonance Heating (ECRH), fuelled by gas puff (collectively referred to as "ECRH" discharges), (2) discharges heated by a mixture of ECRH and neutral beam injection ("NBI") and (3) ECRH-heated discharges in which cryogenic fuel pellets are injected ("HP"). These are referred to as "High Performance" discharges since the pellet injection transiently boosts the core ion temperature, plasma density, stored energy and energy confinement time. In cases (1) and (2), the normalised kinetic gradients (a/L_{ne}, a/L_{Ti}, a/L_{Te}) (where $a/L_A = -d\ln A/d\rho$ is the gradient length scale of A and $\rho = r/a$) vanish on the magnetic axis, become large near the plasma edge, and in the intervening region, either increase monotonically or plateau across part of the core ($0.3 \lesssim r/a \lesssim 0.7$). For $r/a = 0.7$, the ranges of the gradients are ($a/L_{ne} \lesssim 1$, $a/L_{Ti} \lesssim 5$ and $3 \lesssim a/L_{Te} \lesssim 5$). In case (3), a/L_{ne} and a/L_{Te} increase monotonically across the plasma with ($a/L_{ne}(r/a = 0.7) \sim 2$, $a/L_{Te}(r/a = 0.7) \sim 6$). a/L_{Ti} peaks around $r/a = 0.8$ and has $a/L_{Ti}(r/a = 0.7) \sim 6$. Applying this range of gradients to other magnetic geometries is a theoretical, rather than validation, exercise.

In this work I perform gyrokinetic simulations with `stella` (commit `5a0c0b`), scanning $\tilde{k}_y$ and $(a/L_{n,T})$. I take the ion species as the reference species (such that $\tilde{m}_i = \tilde{n}_i = \tilde{T}_i = 1$ and $\tilde{k}_y = k_y\rho_i$) and assume a deuterium plasma (so that $\tilde{m}_e = 2.8 \times 10^{-4}$). Impurity species are ignored in this work, although they would likely have some effect on the microstability and turbulence.

It should also be noted that in these simulations I only consider a single magnetic field line ($\alpha = 0$) (i.e. the toroidal location at which the magnetic field line passes through the outboard midplane is the centre of a field period), which is a common choice as it often corresponds to the most unstable field line [123]. This could be relaxed in future work. A gyrokinetic electron species is included in all results presented here.

The dependence of the complex frequency $\tilde{\Omega} = \tilde{\omega} + i\tilde{\gamma}$ on non-physical simulation parameters is tested as follows. I first construct a fiducial simulation using the "EIM" equilibrium with physical parameters ($\tilde{k}_y = 3.5$, $a/L_n = a/L_T = 3$) and reasonably-chosen non-physical parameters. This simulation is run for sufficiently long $\tilde{t}$ that $\tilde{\Omega}(t)$ converges (so that $\tilde{\Omega}$ does not change with increasing $\tilde{t}$ to within $\sim \mathcal{O}(10^{-6}\%)$). I then independently adjust the non-physical parameters which determine the simulation timestep, the z grid and the velocity-space grid, until $\tilde{\Omega}$ varies by less than 2% with increased fidelity. These parameters are used to construct a template for the simulations. I again test

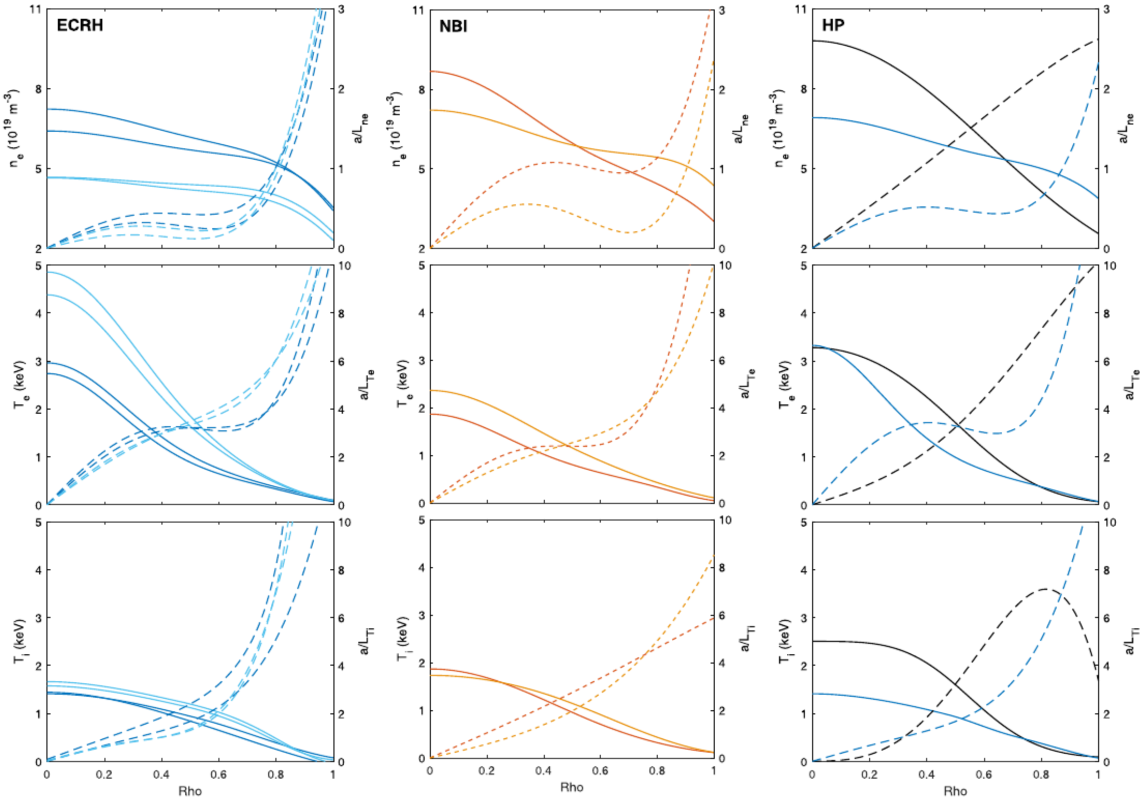

Figure 7.2: Experimentally measured profiles of plasma density n_e and ion (electron) temperature $T_{i(e)}$. $\rho \equiv r/a$. Reproduced from Carralero *et al.* [119]."HP" includes profiles before pellet injection (blue) and post-pellet injection (black).

the variation of $\tilde{\Omega}$ against non-physical parameters using this template. The results, shown in table 7.1, indicate a change in $\tilde{\Omega}$ of under 2% with increasing fidelity in the simulation parameters n_z, n_{fp}, `nvgrid`, $n_{\tilde{\mu}_s}$, $\tilde{v}_{\|,\text{max}}$, $\tilde{v}_{\perp,\text{max}}$ $\Delta\tilde{t}$. When increasing n_{fp}, n_z was also increased by the same factor to keep the z resolution (n_z/n_{fp}) constant. Similarly, $n_{\tilde{v}_\|}$ and $n_{\tilde{\mu}_s}$ were increased when $\tilde{v}_{\|,\text{max}}$ and $\tilde{v}_{\perp,\text{max}}$ were increased, respectively.

I show the shape of the flux surfaces for the EIM equilibrium, including the flux surface chosen, in figure 7.3. I also show the magnitude of the equilibrium magnetic field $\tilde{B}_0$ within the parallel simulation domain used and the distribution of gridpoints in $(\tilde{v}_\|, \tilde{\mu}_s)$ space in figure 7.4.

Some illustratory characteristics of a gyrokinetic simulation performed with $\tilde{k}_y = 3.5$, $a/L_n = a/L_{Ti} = a/L_{Te} = 3$ are shown: $\tilde{\Omega}(\tilde{t})$ (figure 7.5, left), the mode structure $\tilde{\varphi}_{1\mathbf{k}}(z)$ corresponding to $\tilde{g}_{\mathbf{k},s}(\tilde{t} = \tilde{t}_{\text{final}})$ (figure 7.5, right) and $\tilde{g}_{\mathbf{k},s}(\tilde{v}_\|, \tilde{\mu}_s, \tilde{t} = \tilde{t}_{\text{final}})$ in velocity space (figure 7.6). These serve to illustrate some general features of local linear gyrokinetic simulations and stellarator microinstabilities: (1) $\tilde{\Omega}(t)$ converges after some initial transient behaviour, (2) instability amplitudes tend to peak in the region(s) of weak magnetic field (3) the instability distribution functions g_i, e have fine

Simulation parameter	Value	higher-fidelity value	$\Delta\tilde{\omega}(\%)$	$\Delta\tilde{\gamma}(\%)$
n_z	256	512	2.2	1.1
n_{fp}	20	40	0.21	0.58
$n_{\tilde{v}_\parallel}$	72	144	0.91	1.2
$n_{\tilde{\mu}_s}$	24	48	0.023	0.16
$\tilde{v}_{\parallel,\mathrm{max}}$	3.0	4.0	0.16	0.0085
$\tilde{v}_{\perp,\mathrm{max}}$	3.0	4.0	0.070	0.19
$\Delta\tilde{t}$	0.05	0.025	0.40	1.6

Table 7.1: Non-physical simulation parameters used in linear parameter scans for this investigation. The change in $\tilde{\Omega} = \tilde{\omega} + i\tilde{\gamma}$ when these parameters are replaced with higher-fidelity values is shown.

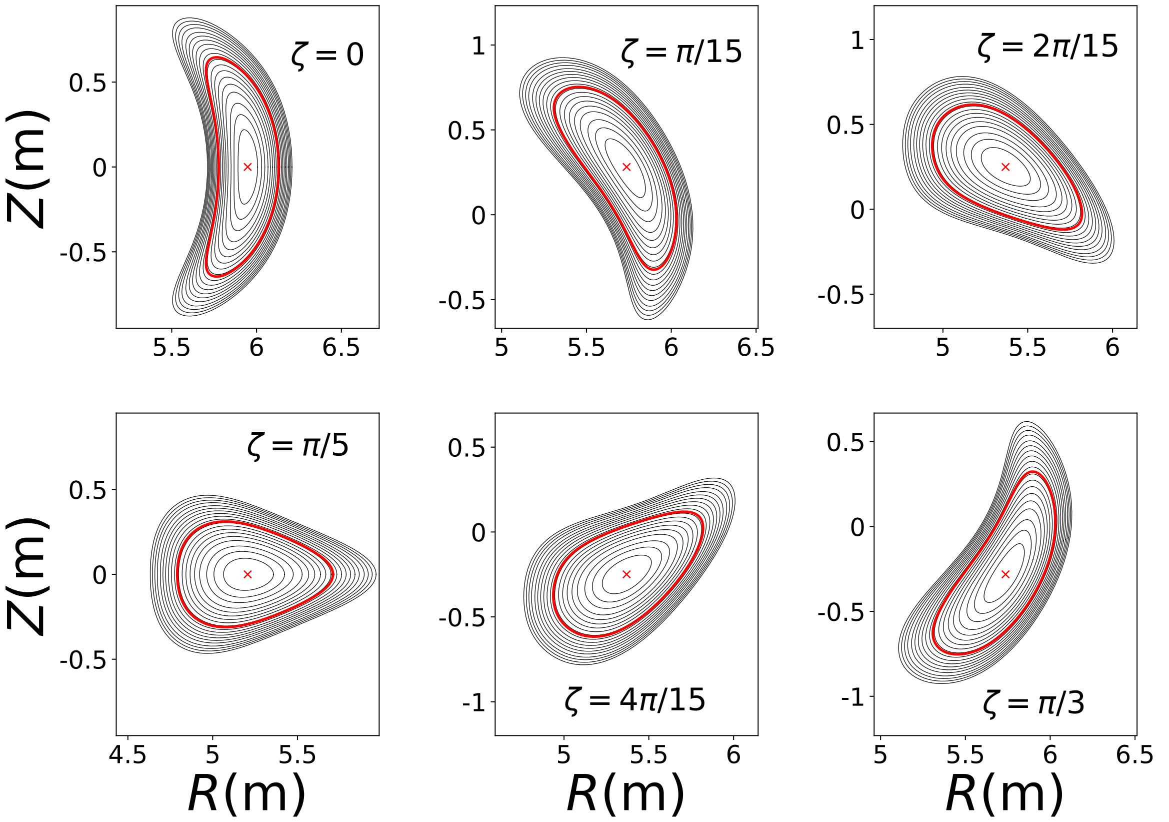

Figure 7.3: Flux surface shapes at varying toroidal angle ζ, spanning a single toroidal field period, with the flux surface used for this study ($r/a = 0.7$) in red. Generated using STELLOPT [132].

and non-Maxwellian structure in $(\tilde{v}_\parallel, \tilde{\mu}_s)$.

7.4 Instability characteristics

I first present (in figure 7.7) $\tilde{\Omega}(\tilde{k}_y)$ for the "standard" (EIM) W7-X configuration, and some example mode structures, for three sets of kinetic gradients: (1) $a/L_n = 0, a/L_{T,i} = a/L_{T,e} = 6$, (2) $a/L_n = 6, a/L_{T,i} = a/L_{T,e} = 0$ and (3) $a/L_n = a/L_{T,i} = a/L_{T,e} = 3$. Properties of these scans are discussed below.

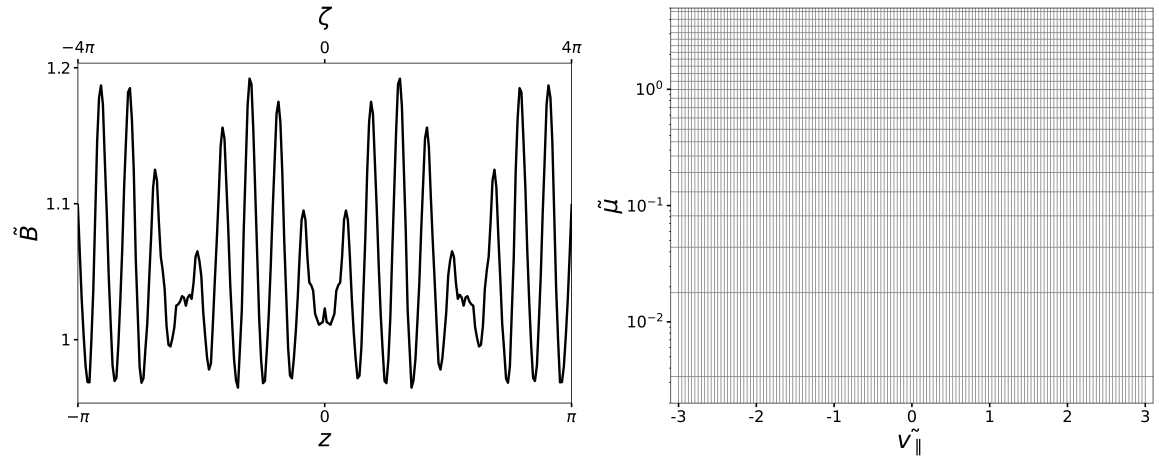

Figure 7.4: Left: $B(z)$ for the simulation domain. Right: values of $\tilde{v}_\parallel$ (indicated by vertical lines) and $\tilde{\mu}_s$ (horizontal lines) simulated.

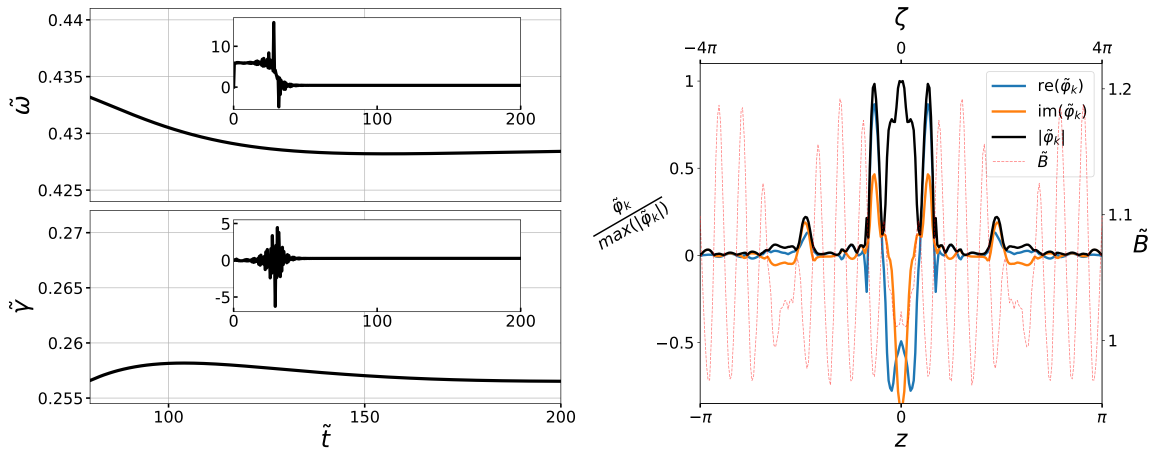

Figure 7.5: Left: $\tilde{\Omega}(t)$. Right: $\tilde{\varphi}_{1\mathbf{k}}(z)$ at $t = t_{\mathrm{final}}$ (solid lines, normalised to 1) with $B(z)$ shown for reference (dotted red line).

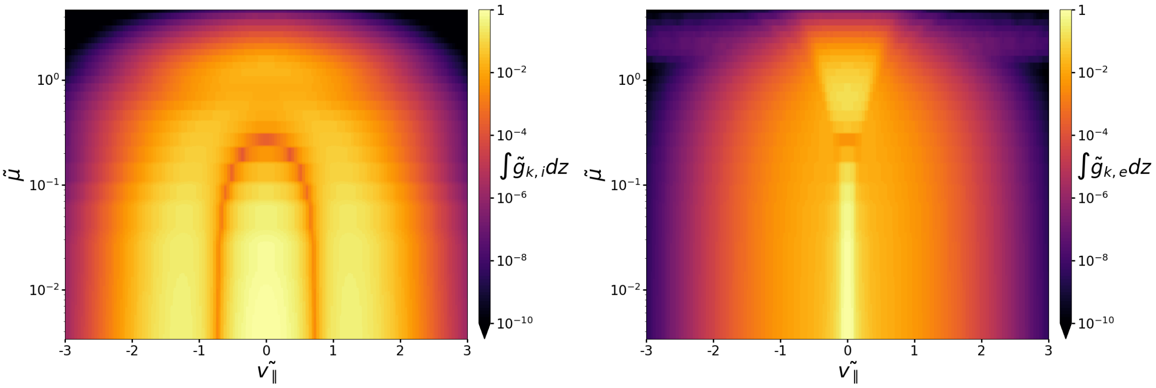

Figure 7.6: Structure of the distribution function $g_{i,e}(\tilde{v}_\parallel, \tilde{\mu}_s)$, averaged over z and normalised to 1.

In all cases, $\tilde{\gamma} \to 0$ as $\tilde{k}_y \to 0$. This can be explained by considering the diamagnetic-like term, $i\omega_{*,\mathbf{k},s} J_0(\gamma_s)\tilde{\varphi}_{1\mathbf{k}}$, responsible for "driving" the mode. If one allows $\tilde{k}_x = 0$, then $J_0(\gamma_s) \to 1$ as $\tilde{k}_y \to 0$ (as the instabilities become spatially large compared to the species gyroradii, gyroaveraging has increasingly little effect on the instability dynamics). However, the prefactor

$$\omega_{*,\mathbf{k},s} = \frac{\tilde{k}_y}{2} a B_r \frac{dy}{d\alpha} e^{-\tilde{v}_s^2} \frac{d \ln F_{0s}}{\psi} \tag{7.4.1}$$

vanishes as $\tilde{k}_y \to 0$. Thus, the driving term vanishes, and the mode becomes linearly stable.

In case (1), the dominant instability is a positive frequency mode (i.e. in the ion diamagnetic direction) which is most strongly growing ($\tilde{\gamma}$ peaks) around $\tilde{k}_y \sim 1.5$. This is the ion temperature gradient mode (ITG) [133]. For $\tilde{k}_y \gtrsim 3$, another mode becomes dominant with the opposite frequency, for which $\tilde{\gamma}$ increases with $\tilde{k}_y$. This is likely a electron temperature-gradient driven trapped electron mode (TEM) [134]. If one sets $a/L_{Te} = 0$, the dominant mode switches sign of frequency and the growth rate is reduced. However, as shown in figure 7.7 (right), these modes are highly extended in z and would need an increased parallel domain to robustly capture the mode properties. Thus, these higher-$\tilde{k}_y$ results presented here should be read qualitatively, rather than quantitatively.

In case (2), several distinct modes, each with their own peak in $\tilde{\gamma}$, appear in at low $\tilde{k}_y$. The negative frequency modes present in the region $\tilde{k}_y \lesssim 5$ are likely the density-driven TEM; these modes are completely stabilised when the electrons are simulated as adiabatic (i.e. when trapped electron dynamics are not simulated). At higher $\tilde{k}_y$ (beyond that shown in figure 7.7), the dominant instability also becomes a positive-frequency electron-scale mode. Both the TEM and the ITG in case (1) have a mode structure largely confined to the central magnetic well of the flux tube.

Case (3), in which the total pressure gradient is the same but "split" between temperature and density contributions, shows reduced $\tilde{\gamma}(\tilde{k}_y)$ across the $\tilde{k}_y$ range scanned. The dominant instability has a smoothly changing mode structure above $\tilde{k}_y \sim 2.4$, and peaks at $\tilde{k}_y \sim 4$. This mode is likely the ITG-TEM "mixed mode" (or "ion-driven trapped electron mode", ITEM) reported by Alcusón *et al.* [32]. As shown in figure 7.7 (right), the mode structure is a little different to the ITG or TEM, and has several large peaks in adjacent magnetic wells. The improved stability, for constant $(a/L_n + a/L_T)$, is the hallmark of the "stability valley".

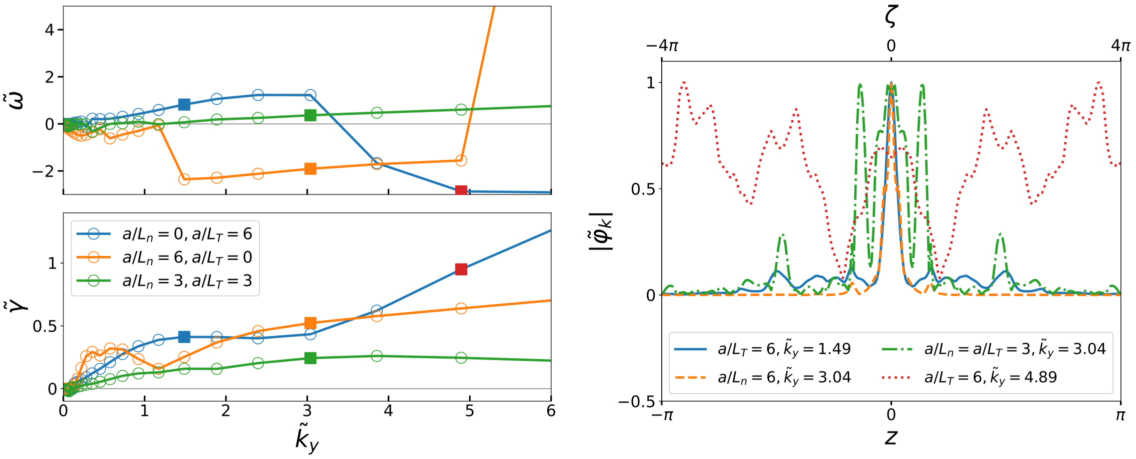

Figure 7.7: Left: Growth rate $\tilde{\gamma}(\tilde{k}_y)$ (upper) and frequency $\tilde{\omega}(\tilde{k}_y)$ for 3 sets of kinetic gradients $(a/L_n, a/L_T)$ EIM W7-X configuration. Right: mode structures $|\phi(z)|$ for distinct instabilities. Filled squares in left plot indicates data points used for the mode structures.

7.5 The stability valley in W7-X equilibria

I next investigate the stability valley in the EIM configuration by scanning a/L_n and a/L_T (with $a/L_{T,i} = a/L_{T,e}$ in all cases). The linear growth rates and frequencies for several $\tilde{k}_y$ values (1.5, 3 and 4.5) are shown in figure 7.8. In all cases some common features are observed: (1) an ITG driven unstable at low (a/L_n), high (a/L_T), (2) a TEM driven unstable at high (a/L_n), low (a/L_T), and a "valley" of reduced $\tilde{\gamma}$ where $L_n \sim L_T$, in which the frequency is positive, corresponding to the mixed mode. The reason for the existence of the valley (argued by Alcusón *et al.* [32]) it that in W7-X the trapped electron population are largely separated from regions of large and unfavourable magnetic curvature [135]. This means that for the ITEM which is dominant, the contribution of the trapped electrons in conjunction with the density gradient has an overall stabilising effect. At $\tilde{k}_y = 4.5$ (figure 7.8, rightmost plot), growth rates increase sharply beyond $a/L_n \gtrsim 7$ for all a/L_T. This could provide a critical density gradient, although the experimental profiles shown in figure 7.2 suggest this is beyond the experimentally relevant range of a/L_n.

The same features appear in the KJM and FSM configurations; figure 7.9 shows $\tilde{\Omega}(a/L_n, a/L_T)$ for both with $\tilde{k}_y = 3$. I also note that the growth rates magnitudes, when appropriately renormalised, are in reasonable agreement with Alcusón *et al.* (who produce similar plots, but showing the largest growth rates over a range of $k_y\rho_i$). Rigorous quantitative comparison between `stella` and Alcusón *et al.* was not performed but would be a valuable piece of future work.

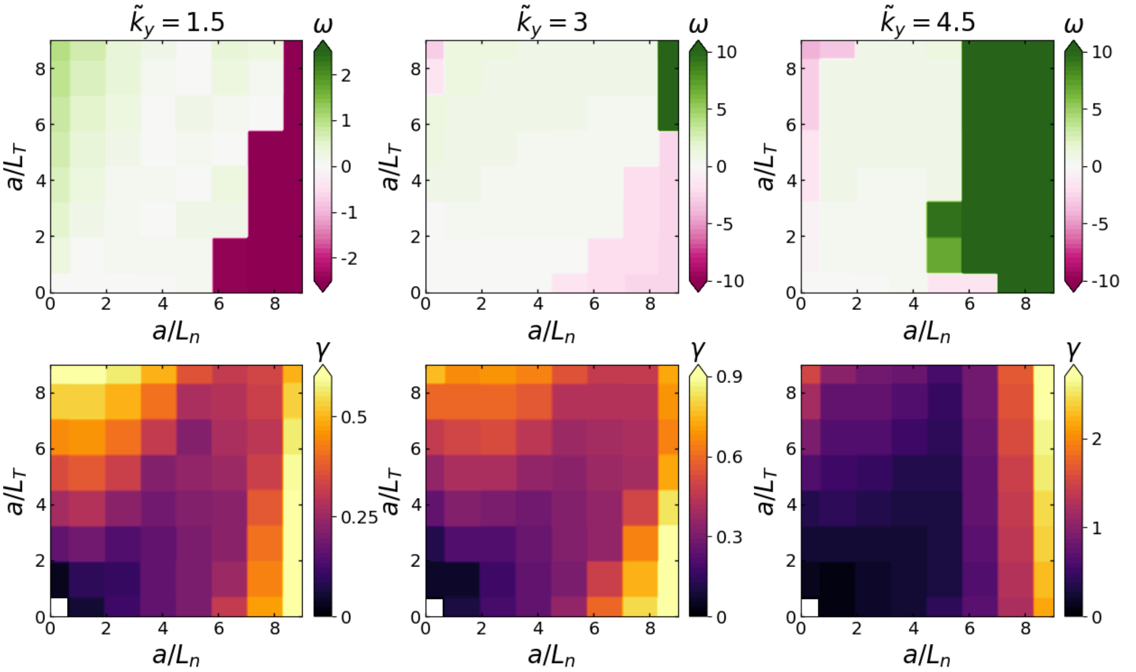

Figure 7.8: (Upper) frequency and (lower) growth rate and for “standard” EIM configuration for varying density and temperature gradients. Left: $k_y\rho_i = 1.5$. Middle: $k_y\rho_i = 3$. Right: $k_y\rho_i = 4.5$

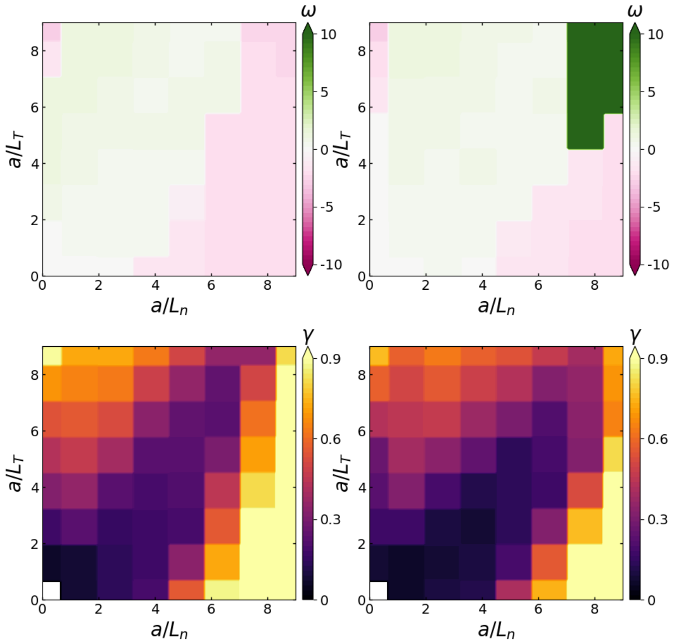

Figure 7.9: $\tilde{\Omega}(a/L_N, a/L_T)$ for “high iota” FTM/FSM (left) and “high mirror” KJM (right) configurations in W7-X.

7.5.1 Validity, complementary research and future work

This linear study illustrates a reduction of microstability growth rates where $a/L_T \sim a/L_n$. One may therefore expect that heat and particle fluxes are reduced where $a/L_T \sim a/L_n$. If so, this could explain the improved performance in the "HP" discharges; pellet injection causes the density profile to peak, increasing a/L_n such that $(a/L_n)/(a/L_T)$ approaches unity. This reduces turbulent transport, hence transiently increasing T_i and τ_E.

However, it is worth making some qualifying remarks for this study. Firstly, I only consider a single value of α (i.e. these results are only valid in the vicinity of a single magnetic field line), and a single value of $\tilde{k}_x$ ($\tilde{k}_x = 0$). ($\alpha = \tilde{k}_x = 0$) often corresponds to the most unstable mode, and is likely to provide the dominant contribution to the turbulence. However, instability characteristics of other $\tilde{k}_x$ values are likely to impact the nonlinear dynamics of the turbulence. A fuller picture of the "stability valley" thus requires nonlinear simulations of multiple flux tubes (or indeed, full flux-surface simulations), which could provide quantitative estimates of heat and particle transport.

One nonlinear study, performed by Thienpondt *et al.* [136, 137], simulates the $\alpha = 0$ flux tube at $r/a = 0.49$ of the EIM vacuum field equilibrium using `stella`. Increasing $a/L_n = 1$ to $a/L_n = 2$ at fixed $a/L_{Ti} = a/L_{Te} = 3$ reduces Q_i/Q_{GB} by a factor of 3 whereas $\tilde{\gamma}$ for the most unstable $\tilde{k}_y < 2$ mode falls by $\sim 12\%$; this weak correlation (which is also seen in other stellarator simulations) indicates that the linear stability valley is not the full picture. A weak correlation between $\tilde{\gamma}$ and turbulent fluxes in stellarators is also reported by García-Regaña *et al.* [123]. A second nonlinear study, performed by Xanthopoulos *et al.* [138], also finds a strong reduction in ion heat diffusivity as the stability valley is entered and concludes that this is the result of a transition from ITG-driven turbulence to ITEM. The authors also note that the poloidal rotation generated by the ambipolar radial electric field in W7-X has an additional stabilising effect.

A final caveat is that these simulations are electrostatic ($\tilde{A}_{1\|\mathbf{k}} = \tilde{B}_{1\|\mathbf{k}} = 0$), and thus only strictly valid in the limit $\beta = 0$. The high-performance shots reported a volume-averaged β of $\langle\beta\rangle = 1.5\%$ and achieving $\langle\beta\rangle$ up to 5% is mooted [118]. Thus, finite β effects may substantially alter the dynamics of the instabilities. I perform some preliminary investigations at finite β in the following section.

7.6 Electromagnetic simulations in W7-X equilibria

Electromagnetic simulations are performed using the electromagnetic version of `stella` (commit `f5355ba`) (I refer to this latter as "`EM stella`" to differentiate from the main branch of the code, which I refer to as "original `stella`" (commit `5a0c0b`)) described in chapter 6. For most of this work I use the EIM $\beta = 0$ ("vacuum field") equilibrium. It should be stressed that this equilibrium is not consistent with finite β, and for a self-consistent W7-X simulation one requires finite-β equilibria. The inconsistent approach is used here to enable β to be scanned easily, and to give qualitative indications of how finite β may change the nature of microinstabilities. To check if the results are similar in a finite-β equilibrium and across different W7-X geometries, some analysis is repeated using a KJM equilibrium with $\langle\beta\rangle = 3\%$.

This work consists of the following: Firstly, I compare the two versions of `stella` electrostatically, since `EM stella` formulates the GKE differently (with source terms in $\tilde{h}_{\mathbf{k},s}$ rather than $\tilde{g}_{\mathbf{k},s}$). Secondly, β is scanned for a given $(a/L_n, a/L_T, \tilde{k}_y)$, showing the transition from drift wave instabilities to the KBM. The "stability valley" plots (figure 7.8) are reproduced at finite β to study the effect on the valley at finite β. Finally, results KJM $\langle\beta\rangle = 3\%$ equilibrium are compared.

7.6.1 Centering of derivatives $\frac{\partial}{\partial z}$, $\frac{\partial}{\partial \tilde{t}}$, $\frac{\partial}{\partial \tilde{v}_\parallel}$

In the EM slab simulations presented in section 6.4.2 it is found that $u_z = 0$ is required for numerical stability and $\tilde{\gamma}$ is sensitive to u_t, resulting in the choice $u_z = u_t = 0$ for fiducial simulations. However, in electrostatic (ES) W7-X simulations this choice it is found to cause numerical instability. EM simulations with small spatial upwinding have also reported numerical instability in `GS2` [139] (which recommends a small amount of spatial upwinding for ES simulations but zero spatial upwinding for EM simulations [140]), and thus may be a general feature of the electromagnetic implicit algorithm. The work presented selects u_z, u_t and $u_{v_\parallel}$ according to the following rules:

1. For original `stella` the default upwinding choices ($u_t = u_z = u_{v_\parallel} = 0.02$) are used.
2. For partially implicit `EM stella` simulations ($u_t = u_z = 0.02$, $u_{v_\parallel} = 0$) are used for ES simulations and ($u_t = u_z = u_{v_\parallel} = 0$) for EM simulations.
3. For fully explicit `EM stella` $u_{z,\mathrm{exp}} = 0.1$ is always used.

7.6.2 Electrostatic comparison between original `stella` and `EM stella`

Electrostatic simulations are run using the EIM vacuum field configuration, with ($a/L_n = 3 = a/L_{T,i} = a/L_{T,e} = 3$, $\tilde{k}_y = (1, 3.5)$), using the simulation parameters given in table 7.1. For each code version, the simulation is run fully explicitly using the SSP-RK2 scheme, and again using the implicit treatment of streaming and the mirror term. In the latter case the simulation timestep is set to $\Delta\tilde{t} = 0.05$; in the former it is restricted by the CFL constraint to $\Delta\tilde{t} = 0.002$. n_{step} is kept constant for fully explicit and partially implicit simulations individually, but is greater in the former case (2×10^5 compared to 5×10^3) due to the smaller timestep. Fully explicit simulations are run in parallel over 16 cores, and partially implicit simulations over 4 cores.

A comparison of computational cost (CPU minutes per unit $\tilde{t}$ simulated) and $\tilde{\Omega} = \tilde{\omega} + i\tilde{\gamma}$ are summarised in table 7.2 and mode structures shown in figure 7.10. For $\tilde{k}_y = 1$, there is agreement to within around 5% between the two original `stella` simulations and partially implicit `EM stella`. There is also particularly good agreement in $|\tilde{\varphi}_{1\mathbf{k}}|(z)$ between partially implicit original `stella` and partially implicit `EM stella`. The fully explicit `EM stella` simulation converges more slowly with $\tilde{t}$, which results in a greater uncertainty in $\tilde{\omega}$ and $\tilde{\gamma}$. There is poorer agreement in $\tilde{\omega}$ and $|\tilde{\varphi}_{1\mathbf{k}}|(z)$ for this simulation.

$\tilde{k}_y = 3.5$ converges more quickly due to the larger instability growth rate. The disagreement across simulations is between (2%-15%) for $\tilde{\omega}$ and between (0.8%-4%) for $\tilde{\gamma}$, with $\Delta\tilde{\omega} \sim \Delta\tilde{\gamma} \sim 2\%$ between partially implicit original `stella` and `EM stella`. This is in qualitative agreement with $|\tilde{\varphi}_{1\mathbf{k}}|(z)$, showing strong similarity between partially implicit schemes. It is possible that the dominant cause of disagreement is caused by different treatments of $\frac{\partial}{\partial z}$, since the mode has sharp variation in z and would therefore be sensitive to how this derivative is calculated (though these difference are expected to vanish in the limit $n_z \to \infty$). $\frac{\partial}{\partial z}$ is calculated in the same way in the partially implicit simulations which would explain their good agreement.

Regarding computational cost, two trends are observed: (1) fully explicit simulations are more expensive per unit $\tilde{t}$ than partially implicit simulations (because the timestep $\Delta\tilde{t}$ is much smaller) and (2) `EM stella` is cheaper than original `stella` by a factor of around $1.5 - 2$ implicitly and $3 - 3.7$ explicitly. A more rigorous investigation would be required to come to a robust conclusion on the savings realised by using `EM stella`, and one should also bear in mind the slow convergence of fully explicit `EM stella`. However, one can speculate that the lower cost is a general feature of the $\tilde{h}_{\mathbf{k},s}$ formulation, occurring because fewer source terms need be calculated in the code and this reduces the number of calculations per timestep.

$\tilde{k}_y$	Code branch	Algorithm	Cost (CPU minutes/$\tilde{t}$)	$\tilde{\omega}$	$\tilde{\gamma}$
1	original `stella`	fully explicit (SSP RK2)	28.4	$0.1135 \pm 3\text{E}-4$	$0.1176 \pm 1\text{E}-4$
1	original `stella`	implicit streaming and mirror	1.01	$0.1180 \pm 1\text{E}-4$	$0.1219 \pm 1\text{E}-4$
1	`EM stella`	fully explicit (SSP RK2)	7.50	0.15 ± 0.02	0.13 ± 0.02
1	`EM stella`	implicit streaming and mirror	0.586	$0.1114 \pm 5\text{E}-5$	$0.1155 \pm 1\text{E}-4$
3.5	original `stella`	fully explicit (SSP RK2)	28.7	$0.3962 \pm 1\text{E}-11$	$0.2475 \pm 2\text{E}-10$
3.5	original `stella`	implicit streaming and mirror	0.891	$0.4285 \pm 3\text{E}-5$	$0.2566 \pm 1\text{E}-5$
3.5	`EM stella`	fully explicit (SSP RK2)	9.17	$0.3722 \pm 1\text{E}-9$	$0.2587 \pm 2\text{E}-9$
3.5	`EM stella`	implicit streaming and mirror	0.616	$0.4195 \pm 5\text{E}-6$	$0.2521 \pm 3\text{E}-6$

Table 7.2: Comparison of electrostatic simulations using the vacuum field EIM equilibrium. The uncertainty in $\tilde{\omega}$ and $\tilde{\gamma}$ are taken as the standard deviation over the final 20% of the simulation time.

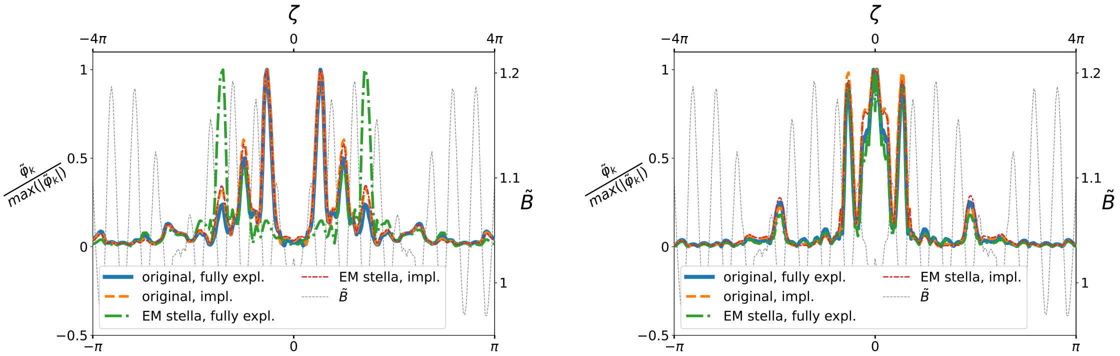

Figure 7.10: $|\tilde{\varphi}_{1\mathbf{k}}|(Z)$ comparison for original `stella` and `EM stella` simulations using EIM vacuum fields equilibrium. Left: $\tilde{k}_y = 1$ Right: $\tilde{k}_y = 3.5$.

To conclude, the partially implicit implementation of `EM stella` shows good agreement with the original `stella` implementation ($\Delta\tilde{\Omega} \lesssim 5\%$) for the simulation parameters used throughout this chapter, and is the cheapest of all variations tried in terms of CPU minutes per unit $\tilde{t}$. There is particularly good agreement with partially implicit original `stella` for $\tilde{k}_y = 3.5$ ($\Delta\tilde{\Omega} \sim 2\%$). The fully explicit version of `EM stella` is cheaper than fully explicit original `stella` but shows slow convergence at $\tilde{k}_y = 1$ and also poorer agreement in $\tilde{\omega}$ at $\tilde{k}_y = 3.5$ ($\Delta\tilde{\omega} = 6\%$-$15\%$).

7.6.3 Kinetic ballooning modes in the EIM vacuum field equilibrium

For the EIM vacuum field equilibrium, the “dynamical β” (i.e. β appearing in the field equations) is scanned for several values of $\tilde{k}_y$ for ($a/L_n = 3 = a/L_{T,i} = a/L_{T,e} = 3$). $\tilde{\Omega}(\beta)$ is shown in figure 7.11, left. In simulations where the growth rate is low, slow convergence can result in spurious values of $\tilde{\omega}$ and $\tilde{\gamma}$ as reported by `stella` (which are here referred to as $\tilde{\omega}_{\text{stella}}$, $\tilde{\gamma}_{\text{stella}}$). As an additional diagnostic, figure 7.11 shows $\tilde{\gamma}_2(\beta)$, defined as

$$\tilde{\gamma}_2^n = \frac{1}{2(\tilde{t}^n - \tilde{t}^m)} \log\left(\frac{\langle|\tilde{\varphi}_{1\mathbf{k}}^n|^2\rangle_z}{\langle|\tilde{\varphi}_{1\mathbf{k}}^m|^2\rangle_z}\right), \tag{7.6.1}$$

where n is the timestep and $m = \texttt{floor}(n/2)$. $\tilde{\gamma}_2^n$ calculates the growth rate averaged over a long time and is thus less susceptible to transient events in slowly-converging simulations.

For each $\tilde{k}_y$ value, a mode transition occurs at some critical β (β_{KBM}) to a positive-frequency mode (i.e. in the ion diamagnetic direction) with a growth rate increasing with increasing β. Qualitatively similar results have been reported by Mulholland *et al.* in W7-X simulations using `GENE`, albeit at lower $\tilde{k}_y$ values ($\tilde{k}_y = 0.025$) and using different equilibria [141], reporting the instability to be a KBM (`EM stella` simulations at $\tilde{k}_y = 0.025$ are found to display numerical instabilities which are currently being investigated, and so are not included here). The KBM seems to be the likely instability here as well, with $\tilde{\Omega}(\beta)$ showing similar trends to the CBC at fixed geometrical β as shown in figure 6.7. In addition, the instability preferentially occurs at lower $\tilde{k}_y$ (with lower β_{KBM} and higher $\tilde{\gamma}$), is stabilised when $B_{1\|}$ fluctuations are ignored and has twisting parity (see figure 7.11, right); all properties which were identified in chapter 5 as KBM properties. The minimum value of β_{KBM} is between 2% and 3%, which is within the range of experimental relevance.

As can be seen by figure 7.11, right, the mode structure in z is well-confined, unlike the drift wave modes seen hitherto. This raises the possibility of studying KBMs even more efficiently by careful tuning of non-physical parameters. For example, the ($\tilde{k}_y = 1$, $\beta = 4\%$) simulation, repeated with modified non-physical parameters (n_{fp}: 20 $\rightarrow$ 4, n_z: 256 $\rightarrow$ 128, $n_{\tilde{v}_\|}$: 72 $\rightarrow$ 24, $n_{\tilde{\mu}_s}$: 24 $\rightarrow$ 12), was able to better resolve the mode structure in z and cost only 0.24 CPU seconds per unit $\tilde{t}$ (compared with 2.7 for the original simulation). The two simulations agreed in $\tilde{\omega}$ an $\tilde{\gamma}$ to within 0.1% and 2% respectively, showing that KBMs can be efficiently simulated at low computational cost.

The stability valley plots (figure 7.8), reproduced with $\beta = 1\%$ and $\beta = 3\%$, are shown in figures 7.12 and 7.13. At low $\tilde{k}_y$, the stability valley can still be seen, with $\tilde{\gamma}$ increasing at (high a/L_T, low a/L_n) and (low a/L_n, high a/L_T). As $\tilde{k}_y$ increases, the stability valley is wiped out by a positive-frequency pressure-driven mode. The mode structure for ($\beta = 1\%$, $a/L_n = a/L_T = 7.7$, $\tilde{k}_y = 4.5$), shown in figure 7.14, reveals tearing parity and this mode is not stabilised by setting $\tilde{B}_{1\|\mathbf{k}} = 0$. $\tilde{\Omega}$ and the mode structures are sensitive to the putting all of the pressure gradient contribution into the density gradient or temperature gradient, and to scaling β at fixed β'; these phenomena point against the instability being a KBM. The overall conclusion is that electromagnetic effects may ruin the stability valley, but the picture is more complex picture than simply KBM destabilisation.

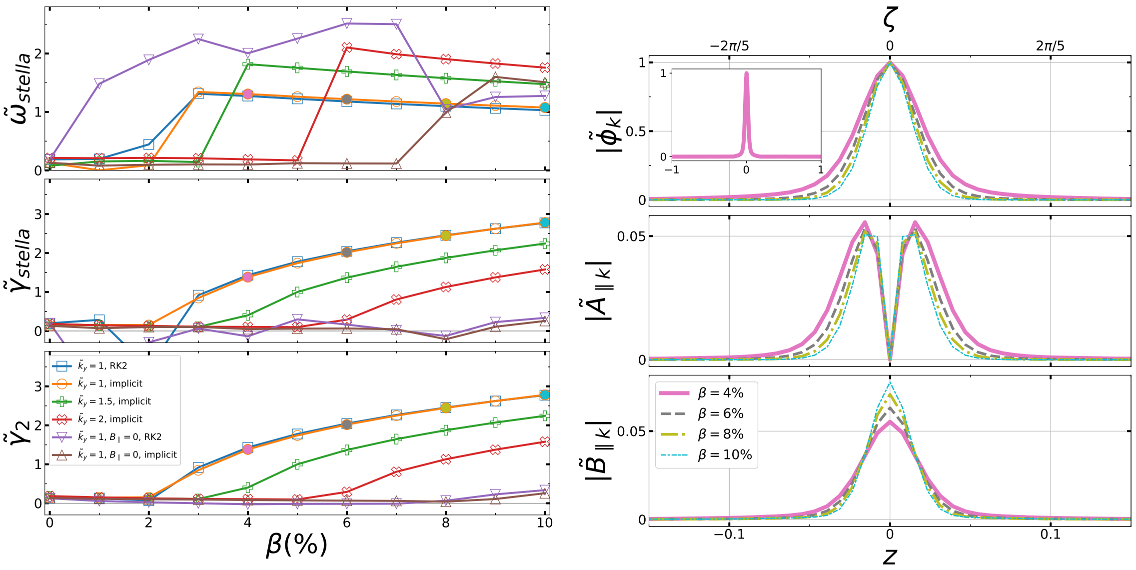

Figure 7.11: $\tilde{\Omega}(\beta)$ and mode structures for the EIM $\beta = 0$ configuration.

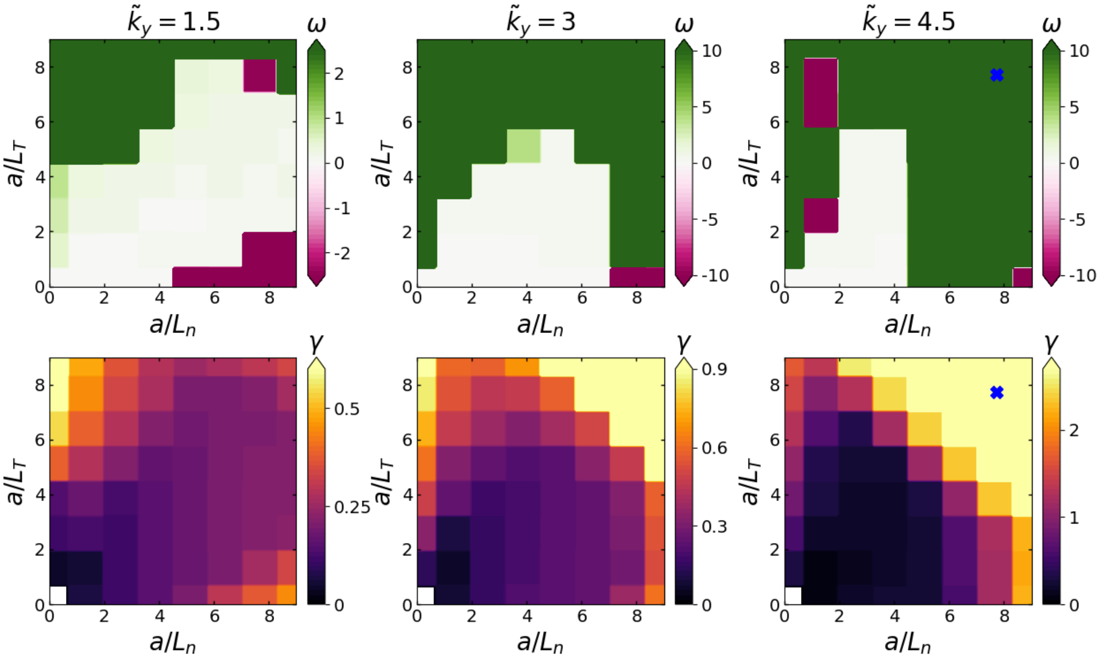

Figure 7.12: $\tilde{\Omega}(a/L_n, a/L_T)$ for the EIM vacuum field equilibrium with dynamic $\beta = 1\%$. Blue cross marks a simulation for which the mode structure is plotted in figure 7.14.

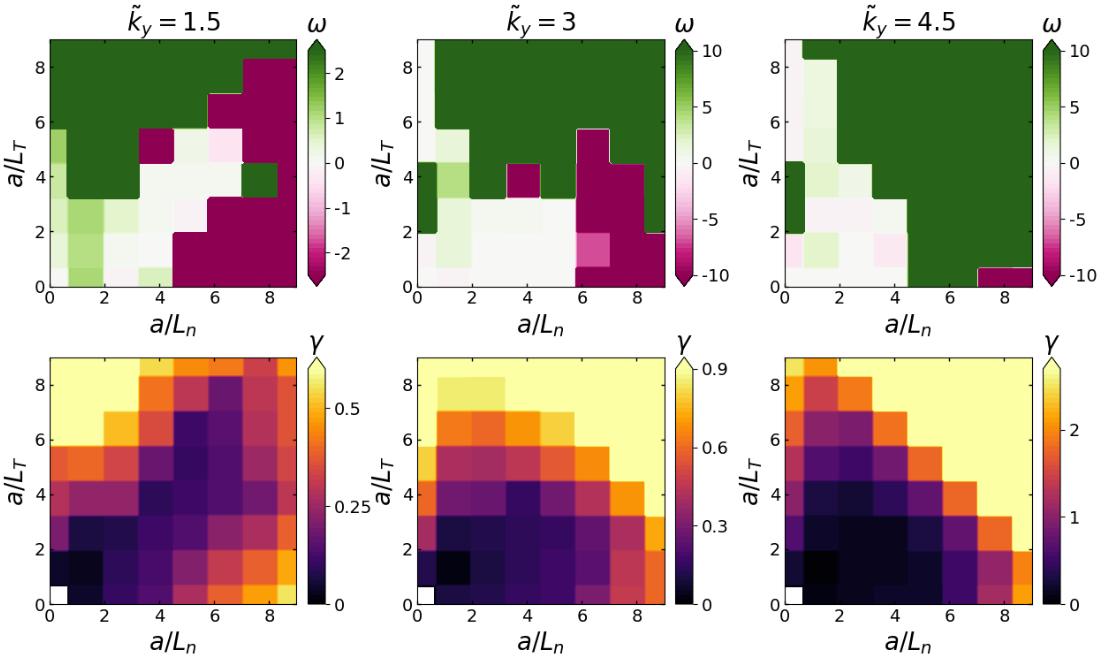

Figure 7.13: $\tilde{\Omega}(a/L_n, a/L_T)$ for the EIM vacuum field equilibrium with dynamic $\beta = 3\%$.

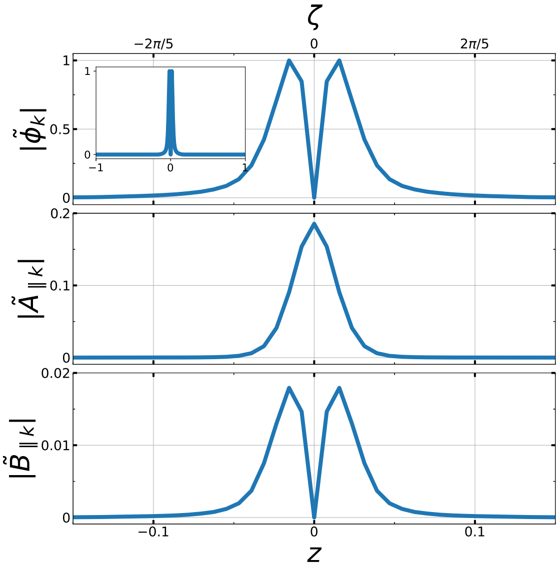

Figure 7.14: Mode structure for instability at ($\beta = 1\%$, $a/L_n = a/L_T = 7.7$, $\tilde{k}_y = 4.5$) in EIM vacuum field configuration.

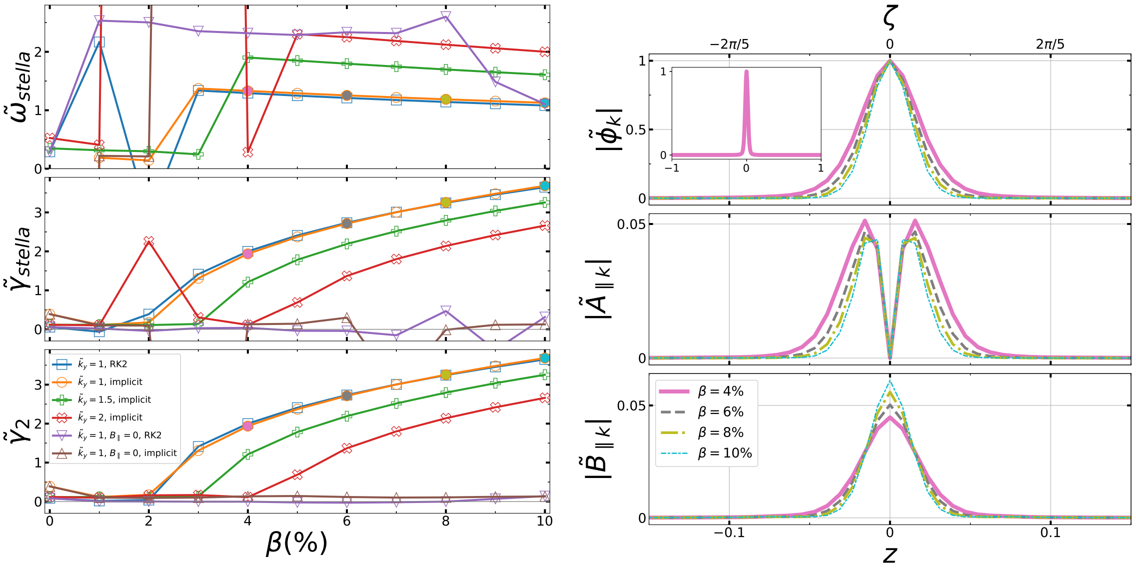

Figure 7.15: $\tilde{\Omega}(\beta)$ and mode structures for the KJM $\langle\beta\rangle = 3\%$ configuration.

7.6.4 The KJM $\beta = 3\%$ equilibrium

The simulations of section 7.6.3 is repeated using a KJM $\langle\beta\rangle = 3\%$ equilibrium. It should be noted that in these simulations, as in the EIM vacuum equilibrium, the equilibrium is not regenerated as the dynamical plasma β and/or gradients are scanned, meaning that the equilibrium β' is inconsistent with the dynamical β'. Aleynikova *et al.* [79] report that such "inconsistent" simulations significantly alter KBM stability, specifically, that long-wavelength ($\tilde{k}_y \lesssim 0.4$) KBMs are spuriously destabilised when a $\beta = 0$ W7-X equilibrium is used.

The KBM transition with β, shown in figure 7.15, shows the same trends as in the EIM configuration: a $\tilde{B}_{1\|\mathbf{k}}$-dependent KBM destabilised at $\beta_{\text{KBM}} \sim 2\%$ for $\tilde{k}_y = 1$. The robustness of this result across different equilibria confirms that KBMs are likely to exist in the operational space of W7-X. That this result is the same between a vacuum field and finite-β equilibrium is not in direct contradiction with Aleynikova *et al.* [79] since their results address KBMs at lower $\tilde{k}_y$.

The stability valley plots at $\beta = 1\%$ are shown in figure 7.16. As was the case in the EIM simulation, EM effects are preferentially destabilising at higher $\tilde{k}_y$, where a positive-frequency mode tends to eliminate the "valley" of low $\tilde{\gamma}$. An interesting question would be whether nonlinearly the stability valley matches this trend; one then might imagine a crude model for high-performance shots where the kinetic gradients are set by a combination of the electrostatic stability valley at low gradients and a critical limit set by electromagnetic pressure-driven modes.

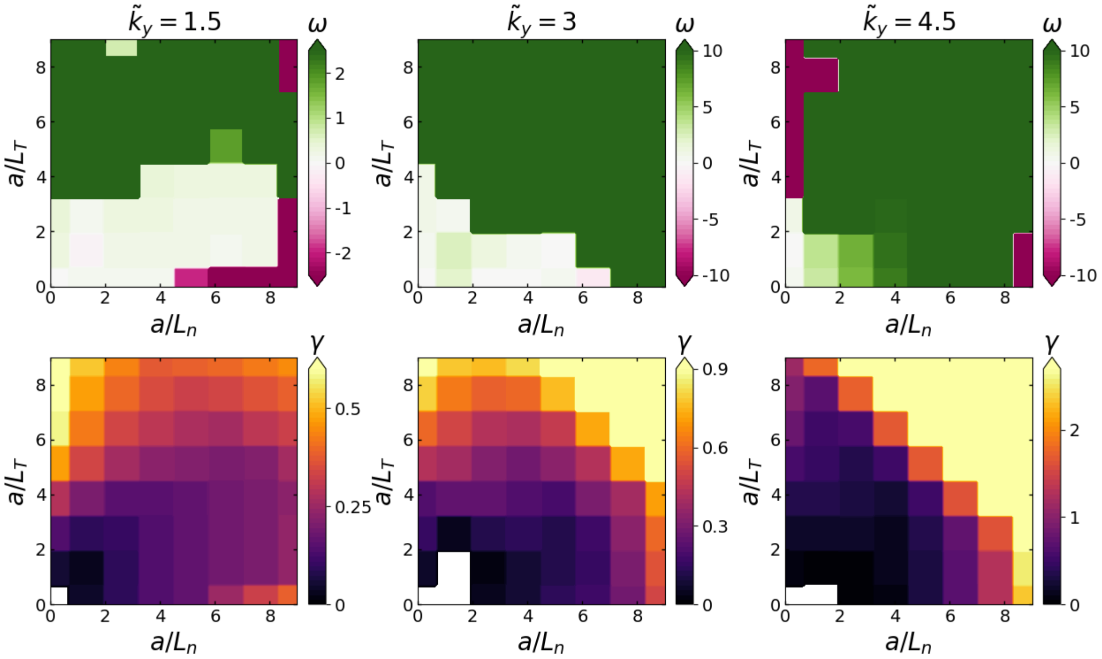

Figure 7.16: $\tilde{\Omega}(a/L_n, a/L_T)$ for the KJM $\langle\beta\rangle = 3\%$ configuration with dynamic $\beta = 1\%$.

7.7 Concluding remarks

To summarise, I study the ion-scale microstability properties of W7-X equilibria as a function of $(a/(L_n), a/(L_T), k_y\rho_i)$ using linear gyrokinetic simulations. I explore the properties of the instabilities as $\tilde{k}_y$ varies and map the “stability valley” in three $\beta = 0$ W7-X configurations. This serves as a useful validation of recently reported results [32], as well as providing a comparison (although not quantitative) between gyrokinetic codes.

These linear results suggest, as proposed by others, that the “stability valley” could be an attractive operating regime for W7-X. This could also explain the improved performance which occurs in the “HP” discharges. Nonlinear studies performed by other researchers [123, 136, 138] also support the picture that higher gradients can suppress turbulence. However, the changes to nonlinear fluxes tend to be much greater than the changes to the obvious linear stability metrics such as $\tilde{\gamma}$ for the most unstable mode. It is therefore not entirely clear that the reduction in fluxes arises as a direct consequence of the stability valley, rather than other physical effects such as sub-dominant mode characteristics and saturation dynamics. McKinney *et al.* [142], for example, have shown in a comparison between two quasi-symmetric devices (HSX and NCSX) that nonlinear fluxes can display the opposite trend to peak growth rates, emphasising the importance of nonlinear effects. Their study concludes that this reversal can be explained by the increased number of sub-dominant modes and more extended mode structures in HSX (which has larger peak $\tilde{\gamma}$ but lower nonlinear heat fluxes), enabling a more efficient energy transfer to stable modes.

I also examine electromagnetic (EM) effects in the EIM equilibrium using the electromagnetic implementation of the `stella` code ("`EM stella`"). I first compare the code to the regular implementation in the electrostatic limit and find reasonable agreement and lower computational cost for `EM stella` when the streaming and mirror terms are treated implicitly. I then scan dynamical β in the EIM vacuum field equilibrium. A transition from drift wave instabilities to KBM is observed as β rises, with the KBMs showing many similar characteristics to those studied in chapters 5 and 6. The KBM critical β for gradients $a/L_{n_{i,e}} = a/L_{T_{i,e}} = 3$ is within the experimentally relevant range for W7-X. The same qualitative result is found when using a finite β ($\langle\beta\rangle = 3\%$) KJM equilibrium.

The stability valley is simulated at $\beta = 1\%$ and $\beta = 3\%$ using the EIM vacuum field equilibrium and the finite β KJM equilibrium. In both cases, the stability valley is most modified at high $\tilde{k}_y$ by a (currently unidentified, but apparently non-KBM) electromagnetic tearing-parity mode. Since this study does not recalculate the equilibrium to be self-consistent with β' (which has been reported to have significant impact on instability growth rates [143]), these results are suggestive rather than predictive. However, they do indicate a how EM instabilities could play a role in future W7-X experiments.

Electromagnetic microinstability research in W7-X remains a fascinating and largely unexplored field of study. `EM stella` has shown that is has the potential to efficiently study such phenomena. Continuing this work would be an interesting and worthwhile area of future research.

Chapter 8

Eliminating the Courant-Friedrichs-Lewy timestep constraint in nonlinear gyrokinetics

8.1 Introduction

A principal motivation for many fusion plasma researchers is to better understand how commercial MCF reactors should be designed and operated. One requires, for example, a plasma with sufficiently high density, temperature and confinement to satisfy the fusion triple product $nT\tau_E$ (defined in section 1.1). Nonlinear gyrokinetic simulation can help inform whether the triple product can be met by predicting (within the limitations of the model) turbulent transport properties for a given plasma. Nonlinear gyrokinetics (i.e. simulations which include the $\langle \mathbf{v}_\chi \rangle_{\mathbf{X}_s} \cdot \boldsymbol{\nabla}_{\mathbf{X}_s} h_s$ term in the GKE) are more expensive than the linear simulations I have described thus far, but their ability to make quantitative predictions of turbulent fluxes is a great advantage. To perform such simulations with as great computational efficiency as possible is desirable.

Codes such as `stella`, `GS2`, `GENE`[144] and `CGYRO` [145] evaluate the nonlinear source term $\mathcal{N}_s$ using explicit numerical schemes. This is algorithmically straightforward but places an upper bound on the simulation timestep, beyond which numerical instability befalls the simulation. This is known as the Courant-Friedrichs-Lewy (CFL) timestep constraint and as I discuss in 8.3.2, may be restrictive in physically relevant scenarios (particularly in electromagnetic simulations with gyrokinetic electrons). It could be beneficial to avoid this constraint by using an implicit numerical scheme to evaluate the nonlinearity.

In this chapter I describe such an implementation, in which semi-Lagrangian (SL) schemes are used to advance $\mathcal{N}_s$ in the electrostatic version of the code `stella`. Circumventing the CFL condition allows the simulation timestep to be selected on a physical (rather than numerical stability) basis, and hence may enable greater computational efficiency. Unfortunately, the results presented here are largely negative, but may offer some useful guidance for further development.

This chapter is organised as follows. Firstly, I describe the CFL constraint, as it applies to `GS2` and `stella`. I then provide some background on SL schemes. In particular, I describe a leapfrog-like three-level SL algorithm, and a variation proposed by Harold Ritchie [146], which avoids interpolation (I refer to this throughout as the non-interpolating SL, or NISL, approach). Since these algorithms are multistep (and ergo not obviously compatible with `stella`'s operator splitting), I propose a new splitting scheme (described in section 8.5.1) which mixes single-step algorithms with a leapfrog-like multistep scheme. Next, I describe the implementation of the splitting and SL schemes in the code `stella` and report the behaviour observed when nonlinear simulations are performed. Conclusions and future work are then described (section 8.7).

8.2 Timestep restrictions in explicit schemes

For a simple example, consider the advection of a function $f(x,t)$ in x by a velocity U, which I initially take to be spatially and temporally constant. Such a system is described by the equation:

$$\frac{\partial f}{\partial t} + U\frac{\partial f}{\partial x} = 0. \tag{8.2.1}$$

An analytic solution can be found by noting that f can be written as a function of a single variable $f(x,t) = f(p)$, where $p = (x - Ut)$. Thus, f is constant along trajectories of constant p, and the general solution is

$$f(x,t) = f(x - U(t - t_0), t_0), \tag{8.2.2}$$

where t_0 is an arbitrary time. It is helpful to express $f(x,t)$ as a sum of Fourier harmonics $f = \sum_{k=-\infty}^{\infty} F_k = \sum_{k=-\infty}^{\infty} f_k(t)\exp(ikx)$. Each F_k independently satisfies (8.2.1), has the analytic spatial derivative

$$\frac{\partial F_k}{\partial x} = ikF_k, \tag{8.2.3}$$

and has the exact solution

$$\begin{align} F_k(x,t) = f_k(t)\exp(ikx) &= f_k(t_0)\exp(ik(x - U(t-t_0))) \tag{8.2.4} \\ &= F_k(x,t_0)\exp(-ikU(t-t_0)). \tag{8.2.5} \end{align}$$

Suppose one wishes to solve 8.2.1 using a time-marching scheme; for example the second-order Runge-Kutta (RK2) scheme:

$$\begin{align} l_1 &= \Delta t \left(\frac{\partial f}{\partial t}\right)_{(f^n,t^n)} \tag{8.2.6} \\ f^{n\dagger} &= f^n + \frac{l_1}{2} \tag{8.2.7} \\ l_2 &= \Delta t \left(\frac{\partial f}{\partial t}\right)_{(f^{n\dagger},t^n+\Delta t/2)}, \tag{8.2.8} \\ \tilde{f}^{n+1} &= f^n + l_2, \tag{8.2.9} \end{align}$$

where the tilde ($\tilde{}$) indicates that this is an approximate solution, and the dagger (^{n†}) denotes an intermediate variable. One can examine numerical stability by taking a single step using the RK2 scheme, and examining the "amplification factor" $G \equiv |\tilde{f}^{n+1}/f^n|$. The exact solution is $f_k^{n+1} = f_k^n \exp(-ikU\Delta t)$ and has $|\tilde{f}^{n+1}/f^n| = 1$. Assuming the spatial derivatives are calculated exactly, applying the RK2 step to a Fourier component F_k gives:

$$\begin{align} \tilde{F}_k^{n+1} &= \left(1 - ikU\Delta t - \frac{(kU\Delta t)^2}{2}\right) F_k^n \tag{8.2.10} \\ G &= \left|\frac{\tilde{F}_k^{n+1}}{F_k^n}\right| = \left(1 + \frac{(kU\Delta t)^4}{4}\right)^{1/2}. \tag{8.2.11} \end{align}$$

One sees that $G > 1$ for all values of $(kU\Delta t)$. Thus, the amplitude of the solution will (unphysically) exponentially grow with the number of steps; a numerical instability. Since the scheme is unstable for any finite timestep ($\Delta t > 0$), it is said to be *unconditionally unstable*.

Such analysis is known as von Neumann's method for calculating stability. It should be emphasised that numerical stability depends not only on the choice of marching scheme, but on other algorithmic choices, such as how the derivatives are calculated (the RK2 scheme is conditionally stable, for example, if the spatial derivative is taken using a first-order upwinded scheme.) As another example, if (8.2.1) is advanced using the strong stability-preserving (SSP) RK3 scheme and spectral spatial derivatives, one finds

$$|G|^2 = 1 - \frac{(kU\Delta t)^4}{12} + \frac{(kU\Delta t)^6}{36}. \tag{8.2.12}$$

This is conditionally stable, since $|G| \leq 1$ provided $|kU\Delta t| \leq \sqrt{3}$. The constraint on the timestep, for given (U, k) is an example of the Courant-Friedrichs-Lewy (CFL) condition. This is summarised by Durran [103] as: "*The CFL condition requires that the numerical domain of dependence of a finite-difference scheme include the domain of dependence of the associated partial differential equation.*" Boyd [58] offers this useful rule-of-thumb: "*The maximum timestep is the same order of magnitude as the time scale for advection or diffusion or wave propagation or whatever across the SMALLEST distance* h *between two grid points.*" In this example, one can define $h \equiv \pi/k_{max}$ where k_{max} is the maximum wavenumber simulated, since k_{max} is the shortest-wavelength mode which can be resolved on a grid with spacing h.

8.3 Advancing the E × B nonlinearity explicitly

The **E** × **B** nonlinear term in the electromagnetic gyrokinetic equation (eq. (2.2.46)), $\langle \mathbf{v}_\chi \rangle_{\mathbf{X}_s} \cdot \boldsymbol{\nabla}_{\mathbf{X}_s} h_s$, physically represents advection of h_s by $\langle \mathbf{v}_\chi \rangle_{\mathbf{X}_s}$, a generalised drift arising from the perturbed electromagnetic fields. To date, the nonlinear **E** × **B** term has been evaluated explicitly both in `stella` (using either SSP RK2, SSP RK3 or SSP RK4) and `GS2` (which uses the third-order Adams-Bashforth scheme).

Electrostatically, the nonlinear term in real space is $\langle \mathbf{v}_E \rangle_{\mathbf{X}_s} \cdot \boldsymbol{\nabla}_{\mathbf{X}_s} h_s$ where $\langle \mathbf{v}_E \rangle_{\mathbf{X}_s} \equiv -\frac{1}{B_0} \boldsymbol{\nabla}_{\mathbf{X}_s} \langle \varphi_1 \rangle_{\mathbf{X}_s} \times \mathbf{b}$. The nonlinear term as evaluated in electrostatic `stella` is (equation (3.5.5), reproduced here):

$$\mathcal{N}_{\mathbf{k},s} = \frac{B_r}{2} \frac{dy}{d\alpha} \frac{dx}{d\psi} \mathcal{F}_{\mathbf{k}} \left[\mathcal{F}_{\mathbf{k}}^{-1} \left[i\tilde{k}_y J_0(\gamma_s) \tilde{\varphi}_{1\mathbf{k}} \right] \mathcal{F}_{\mathbf{k}}^{-1} \left[i\tilde{k}_x \tilde{g}_{\mathbf{k},s} \right] - \mathcal{F}_{\mathbf{k}}^{-1} \left[i\tilde{k}_x J_0(\gamma_s) \tilde{\varphi}_{1\mathbf{k}} \right] \mathcal{F}_{\mathbf{k}}^{-1} \left[i\tilde{k}_y \tilde{g}_{\mathbf{k},s} \right] \right], \tag{8.3.1}$$

with gradients calculated spectrally and the source term calculated in real space. Being nonlinear, the properties of explicit numerical schemes used to evaluate this source term are considerably more difficult to assess. However, given that this problem suffers a CFL condition in the limit of a spatio-

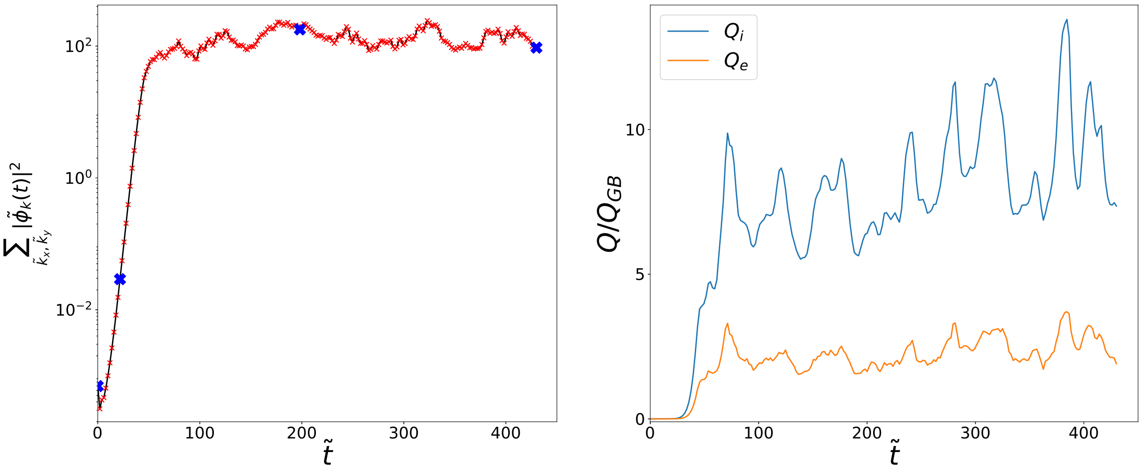

Figure 8.1: $\sum_{\tilde{k}_x,\tilde{k}_y} \left\langle |\tilde{\varphi}_{1\mathbf{k}}|^2 \right\rangle_z (t)$ for example CBC simulation. Data points (in red) are written every `nwrite` $= 50$ steps. Blue crosses mark the times for which $\left\langle |\tilde{\varphi}_{1\mathbf{k}}|^2 \right\rangle_z (\tilde{k}_x, \tilde{k}_y)$ are plotted in figure 8.2. Right: normalised ion and electron heat flux for the simulation.

temporally constant advecting velocity, and bearing in mind the remarks of Durran and Boyd, it is unreasonable to expect unconditional stability. As a result, `stella` prescribes the maximum allowable timestep $\Delta\tilde{t}_{\text{max}} = \texttt{cfl\_dt} * \texttt{cfl\_cushion}$, where, for the nonlinear term,

$$\texttt{cfl\_dt} \equiv \texttt{min} \left(\frac{2\pi}{\texttt{max}\left(\mathcal{F}_{\mathbf{k}}^{-1}\left[i\tilde{k}_x J_0(\gamma_s)\tilde{\varphi}_{1\mathbf{k}}\right]\right) \cdot \texttt{max}(\tilde{k}_y)}, \frac{2\pi}{\texttt{max}\left(\mathcal{F}_{\mathbf{k}}^{-1}\left[i\tilde{k}_y J_0(\gamma_s)\tilde{\varphi}_{1\mathbf{k}}\right]\right) \cdot \texttt{max}(\tilde{k}_x)} \right), \tag{8.3.2}$$

is the rule-of-thumb magnitude of the CFL-limited $\Delta\tilde{t}$ (where the `max` operator is taken over all combinations of $(\tilde{k}_x, \tilde{k}_y, z)$, the `min` operator is taken over the two arguments). `cfl_cushion` is a user-controlled parameter (`cfl_cushion` $= 0.5$ by default). The difficulty in assessing numerical stability means that `cfl_cushion` is not usually selected in a theoretically rigorous way. Indeed, in the limit that $\langle \tilde{\mathbf{v}}_E \rangle_{\mathbf{X}_s}$ ($\langle \mathbf{v}_E \rangle_{\mathbf{X}_s}$ in normalised `stella` units) is spatially and temporally constant, advancing the nonlinear term using `stella`'s SSP RK2 scheme is unconditionally unstable. One might therefore expect this to present numerical difficulty for any finite timestep. However (as I later show), nonlinear simulations have been successfully run using the SSP RK2 scheme, suggesting that the numerical instability is unimportant compared to the linear source terms, which themselves induce exponential-like growth and decay for each mode.

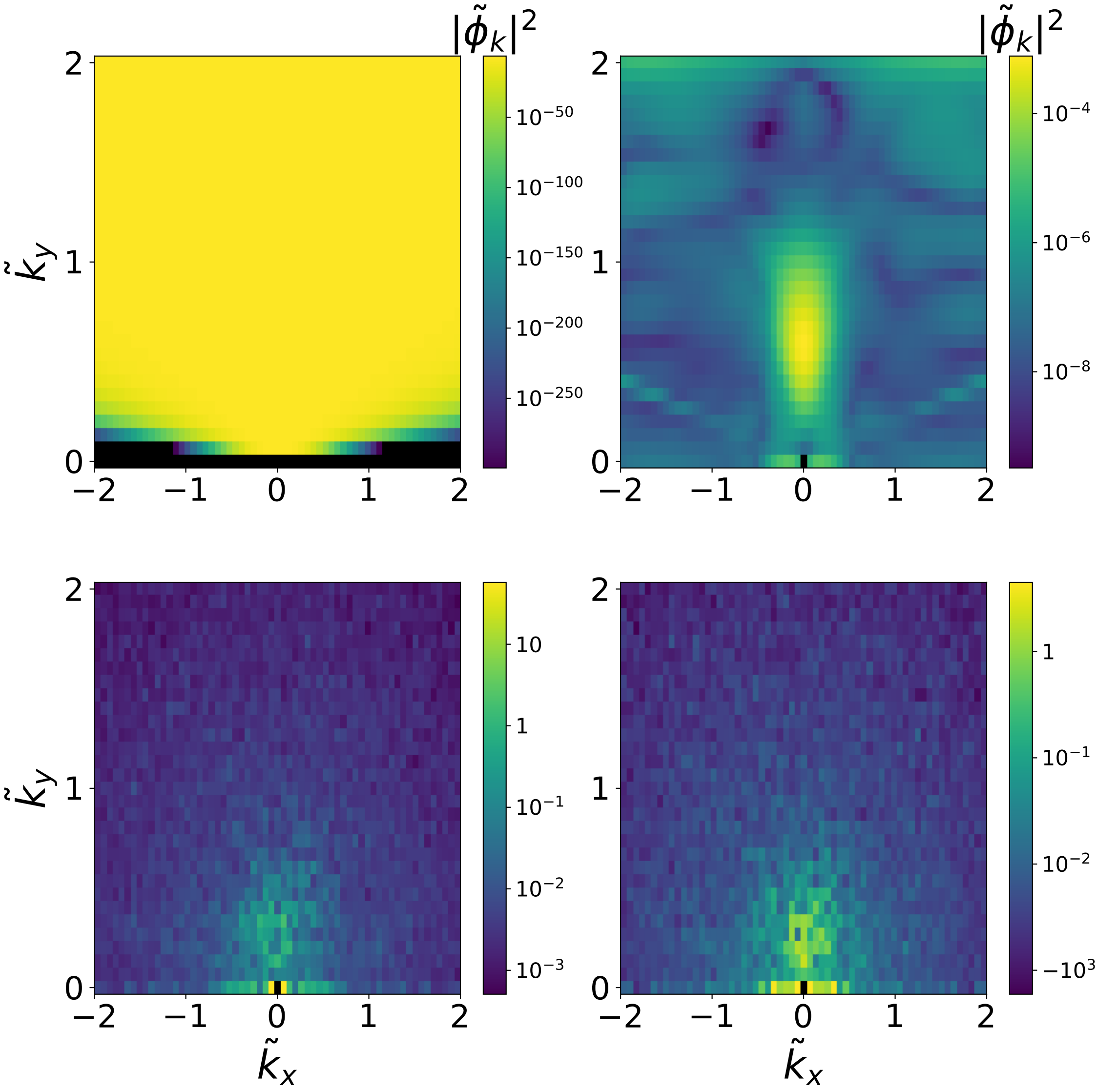

Figure 8.2: $\left\langle |\tilde{\varphi}_{1\mathbf{k}}|^2 \right\rangle_z (\tilde{k}_x, \tilde{k}_y)$ at four simulation times. Top left ($\tilde{t} = 0$): the simulation initialised to small amplitude everywhere. Top right ($\tilde{t} = 22$): linear growth phase. Bottom left ($\tilde{t} = 198$) and bottom right ($\tilde{t} = 430$): snapshots of the saturated turbulence phase.

8.3.1 Nonlinear simulations and saturation

Qualitatively typical plots of a saturated nonlinear (electrostatic) simulation are shown in figures 8.1 and 8.2. The simulation is performed by `stella` using physical parameters corresponding to the cyclone base case (CBC). The input file is included in Appendix D.

Figure 8.1 (left) shows $\sum_{k_x,k_y}\left\langle|\tilde{\varphi}_{1\mathbf{k}}|^2\right\rangle_z$ against $\tilde{t}$, which is equivalent to $\left\langle|\tilde{\varphi}|^2\right\rangle_{x,y,z}$ [147], where $\langle\rangle_z$ denotes the field line average and $\left\langle|\tilde{\varphi}_{1\mathbf{k}}|^2\right\rangle_{x,y,z}$ the average over x, y, z for the flux tube. Figure 8.1 (right) shows the gyro-Bohm-normalised ion and electron heat fluxes $Q_{i,e}/Q_{GB}$, where $Q_{GB} = n_i T_i v_{th,i}\rho_i^2/a^2$. Figure 8.2 shows $|\left\langle\tilde{\varphi}^2_{1\mathbf{k}}\right\rangle_z|^2(\tilde{k}_x, \tilde{k}_y)$ at four different times showing the initial condition, the exponential growth phase and saturation.

Since $\langle\tilde{\mathbf{v}}_E\rangle_{\mathbf{X}_s}$ scales with the magnitude of the distribution function and the distribution is initialised with a small amplitude (see figure 8.2 (upper left)), $\mathcal{N}_{\mathbf{k},s}$ is negligible at early simulation times. The system therefore evolves linearly such that the dominant mode(s) quickly emerge and grow exponentially, dominating the behaviour of the system. This can be seen in figure 8.2 (upper right): $\left\langle|\tilde{\varphi}_{1\mathbf{k}}|^2\right\rangle_z$ is at its largest over the region ($0.4 \lesssim \tilde{k}_y \lesssim 1$, $-0.2 \lesssim \tilde{k}_x \lesssim 0.2$), which is typical for the ITG instability. As the simulation evolves, $\mathcal{N}_{\mathbf{k},s}$ grows more rapidly than the linear source terms until it competes with the linear behaviour at $\tilde{t} \sim 60$.

As previously noted, $\mathcal{N}_{\mathbf{k},s}$ can be interpreted as nonuniform advection in (x, y); this "transfers" $\tilde{g}_{\mathbf{k},s}$ in $\mathbf{k}$-space, with each mode pair ($\mathbf{k}_1 = k_{x1}\hat{\mathbf{x}} + k_{y1}\hat{\mathbf{y}}$, $\mathbf{k}_2 = k_{x2}\hat{\mathbf{x}} + k_{y2}\hat{\mathbf{y}}$; $\mathbf{k}_1 \neq \mathbf{k}_2$) providing a source term for modes ($\mathbf{k}_3 = k_{x3}\hat{\mathbf{x}} + k_{y3}\hat{\mathbf{y}}$) which have ($k_{x3} = k_{x1} \pm k_{x2}$, $k_{y3} = k_{y1} \pm k_{y2}$). The unstable modes tend to "transfer" energy to the stable modes, which removes energy from the system. This settles the simulation into a chaotic but statistically steady state (from times $\tilde{t} \gtrsim 100$ in figure 8.1); one sees (in figure 8.2 (bottom left and bottom right)) broadly the same features throughout the saturated period. The heat fluxes (figure , left) also fluctuates around a mean value comparable with a published results by Barnes *et al.* [45] for the same equilibrium using `GS2` and `stella`.

A particularly noteworthy feature of turbulent plasmas are *zonal modes*, defined as modes with $\tilde{k}_y = 0$, which have several interesting properties [39, 148, 149]. One is that these modes are linearly stable, since the driving term:

$$i\omega_{*,\mathbf{k},s}J_0(\gamma_s)\tilde{\varphi}_{1\mathbf{k}} = \frac{\tilde{k}_y}{2}aB_r\frac{dy}{d\alpha}e^{-\tilde{v}_s^2}\frac{d\ln F_{0s}}{\psi} \tag{8.3.3}$$

clearly vanishes when $\tilde{k}_y = 0$; they are only fed by nonlinear interactions. Similarly, these modes also do not contribute to radial fluxes in the plasma. These modes can then be considered a benign sink for turbulent energy, which is dissipated by Landau damping or, if included in the simulations, collisions. The other stabilising role the zonal mode plays is via sheared zonal flows. That is, the $\langle \tilde{\mathbf{v}}_E \rangle_{\mathbf{X}_s}$ drift generated by the zonal flows drives transfer from unstable to stable modes[150, 151]. As can be seen from 8.2 (bottom left and bottom right), low-$\tilde{k}_x$ zonal modes have relatively large amplitudes during the saturated period and so are generating relatively large $\mathbf{E} \times \mathbf{B}$ flows.

A final comment is that the dominant modes in the saturated region differ to the dominant modes in the linear phase, illustrating the nontrivial relationship between linear stability and nonlinear dynamics.

8.3.2 Restrictiveness of the CFL condition

Since $\tilde{\varphi}_{1\mathbf{k}}$ scales with the distribution function, eq. (8.3.2) indicates that `cfl_dt` will decrease over the initial linear phase of the simulation. This may result in the timestep being decreased, incurring additional computational expense since more steps are required to advance some given simulation time. There are two cases where the CFL condition is particularly restrictive:

1. In electromagnetic simulations, wherein $\langle \mathbf{v}_\chi \rangle_{\mathbf{X}_s}$ contains a term which scales with species thermal velocity:

$$\langle \mathbf{v}_{\chi\mathbf{k}} \rangle_{\mathbf{X}_s} = i\mathbf{k}\left(J_0(\gamma_s)\tilde{\varphi}_{1\mathbf{k}} - 2\tilde{v}_\parallel \tilde{v}_{th,s} J_0(\gamma_s)\tilde{A}_{1\parallel\mathbf{k}} - 4\tilde{\mu}_s \frac{\tilde{T}_s}{Z}\frac{J_1(\gamma_s)}{\gamma_s}\tilde{B}_{1\parallel\mathbf{k}} \right). \tag{8.3.4}$$

The rule-of-thumb CFL condition then becomes:

$$\begin{aligned}
&\texttt{cfl\_dt} \equiv \\
&\texttt{min}\left(\frac{2\pi}{\texttt{max}\left(\mathcal{F}^{-1}_{\mathbf{k}}\left[i\tilde{k}_x \left(J_0(\gamma_s)\tilde{\varphi}_{1\mathbf{k}} - 2\tilde{v}_\parallel \tilde{v}_{th,s} J_0(\gamma_s)\tilde{A}_{1\parallel\mathbf{k}} - 4\tilde{\mu}_s \frac{\tilde{T}_s}{Z}\frac{J_1(\gamma_s)}{\gamma_s}\tilde{B}_{1\parallel\mathbf{k}} \right)\right]\right) \cdot \texttt{max}(\tilde{k}_y)}, \right. \\
&\left. \frac{2\pi}{\texttt{max}\left(\mathcal{F}^{-1}_{\mathbf{k}}\left[i\tilde{k}_y \left(J_0(\gamma_s)\tilde{\varphi}_{1\mathbf{k}} - 2\tilde{v}_\parallel \tilde{v}_{th,s} J_0(\gamma_s)\tilde{A}_{1\parallel\mathbf{k}} - 4\tilde{\mu}_s \frac{\tilde{T}_s}{Z}\frac{J_1(\gamma_s)}{\gamma_s}\tilde{B}_{1\parallel\mathbf{k}} \right)\right]\right) \cdot \texttt{max}(\tilde{k}_x)} \right).
\end{aligned} \tag{8.3.5}$$

When $\tilde{A}_{1\parallel\mathbf{k}}$ is finite, this piece of $\langle \mathbf{v}_{\chi\mathbf{k}} \rangle_{\mathbf{X}_s}$ becomes large for electrons from the scaling $v_{th,s} \sim m_s^{-1/2}$. As discussed in section 2.4, B_1 and therefore $\tilde{A}_{1\parallel\mathbf{k}}$ tends to scale with plasma β, so this becomes more important at higher β. Spherical tokamaks for example provide physically interesting cases which suffer badly from the CFL constraint.

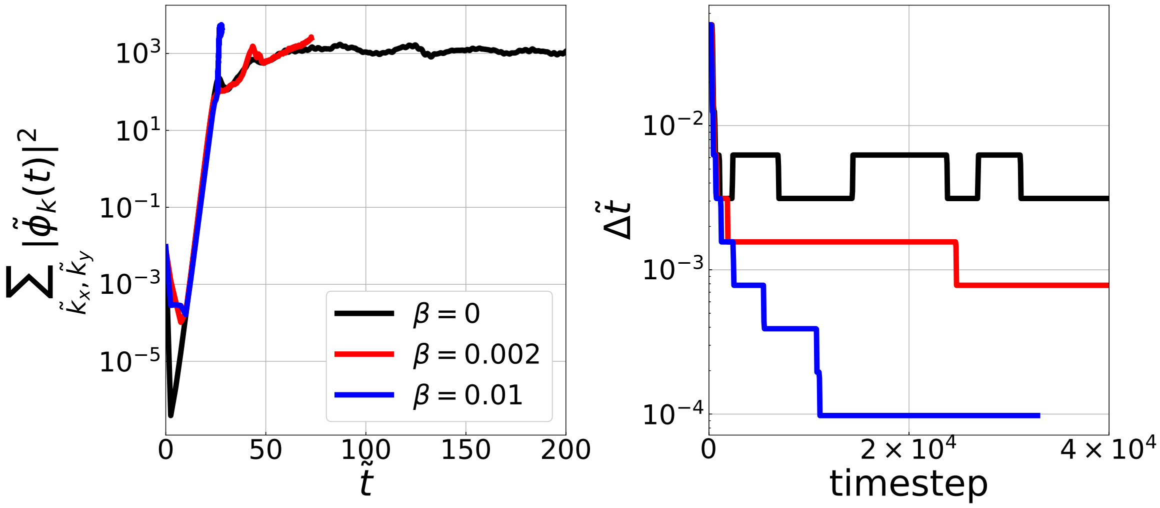

Figure 8.3: Left: $\sum_{\tilde{k}_x,\tilde{k}_y} \left\langle |\tilde{\varphi}_{1\mathbf{k}}|^2 \right\rangle_z (t)$ for GS2 CBC nonlinear simulations for three values of β. Right: simulation timestep size $\Delta\tilde{t}$ throughout the simulations.

2. When the potentials become large. This could happen for several reasons, including:
    2.1. The simulation experiences "bursty" behaviour, in which the distribution becomes transiently large, before settling into a lower state.
    2.2. The simulation fails to saturate, or saturates into an extremely turbulent regime, for physical reasons. There is no *a priori* mathematical evidence that the gyrokinetic system should saturate; one can imagine that if the mechanisms which dissipate energy are sufficiently weak, the simulation could settle into an exponentially growing state. Indeed, a physical mechanism by which electromagnetic simulations fail to saturate beyond a critical β has been proposed by Pueschel *et al.* [152]. Of course, one would expect that simulations of experimentally obtained steady-state plasmas should be able to saturate at a physically reasonable level.

An illustration of timestep restriction is shown in figure 8.3. In these CBC simulations performed with `GS2`, β is varied from 0 to 0.01. As β rises, $\Delta\tilde{t}$ falls by several orders of magnitude. It is not clear whether the $\beta = 0.01$ simulation will saturate, for example, but to find out would require high computational cost since $\Delta\tilde{t}$ becomes small.

Given this motivation, I now briefly describe SL schemes, which may be able to address this issue.

8.4 Semi-Lagrangian schemes

In the example problem in section 8.2 (eq. 8.2.1), it was noted that f was conserved along trajectories of constant $p = x - U(t - t_0)$. More generally in advection problems, f is conserved along trajectories of constant $p = x - \int_{t_0}^{t} U(x, t')dt'$. One might then be tempted to move away from advancing $f(x, t)$ on a fixed spatial grid (an Eulerian scheme) to a "moving grid", or Lagrangian, approach, whereby f is initially sampled on a regular x grid of "markers", and the spatial location of the markers are advanced along the trajectory p. These schemes do not suffer from the CFL constraint. However, they suffer a drawback that the markers tend to accumulate, leading to an uneven sampling of f in phase space. Some regions end up highly sampled by accumulating many markers, whereas other regions are poorly sampled. Unless remedied (for example, by periodically resampling the phase space), this can lead to low accuracy in the poorly sampled regions. [103]

A modification, which eliminates the CFL constraint whilst retaining the even sampling of Eulerian schemes, is the *semi-Lagrangian* (SL) approach. Here, one evaluates f on a regular grid by taking each gridpoint to be a marker, and estimating the trajectory of each point backwards in time. Having found the location of the marker at an earlier timestep (the "departure point" or "trajectory foot"), one then calculates the value of f at the marker at the earlier time. Since the departure point is, in general, not on a gridpoint, this is usually done by interpolation. As a concrete example, I describe an SL scheme (which I will refer to as the "leapfrog three-level SL scheme") for advection in one spatial dimension in the following section.

8.4.1 The leapfrog three-level SL scheme

In this scheme equation (8.2.1) is solved as [153]

$$\frac{f(x_i, t^{n+1}) - f(x_i - 2\alpha_i, t^{n-1})}{2\Delta t} = 0, \tag{8.4.1}$$

where α_i is the distance travelled by the trajectory arriving at the location (x_i, t^{n+1}) over one timestep Δt. With this approach, the major algorithmic choices are: (1) how to calculate α_i and (2) the interpolation used to calculate f at the departure point $(x_i - 2\alpha_i, t^{n-1})$. To address (1), Staniforth and Côte[153] give the approximation

$$\alpha_i = \Delta t U(x_i - \alpha_i, t^n), \tag{8.4.2}$$

which is second-order accurate but requires interpolation to find $U(x_i - \alpha_i, t^n)$. α_i can be found by iteratively solving (8.4.2) a small number of times ($\lesssim 3$ [58, 153]) (using an initial guess e.g. $\alpha_i = 0$).

To address (2), many interpolation schemes are available [58, 103, 153]. The trade-off between schemes is usually computational cost vs accuracy, with inaccuracy typically resulting in numerical dissipation. Of course, in a spectral scheme, one can evaluate f at an arbitrary location with complete accuracy (i.e. limited only by machine precision), but this cannot be done by Fast Fourier Transform. Instead, one would need to sum the $(n_x n_y)$-term Fourier series to calculate the value at a particular location. This would need to be done for each (x, y) location to advance the nonlinearity for a given $(z, \tilde{v}_\parallel, \tilde{\mu}_s, s)$ so would require ($\mathcal{O}\left(n_z n_{\tilde{v}_\parallel} n_{\tilde{\mu}_s} (n_x n_y)^2\right)$) operations per timestep, which would likely be prohibitively expensive.

In the following section, I describe a scheme with avoids interpolation altogether: the non-interpolating SL scheme.

8.4.2 The non-interpolating SL scheme

This scheme was proposed by Ritchie [146] and for eq. (8.2.1) can be written

$$\frac{f(x_i, t^{n+1}) - f(x_i - p_i \Delta x, t^{n-1})}{2\Delta t} = -U_{1i} \left.\frac{\partial f}{\partial x}\right|_{x_i - \frac{p_i \Delta x}{2}, t^n}, \tag{8.4.3}$$

where

$$p_i = \mathtt{nint}\left(\frac{2\Delta t}{\Delta x} U\left(x_i - \frac{p_i \Delta x}{2}\right)\right), \tag{8.4.4}$$

$$U_{1i} = U\left(x_i - \frac{p_i \Delta x}{2}, t^n\right) - \frac{p_i \Delta x}{2\Delta t}. \tag{8.4.5}$$

The basic idea is that rather than the markers following the trajectory of f exactly, they instead follow the approximate trajectory of f such that the departure point coincides with a gridpoint. This is shown pictorially in figure 8.4 (left). The residual velocity U_{1i} accounts for the difference between this trajectory and the actual trajectory of the gridpoint.

The residual velocity source term is explicit in (8.4.3) which introduces a CFL condition. However, Ritchie shows the scheme to be unconditionally stable when applied to two-dimensional advection by a spatio-temporally constant velocity, since the residual velocity is always sufficiently small $\left(\left|\frac{U_{1i}\Delta t}{\Delta x}\right| \leq \frac{1}{4}\right)$ that the CFL condition is always satisfied. However, I claim that when U is spatially varying, this is not guaranteed. As an example, consider figure 8.4, in which U is spatially varying.

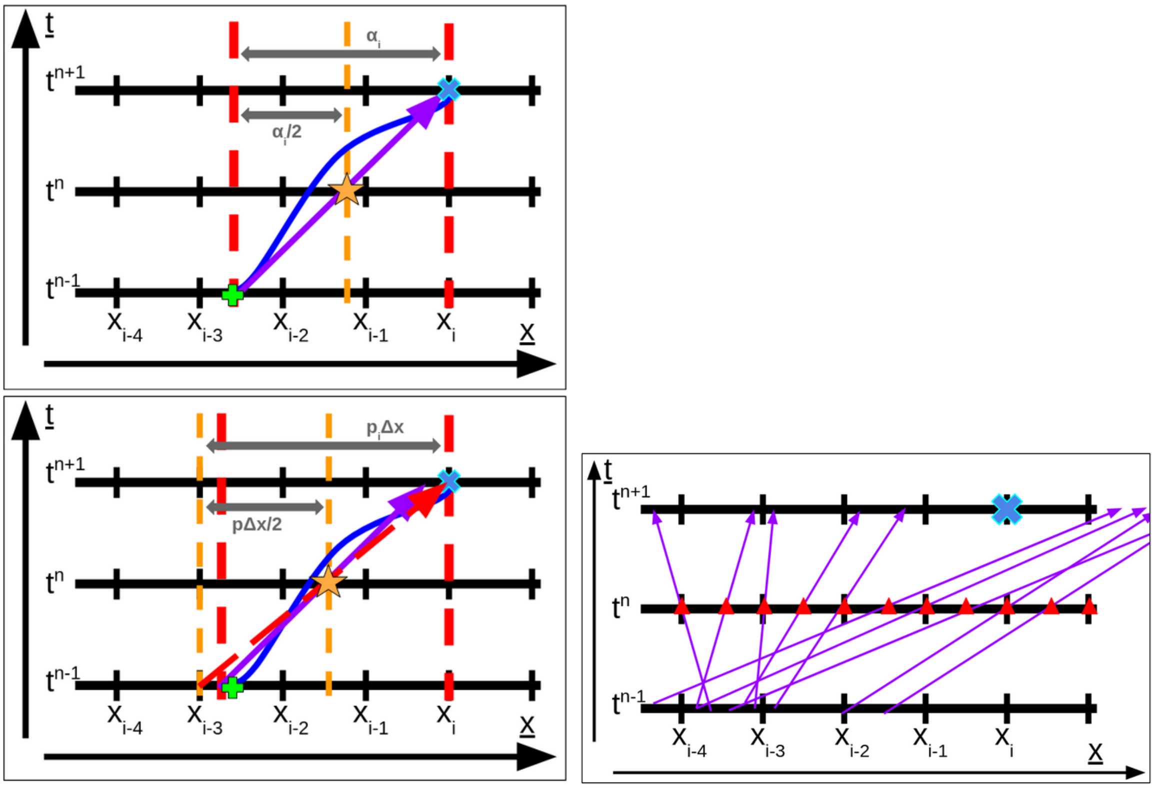

Figure 8.4: Schematic diagrams of SL schemes in one dimension. Upper left: a three-level SL scheme. The trajectory arriving at x_i at time t^{n+1}, represented by the blue curve, is approximated by an equivalent trajectory (purple arrow) with the same departure point (green plus). This trajectory is determined based on the velocity at $(x_i - \alpha_i, t^n)$ (orange star). Lower left: the NISL scheme. The approximate trajectory (purple arrow) is split into a gridpoint-to-gridpoint trajectory (dashed red arrow) and a small residual. Lower right: An issue with the NISL scheme as described by Ritchie [146], in which no candidate trajectory (purple lines) arrive near to x_i and thus the residual velocity is not guaranteed small.

For an example gridpoint α_i, no choice of p_i satisfies $\left|\frac{U_{1i}\Delta t}{\Delta x}\right| \leq \frac{1}{4}$. This could be made stable by reducing $\Delta\tilde{t}$, but the motivation of the SL scheme is to avoid numerical timestep constraints. This issue regarding the magnitude of the residual velocity for spatially-varying velocity fields is not mentioned by Ritchie [146] or other works which describe the scheme [58, 103, 153]. Possibly this indicates that, so far, the scheme is numerically well-behaved where it has been applied. Given this potential pitfall, I deploy an alternative scheme to calculating p_i and U_i for `stella` (described in section 8.6.2.1).

One may be tempted to incorporate the NISL scheme into a gyrokinetic code such as `stella`. However, a challenge remains to combine the NISL scheme (which is multistep, requiring information from two previous times) with single-step schemes used by `stella` to advance the linear terms. This is addressed in the following section.

8.5 Operator splitting with multi-step numerical schemes

Consider the system

$$\frac{\partial f}{\partial t}+\mathcal{A}(f)+\mathcal{B}(f)+\mathcal{C}(f)=0, \tag{8.5.1}$$

where $\mathcal{A},\mathcal{B},\mathcal{C}$ are generic operators. Suppose that one wishes to treat the operator $\mathcal{A}$ using a leapfrog-like operator, i.e.

$$\tilde{f}^{n+1}=\tilde{f}^{n-1}+2\Delta t\mathcal{A}(f^n), \tag{8.5.2}$$

and operators $\mathcal{B}$ and $\mathcal{C}$ using single-step operators. Lie-Trotter splitting prescribes the approach

$$\left(\frac{\mathrm{d}f}{\mathrm{d}t}\right)_1=\mathcal{A}(f) \tag{8.5.3}$$

$$\left(\frac{\mathrm{d}f}{\mathrm{d}t}\right)_2=\mathcal{B}(f) \tag{8.5.4}$$

$$\left(\frac{\mathrm{d}f}{\mathrm{d}t}\right)_3=\mathcal{C}(f), \tag{8.5.5}$$

where f^n is inserted into (8.5.3) and solved to obtain an intermediate solution $f^{n\dagger}$, which is inserted into (8.5.4) to obtain $f^{n\ddagger}$, which is finally inserted into (8.5.5) to obtain f^{n+1}. Lie-Trotter splitting is ambiguous for multistep scheme. For example, should one use f^n and f^{n-1} in (8.5.2), or some intermediate variables such as $f^{(n-1)\dagger}$?

A straightforward solution which incorporates SL scheme and non-advective source terms would be to simply make the entire algorithm three-level by adding a source term to the right-hand side of (8.4.1). For 2D advection, as is the case in the GKE, this looks like

$$\frac{f(x_i,y_j,t^{n+1})-f(x_i-2\alpha_i,y_j-2\beta_j,t^{n-1})}{2\Delta t}=\mathrm{R}(x_i-\alpha_i,y_j-\beta_j,t^n) \tag{8.5.6}$$

$$f(x,y,t^{n+1})=f(x_i-2\alpha_i,y_j-2\beta_j,t^{n-1})+2\Delta t\mathrm{R}(x_i-\alpha_i,y_j-\beta_j,t^n), \tag{8.5.7}$$

where $\mathrm{R}(x_i-\alpha_i,y_j-\beta_j,t^n)$ represents all of the linear terms from the GKE (and if the NISL scheme is used, the residual $\langle\tilde{\mathbf{v}}_E\rangle_{\mathbf{X}_s}$). The source term could be calculated spectrally on the $(\tilde{k}_x,\tilde{k}_y)$ grid, transformed to real space and then interpolated to $(x_i-\alpha_i,y_j-\beta_j)$. However, I choose not to employ this approach for two reasons. The first is to preserve the spectral accuracy of the linear terms in the GKE. The second is that computing the linear source terms using an explicit leapfrog approach would be CFL-constrained, and would lose the benefits of `stella`'s implicit schemes and the stability-preserving properties of the RK algorithms.

To take full advantage of these sophisticated linear algorithms, one could instead develop a new operator splitting scheme which mixes general single-step schemes with a multistep scheme. This would allow the user to mix numerical schemes for different terms in the GKE with full flexibility. I present such a scheme in the following section.

8.5.1 A new splitting scheme

The proposed scheme for solving eq. (8.5.1) is as follows:

1. Advance f^{n-1} by $\mathcal{B}$ and then $\mathcal{C}$ using Lie-Trotter splitting:

$$\left(\frac{\mathrm{d}f}{\mathrm{d}t}\right)_1 = \mathcal{B}(f) \tag{8.5.8}$$

$$\left(\frac{\mathrm{d}f}{\mathrm{d}t}\right)_2 = \mathcal{C}(f) \tag{8.5.9}$$

   to obtain an intermediate variable $f^{(n-1)\dagger}$.

2. Advance $f^{(n-1)\dagger}$ with the operator $\mathcal{A}$ using a leapfrog scheme to obtain $f^{(n+1)\ddagger}$:

$$f^{(n+1)\ddagger} = f^{(n-1)\dagger} + 2\Delta t\mathcal{A}(f^n) \tag{8.5.10}$$

3. Advance $f^{(n+1)\ddagger}$ by $\mathcal{C}$ and then $\mathcal{B}$ using Lie-Trotter splitting:

$$\left(\frac{\mathrm{d}f}{\mathrm{d}t}\right)_4 = \mathcal{C}(f) \tag{8.5.11}$$

$$\left(\frac{\mathrm{d}f}{\mathrm{d}t}\right)_5 = \mathcal{B}(f) \tag{8.5.12}$$

By Taylor expansion it can be shown that the local truncation error is $\mathcal{O}(\Delta t^3)$ if A, B and C are linear time-independent operators. In this case, the exact solution $f^{n\pm1}$ in terms of f^n can be written:

$$f^{n\pm1} = \exp(\pm(A+B+C)\Delta t)f^n \tag{8.5.13}$$

$$= \left[1 \pm (A+B+C)\Delta t + \frac{(\Delta t)^2}{2}(A+B+C)^2 + \mathcal{O}(\Delta t^3)\right] f^n, \tag{8.5.14}$$

where A, B and C are time-independent matrices. By Taylor expanding the exponential, the scheme gives us

$$
\begin{aligned}
f^{(n-1)\dagger} &= \exp(B\Delta t)\exp(C\Delta t)f^{n-1} && (8.5.15)\\
&= \left[1 + B\Delta t + \frac{\Delta t^2}{2}B^2 + ...\right]\left[1 + C\Delta t + \frac{\Delta t^2}{2}C^2 + ...\right]\cdot\\
&\quad \left[1 - (A+B+C)\Delta t + \frac{(\Delta t)^2}{2}(A+B+C)^2 + ...\right] f^n && (8.5.16)\\
&= \left[1 - A\Delta t + \frac{(\Delta t)^2}{2}(A^2 + AB + AC - BA + BC - CA - CB) + ...\right] f^n && (8.5.17)\\
f^{(n+1)\ddagger} &= \left[1 + A\Delta t + \frac{(\Delta t)^2}{2}(A^2 + AB + AC - BA + BC - CA - CB) + ...\right] f^n && (8.5.18)\\
f^{n+1} &= \left[1 + C\Delta t + \frac{\Delta t^2}{2}C^2 + ...\right]\left[1 + B\Delta t + \frac{\Delta t^2}{2}B^2 + ...\right]\cdot\\
&\quad \left[1 + A\Delta t + \frac{(\Delta t)^2}{2}(A^2 + AB + AC - BA + BC - CA - CB) + ...\right] f^n && (8.5.19)\\
&= \left[1 + (A+B+C)\Delta t + \frac{(\Delta t)^2}{2}(A+B+C)^2 + ...\right] f^n. && (8.5.20)
\end{aligned}
$$

(8.5.20) matches the exact solution up to and including $(\Delta t)^2$, so the truncation error is $\mathcal{O}(\Delta t^3)$ and the splitting scheme is second-order accurate.

This scheme requires $(2N-1)$ steps per timestep advanced for N single-step operations, making it roughly twice as expensive as the Lie-Trotter or flip-flop schemes. However, this may be acceptable if it allows the nonlinear CFL constraint to be avoided, which can reduce the timestep (and hence raise the expense) by orders of magnitude (as shown in figure 8.3).

8.5.1.1 Starting the scheme

A problem with multistep schemes in general is that they are not self-starting. This is true of the scheme presented here. To begin the scheme, I therefore use ordinary Lie-Trotter splitting for the first step (to get from $f^0 = f(t=0)$ to f^1), using a single-step scheme such as RK for the operator $\mathcal{A}$. If one wishes to take a large timestep, which breaks the CFL condition for $\mathcal{A}$ using an RK scheme, one can take multiple steps with a smaller timestep to go from f^0 to f^1. Once f^1 is obtained, one can revert to the larger timestep if the multistep scheme permits. This could be useful in `stella`, for example, if one wishes to restart a simulation in which $\tilde{g}_{\mathbf{k},s}$ is large.

8.6 Implementation in `stella`

The implementation described here (and results presented) correspond to the `stella` commit `b777f76`.

8.6.1 Operator splitting

As a starting point, I implement the splitting scheme described in section 8.5.1 linearly in `stella`; the streaming and mirror terms are treated using the usual implicit schemes and the magnetostatic drifts and diamagnetic-like drifts are evaluated using the leapfrog scheme.

The result for the cyclone base case (CBC) with ($\tilde{k}_y = 0.5$, $\tilde{k}_x = 0$) is shown in figure 8.5. There is good agreement in the mode structure, but curious oscillations in the mode complex frequency around the values predicted by conventional `stella` and `GS2`. It is possible that this is peculiar to the algorithm used by `stella` to calculate $\tilde{\Omega}$. `stella`'s approach compares the field-line average of $\tilde{\varphi}_{1\mathbf{k}}$ on two successive steps:

$$\tilde{\Omega}^n_{\texttt{stella}} = \frac{i}{\Delta\tilde{t}} \ln\left(\frac{\langle\tilde{\varphi}^n_{1\mathbf{k}}\rangle_z}{\langle\tilde{\varphi}^{n-1}_{1\mathbf{k}}\rangle_z}\right). \tag{8.6.1}$$

However, when one computes γ over a longer time range:

$$\tilde{\gamma}^n_2 = \frac{1}{2(\tilde{t}^n - \tilde{t}^m)} \ln\left(\frac{\langle|\tilde{\varphi}^n_{1\mathbf{k}}|^2\rangle_z}{\langle|\tilde{\varphi}^m_{1\mathbf{k}}|^2\rangle_z}\right), \tag{8.6.2}$$

where $m = \texttt{floor}(n/2)$, one finds that the growth rate converges to the conventional `stella` result to within 0.08% ($\tilde{\gamma}_2(\tilde{t})$ is shown in the lower left plot of figure 8.5). This discrepancy could plausibly be the result of divergence between the solutions on odd and even timesteps, as sometimes happens in leapfrog-like schemes. $\tilde{\gamma}_2$ averages over many steps which would smooth out these high-frequency features.

One can also use the splitting scheme to advance all of the linear terms in the usual way (implicit and RK schemes), and advance the nonlinear term using a leapfrog-like scheme (rather than an SL scheme). I show benchmarking results for this in the following section.

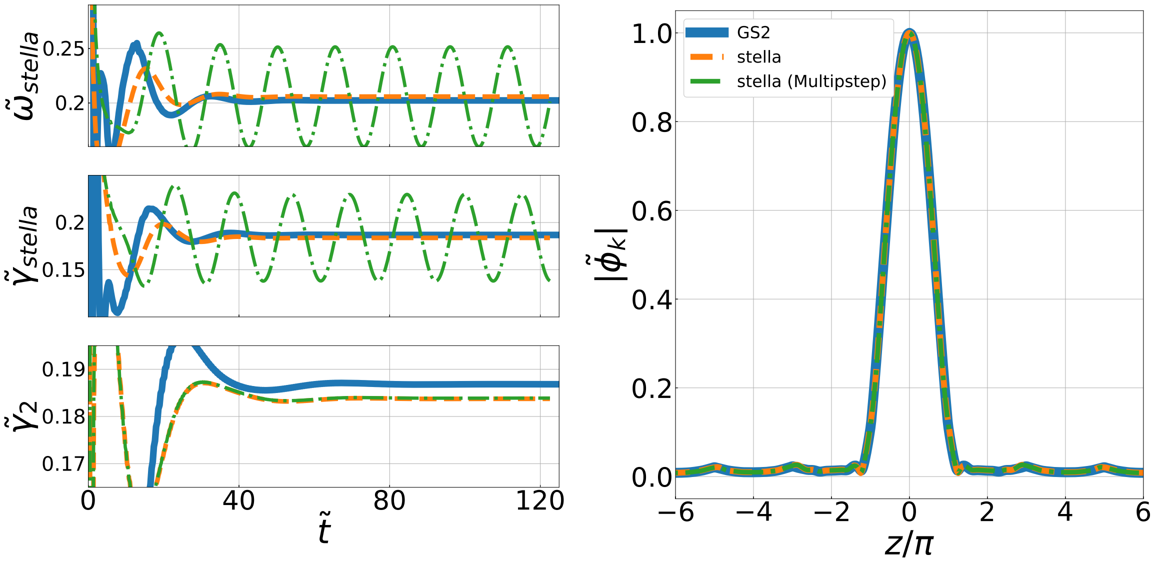

Figure 8.5: Linear operator splitting benchmarking in (CBC, $\tilde{k}_y = 0.5$). Left: Ω as calculated by `stella` and (bottom) $\tilde{\gamma}$ as calculated over many steps. Right: Normalised mode structure $|\tilde{\varphi}_{1\mathbf{k}}|(z)$.

8.6.2 Implementation of the NISL scheme and nonlinear benchmarks

8.6.2.1 NISL implementation

There is a danger that implementing the NISL scheme as presented by Ritchie brings about large residual velocities, which could give rise to numerical instability (see section 8.4.2). To avoid this, I implement a finite volume scheme to approximate the departure point for each gridpoint.

In my approach, the trajectory of the gridpoint is "traced back" through cells to find the departure point. The velocity in each cell is taken to be the velocity of the gridpoint at the cell centre at time $\tilde{t}^n$, and the $(\tilde{x}, \tilde{y})$ grid is upsampled for $\langle \tilde{\mathbf{v}}_E \rangle^n_{\mathbf{X}_s}$ such that it is evaluated on a grid with spacing $(\Delta\tilde{x}/2, \Delta\tilde{y}/2)$. An illustrative example of the original and upsampled $(\tilde{x}, \tilde{y})$ grids are shown in figure 8.6. The cell boundaries corresponding to these grids and an example map of $\langle \tilde{\mathbf{v}}_E \rangle^n_{\mathbf{X}_s}$ (generated from an example nonlinear simulation with $n_x = 10, n_y = 14$) is shown in figure 8.7. The trajectories for each gridpoint calculated using this finite volume scheme is shown in figure 8.8 and the approximate departure points for each gridpoint shown in figure 8.9. In this example, the velocities have been linearly scaled from the simulation values such that the typical Courant number exceeds one ($C_{max} \equiv \mathtt{max}\left(\left|\langle \tilde{\mathbf{v}}_E \rangle^n_{\mathbf{X}_s\,x} \Delta\tilde{t}/\Delta\tilde{x} + \langle \tilde{\mathbf{v}}_E \rangle^n_{\mathbf{X}_s\,y} \Delta\tilde{t}/\Delta\tilde{y}\right|\right) = 3.47$).

Once the estimated departure point $(\tilde{x}'_{ij}, \tilde{y}'_{ij})$ for each gridpoint $(\tilde{x}_i, \tilde{y}_j)$ is found, the effective velocity ($\mathbf{U}_{ij} = U_{x,ij}\hat{\mathbf{x}} + U_{y,ij}\hat{\mathbf{y}}$) is calculated:

$$U_{x,ij} = \frac{\tilde{x}_i - \tilde{x}'_{ij}}{2\Delta\tilde{t}} \qquad\qquad U_{y,ij} = \frac{\tilde{y}_j - \tilde{y}'_{ij}}{2\Delta\tilde{t}}. \tag{8.6.3}$$

$U_{x(y),ij}$ is then split into a gridpoint-to-gridpoint trajectory $U_{0x(y),ij}$ and a residual $U_{1x(y),ij}$:

$$U_{0x,ij} = p_{ij}\frac{\Delta\tilde{x}}{2\Delta\tilde{t}}; \qquad\qquad U_{1x,ij} = U_{x,ij} - U_{0x,ij} \tag{8.6.4}$$

$$U_{0y,ij} = q_{ij}\frac{\Delta\tilde{y}}{2\Delta\tilde{t}}; \qquad\qquad U_{1y,ij} = U_{y,ij} - U_{0y,ij}, \tag{8.6.5}$$

where

$$p_{ij} = \mathtt{nint}\left(\frac{2\Delta\tilde{t}U_{x,ij}}{\Delta\tilde{x}}\right); \qquad q_{ij} = \mathtt{nint}\left(\frac{2\Delta\tilde{t}U_{y,ij}}{\Delta\tilde{y}}\right). \tag{8.6.6}$$

The distribution function g_s is then updated in real space:

$$\begin{aligned} g_s^{n+1}(\tilde{x}_i, \tilde{y}_j) = g_s^{n-1}(\tilde{x}_i - p_{ij}\Delta\tilde{x}, \tilde{y}_j - q_{ij}\Delta\tilde{y}) - U_{1x,ij}\left.\frac{\partial g_s^n}{\partial x}\right|_{(\tilde{x}_i - p_{ij}\Delta\tilde{x}/2, \tilde{y}_j - q_{ij}\Delta\tilde{y}/2)} \\ - U_{1y,ij}\left.\frac{\partial g_s^n}{\partial \tilde{y}}\right|_{(\tilde{x}_i - p_{ij}\Delta\tilde{x}/2, \tilde{y}_j - q_{ij}\Delta\tilde{y}/2)}, \end{aligned} \tag{8.6.7}$$

before finally being converted back to Fourier space. $\frac{\partial g^n}{\partial \tilde{x}(\tilde{y})}$ is also upsampled onto the finer grid, such that it can be evaluated when $p_{ij}(q_{ij})$ is odd.

It should be emphasised that although this approach seems reasonable and guarantees small residual velocities $\left(|U_{1x(y),ij}| \leq \frac{\Delta\tilde{x}(\tilde{y})}{4\Delta\tilde{t}}\right)$, the accuracy of this scheme is not proven. It also tends to lead (see figure 8.9) to an accumulation of departure points in regions where the velocity is small and a low density of departure points in regions of large velocity.

For completeness, the NISL approach as described by Ritchie [146] is illustrated in figures 8.10 and 8.11 for the same velocity field as shown in figure 8.7. Figure 8.10 shows the trajectories corresponding to every location in the upsampled (x, y) grid. Figure 8.11 shows the departure and arrival points for each of these trajectories. It can be seen here that certain locations on the (x, y) grid have no nearby arrival points, which would result in large (i.e. CFL-breaking) residual velocities.

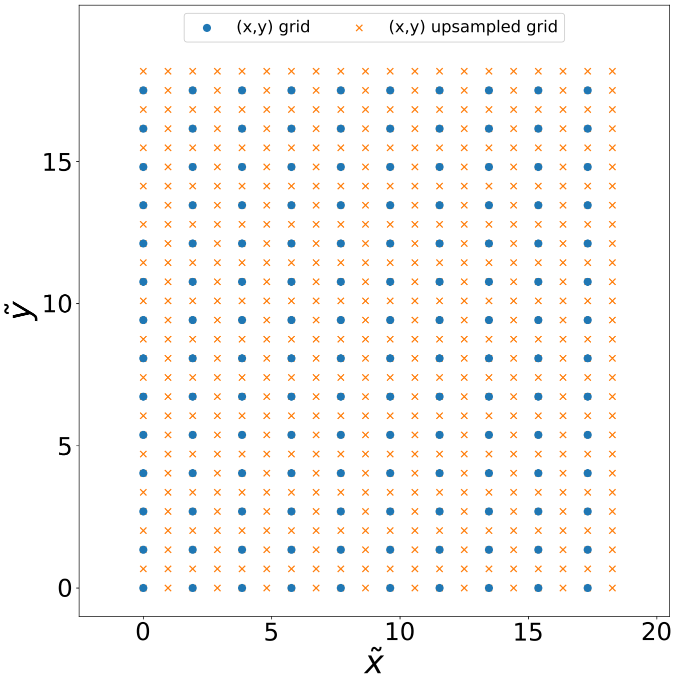

Figure 8.6: Illustration of the NISL implementation: The $(\tilde{x}, \tilde{y})$ grid for a `stella` simulation with $(n_x = 10, n_y = 14)$ (blue dots) and the upsampled grid (orange crosses) on which $\langle \tilde{\mathbf{v}}_E \rangle_{\mathbf{X}_s}$ and $\frac{\partial g_s}{\partial x,y}$ are evaluated.

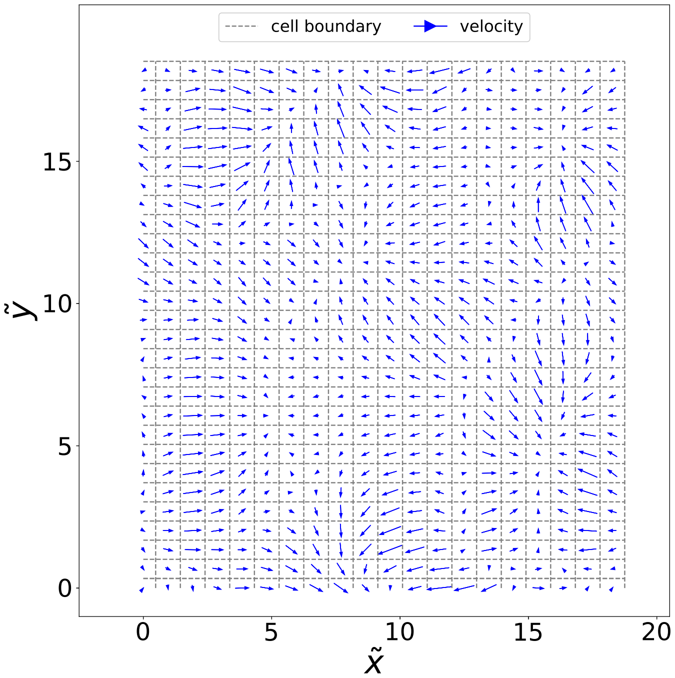

Figure 8.7: Illustration of the NISL implementation: The cells used in the finite volume trajectory-tracing approach (boundaries marked by grey lines). In each cell, the velocity is estimated using the upsampled grid. Blue arrows indicate relative magnitude and direction of $\langle \tilde{\mathbf{v}}_E \rangle_{\mathbf{X}_s}$ field for example simulation.

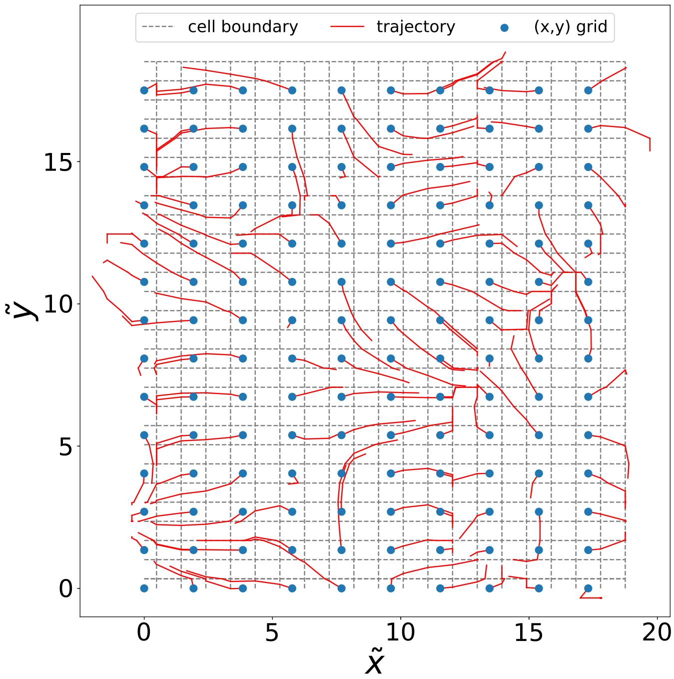

Figure 8.8: Illustration of the NISL implementation: For each point on the (non-upsampled) grid (blue dots), the departure point is estimated by tracking backwards through cells. Trajectories are shown by red lines.

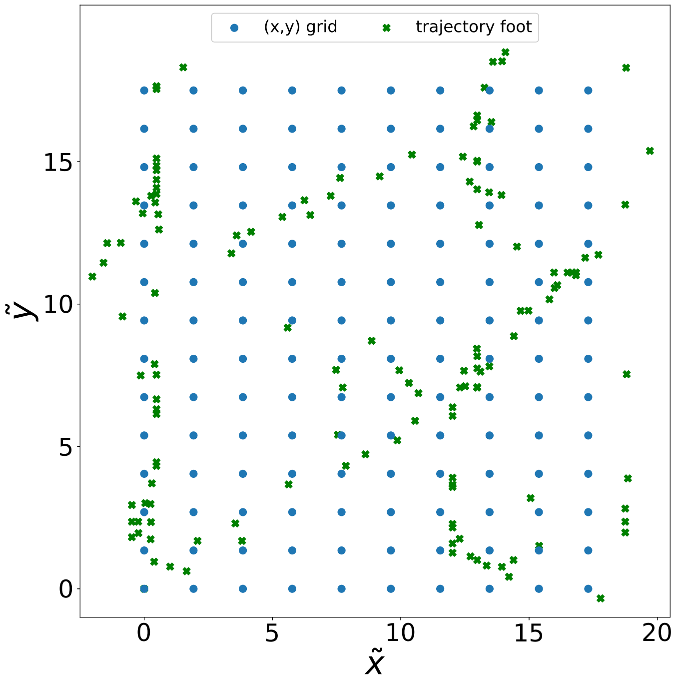

Figure 8.9: Illustration of the NISL implementation: The estimated departure point (green dots) for each grid point (blue dots) using an example velocity field. Departure points tend to accumulate in regions of small $| \langle \tilde{\mathbf{v}}_E \rangle_{\mathbf{X}_s} |$.

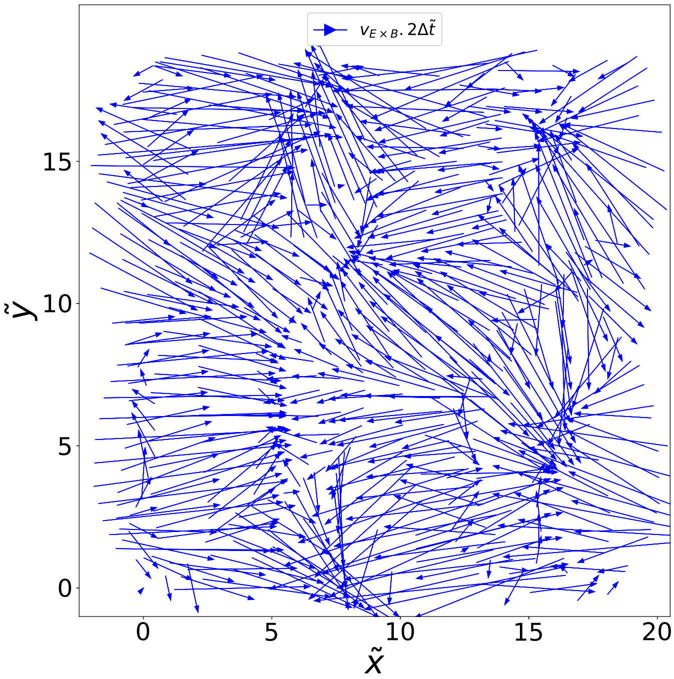

Figure 8.10: Illustration of the Ritchie's NISL scheme: trajectories (blue arrows) from t^{n-1} to t^{n+1} are shown for every upsampled gridpoint using $\langle\tilde{\mathbf{v}}_E\rangle_{\mathbf{X}_s}$ evaluated at t^n.

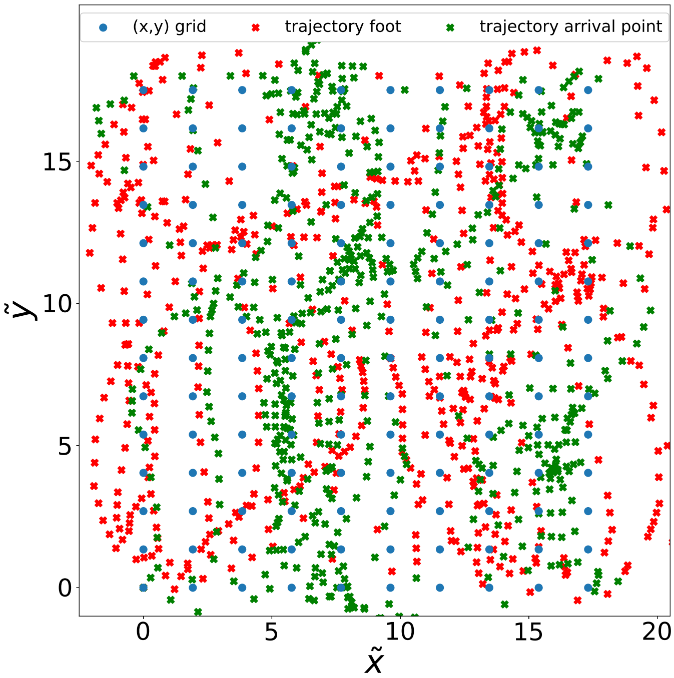

Figure 8.11: Illustration of the Ritchie's NISL scheme: departure points (red crosses) and arrival point (green crosses) of each possible trajectory are shown. Each point on the regular grid (blue dots) selects one of these trajectories to decompose into a gridpoint-to-gridpoint trajectory and a residual.

8.6.2.2 Interpolating SL implementation

Although the focus of this research is on the NISL scheme, the simple leapfrog three-level SL scheme is also implemented, with interpolation performed using simple bilinear interpolation. The accuracy of this approach is low and likely leads to unacceptable numerical dissipation, but serves as a starting point for investigations.

8.6.2.3 Results: advancing the $\mathbf{E} \times \mathbf{B}$ nonlinearity only

Figure 8.12 shows results for low-resolution simulations in which all terms except the nonlinearity are excluded. These simulations are not intended to accurately represent fusion plasmas, but enable the properties of different numerical schemes to be tested.

In the first simulation set, shown in figure 8.12 (upper left), $\langle \tilde{\mathbf{v}}_E \rangle_{\mathbf{X}_s}$ is overridden to be spatially and temporally constant with $\langle \tilde{\mathbf{v}}_E \rangle_{\mathbf{X}_s\,x} = 1, \langle \tilde{\mathbf{v}}_E \rangle_{\mathbf{X}_s\,y} = 0$. $\texttt{max}(\tilde{k}_x)$ is set to 1, which determines `stella`'s CFL timestep as $\texttt{cfl\_dt} = 2\pi \sim 6.28$. The timestep is set to $\Delta\tilde{t} = 0.02 \ll \texttt{cfl\_dt}$; ergo, this simulates the case where the Courant number is much less than unity. The exact solution is simply a change in phase of each mode with no growth or decay.

Figure 8.12, upper left shows how $\sum_{kx,ky} \left\langle |\tilde{\varphi}_{1\mathbf{k}}|^2 \right\rangle_z (t)$ changes over the simulation time. The solution for SSP RK2 increases in amplitude steadily over the simulation time, while SSP RK3 falls. This is consistent with remarks made in section 8.2; $|G| > 1$ for SSP RK2 since the scheme is unconditionally unstable, whereas $|G| < 1$ for SSP RK3 since $(\tilde{k}_x \langle \tilde{\mathbf{v}}_E \rangle_{\mathbf{X}_s\,x} \Delta\tilde{t}) < \sqrt{3}$ for all $\tilde{k}_x$. SSP RK4, leapfrog and NISL schemes have very small deviation in $\sum_{kx,ky} \left\langle |\tilde{\varphi}_{1\mathbf{k}}|^2 \right\rangle_z (t)$ $(\leq 2 \times 10^{-6}\%)$, indicating a greater level of accuracy. The disagreement between leapfrog and NISL is comparable with machine precision error ($\sim 10^{-13}$), as expected; in the limit that the advecting velocity is small compared to $(\Delta\tilde{x}/\Delta\tilde{t})$, the NISL scheme reduces to the leapfrog scheme, with essentially the same algorithm implemented by two independent subroutines. The SL scheme with bilinear interpolation shows a large change in $\sum_{kx,ky} |\tilde{\varphi}_{1\mathbf{k}}|^2(t)$ ($\sim 80\%$) and so is not included in figure 8.12 (upper left).

In the second simulation set, shown in figure 8.12 (upper right), $\langle \tilde{\mathbf{v}}_E \rangle_{\mathbf{X}_s}$ is again overridden, now with $\langle \tilde{\mathbf{v}}_E \rangle_{\mathbf{X}_s\,x} = 10, \langle \tilde{\mathbf{v}}_E \rangle_{\mathbf{X}_s\,y} = 0$ (such that $\texttt{cfl\_dt} = \pi/5 \sim 0.628$), and $\Delta\tilde{t}$ increased to 0.2. In this case, the leapfrog, SSP RK2 and SSP RK3 schemes experience rapid exponential growth ("numerical blowup"), consistent with $|G| > 1$ (NB stability for the SSP RK3 scheme requires $\Delta\tilde{t} \leq \sqrt{3}/(\texttt{max}(\tilde{k}_x) \langle \tilde{\mathbf{v}}_E \rangle_{\mathbf{X}_s\,x}) \sim 0.17$). SSP RK4 remains stable but rapidly decays, presumably since $|G|$ is no longer close to 1. The NISL scheme, started with an SSP RK4 step, shows an oscillating error at around 10%. However, when the analytic solution is used to solve the first timestep, the NISL

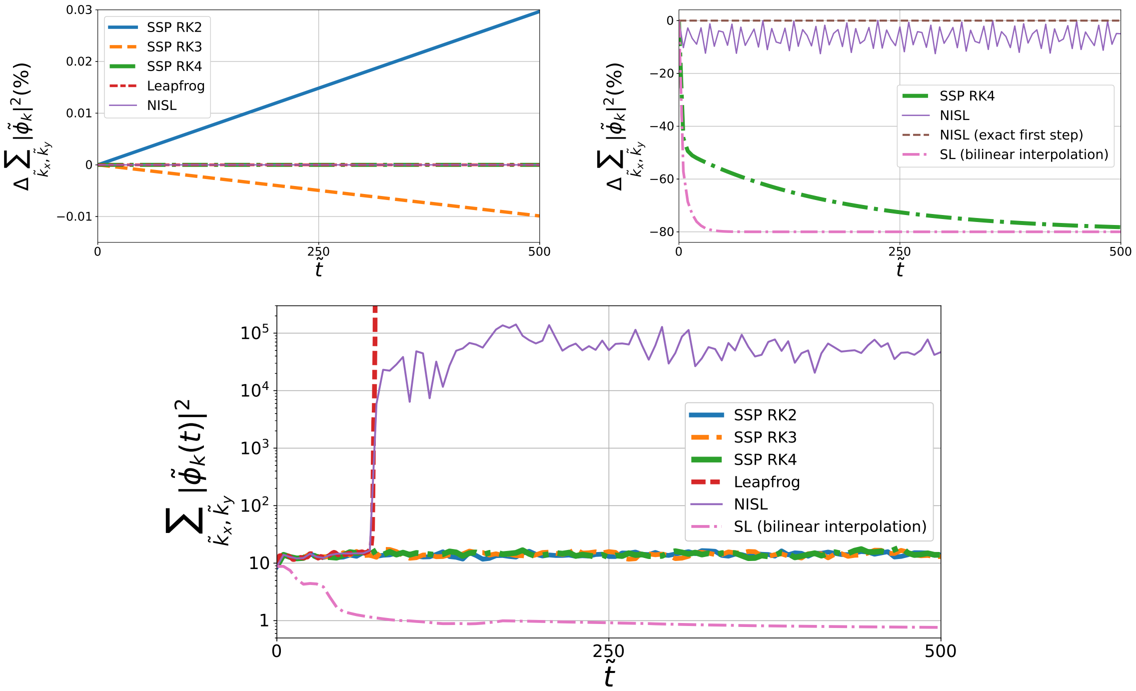

Figure 8.12: `stella` simulations where only the nonlinear source term is included. Upper left: constant velocity field with low Courant number ($\Delta\tilde{t}/\texttt{cfl\_dt} = 0.003$). Upper right: constant velocity field with moderate Courant number ($\Delta\tilde{t}/\texttt{cfl\_dt} = 0.3$). Bottom plot: $\langle \tilde{\mathbf{v}}_E \rangle_{\mathbf{X}_s}$ calculated consistently with $\tilde{g}_{\mathbf{k},s}$.

scheme becomes highly accurate, with a maximum error in $\sum_{kx,ky} |\tilde{\varphi}_{1\mathbf{k}}|^2(t)$ of $\sim 0.01\%$. Therefore, in this test the NISL scheme's accuracy is highly sensitive to how the scheme is started. The solution when using the SL scheme using bilinear interpolation is quickly damped. I speculate this is due to numerical "smoothing out" causing $\tilde{g}_{\mathbf{k},s}$ to be transferred to the $(\tilde{k}_x = \tilde{k}_y = 0)$ mode, which is then zeroed out by `stella`.

The third simulation set uses $\Delta\tilde{t} = 0.02$ but does not override $\langle \tilde{\mathbf{v}}_E \rangle_{\mathbf{X}_s}$; thus the advecting velocity is spatio-temporally varying in an unprescribed manner. Physical intuition suggests that $\sum_{kx,ky} \left\langle |\tilde{\varphi}_{1\mathbf{k}}|^2 \right\rangle_z$ should be approximately constant, since $\tilde{g}_s(\tilde{x}, \tilde{y})$ is conserved. Figure 8.12, lower shows the simulation results: SSP RK2, SSP RK3 and SSP RK4 behave reasonably and the interpolating SL scheme rapidly damps. The leapfrog scheme and NISL schemes behave similarly until around $\tilde{t} = 100$, whereupon some kind of numerical instability occurs. For the leapfrog scheme, this results in numerical blowup and an extremely small timestep. For NISL, this appears to cause a bifurcation to a high-amplitude state.

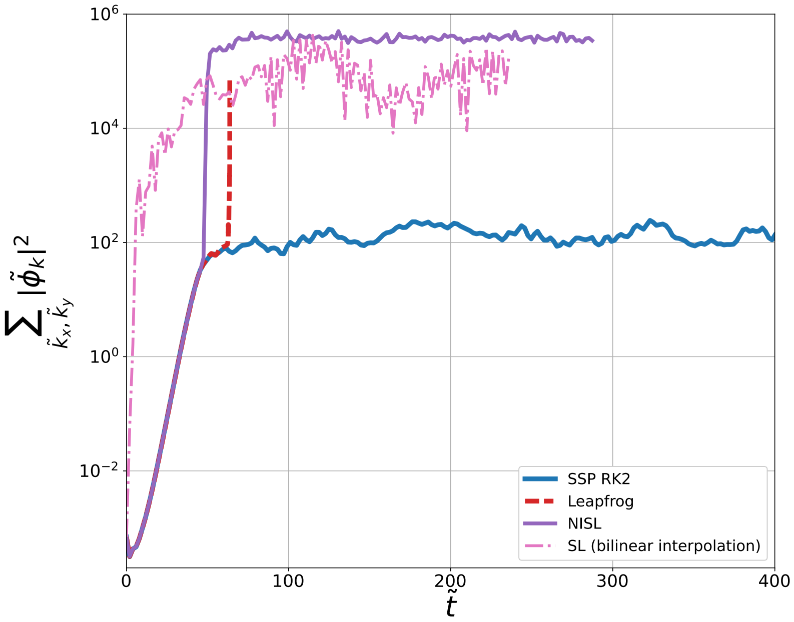

Figure 8.13: $\sum_{\tilde{k}_x,\tilde{k}_y}\left\langle|\tilde{\varphi}_{1\mathbf{k}}|^2\right\rangle_z(t)$ for different numerical schemes for CBC nonlinear simulations containing linear source terms. $\Delta\tilde{t}(\tilde{t}=0)$ is the same for all simulations, but drops in the Leapfrog scheme as `stella`'s CFL condition is hit.

8.6.2.4 Results: nonlinear Cyclone Base Case simulations

Figure 8.13 shows "full" nonlinear simulations for the CBC, in which all linear source terms are included. The SSP RK2 simulation is the same as presented in section 8.3.1; the input file is included for reference in appendix D. The leapfrog and NISL implementations (which have all the same simulation parameters except for specifying the leapfrog/NISL schemes) show similar behaviour to the nonlinear-only simulations, with leapfrog experiencing a numerical instability and NISL bifurcating to a higher-turbulence state. The interpolating SL scheme shows different behaviour to the nonlinear-only simulations, also entering a high-turbulence state.

Figure 8.14 shows $\tilde{\varphi}_{1\mathbf{k}}(\tilde{k}_x,\tilde{k}_y)$ for the last timestep of each simulation. It is interesting to note that the three misbehaving simulations (leapfrog, NISL and interpolating SL) all display different (and currently unexplained) characteristics. The leapfrog simulation is dominated by zonal modes, but shows some fine structure in $(\tilde{k}_x,\tilde{k}_y)$. The NISL simulation shows a strong contribution from the lowest nonzero $\tilde{k}_y$ modes and a great degree of symmetry in $\tilde{k}_x$ about $\tilde{k}_x=0$. The SL implementation with bilinear interpolation is dominated by zonal modes (possibly a result of numerical smoothing).

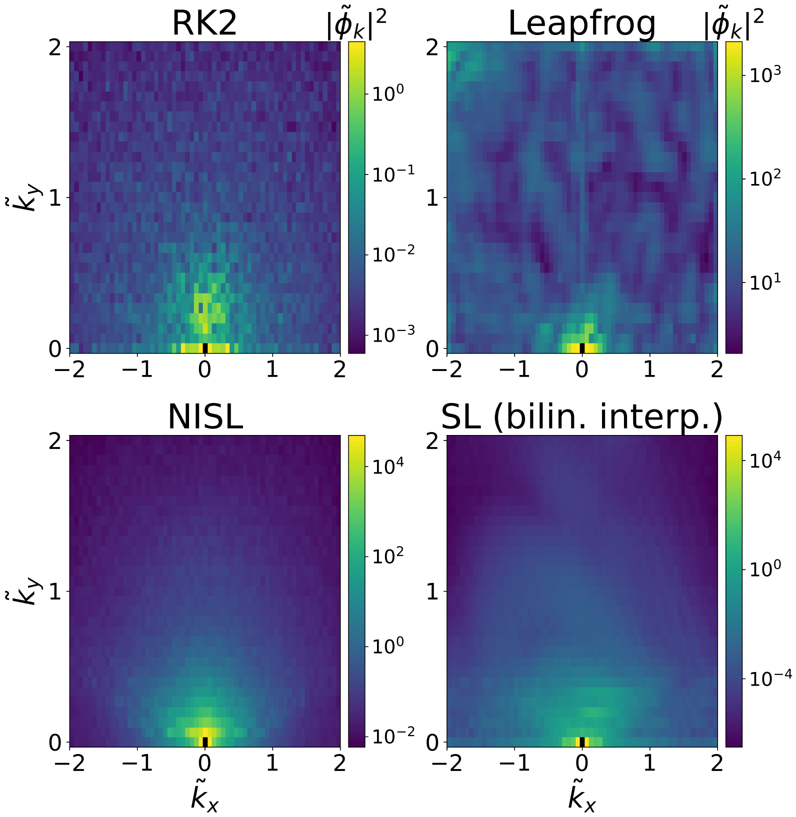

Figure 8.14: $\left\langle |\tilde{\varphi}_{1\mathbf{k}}|^2 \right\rangle_z (\tilde{k}_x, \tilde{k}_y, \tilde{t} = \tilde{t}_{\text{final}})$ for different numerical schemes for CBC nonlinear simulations.

8.7 Concluding remarks

In this chapter, I develop a non-interpolating SL (NISL) scheme and novel operator splitting algorithm and implement these in the electrostatic `stella` code. A linear test of the splitting scheme, while showing curious oscillations in $\Omega(\tilde{t})$ as calculated by `stella`, shows good agreement in mode structure compared with the original `stella` and `GS2`. When averaged over many steps, the growth rate also shows good agreement. The NISL scheme shows a greater level of accuracy for a spatio-temporally constant velocity field than the SSP schemes and does not have a CFL constraint. However, when $\langle \tilde{\mathbf{v}}_E \rangle_{\mathbf{X}_s}$ is allowed to vary, as is the case in gyrokinetics, the NISL simulation encounters some kind of numerical instability and bifurcates to a higher-turbulence state. Numerical instability also occurs when the nonlinear source term is calculated using a leapfrog approach, without SL. An SL scheme using bilinear interpolation is also implemented, but in all tests the solution departs rapidly from the expected behaviour and other schemes. This is likely due to a high level of numerical diffusion arising from the low-accuracy interpolation scheme.

The reasons behind the poor performance of the NISL scheme are less easily explained. One possibility is that the finite volume scheme used to estimate the departure points is simply too inaccurate. `stella`'s default approach calculates a source term in real space with spectral accuracy. By departing from this, NISL may introduce unacceptably large errors. Another possibility is that the leapfrog-like source term used to handle the residual velocity has poor stability properties, and some particular feature of $\tilde{g}_{\mathbf{k},s}$ and/or $\langle \tilde{\mathbf{v}}_E \rangle_{\mathbf{X}_s}$ causes a rapidly growing numerical instability. This would explain why the leapfrog and NISL schemes both experience sharp jumps in $\sum_{\tilde{k}_x,\tilde{k}_y} \left\langle |\tilde{\varphi}_{1\mathbf{k}}|^2 \right\rangle_z$ at specific times. A third possibility is that the splitting scheme gives rise to instability in some cases.

With the last point in mind, a useful area of research could be whether a noninterpolating SL scheme could be combined with an SSP RK method, with the latter used to calculate the source term arising from the residual velocity. This may have improved stability properties compared to the leapfrog approach. It would also avoid the need to use multistep splitting scheme with its $(2N-1)$ advances per timestep, and hence reduce the computational cost further.

Chapter 9

Summary and discussion

Magnetically confined fusion (MCF) as a power source is likely within our reach. However, fusion power plant optimisation remains an open question. A basic challenge is how to sustain a sufficiently hot, dense plasma with an economically and technically acceptable level of external heating and fuelling. This can be addressed by better understanding the physical processes by which heat and particles are transported in the plasma. Often this transport is dominated by turbulence driven by Larmor radius-scale microinstabilities. Thus, studying magnetised plasma turbulence and the underlying instabilities in reactor-relevant conditions can inform fusion power plant design and operation. The trend towards higher plasma β (for reasons of commercial viability) makes electromagnetic microinstabilities an increasingly important area of research.

Turbulence in strongly magnetised plasmas is often well-described by the theoretical framework of gyrokinetics, consisting of a five-dimensional, integro-differential, multiscale and nonlinear system of equations. The particular focus of this thesis is local spectral Eulerian δf time-marching gyrokinetic codes which are able to simulate microinstabilities and turbulence in realistic geometry at relatively low computational cost, thus making them a useful investigative tool. This thesis covers two main categories: (1) the use of gyrokinetics to explore instabilities in advanced MCF reactor concepts (namely, spherical tokamaks (STs) and the optimised stellarator Wendelstein 7-X (W7-X)) and (2) the development of the gyrokinetic code `stella` to efficiently simulate electromagnetic gyrokinetics using novel schemes. The material presented here can be posed as answers to three research questions:

Is negative plasma triangularity viable in commercial spherical tokamaks?

Probably not, based on linear gyrokinetic simulations of hypothetical ST equilibria. Negative triangularity, by increasing the bad curvature region of the field line, tends to have a destabilising effect on kinetic ballooning modes (KBMs). For the model negative triangularity ST equilibrium studied, the KBM growth rate is large across the core (which is unstable to $n = \infty$ ideal MHD ballooning modes (IBMs)) and would likely lead to unacceptably high levels of turbulent transport.

This poor stability can be interpreted as a closing of the window of "second stability" in $(\hat{s}, \alpha)$ space, in which reactor-plausible ST equilibria typically operate, meaning that the attainable β gradient is restricted to the "first stable region" (typically a factor of 2-3 lower than the equilibrium β gradient). The closing of second stability occurs in both STs and conventional aspect ratio tokamaks (CTs); however, the latter typically do not require second stability access across the core, and so may retain reasonable density and temperature profiles with negative triangularity. By contrast, a negative triangularity ST fusion power plant would either need to have a large machine size to maintain large core β or would have to operate at a lower β, by reducing the plasma pressure and/or increasing the magnetic field strength. A larger device increases the capital cost as well as presenting engineering issues. Reducing the plasma pressure would significantly reduce the fusion power generated, and a larger magnetic field would be challenging to achieve given the limited space in the ST central column (and would likely be expensive to build and run). It is possible that these KBMs could be stabilised by flow shear but since the KBM growth rate increases quickly above marginal stability, this level of flow shear would need to be large, and thus unlikely to be achieved by external means in a reactor. A parametric study of the dependence of the second stability window $\hat{s}_{\text{min}}$ on Miller parameters finds that fairly extreme changes are required to achieve $\hat{s}_{\text{min}} > 0$ for negative triangularity flux surfaces (for example, reducing elongation from $\kappa = 3.3$ to $\kappa < 2$ or increasing the safety factor from $q = 3.0$ to $q = 5.4$ on the $\psi/\psi_{LCFS} = 0.5$ flux surface).

In contrast, hypothetical power plant ST equilibria with positive triangularity are able to completely avoid IBMs, provided the on-axis safety factor is sufficiently high (which could be achieved by a hollow current profile, for example by off-axis heating or a large bootstrap current). The gyrokinetic growth rates are correspondingly lower. However, the dominant instability over much of the core is still a KBM, albeit weakly growing, which is destabilised by some (yet undiagnosed) kinetic effect. It would be interesting to examine how such equilibria behave nonlinearly to infer the levels of turbulent transport in these model equilibria.

How do microinstabilities in optimised W7-X geometries depend on temperature and density gradients?

This work reproduces and builds on the electrostatic "stability valley" first reported by Alcusón *et al.* [32]. Electrostatically, the ion-scale instabilities are the ion temperature gradient (ITG)-driven mode, the trapped electron mode (TEM) driven by density gradients and an ITG-TEM "mixed" mode. The growth rate is lower when the density and temperature gradients are approximately equal, producing a "valley" of stability. Reproduction of these results using a new gyrokinetic code `stella` serves as a useful validation of both the physics and the codes.

Simulations at finite β using the electromagnetic implementation of `stella` reveal electromagnetic instabilities which are likely to complicate the stability valley. At fixed gradients and magnetic geometry, scanning β is found to destabilise the KBM at some critical β, β_{crit}. These KBMs show similar behaviour to those examined in STs: in particular they preferentially occur at shorter wavelength, grow strongly for $\beta > \beta_{\text{crit}}$ and are stabilised in the absence of $B_{1\|}$ fluctuations. When gradients are scanned at fixed geometry and fixed β, tearing-parity electromagnetic instabilities occur even before the KBM is destabilised. These occur at larger $k_y\rho_i$ and appear to be pressure-driven, which could provide a stiff limit on kinetic profiles in W7-X plasmas. Given the rich and relatively unexplored microinstability landscape of optimised stellarators, and the ability of the electromagnetic `stella` code to simulate such geometries at low cost, this would be an exciting topic of future research.

Can novel algorithmic approaches be used to accurately simulate electromagnetic gyrokinetics in complex geometry at lower computational cost?

The motivation for this research is that source terms appear in the electromagnetic GKE which are proportional to $v_\| A_{1\|}$ (physically corresponding to streaming along a fluctuating magnetic field), which scale with the species thermal velocity and plasma β. This can be challenging when electrons are included in simulations by virtue of their large thermal velocity, which constrains explicit time-marching schemes by the CFL condition. Reducing the computational cost of gyrokinetic codes enables more results to be obtained for a given computational budget and so reduces the "time to science". `stella` is an ideal code in which to implement novel schemes due to its flexible operator-splitting scheme and its ability to simulate stellarator geometries.

To this end, electromagnetic effects are implemented in `stella`, using a GKE formulation which ensures that no source terms are unphysically large (which is shown to lead to cancellation problems) while still permitting fully general operator splitting. An additional benefit of this formulation is to reduce the number of source terms, which are found to lower the computational cost in stellarator simulations when compared with the original `stella` code by a factor of 1.5-3.7 in like-for-like simulations. An electromagnetic form of Kotschenreuter's implicit algorithm for the streaming and mirror terms is implemented and benchmarked, and is shown to increase the timestep by an order of magnitude in sensible-fidelity stellarator simulations compared to a fully explicit approach. The numerical stability of the electromagnetic implementation is sometimes sensitive to how finite-difference derivatives are treated and is in poor agreement with the code `GS2` for the test case of the kinetic shear Alfvén wave (with damping rate γ in disagreement by $\geq 50\%$). However, the code is shown to be in good agreement with `GS2` for electromagnetic tokamak (cyclone base case) simulations with typical differences in complex frequency $\tilde{\Omega}$ of $< 10\%$. It also gives reasonable agreement with the electrostatic version of the `stella` code (which formulates the GKE differently) (typical $\Delta\Omega < 10\%$) when performing simulations with W7-X geometry.

Finally, a non-interpolating semi-Lagrange (NISL) treatment of the $\mathbf{E} \times \mathbf{B}$ nonlinearity is implemented, with the ambition of reducing the cost of nonlinear electromagnetic simulations. The mixing of single-step and multi-step algorithms is permitted by the development of a new operator splitting scheme. A test of the splitting scheme for a linear problem shows promising results although oscillatory behaviour is seen in the complex frequency $\tilde{\Omega}$ as calculated by `stella`. The NISL scheme currently shows poor results, with unphysical behaviour being displayed. There are several avenues of future research, including the use of conventional SL schemes for the treatment of the nonlinear term.

9.1 Final remarks

This thesis addresses the numerical simulation of microinstabilities and turbulence in advanced MCF plasmas; in particular, the spherical tokamak and optimised stellarator. Both of these are the subject of immense interest as reactor concepts around the world. Future theoretical research into these topics, including by means of electromagnetic gyrokinetic simulation, is likely to lead to steadily greater device performance and will ultimately increase the viability of controlled fusion as a power source.

Appendix A

Pseudocode for implicit parallel streaming in `stella`

A.1 The electrostatic algorithm (original `stella`)

```
Before the first timestep is taken:

1.          | For each $k_y$:
1.1.            | For each extended $z$ domain:
1.1.1.              | Construct an $n_{z,ext} \times n_{z,ext}$ array $\mathbf{R}$.
1.1.2.              | For each $z$ value (labelled $z_j$) in the extended domain:
1.1.2.1.                | For each value of $\tilde{v}_{\parallel}, \tilde{\mu}_s$:
1.1.2.1.1.                  | Calculate the source terms in (3.10.11) arising from a unit impulse $\tilde{\varphi}_{1\mathbf{k}}$ at $z_j$ . These are
                            | equal to $C_{1,j*}$ at location $z_{j*}$, and $C_{2,(j-1)*}$ at location $z_{(j-1)*}$.
1.1.2.1.2.                  | Solve (3.10.11) to find $g_h(z)$ arising from the unit impulse at $z_j$.
1.1.2.2.                | Solve quasi-neutrality to find $\tilde{\varphi}_{1\mathbf{k}}$ arising from $g_h(z, \tilde{v}_{\parallel}, \tilde{\mu}_s)$; this is equal to $\frac{\mathbf{I}_1\left(\frac{\partial g_h}{\partial \tilde{\varphi}^{n+1}_{1\mathbf{k}\ \ j}}\right)}{K_{11}}$
1.1.2.3.                | Store $\delta_{ij} - \frac{\mathbf{I}_1\left(\frac{\partial g_h}{\partial \tilde{\varphi}^{n+1}_{1\mathbf{k}\ \ j}}\right)}{K_{11}}$ in the $j$th column of $\mathbf{R}$ (where $i$ is the row index and $\delta_{ij}$ is
                        | the kronecker-delta function).
1.1.3.              | Perform $LU$ decomposition on $\mathbf{R}$ and store the result in $\mathbf{R}$
```

In each timestep:

```
1.        | For each $k_y$:
1.1.          | For each extended $z$ domain:
1.1.1.            | For each value of $z, \tilde{v}_\parallel, \tilde{\mu}_s$:
1.1.1.1.              | Calculate the source terms for the inhomogeneous equation (3.10.10).
1.1.2.            | Solve (3.10.10) to find $g_{inh}(z)$.
1.1.3.            | Solve quasi-neutrality (3.10.14) to find $\varphi_{inh}(z)$.
1.1.4.            | Use R to calculate $\tilde{\varphi}_{1\mathbf{k}}^{n+1}(z)$ using (3.10.18)
1.1.5.            | Calculate $\tilde{g}_{\mathbf{k},s}^{n+1}(z)$ using (3.10.8)
```

A.2 The electromagnetic algorithm (`EM stella`)

Before the first timestep is taken:

```
1.          | For each $k_y$:
1.1.            | For each extended $z$ domain:
1.1.1.              | Construct an $(\texttt{nfield} \cdot n_{z,ext}) \times (\texttt{nfield} \cdot n_{z,ext})$ array $\mathbf{R}$ (where
                    | $\texttt{nfield} = 3$ when $\tilde{\varphi}_{1\mathbf{k}}$, $\tilde{A}_{1\|\mathbf{k}}$, $\tilde{B}_{1\|\mathbf{k}}$ are included).
1.1.2.              | Set $\texttt{ifield} = 1$.
1.1.3.              | For each $z$ value (labelled $z_j$) in the extended domain:
1.1.3.1.                | For each value of $\tilde{v}_\|, \tilde{\mu}_s$:
1.1.3.1.1.                  | Calculate the source terms in (3.10.11) arising from a unit impulse in $\Delta\tilde{\varphi}_{1\mathbf{k}}$ at $z_j$ .
1.1.3.1.2.                  | Solve (6.3.31) to find $\tilde{h}_{\mathbf{k},s,\mathrm{hom}}(z)$ arising from the unit impulse at $z_j$.
1.1.3.2.                | Solve the field equations to find $(\Delta\tilde{\varphi}_{1\mathbf{k}}, \Delta\tilde{A}_{1\|\mathbf{k}}, \Delta\tilde{B}_{1\|\mathbf{k}})$ arising from $\tilde{h}_{\mathbf{k},s,\mathrm{hom}}(z, \tilde{v}_\|, \tilde{\mu}_s)$; this
                        | is equal to $\underline{\underline{K}}_h^{-1}\mathbf{l}\left(\frac{\partial \tilde{h}_{\mathbf{k},s,\mathrm{hom}}}{\partial \Delta\tilde{\varphi}_{1\mathbf{k}j}}\right)$
1.1.3.3.                | Store $\delta_{ij} - \underline{\underline{K}}_h^{-1}\mathbf{l}\left(\frac{\partial \tilde{h}_{\mathbf{k},s,\mathrm{hom}}}{\partial \Delta\tilde{\varphi}_{1\mathbf{k}j}}\right)$ in the $(\texttt{ifield} - 1) \cdot n_{z,ext} + j$th column of $\mathbf{R}$ (where $i$ is the
                        | row index and $\delta_{ij}$ is the kronecker-delta function).
1.1.4.              | Repeat 1.1.3. with $\texttt{ifield} = 2$, applying a unit impulse in $\Delta\tilde{A}_{1\|\mathbf{k}}$.
1.1.5.              | Repeat 1.1.3. with $\texttt{ifield} = 3$, applying a unit impulse in $\Delta\tilde{B}_{1\|\mathbf{k}}$.
1.1.6.              | Perform $LU$ decomposition on $\mathbf{R}$ and store the result in $\mathbf{R}$
```

In each timestep:

```
1.          | For each $k_y$:
1.1.            | For each extended $z$ domain:
1.1.1.              | Calculate $\tilde{h}_{\mathbf{k},s}^n$ from $\tilde{\tilde{g}}_{\mathbf{k},s}^n$ and $\mathbf{f}^n$.
1.1.2.              | For each value of $z, \tilde{v}_\|, \tilde{\mu}_s$:
1.1.2.1.                | Calculate the source terms for the inhomogeneous equation (6.3.30).
1.1.3.              | Solve (3.10.10) to find $\tilde{h}_{\mathbf{k},s,\mathrm{inh}}(z)$.
1.1.4.              | Use (6.3.33) to find $\Delta\mathbf{f}_{\mathrm{inh}}$.
1.1.5.              | Use $\mathbf{R}$ to calculate $\Delta\mathbf{f}(z)$ using (6.3.40).
1.1.6.              | Calculate $\tilde{h}_{\mathbf{k},s}^{n+1}(z)$ using (6.3.26).
1.1.7.              | Use $\tilde{h}_{\mathbf{k},s}^{n+1}$ to find $(\tilde{\varphi}_{1\mathbf{k}}^{n+1}, \tilde{A}_{1\|\mathbf{k}}^{n+1}, \tilde{B}_{1\|\mathbf{k}}^{n+1})$ and thus calculate $\tilde{\tilde{g}}_{\mathbf{k},s}^{n+1}$
```

Appendix B

The implicit mirror algorithm in electromagnetic `stella`

By making the replacement $\tilde{\bar{g}}_{\mathbf{k},s} \to \tilde{h}_{\mathbf{k},s} - \frac{Z}{T}e^{-\tilde{v}_s^2}\left\langle\tilde{\chi}_{\mathbf{k}}\right\rangle_{\mathbf{X}_s}$ in eq. (6.3.41) and temporally discretising, one arrives at:

$$\frac{\tilde{h}_{\mathbf{k},s}^{n+1} - \tilde{h}_{\mathbf{k},s}^{n} - \frac{Z}{T}e^{-\tilde{v}_s^2}\left(\left\langle\tilde{\chi}_{\mathbf{k}}\right\rangle_{\mathbf{X}_s}^{n+1} - \left\langle\tilde{\chi}_{\mathbf{k}}\right\rangle_{\mathbf{X}_s}^{n}\right)}{\Delta\tilde{t}} - \tilde{v}_{th,s}\tilde{\mu}_s\mathbf{b}\cdot\boldsymbol{\nabla}\tilde{B}_0\left(\frac{\partial\tilde{h}_{\mathbf{k},s}^{n*}}{\partial\tilde{v}_{\|}}\right) = 0, \tag{B.0.1}$$

$$\tilde{h}_{\mathbf{k},s}^{n+1} - \tilde{h}_{\mathbf{k},s}^{n} - \frac{Z}{T}e^{-\tilde{v}_s^2}\left(\Delta\left\langle\tilde{\chi}_{\mathbf{k}}\right\rangle_{\mathbf{X}_s}\right) - \Delta\tilde{t}(\tilde{v}_{th,s}\tilde{\mu}_s\mathbf{b}\cdot\tilde{\boldsymbol{\nabla}}\tilde{B}_0)\left(\frac{\partial\tilde{h}_{\mathbf{k},s}^{n*}}{\partial\tilde{v}_{\|}}\right) = 0, \tag{B.0.2}$$

$$\tilde{h}_{\mathbf{k},s}^{n+1} - \tilde{h}_{\mathbf{k},s}^{n} - \frac{Z}{T}e^{-\tilde{v}_s^2}\left(\Delta\left\langle\tilde{\chi}_{\mathbf{k}}\right\rangle_{\mathbf{X}_s}\right) - \Delta\tilde{t}(\tilde{v}_{th,s}\tilde{\mu}_s\mathbf{b}\cdot\tilde{\boldsymbol{\nabla}}\tilde{B}_0)\left(\frac{1+u_t}{2}\frac{\partial\tilde{h}_{\mathbf{k},s}^{n+1}}{\partial\tilde{v}_{\|}} + \frac{1-u_t}{2}\frac{\partial\tilde{h}_{\mathbf{k},s}^{n}}{\partial\tilde{v}_{\|}}\right) = 0 \tag{B.0.3}$$

$\tilde{h}_{\mathbf{k},s}^{n+1}$ is then split into inhomogeneous and homogeneous pieces, $\tilde{h}_{\mathbf{k},s}^{n+1} = \tilde{h}_{\mathbf{k},s,\text{inh}} + \tilde{h}_{\mathbf{k},s,\text{hom}}$, where

$$\tilde{h}_{\mathbf{k},s,\text{inh}} - \tilde{h}_{\mathbf{k},s}^{n} - \Delta\tilde{t}(\tilde{v}_{th,s}\tilde{\mu}_s\mathbf{b}\cdot\tilde{\boldsymbol{\nabla}}\tilde{B}_0)\left(\frac{1+u_t}{2}\frac{\partial\tilde{h}_{\mathbf{k},s,\text{inh}}}{\partial\tilde{v}_{\|}} + \frac{1-u_t}{2}\frac{\partial\tilde{h}_{\mathbf{k},s}^{n}}{\partial\tilde{v}_{\|}}\right) = 0, \tag{B.0.4}$$

$$\tilde{h}_{\mathbf{k},s,\text{hom}} - \Delta\tilde{t}(\tilde{v}_{th,s}\tilde{\mu}_s\mathbf{b}\cdot\tilde{\boldsymbol{\nabla}}\tilde{B}_0)\frac{1+u_t}{2}\frac{\partial\tilde{h}_{\mathbf{k},s,\text{hom}}}{\partial\tilde{v}_{\|}} - \frac{Z}{T}e^{-\tilde{v}_s^2}\Delta\left\langle\tilde{\chi}_{\mathbf{k}}\right\rangle_{\mathbf{X}_s} = 0. \tag{B.0.5}$$

To advance from $\tilde{\bar{g}}_{\mathbf{k},s}^{n}$ to $\tilde{\bar{g}}_{\mathbf{k},s}^{n+1}$, $\tilde{h}_{\mathbf{k},s}^{n}$ is calculated and (B.0.4) is solved to find $\tilde{h}_{\mathbf{k},s,\text{inh}}$. The fields are then calculated using the mirror response matrix:

$$\Delta\mathbf{f} = \underline{\underline{R}}_m^{-1}\Delta\mathbf{f}_{\text{inh}}, \tag{B.0.6}$$

where

$$\Delta\mathbf{f} = \Delta\mathbf{f}_{\text{inh}} + \Delta\mathbf{f}_{\text{hom}} = \underline{\underline{K}}_h^{-1}\left(\mathbf{l}(\tilde{h}_{\mathbf{k},s,\text{inh}}) - \mathbf{l}(\tilde{h}_{\mathbf{k},s}{}^{n})\right) + \underline{\underline{K}}_h^{-1}\mathbf{l}(\tilde{h}_{\mathbf{k},s,\text{hom}}) \tag{B.0.7}$$

$\Delta\mathbf{f}$ is used to calculate $\tilde{h}_{\mathbf{k},s}^{n+1}$ using eq. (B.0.3) which is then converted to $\tilde{\tilde{g}}_{\mathbf{k},s}^{n+1}$.

It should be noted that this scheme fails if $\Delta\mathbf{f}_{\text{inh}} = 0$ (consider e.g. eq. (B.0.6)), and it is worth considering if this occurs in practice. As an example, one could consider an electrostatic simulation ($A_{1\|} = B_{1\|} = 0$). Eq. (B.0.7) then becomes

$$\Delta\tilde{\varphi}_{1\mathbf{k}} = \Delta\tilde{\varphi}_{1\mathbf{k},\text{inh}} + \Delta\tilde{\varphi}_{1\mathbf{k},\text{hom}} = \frac{l_1(\tilde{h}_{\mathbf{k},s,\text{inh}}) - l_1(\tilde{h}_{\mathbf{k},s}{}^{n})}{K_{11,h}} + \frac{l_1(\tilde{h}_{\mathbf{k},s,\text{hom}})}{K_{11,h}}. \tag{B.0.8}$$

Since (B.0.4) is just an advection equation for $\tilde{h}_{\mathbf{k},s}$ in $\tilde{v}_{\|}$, one would expect $l_1(\tilde{h}_{\mathbf{k},s,\text{inh}}) = l_1(\tilde{h}_{\mathbf{k},s}{}^{n})$ and therefore $\Delta\tilde{\varphi}_{1\mathbf{k},\text{inh}}$ to vanish analytically, breaking the scheme. However, this scheme has been benchmarked electrostatically without encountering any problems and has shown good agreement with `GS2` and the original `stella` implementation (see sections 6.4.3 and 7.6.2). It is possible that this problem is averted by the fact that numerical inaccuracy ensures that $l_1(\tilde{h}_{\mathbf{k},s,\text{inh}}) - l_1(\tilde{h}_{\mathbf{k},s}{}^{n})$ does not vanish, thereby allowing the scheme to remain well-behaved. It is possible this scheme would become badly behaved if the velocity space is treated with extremely high fidelity.

Appendix C

Input parameters for linear `stella` benchmarks

The fiducial parameters used in the linear `stella` tests described in section 6.4.2 are as follows:

1. For the unsheared slab geometry:
    1.1. `GS2`: $n_{\text{period}} = 1, n_z = 32, \Delta\tilde{t} = 0.04, n_{\text{step}} = 1000, u_z = 0.05, u_{t,\texttt{GS2}} = 0.45, n_E = 16$
    1.2. `stella`, implicit: $n_{\text{period}} = 1$, $n_z = 32$, $\Delta\tilde{t} = 0.04$, $n_{\text{step}} = 1000$, $u_z = 0$, $u_t = 0$, $n_{\tilde{v}_{||}} = 24$, $n_{\tilde{\mu}_s} = 12$, $\tilde{v}_{||,\text{max}} = 3$, $\tilde{v}_{\perp,\text{max}} = 3$
    1.3. `stella`, fully explicit: $n_{\text{period}} = 1$, $n_z = 32$, $\Delta\tilde{t} = 4\text{E} - 4$, $n_{\text{step}} = 1te5$, $n_{\tilde{v}_{||}} = 24$, $n_{\tilde{\mu}_s} = 12$, $\tilde{v}_{||,\text{max}} = 3$, $\tilde{v}_{\perp,\text{max}} = 3$
2. For the CBC simulation:
    2.1. `GS2`: $\Delta\tilde{t} = 0.05$, $n_{\text{step}} = 2000$, $u_z = 0.05$, $u_{t,\texttt{GS2}} = 0.45$, $n_{\text{gauss}} = 18$, $n_E = 18$
    2.2. `stella`, partially implicit: $\Delta\tilde{t} = 0.01$, $n_{\text{step}} = 2000$, $u_z = 0$, $u_t = 0.02$, $u_{v||} = 0.02$, $n_{\tilde{v}_{||}} = 18$, $n_{\tilde{\mu}_s} = 12$, $\tilde{v}_{||,\text{max}} = 3$, $\tilde{v}_{\perp,\text{max}} = 3$
    2.3. `stella`, fully explicit: $\Delta\tilde{t} = 0.001$, $n_{\text{step}} = 4E4$, $n_{\tilde{v}_{||}} = 18$, $n_{\tilde{\mu}_s} = 12$, $\tilde{v}_{||,\text{max}} = 3$, $\tilde{v}_{\perp,\text{max}} = 3$

Appendix D

Nonlinear CBC input file for `stella`

```
&physics_flags
 nonlinear = .true.
 full_flux_surface = .false.
/
&init_g_knobs
 chop_side = F
 phiinit = 0.001 ! 1.0
 !restart_file = "restart.nc"
 restart_dir = "restart"
 ginit_option = "default"
 width0 = 1.0
/
&millergeo_parameters
 nzed_local = 128
 rhoc = 0.5
 shat = 0.78
 qinp = 1.38
 rmaj = 2.72
 rgeo = 2.72
 shift = 0.0
 kappa = 1.0
 kapprim = 0.0
 tri = 0.0
 triprim = 0.0
 betaprim = 0.0
 d2qdr2 = 0.0
 d2psidr2 = 0.0
 betadbprim = 0.0
/
&parameters
 zeff = 1.0
 beta = 0.0
 rhostar = 0.0
 vnew_ref = 0.0
 nine = 1.0
 tite = 1.0
/
&species_knobs
 nspec = 2
 species_option = ’stella’
/
&species_parameters_1
 z = 1.0
 mass = 1.0
 dens = 1.0
 temp = 1.0
 tprim = 2.537
 fprim = 0.809
/
&species_parameters_2
 z=     -1.0
 mass=   2.7e-4
```

```
 dens=   1.0
 temp=   1.0
 tprim=  2.49
 fprim=  0.8
 type='electron'
/
&kt_grids_box_parameters
 ny = 91
 nx = 91
 y0 = 15
/
&zgrid_parameters
 nzed = 64
 nperiod = 1
 boundary_option = 'linked'
 zed_equal_arc = T
/
&vpamu_grids_parameters
 nvgrid = 24
 nmu = 12
 vpa_max = 3.0
 vperp_max = 3.0
/
&knobs
 fphi = 1.0
 fapar = 0.0
 fbpar = 0.0
 delt = 0.05
 nstep = 30000
 cfl_cushion = 0.250
 mat_read = .false.
 mat_gen = .false.
 LU_option = 'local'
/
&stella_diagnostics_knobs
 nwrite = 100
 nsave = 5000
 save_for_restart = .true.
 write_omega = .false.
 write_kspectra = .true.
 write_phi_vs_time = .false.
 write_gvmus = .false.
 write_moments = .true.
 write_gzvs = .false.
/
&layouts_knobs
 xyzs_layout = 'yxzs'
 vms_layout = 'vms'
/
&neoclassical_input
 include_neoclassical_terms = .false.
/
&sfincs_input
 nproc_sfincs = 2
 nxi = 16
 nx = 5
/
&dissipation
 hyper_dissipation = .false.
/
&geo_knobs
 geo_option = 'miller'
/
&reinit_knobs
 delt_adj = 2.0
 delt_minimum = 1.e-4
/
&dist_fn_knobs
 adiabatic_option = "iphi00=2"
/
&time_advance_knobs
 explicit_option = "rk2"
/
&kt_grids_knobs
 grid_option = 'box'
/
&kt_grids_range_parameters
 nalpha = 1
/
```

Bibliography

[1] R. F. Post. Controlled fusion research—an application of the physics of high temperature plasmas. *Rev. Mod. Phys.*, 28:338, 1956.

[2] R. Post. High-temperature plasma research and controlled fusion. *Annual Review of Nuclear Science*, 9(1):367, 1959.

[3] M. Barbarino. A brief history of nuclear fusion. *Nature Physics*, 16(9):890, 2020.

[4] S. C. Cowley. The quest for fusion power. *Nature physics*, 12(5):384, 2016.

[5] `https://assets.publishing.service.gov.uk/government/uploads/system/uploads/attachment_data/file/1022540/towards-fusion-energy-uk-government-fusion-strategy.pdf`. Accessed: 2022-05-07.

[6] `https://www.whitehouse.gov/ostp/news-updates/2022/03/15/fact-sheet-developing-a-bold-vision-for-commercial-fusion-energy/`. Accessed: 2022-05-07.

[7] G. H. Miley, H. Towner, and N. Ivich. Fusion cross sections and reactivities. Technical report, Illinois Univ., Urbana (USA), 1974.

[8] J. Wesson. *Tokamaks*. Oxford University Press, 2011.

[9] F. F. Chen et al. *Introduction to plasma physics and controlled fusion*, volume 1. Springer, 1984.

[10] R. Post. The magnetic mirror approach to fusion. *Nuclear Fusion*, 27(10):1579, 1987.

[11] A. Burdakov, A. Ivanov, and E. Kruglyakov. Modern magnetic mirrors and their fusion prospects. *Plasma Physics and Controlled Fusion*, 52(12):124026, 2010.

[12] J. P. Freidberg. *ideal MHD*. Cambridge University Press, 2014.

[13] L. A. El-Guebaly. Fifty years of magnetic fusion research (1958–2008): brief historical overview and discussion of future trends. *Energies*, 3(6):1067, 2010.

[14] L. Artsimovich. Research into controlled thermonuclear reactions in the ussr. *The Soviet Journal of Atomic Energy*, 5(5):1411, 1958.

[15] M. Keilhacker, M. Watkins, J. Team, et al. D–t experiments in the jet tokamak. *Journal of nuclear materials*, 266:1, 1999.

[16] E. Gibney. Nuclear-fusion reactor smashes energy record. https://www.nature.com/articles/d41586-022-00391-1, 2022.

[17] R. Aymar. The iter project. *IEEE transactions on plasma science*, 25(6):1187, 1997.

[18] https://www.euro-fusion.org/programme/demo/. Accessed: 2022-05-24.

[19] M. Ono and R. Kaita. Recent progress on spherical torus research. *Physics of Plasmas*, 22(4):040501, 2015.

[20] Y. M. Peng and D. J. Strickler. Features of spherical torus plasmas. *Nuclear Fusion*, 26(6):769, 1986.

[21] T. Hender, et al. Magneto-hydro-dynamic limits in spherical tokamaks. *Physics of Plasmas*, 6(5):1958, 1999.

[22] F. Troyon and R. Gruber. A semi-empirical scaling law for the β-limit in tokamaks. *Physics Letters A*, 110(1):29, 1985.

[23] J. E. Menard, et al. Aspect ratio scaling of ideal no-wall stability limits in high bootstrap fraction tokamak plasmas. *Physics of Plasmas*, 11(2):639, 2004.

[24] P. Helander, et al. Stellarator and tokamak plasmas: a comparison. *Plasma Physics and Controlled Fusion*, 54(12):124009, 2012.

[25] Y. Xu. A general comparison between tokamak and stellarator plasmas. *Matter and Radiation at Extremes*, 1(4):192, 2016.

[26] S. Gori. Theory of fusion plasmas. In *Proc. Workshop Varenna, 1996*, volume 335. Editrice Compositori, 1997.

[27] A. H. Boozer. Quasi-helical symmetry in stellarators. *Plasma Physics and Controlled Fusion*, 37(11A):A103, 1995.

[28] J. Nührenberg. Development of quasi-isodynamic stellarators. *Plasma Physics and Controlled Fusion*, 52(12):124003, 2010.

[29] R. Wolf, et al. Performance of wendelstein 7-x stellarator plasmas during the first divertor operation phase. *Physics of Plasmas*, 26(8):082504, 2019.

[30] J. H. E. Proll, P. Helander, J. W. Connor, and G. Plunk. Resilience of quasi-isodynamic stellarators against trapped-particle instabilities. *Physical Review Letters*, 108(24):245002, 2012.

[31] J. Proll, H. Mynick, P. Xanthopoulos, S. Lazerson, and B. Faber. Tem turbulence optimisation in stellarators. *Plasma Physics and Controlled Fusion*, 58(1):014006, 2015.

[32] J. Alcusón, P. Xanthopoulos, G. Plunk, P. Helander, F. Wilms, Y. Turkin, A. Von Stechow, and O. Grulke. Suppression of electrostatic micro-instabilities in maximum-j stellarators. *Plasma Physics and Controlled Fusion*, 62(3):035005, 2020.

[33] H. Grad and H. Rubin. Hydromagnetic equilibria and force-free fields. *Journal of Nuclear Energy (1954)*, 7(3-4):284, 1958.

[34] J. M. Greene and J. L. Johnson. Determination of hydromagnetic equilibria. *The Physics of Fluids*, 4(7):875, 1961.

[35] R. D. Hazeltine and J. D. Meiss. *Plasma confinement*. Courier Corporation, 2003.

[36] A. W. Leonard. Edge-localized-modes in tokamaks. *Physics of Plasmas*, 21(9):090501, 2014.

[37] J. Connor, A. Kirk, and H. Wilson. Edge localised modes (elms): experiments and theory. In *AIP Conference Proceedings*, volume 1013, pages 174–190. American Institute of Physics, 2008.

[38] A. Loarte, et al. Transient heat loads in current fusion experiments, extrapolation to iter and consequences for its operation. *Physica Scripta*, 2007(T128):222, 2007.

[39] X. Garbet, Y. Idomura, L. Villard, and T. Watanabe. Gyrokinetic simulations of turbulent transport. *Nuclear Fusion*, 50(4):043002, 2010.

[40] P. Terry, et al. Overview of gyrokinetic studies of finite-β microturbulence. *Nuclear Fusion*, 55(10):104011, 2015.

[41] D. Dickinson. *Effects of profiles on microinstabilities in tokamaks*. Ph.D. thesis, University of York, 2012.

[42] I. G. Abel, G. G. Plunk, E. Wang, M. Barnes, S. C. Cowley, W. Dorland, and A. A. Schekochihin. Multiscale gyrokinetics for rotating tokamak plasmas: fluctuations, transport and energy flows. *Reports on Progress in Physics*, 76(11):116201, 2013.

[43] F. Wagner, et al. Regime of improved confinement and high beta in neutral-beam-heated divertor discharges of the asdex tokamak. *Physical Review Letters*, 49(19):1408, 1982.

[44] F. I. Parra, M. Barnes, and A. G. Peeters. Up-down symmetry of the turbulent transport of toroidal angular momentum in tokamaks. *Physics of Plasmas*, 18(6):062501, 2011.

[45] M. Barnes, F. I. Parra, and M. Landreman. stella: An operator-split, implicit–explicit δf-gyrokinetic code for general magnetic field configurations. *Journal of Computational Physics*, 391:365, 2019.

[46] Y. Idomura, M. Ida, T. Kano, N. Aiba, and S. Tokuda. Conservative global gyrokinetic toroidal full-f five-dimensional vlasov simulation. *Computer Physics Communications*, 179(6):391, 2008.

[47] A. H. Hakim, N. R. Mandell, T. Bernard, M. Francisquez, G. Hammett, and E. Shi. Continuum electromagnetic gyrokinetic simulations of turbulence in the tokamak scrape-off layer and laboratory devices. *Physics of Plasmas*, 27(4):042304, 2020.

[48] M. Barnes, et al. stella.

[49] M. Barnes, et al. Gs2 v8.1.0, 2021. Supported by CCP Plasma (https://gow.epsrc.ukri.or g/NGBOViewGrant.aspx?GrantRef=EP/M022463/1) and HEC Plasma (https://gow.epsrc.ukri.org/NGBOViewGra nt.aspx?GrantRef=EP/R029148/1).

[50] J. Baumgaertel, E. Belli, W. Dorland, W. Guttenfelder, G. Hammett, D. Mikkelsen, G. Rewoldt, W. Tang, and P. Xanthopoulos. Simulating gyrokinetic microinstabilities in stellarator geometry with gs2. *Physics of Plasmas*, 18(12):122301, 2011.

[51] E. Sánchez, et al. Gyrokinetic simulations in stellarators using different computational domains. *Nuclear Fusion*, 61(11):116074, 2021.

[52] A. González-Jerez, P. Xanthopoulos, J. García-Regaña, I. Calvo, J. Alcusón, A. B. Navarro, M. Barnes, F. Parra, and J. Geiger. Electrostatic gyrokinetic simulations in wendelstein 7-x geometry: benchmark between the codes stella and gene. *Journal of Plasma Physics*, 88(3), 2022.

[53] E. G. Highcock. The Zero Turbulence Manifold in Fusion Plasmas. *arXiv e-prints*, arXiv:1207.4419, 2012.

[54] M. D. Kruskal and R. Kulsrud. Equilibrium of a magnetically confined plasma in a toroid. *The Physics of Fluids*, 1(4):265, 1958.

[55] R. L. Miller, M. S. Chu, J. M. Greene, Y. R. Lin-Liu, and R. E. Waltz. Noncircular, finite aspect ratio, local equilibrium model. *Physics of Plasmas*, 5(4):973, 1998.

[56] K. F. Riley, M. P. Hobson, and S. J. Bence. Mathematical methods for physics and engineering, 1999.

[57] C. Roach. Private correspondance.

[58] J. P. Boyd. *Chebyshev and Fourier spectral methods*. Courier Corporation, 2001.

[59] M. Kotschenreuther, G. Rewoldt, and W. Tang. Comparison of initial value and eigenvalue codes for kinetic toroidal plasma instabilities. *Computer Physics Communications*, 88(2):128, 1995.

[60] P. Snyder, et al. Pedestal stability comparison and ITER pedestal prediction. *Nuclear Fusion*, 49(8):085035, 2009.

[61] P. B. Snyder, R. J. Groebner, A. W. Leonard, T. H. Osborne, and H. R. Wilson. Development and validation of a predictive model for the pedestal height. *Physics of Plasmas*, 16(5):056118, 2009.

[62] P. B. Snyder, et al. The EPED Pedestal Model: Validation, Super H-Mode, and Core-Pedestal Coupling. In *APS Meeting Abstracts*, page TP12.090. 2015.

[63] P. B. Snyder, O. Meneghini, M. N. A. Beurskens, J. W. Hughes, T. H. Osborne, and H. R. Wilson. Prediction and Optimization of the ITER Pedestal. In *APS Meeting Abstracts*, page TO4.002. 2016.

[64] I. B. Bernstein, E. Frieman, M. D. Kruskal, and R. Kulsrud. An energy principle for hydromagnetic stability problems. *Proceedings of the Royal Society of London. Series A. Mathematical and Physical Sciences*, 244(1236):17, 1958.

[65] J. W. Connor, R. Hastie, and J. B. Taylor. High mode number stability of an axisymmetric toroidal plasma. *Proceedings of the Royal Society of London. A. Mathematical and Physical Sciences*, 365(1720):1, 1979.

[66] C. Mercier. A necessary condition for hydromagnetic stability of plasma with axial symmetry. *Nuclear Fusion*, 1(1):47, 1960.

[67] M. S. Anastopoulos Tzanis. *Beyond Axisymmetry in Tokamak Plasmas*. Ph.D. thesis, University of York, 2019.

[68] W. A. Newcomb. Hydromagnetic stability of a diffuse linear pinch. *Annals of Physics*, 10(2):232, 1960.

[69] B. Patel, D. Dickinson, C. Roach, and H. Wilson. Linear gyrokinetic stability of a high β non-inductive spherical tokamak. *Nuclear Fusion*, 62(1):016009, 2021.

[70] A. Dimits, B. Cohen, N. Mattor, W. Nevins, D. Shumaker, S. Parker, and C. Kim. Simulation of ion temperature gradient turbulence in tokamaks. *Nuclear Fusion*, 40(3Y):661, 2000.

[71] J. Greene and M. Chance. The second region of stability against ballooning modes. *Nuclear Fusion*, 21(4):453, 1981.

[72] H. Wilson, et al. Integrated plasma physics modelling for the culham steady state spherical tokamak fusion power plant. *Nuclear Fusion*, 44(8):917, 2004.

[73] T. M. Antonsen Jr and B. Lane. Kinetic equations for low frequency instabilities in inhomogeneous plasmas. *The Physics of Fluids*, 23(6):1205, 1980.

[74] W. Tang, J. Connor, and R. Hastie. Kinetic-ballooning-mode theory in general geometry. *Nuclear Fusion*, 20(11):1439, 1980.

[75] K. Aleynikova and A. Zocco. Quantitative study of kinetic ballooning mode theory in simple geometry. *Physics of Plasmas*, 24(9):092106, 2017.

[76] R. Hastie and K. Hesketh. Kinetic modifications to the mhd ballooning mode. *Nuclear Fusion*, 21(6):651, 1981.

[77] C. Cheng. Kinetic theory of collisionless ballooning modes. *The Physics of Fluids*, 25(6):1020, 1982.

[78] E. Belli and J. Candy. Fully electromagnetic gyrokinetic eigenmode analysis of high-beta shaped plasmas. *Physics of Plasmas*, 17(11):112314, 2010.

[79] K. Aleynikova, A. Zocco, P. Xanthopoulos, P. Helander, and C. Nührenberg. Kinetic ballooning modes in tokamaks and stellarators. *Journal of Plasma Physics*, 84(6), 2018.

[80] R. Davies, D. Dickinson, and H. Wilson. Kinetic ballooning modes as a constraint on plasma triangularity in commercial spherical tokamaks. *Plasma Physics and Controlled Fusion*, 64(10):105001, 2022.

[81] A. E. Costley and S. A. M. McNamara. Fusion performance of spherical and conventional tokamaks: implications for compact pilot plants and reactors. *Plasma Physics and Controlled Fusion*, 63(3):035005, 2021.

[82] S. Kaye, et al. NSTX/NSTX-u theory, modeling and analysis results. *Nuclear Fusion*, 59(11):112007, 2019.

[83] M. Gryaznevich. Faster fusion: St40, engineering, commissioning, first results. *AIP Conference Proceedings*, 2179(1):020008, 2019.

[84] J. Harrison, et al. Overview of new MAST physics in anticipation of first results from MAST upgrade. *Nuclear Fusion*, 59(11):112011, 2019.

[85] S. Doyle, et al. Magnetic equilibrium design for the smart tokamak. *Fusion Engineering and Design*, 171:112706, 2021.

[86] M. Banks. UK announces five potential sites for prototype energy plant. *Physics World*, 34(11):10ii, 2021.

[87] J. Shimwell, J. Billingsley, R. Delaporte-Mathurin, D. Morbey, M. Bluteau, P. Shriwise, and A. Davis. The paramak: automated parametric geometry construction for fusion reactor designs. *F1000Research*, 10, 2021.

[88] M. Fontana, L. Porte, S. Coda, and O. S. and. The effect of triangularity on fluctuations in a tokamak plasma. *Nuclear Fusion*, 58(2):024002, 2017.

[89] M. E. Austin, et al. Achievement of reactor-relevant performance in negative triangularity shape in the diii-d tokamak. *Phys. Rev. Lett.*, 122:115001, 2019.

[90] S. Saarelma, M. E. Austin, M. Knolker, A. Marinoni, C. Paz-Soldan, L. Schmitz, and P. B. Snyder. Ballooning instability preventing the h-mode access in plasmas with negative triangularity shape on the DIII–d tokamak. *Plasma Physics and Controlled Fusion*, 63(10):105006, 2021.

[91] S. Medvedev, et al. The negative triangularity tokamak: stability limits and prospects as a fusion energy system. *Nuclear Fusion*, 55(6):063013, 2015.

[92] H. Wilson, D. Dickinson, B. Patel, and M. S. Anastopoulos Tzanis. Tdotp high-beta st plasma equilibria, 2021.

[93] H. Wilson. Scene—simulation of self-consistent equilibria with neoclassical effects, rep. Technical report, UKAEA-FUS-271, UKAEA Govt. Division, Fusion, Culham, UK, 1994.

[94] T. S. Hahm and K. H. Burrell. Flow shear induced fluctuation suppression in finite aspect ratio shaped tokamak plasma. *Physics of Plasmas*, 2(5):1648, 1995.

[95] D. J. Applegate, et al. Microstability in a “mast-like” high confinement mode spherical tokamak equilibrium. *Physics of Plasmas*, 11(11):5085, 2004.

[96] W. Tang, G. Rewoldt, C. Cheng, and M. Chance. Kinetic analysis of MHD ballooning modes in tokamaks. *Nuclear Fusion*, 25(2):151, 1985.

[97] P. Snyder and G. Hammett. Electromagnetic effects on plasma microturbulence and transport. *Physics of Plasmas*, 8(3):744, 2001.

[98] M. J. Pueschel, P. W. Terry, F. Jenko, D. R. Hatch, W. M. Nevins, T. Görler, and D. Told. Extreme heat fluxes in gyrokinetic simulations: A new critical β. *Phys. Rev. Lett.*, 110:155005, 2013.

[99] I. McKinney, M. Pueschel, B. Faber, C. Hegna, A. Ishizawa, and P. Terry. Kinetic-ballooning-mode turbulence in low-average-magnetic-shear equilibria. *Journal of Plasma Physics*, 87(3), 2021.

[100] J. Graves, D. Zullino, D. Brunetti, S. Lanthaler, and C. Wahlberg. Reduced models for parallel magnetic field fluctuations and their impact on pressure gradient driven mhd instabilities in axisymmetric toroidal plasmas. *Plasma Physics and Controlled Fusion*, 61(10):104003, 2019.

[101] T. Taylor. Physics of advanced tokamaks. *Plasma Physics and Controlled Fusion*, 39(12B):B47, 1997.

[102] M. Hardman, et al. New stability parameter to describe low-β electromagnetic microinstabilities driven by passing electrons in axisymmetric toroidal geometry. *arXiv preprint arXiv:2208.10615*, 2022.

[103] D. R. Durran. *Numerical methods for fluid dynamics: With applications to geophysics*, volume 32. Springer Science & Business Media, 2010.

[104] E. Sánchez, et al. Collisionless damping of flows in the TJ-II stellarator. *Plasma Physics and Controlled Fusion*, 55(1):014015, 2012.

[105] M. NUNAMI, T.-H. WATANABE, and H. SUGAMA. Gyrokinetic vlasov code including full three-dimensional geometry of experiments. *Plasma and Fusion Research*, 5:016, 2010.

[106] P. Xanthopoulos, G. Plunk, A. Zocco, and P. Helander. Intrinsic turbulence stabilization in a stellarator. *Physical Review X*, 6(2):021033, 2016.

[107] N. R. Mandell, G. W. Hammett, A. Hakim, and M. Francisquez. Reduction of transport due to magnetic shear in gyrokinetic simulations of the scrape-off layer. *Plasma Physics and Controlled Fusion*, 64(8):085006, 2022.

[108] G. G. Howes, S. C. Cowley, W. Dorland, G. W. Hammett, E. Quataert, and A. A. Schekochihin. Astrophysical gyrokinetics: basic equations and linear theory. *The Astrophysical Journal*, 651(1):590, 2006.

[109] L. Chen, F. Zonca, and Y. Lin. Physics of kinetic alfvén waves: a gyrokinetic theory approach. *Reviews of Modern Plasma Physics*, 5(1):1, 2021.

[110] M. Giacomin. Private correspondance.

[111] L. Spitzer Jr. Project matterhorn report. Technical report, PM-S-1 NYO-993, Princeton University, 1951.

[112] D. D.-M. Ho and R. M. Kulsrud. Neoclassical transport in stellarators. *The Physics of fluids*, 30(2):442, 1987.

[113] P. Helander. Theory of plasma confinement in non-axisymmetric magnetic fields. *Reports on Progress in Physics*, 77(8):087001, 2014.

[114] P. Helander. Theory of plasma confinement in non-axisymmetric magnetic fields. *Reports on Progress in Physics*, 77(8):087001, 2014.

[115] J. Nührenberg and R. Zille. Stable stellarators with medium β and aspect ratio. *Physics Letters A*, 114(3):129, 1986.

[116] R. Wolf, et al. Major results from the first plasma campaign of the wendelstein 7-x stellarator. *Nuclear Fusion*, 57(10):102020, 2017.

[117] C. Beidler, et al. Demonstration of reduced neoclassical energy transport in wendelstein 7-x. *Nature*, 596(7871):221, 2021.

[118] T. Klinger, et al. Overview of first wendelstein 7-x high-performance operation. *Nuclear Fusion*, 59(11):112004, 2019.

[119] D. Carralero, et al. An experimental characterization of core turbulence regimes in wendelstein 7-x. *Nuclear Fusion*, 61(9):096015, 2021.

[120] P. Helander, J. H. E. Proll, and G. G. Plunk. Collisionless microinstabilities in stellarators. i. analytical theory of trapped-particle modes. *Physics of Plasmas*, 20(12):122505, 2013.

[121] J. H. E. Proll, P. Xanthopoulos, and P. Helander. Collisionless microinstabilities in stellarators. ii. numerical simulations. *Physics of Plasmas*, 20(12):122506, 2013.

[122] P. Helander and A. Zocco. Quasilinear particle transport from gyrokinetic instabilities in general magnetic geometry. *Plasma Physics and Controlled Fusion*, 60(8):084006, 2018.

[123] J. García-Regaña, et al. Turbulent impurity transport simulations in wendelstein 7-x plasmas. *Journal of Plasma Physics*, 87(1), 2021.

[124] A. H. Boozer. Plasma equilibrium with rational magnetic surfaces. *The Physics of Fluids*, 24(11):1999, 1981.

[125] D. Garren and A. H. Boozer. Existence of quasihelically symmetric stellarators. *Physics of Fluids B: Plasma Physics*, 3(10):2822, 1991.

[126] J. R. Cary and S. G. Shasharina. Omnigenity and quasihelicity in helical plasma confinement systems. *Physics of Plasmas*, 4(9):3323, 1997.

[127] M. Landreman and E. Paul. Magnetic fields with precise quasisymmetry for plasma confinement. *Physical Review Letters*, 128(3):035001, 2022.

[128] G. Grieger, et al. Physics optimization of stellarators. *Physics of Fluids B: Plasma Physics*, 4(7):2081, 1992.

[129] H. Ringler, U. Gasparino, G. Kuhner, H. Maassberg, H. Renner, and F. Sardei. Confinement studies on the wendelstein vii-as stellarator. *Plasma Physics and Controlled Fusion*, 32(11):933, 1990.

[130] M. N. Rosenbluth. Low-frequency limit of interchange instability. *The Physics of Fluids*, 11(4):869, 1968.

[131] T. Andreeva. Vacuum magnetic configurations of wendelstein 7-x. 2002.

[132] S. Lazerson, J. Schmitt, C. Zhu, J. Breslau, A. STELLOPT Developers, and U. O. of Science. Stellopt, version 2.7.5, 2020.

[133] S. C. Cowley, R. Kulsrud, and R. Sudan. Considerations of ion-temperature-gradient-driven turbulence. *Physics of Fluids B: Plasma Physics*, 3(10):2767, 1991.

[134] A. Mollén, I. Pusztai, T. Fülöp, and S. Moradi. Impurity transport in trapped electron mode driven turbulence. *Physics of Plasmas*, 20(3):032310, 2013.

[135] P. Helander, T. Bird, F. Jenko, R. Kleiber, G. Plunk, J. Proll, J. Riemann, and P. Xanthopoulos. Advances in stellarator gyrokinetics. *Nuclear Fusion*, 55(5):053030, 2015.

[136] H. Thienpondt, J. M. García-Regaña, I. Calvo, M. Barnes, F. Parra, and R. Davies. Turbulent heat flux versus density gradient at finite ion temperature gradient: An intermachine study with the gyrokinetic code stella. *23rd International Stellarator-Heliotron Workshop, Warsaw 2022*, 2022.

[137] H. Thienpondt, J. M. García-Regaña, and I. Calvo. In preparation. *In preparation*, 2022.

[138] P. Xanthopoulos, et al. Turbulence mechanisms of enhanced performance stellarator plasmas. *Physical Review Letters*, 125(7):075001, 2020.

[139] `https://bitbucket.org/gyrokinetics/gs2/issues/97/electromagnetic-case-bakdif-nonzero-gives`. Accessed: 2022-10-05.

[140] `https://gyrokinetics.gitlab.io/gs2/page/namelists/index.html`. Accessed: 2022-10-05.

[141] P. Mulholland. Private correspondance.

[142] I. McKinney, M. Pueschel, B. Faber, C. Hegna, J. Talmadge, D. Anderson, H. Mynick, and P. Xanthopoulos. A comparison of turbulent transport in a quasi-helical and a quasi-axisymmetric stellarator. *Journal of Plasma Physics*, 85(5), 2019.

[143] K. Aleynikova, A. Zocco, and J. Geiger. Influence of magnetic configuration properties on kinetic ballooning modes in w7-x. *Journal of Plasma Physics*, 88(4):905880411, 2022.

[144] F. Jenko, W. Dorland, M. Kotschenreuther, and B. Rogers. Electron temperature gradient driven turbulence. *Physics of plasmas*, 7(5):1904, 2000.

[145] J. Candy, E. A. Belli, and R. Bravenec. A high-accuracy eulerian gyrokinetic solver for collisional plasmas. *Journal of Computational Physics*, 324:73, 2016.

[146] H. Ritchie. Eliminating the interpolation associated with the semi-lagrangian scheme. *Monthly Weather Review*, 114(1):135, 1986.

[147] H. Dudding, F. Casson, D. Dickinson, B. Patel, C. Roach, E. Belli, and G. Staebler. A new

quasilinear saturation rule for tokamak turbulence with application to the isotope scaling of transport. *Nuclear Fusion*, 62(9):096005, 2022.

[148] K. Itoh, S.-I. Itoh, P. Diamond, T. Hahm, A. Fujisawa, G. Tynan, M. Yagi, and Y. Nagashima. Physics of zonal flows. *Physics of plasmas*, 13(5):055502, 2006.

[149] P. H. Diamond, S. Itoh, K. Itoh, and T. Hahm. Zonal flows in plasma—a review. *Plasma Physics and Controlled Fusion*, 47(5):R35, 2005.

[150] H. Biglari, P. Diamond, and P. Terry. Influence of sheared poloidal rotation on edge turbulence. *Physics of Fluids B: Plasma Physics*, 2(1):1, 1990.

[151] T.-H. Watanabe, H. Sugama, and S. Ferrando-Margalet. Gyrokinetic simulation of zonal flows and ion temperature gradient turbulence in helical systems. *Nuclear fusion*, 47(9):1383, 2007.

[152] M. Pueschel, P. Terry, F. Jenko, D. Hatch, W. Nevins, T. Görler, and D. Told. Extreme heat fluxes in gyrokinetic simulations: A new critical β. *Physical Review Letters*, 110(15):155005, 2013.

[153] A. Staniforth and J. Côté. Semi-lagrangian integration schemes for atmospheric models—a review. *Monthly weather review*, 119(9):2206, 1991.